GAS PHASE CATALYTIC HYDROGENATION OF ALKYNOLS OVER PALLADIUM AND NICKEL CATALYTS

ALBERTO GONZÁLEZ-FERNÁNDEZ

Submitted for the degree of Doctor of Philosophy

Heriot-Watt University

School of Engineering and Physical Sciences

April 2020

Abstract

The focus of this thesis is the development of catalytic systems (*i.e.* supported Pd- and Ni-based catalysts and bulk Mo_2N) for partial -C≡C- bond hydrogenation in the transformation of functionalised alkynes directed at sustainable chemical processing. The continuous gas phase hydrogenation of 2-methyl-3-butyn-2-ol (to 2-methyl-3-buten-2-ol), 3-butyn-2-ol (to 3-buten-2-ol, 3BE), 3-butyn-1-ol (to 3-buten-1-ol, 3BEOL), acetylene (to ethylene) and phenylacetylene (to styrene) has been performed at atmospheric pressure at 373-453 K. A range of characterisation techniques (AAS, H_2-TPR, H_2-TPD, H_2 chemisorption, SSA, XPS, SEM, TEM, STEM, EDX) have been used to unravel the bulk and surface catalytic properties. Thermodynamic and mechanistic kinetic analyses have been employed to evaluate catalytic performance. In the hydrogenation of 3-butyn-1-ol , 3-butyn-2-ol and 2-methyl-3-butyn-2-ol over Pd/Al_2O_3 the reaction follows an electrophilic mechanism where the triple bond electron density is affected by the number of electron donating methyl groups and the position of the hydroxyl functionality, *i.e.* increase activity increasing the number of $-CH_3$ groups. Thermal treatment of Pd/ZnO results in the formation of a β-phase PdZn alloy that promotes partial -C≡C- → -C=C- bond hydrogenation but at low conversions, attributed to metal particle encapsulation by the ZnO support. The synthesis of Al_2O_3 supported colloidal Pd-Zn catalysts serves to control alloy composition and avoid metal encapsulation while attaining high selectivity to target alkenol. We probe a direct correlation between alkynol hydrogenation rate and surface hydrogen where the nature of the carrier (carbon, Al_2O_3, MgO, CeO_2) affects the electronic properties of the palladium phase but does not alter significantly catalytic performance. Undesired isomerisation (to 2-butanone) is promoted in the hydrogenation of 3-butyn-2-ol over Pd but not over Ni, although the latter delivers low activity due to limited hydrogen uptake capacity. A $Pd\text{-}Ni/Al_2O_3$ catalyst (Pd: Ni = 1:1) delivers increase activity and 3-buten-2-ol (selectivity, which we attribute to formation of PdNi nanoparticles. We have also considered the catalytic response over bulk NiZn alloys and Mo nitride catalysts. Variations in Zn content results in the generation of several NiZn alloys with different crystallographic phase (*i.e.* α-NiZn, β-NiZn and δ-NiZn) with α-NiZn delivering the highest alkenol production in the hydrogenation of 3-butyn-2-ol. We also demonstrate that catalytic activity can be enhanced by spillover hydrogen for reaction over α-NiZn/ZnO. γ-Mo_2N promotes the partial hydrogenation of acetylene, phenylacetylene and 2-methyl-3-butyn-2-ol where incorporation of palladium in trace amounts serves to elevate surface hydrogen concentration and catalytic activity.

Dedication

To my beloved grandparents (Tomás, Concepción, Antonio and Antonia) and uncles (Rafael and Tomás). I will never forget you.

Research Thesis Submission

Please note this form should be bound into the submitted thesis.

Name:	Alberto González-Fernández		
School:	Engineering and Physical Sciences		
Version: *(i.e. First, Resubmission, Final)*	Final	Degree Sought:	Doctor of Philosophy

Declaration

In accordance with the appropriate regulations I hereby submit my thesis and I declare that:

1. The thesis embodies the results of my own work and has been composed by myself
2. Where appropriate, I have made acknowledgement of the work of others
3. The thesis is the correct version for submission and is the same version as any electronic versions submitted*.
4. My thesis for the award referred to, deposited in the Heriot-Watt University Library, should be made available for loan or photocopying and be available via the Institutional Repository, subject to such conditions as the Librarian may require
5. I understand that as a student of the University I am required to abide by the Regulations of the University and to conform to its discipline.
6. I confirm that the thesis has been verified against plagiarism via an approved plagiarism detection application e.g. Turnitin.

ONLY for submissions including published works

Please note you are only required to complete the Inclusion of Published Works Form (page 2) if your thesis contains published works)

7. Where the thesis contains published outputs under Regulation 6 (9.1.2) or Regulation 43 (9) these are accompanied by a critical review which accurately describes my contribution to the research and, for multi-author outputs, a signed declaration indicating the contribution of each author (complete)
8. Inclusion of published outputs under Regulation 6 (9.1.2) or Regulation 43 (9) shall not constitute plagiarism.

* *Please note that it is the responsibility of the candidate to ensure that the correct version of the thesis is submitted.*

Signature of Candidate:	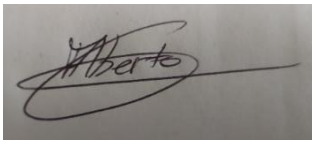	Date:	26/08/2020

Submission

Submitted By *(name in capitals):*	ALBERTO GONZÁLEZ-FERNÁNDEZ
Signature of Individual Submitting:	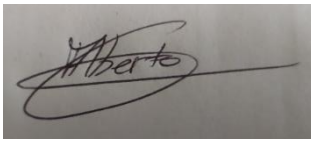
Date Submitted:	26/08/2020

For Completion in the Student Service Centre (SSC)

Limited Access	Requested	Yes		No		Approved	Yes		No	
E-thesis Submitted (mandatory for final theses)										
Received in the SSC by *(name in capitals):*						Date:				

Inclusion of Published Works

Please note you are only required to complete the Inclusion of Published Works Form if your thesis contains published works under Regulation 6 (9.1.2)

Declaration

This thesis contains one or more multi-author published works. In accordance with Regulation 6 (9.1.2) I hereby declare that the contributions of each author to these publications is as follows:

Citation details	Alberto González-Fernández and Chiara Pischetola, Gas Phase Catalytic Hydrogenation of C4 Alkynols over Pd/Al_2O_3, Catalysts, 9, 924--936
Author 1	Experimental and writing work
Author 2	Assistance in writing work and graphical editing/formatting
Signature:	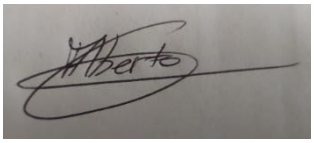
Date:	26/08/2020

Citation details	Alberto González-Fernández and Chiara Pischetola, Partial Hydrogenation of 2-Methyl-3-butyn-2-ol over Pd/ZnO: Effect of Reduction Temperature on Alloy Formation and0 Catalytic Response, Journal of Physical Chemistry C, 124, 3681-3691 (2020).
Author 1	Experimental and writing work
Author 2	Assistance in writing work and graphical editing/formatting
Signature:	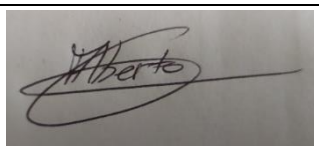
Date:	26/08/2020

Citation details	A. González-Fernández, Á. Berenguer-Murcia, D. Cazorla-Amorós, F. Cárdenas-Lizana, Zn-Promoted Selective Gas-Phase Hydrogenation of Tertiary and Secondary C4 Alkynols over Supported Pd, ACS Appl. Mater. Interfaces. 12 28158–28168 (2020).
Author 1	Experimental and writing work
Author 2	Assistance in experimental and writing work
Signature:	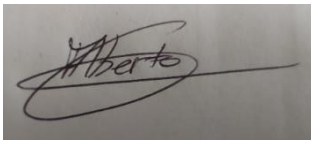

Date:	26/08/2020

Please included additional citations as required.

Acknowledgements

I would like to express my sincere appreciation to my supervisors Fernando Cárdenas-Lizana and Mark A. Keane for their guidance during these years. There have been difficult moments where things were not working well and you were able to motivate me to keep pushing and pursuing where I am now. Also, I would like to thank Prof. Stuart Macgregor and Kevin Jones for their assistance and training in the early stages of my PhD as CRITICAT coordinators. It has been a pleasure to meet you and I learned a lot from all of you.

I would like to acknowledge my colleagues Pedro Benavente, Kamil Mustafin and Jaime García. I wish you could have been typing the same acknowledgment words that I am doing now. They deserved a better ending and I feel that part of this thesis belongs to them too. Also, I would like to thank my research colleague Chiara Pischetola for her help and aiding in part of my work: In a few months she will become a doctor and I wish her the best. Also, I would like to thank my office mate, Kelly Stewart as well as Francisca Navarro, Riccardo Maione, Lyes Ait Ali Yahia, Laura Collado and Javier Formo, for all the unforgettable conversations and moments that we shared, either by walking through the endless University corridor or by having a fancy coffee during break times. I considered them as a part of my family in these years that we shared together.

Many thanks to the staff in the chemical engineering department, with special mention to Cameron Smith, Douglas Wagener, Richard Kinsella and Mary Pratt: Your assistance was essential and made the rest of the work easier. My eternal gratitude to all the people that makes the university work. Heriot Watt administration staff office and CRITICAT-CDT for financial support are also acknowledged.

To end with, the special dedication goes to the people I love most. To my parents, Antonio and Concepción, for all the unconditional affection and support that they showed me during all my life. I could not be the person I am now without the meaningful life lessons I learnt from them and I wish they could be by my side in these hard moments of confinement. The last dedication goes to my girlfriend and partner in life, Angela García, who has suffered me during all these years of hard work: you have helped me in making my life happier and easier in all the senses. Half of this thesis at least belongs to you.

Table of Contents

List of Tables

List of Figures

Glossary:

Acronym	
3BYOL	3-butyn-1-ol
3BEOL	3-buten-1-ol
BOL	1-butanol
2BEOL	Crotyl alcohol
BHDE	butyraldehyde
AAS	Atomic Absorption Spectroscopy
BA	2-butanol
BE	Binding Energy
3BE	3-buten-2-ol
BET	Brunauer-Emmet-Teller theory; measurements of surface area
BONE	2-Butanone
3BY	3-butyn-2-ol
DP	Deposition-Precipitation
EDX	Energy Dispersive X-Ray
EXAFS	Extended X-ray Atomic Fine Structure
FCC	Face Centred Cubic
FWHM	Full Width at Half Maximum
GHSV	Gas Hourly Space Velocity
GL	Gaussian Lorentzian
HCP	Hexagonal Close Packed
HRSEM	High Resolution Scanning Electron Microscopy
ICP-OES	Inductively Coupled Plasma-Optical Emission Spectroscopy
JCPDS-	Joint Committee on Powder Diffraction Standards-
ICDD	International Centre for Diffraction Data
MBA	2-methyl-butan-2-ol
MBE	2-methyl-3-buten-2-ol
MBY	2-methyl-3-butyn-2-ol
PVP	Polyvinylpyrrolidone
SEM	Scanning Electron Microscopy
SSA	Specific Surface Area
STEM	Scanning Transmission Electron Microscopy
TCD	Thermal Conductivity Detector

TEM	Transmission Electron Microscopy
TOF	Turnover Frequency
TPD	Temperature-Programmed Desorption
TPR	Temperature-Programmed Reduction
XANES	X-ray Absorption Near Edge Structure
XPS	X-ray Photoelectron Spectroscopy
XRD	X-Ray Diffraction
SMSI	Strong Metal Support Interaction

Symbols

d_i	Diameter of particles counted on TEM analysis
d	Number weighted mean metal diameter
d_{TEM}	Surface area weighted metal particle size estimated from TEM analysis
d_{hkl}	Crystal particle size determined by Sherrer equation
d_{H_2}	Particle size determined by room temperature H_2 chemisorption
D	Metal dispersion
E_{ads}	Adhesion energy
F_{in}	Inlet organic reactant molar flow
$I_{(hkl)}$	Diffraction peak intensity on (hkl) plane
(*i.d.*)	Internal diameter
k_i	Pseudo-first order kinetic rate constant
m	Mass of the catalysts
$n_{i\ in}$	Number of moles of reactant in the inlet stream
$n_{i\ out}$	Number of moles of reactant in the outlet stream
n_i	Number of particles counted on TEM analysis
N/Mo	Surface mol ratio nitrogen to Molybdenum
R	Reactant transformation rate
S	Selectivity
t	Sample thickness
W	Catalysts mass
X_i	Reactant conversion
Z	Atomic number contrast
x_i	Mol fraction
β	Peak width at the half maximum intensity
ΔNi 2p	Satellite intensity difference with the main Ni 2$p_{3/2}$ and Ni 2$p_{1/2}$ peaks
ΔG	Gibbs free energy formation
θ	Diffraction angles corresponding to the main planes
$[\ ]_{in}$	Reactant/product mol inlet
$[\ ]_{out}$	Reactant/product mol outlet

List of Publications by the candidate:

[1] González-Fernández, A.; Pischetola, C.; Cárdenas-Lizana, F. Gas Phase Catalytic Hydrogenation of C4 Alkynols over Pd/Al_2O_3. *Catalysts* **2019**, *9* (11), 924–936. **(Chapter 2).**

[2] González-Fernández, A.; Pischetola, C.; Kiwi-Minsker, L.; Cardenas-Lizana, F. Partial Hydrogenation of 2-Methyl-3-Butyn-2-ol over Pd/ZnO: Effect of Reduction Temperature on Alloy Formation and Catalytic Response. *J. Phys. Chem. C* **2020**, *124*, 3681-3691 **(Chapter 3).**

[3] González-Fernández, A.; Berenguer-Murcia, D; Cazorla-Amorós, A.; Cardenas-Lizana, Zinc Promoted Selective Gas Phase Hydrogenation of Tertiary and Secondary C4 Alkynols over Supported Pd, *ACS Appl. Mater. Interf.* **2020**, *12*, 28158-28168. **(Chapter 4).**

List of presentations by the Candidate:

[1] Oral presentation at SURCAT ECOSSE (10-2018).

[2] Oral presentation at CRITICAT CONFERENCE (4-2018).

Chapter 1:

Introduction and Scope of the Thesis

This chapter shows a short overview of the sustainable chemical processing, with a focus on selective hydrogenation of alkynols over different transition metals (*e.g.* Pd and Ni). The objectives of this PhD research are defined, and the approach taken is described.

1.1 Sustainable Chemical Processing and Selective Hydrogenation.

The chemical industry has a direct impact on the environment [1] due to production of toxic waste and high energy demand [2]. As a result, over the last decade more restrictive environmental legislation has resulted in a pressing demand for the development of more sustainable processes [3]. “Green chemistry” aims to minimise waste and can be effectively quantified by the "E factor" (kg waste produced kg product^{-1}) [2]. The selective hydrogenation of alkynols plays a key role in the synthesis of vitamins (*e.g.* A, E, K [4,5]), nutraceuticals and carotenoids (*e.g.* resveratrol and β-carotene [6]), bioactive ingredients of the fine chemical sector [5]. The fine chemical industry has a high associated E factor (5-50 kg waste kg product^{-1} *vs.* 0.1-5 kg waste kg product^{-1} for the oil and bulk chemicals industry) [7]. Consequently, process optimisation is key in this sector.

The demand for bioactive chemicals has increased significantly in recent years [8] with research on selective alkynol hydrogenation focused on: i) alternative reactor configurations that improve energy efficiency, reducing operational costs [9,10] and ii) catalyst design to maximise alkenol selectivity [11]. A transition from batch to continuous operation has gained increasing attention since it is favoured by large scale production with easy scale-up, higher throughput and without dead times [12]. A short review on the lines of investigation in catalyst optimisation directed at increasing -C=C- bond selectivity in alkynol hydrogenation is provided in the following section.

1.2 Transition Metal Catalysts Used in Selective Hydrogenation

Selective -C≡C- → -C=C- bond hydrogenation has been extensively studied since the 50s-60s, at which point there was a fast development of polyethylene and stereoselective hydrogenated chemicals in the pharma industry [13,14]. Among all the transition metals considered, Pd is the transition metal that delivers the highest olefin yield and selectivity [15]. The great catalytic performance of Pd in selective -C≡C- hydrogenation, is ascribed to its unique electronic properties as it is the only transition metal with a $4d^{10}5s^{0}$ electronic valence (in which 0.36 e^- in the d orbital are transferred to the 5s.) [16]. The Pd d-valence band feature enhances H_2 chemisorption compared to other group VIII transition metals [17] and minimizes the C≡C- and -C=C- adsorption strength due to an e^- donation decrease between the π-bond of the unsaturations and the metal catalysts. A reduction in the electronic transfer between the substrates and the catalyst in selective hydrogenation avoids: i) the formation of very stable and unreactive chemisorbed C≡C species and/or ii) the presence of highly coordinated chemisorbed -C=C- intermediates that do not desorb from the catalyst surface until they are fully hydrogenated [18]. **Figure 1.1** depicts a typical reaction scheme on -C≡C- hydrogenation. In order to be selective to -C=C- manufacture, several strategies can be followed where one of the following factors must control the catalytic hydrogenation:

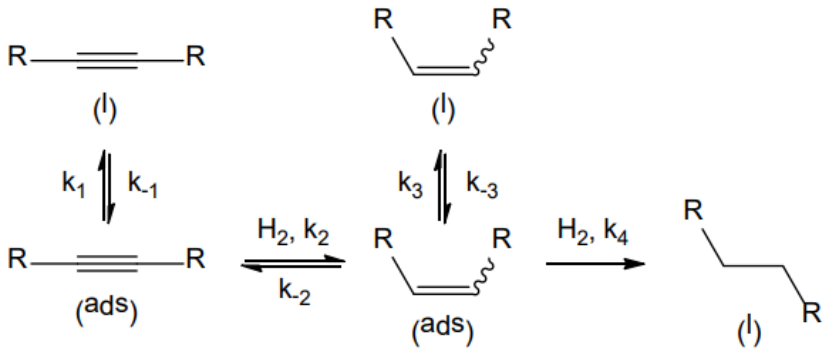

Figure 1.1: Proposed reaction steps on selective hydrogenation using a model alkyne [19].

a) **Kinetic factor:** When the rate of formation of the intermediate (k_2 in **Figure 1.1**) on the catalyst is considerably higher than its rate of consumption (k_4 in **Figure 1.1**).

b) **Thermodynamic factor:** When the adsorption equilibrium (k_1/k_{-1}) of the reactant on the catalyst is considerably higher than for the intermediate (k_3/k_{-3}), forcing the intermediate surface desorption and preventing its readsorption.

The high selectivities achieved on -C≡C- hydrogenation using Pd based catalysts are conventionally linked to the thermodynamic factor, considering the higher adsorption strength of -C≡C- (-1.6 eV) compared to -C=C- (1.0 eV) [20]. Nonetheless, still the C=C-bond selectivities achieved by using monometallic Pd catalysts are far from satisfactory to the industrial requirements [21]. The impossibility to be fully -C=C- selective, is linked to the complex number of surface intermediates identified by using surface science techniques (*e.g*. FT-IR, EELS, etc.) over Pd surface [22] (see **Figure 1.2),** each of them having a different role in the products formed in the reaction.

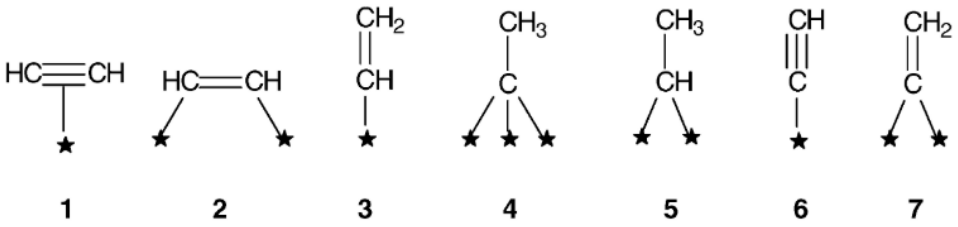

Figure 1.2: Suggested surface intermediates formed in acetylene hydrogenation. Reprinted from Ref. [22]**.** Copyright 2001, with permission from Elsevier.

The -C≡C- functional group can chemisorb to Pd either associatively, *via* π or di-σ chemisorbed bonds, (**Figure 1.2**, 1 and 2) or dissociatively (**Figure 1.2,** 6 and 7). On associatively chemisorbed fashion mode, the semi-hydrogenation of π /di-σ chemisorbed -C≡C- leads to the chemisorbed vinyl specie (**Figure 1.2**, 3) which with a further semi-hydrogenation step leads to -C=C- formation. During hydrogenation, also multi-bonded carbon species with the catalysts such as ethylidyne (**Figure 1.2**, 4) and ethylidene (**Figure 1.2**, 5) are formed, which are responsible for the single bond formation during over-hydrogenation [23]. Additionally, on longer aliphatic -C≡C- chains (*e.g*. propyne, butyne), other side reactions such as double bond migration occurs, linked to the π-allyl intermediate formation [24]. The multi-bonded chemisorbed species formed between the (-C≡C- and -C=C-) unsaturations and the catalysts is linked to two main factors:

a) **Electronical factor:** Electron deficient Pd active sites promotes C-H cleavage leading to the formation of multi-bonded chemisorbed -C≡C- [25] (*e.g*. ethylidyne) that favours over-hydrogenation and double bond migration side reaction steps [26,27].

b) **Geometrical factor:** The chemisorbed multi-bonded species requires the coordination of the -C≡C- with several Pd atoms and their accommodation is easier on big ensembles sizes [28].

With respect to the dissociatively -C≡C- chemisorbed species (**Figure 1.2,** 6 and 7 species) are linked to green oil formation [29]. Due to the variety of surface intermediates found on Pd surface, several reaction schemes have been proposed during the last decades [30–32]. As an illustrate example, **Figure 1.3 s**hows the reaction mechanism proposed by Molnar *et. al* [22] , using acetylene as a probe molecule.

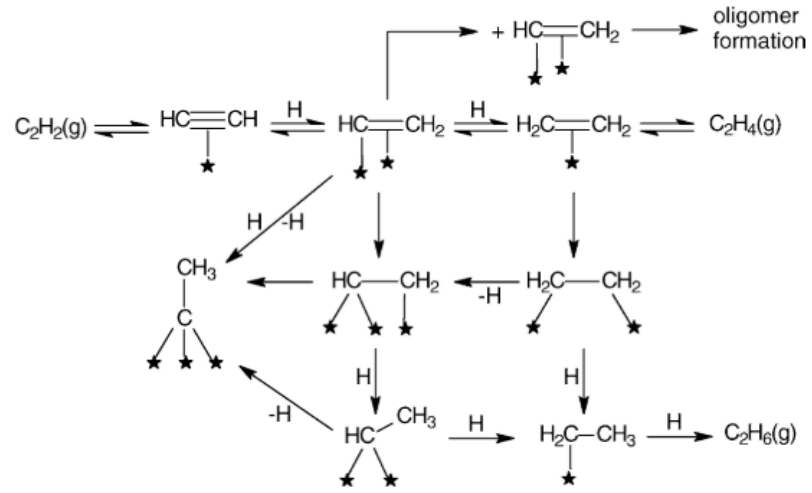

.

Figure 1.3: Proposed reaction scheme in acetylene hydrogenation. Reprinted from Ref. [22]**.** Copyright 2001, with permission from Elsevier.

Several strategies have been considered to improve the selectivity to the target alkene, primarily

a) **Use of additives**: The usage of additives in trace amounts act as a transient selective poison competing with olefin for adsorption sites. In gas phase operation, CO has been used as a promoter for partial acetylene hydrogenation [22]. The Pd adsorption strength with hydrocarbons can be classified in the following order [21]:

CO > Alkyne > > alkadiene > >olefins.

In an industrial operation, in conditions in which acetylene concentrations are low (1-5 ppm) there would be an insufficient number of -C≡C- molecules that inhibits the adsorption of -C=C- [21]. For those cases, the CO molecules used as promoter tend to occupy those active sites. On the other hand, nitrogen-based molecules (*e.g.* piperidine, quinoline) have been employed in the liquid phase hydrogenation of (1-butyne and 3-methyl-1-pentyn-3-ol) [33,34]. Furthermore, the interaction of N with Pd leads to changes in palladium electron density that impact on catalytic activity and selectivity [22].

b) **Use of a second metal:** The addition of a second metal aims to modify, at the same time, both the electronic and geometric structure of monometallic Pd, leading to an increase in -C=C- bond selectivity [35]. With regards to Pd electronical configuration, the addition of a second metal can impact in a decrease of the reactants and intermediate adsorption strengths that favours the (-C≡C-/-C=C-) surface displacement ratio. The changes in the adsorption energy is visualized in **Figure 1.4,** where the different adsorption strength of the reactant and intermediate has been calculated *via* DFT calculations.

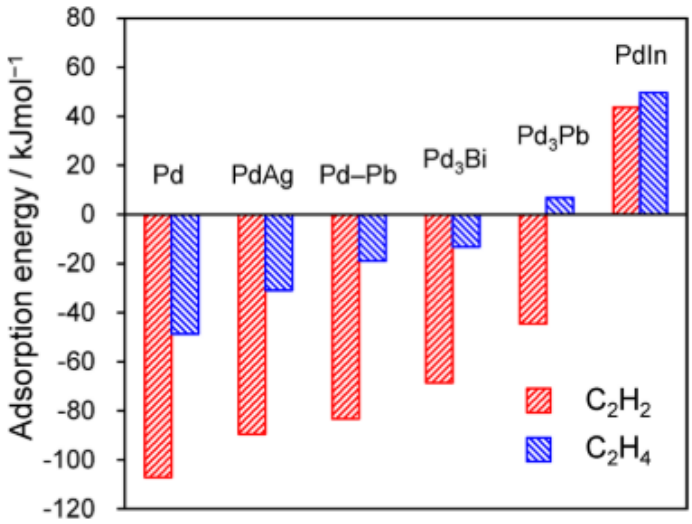

Figure 1.4: Calculated adsorption energies of di-σ bonded acetylene and ethylene on the surfaces of various Pd-based surfaces: Pd (111). Reprinted from Ref [36]**.** Copyright 2006, with permission from American Chemical Society**.**

With respect to the geometrical modifications induced on Pd catalysts, the addition of a second metal can dilute the Pd surface, reducing the Pd surface ensembles sizes. The effect of a second metal in the Pd surface ensembles effects can be clearly visualised in **Figure 1.5,** in which the isolation of Pd atoms in the surface force the -C≡C- to be chemisorbed exclusively *via* π-bond, preventing its surface complexation.

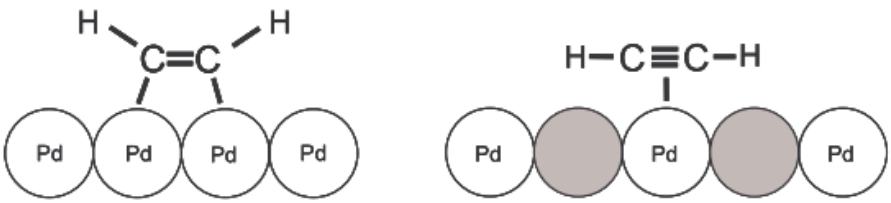

Figure 1.5: Representation of a di- σ bonded chemisorbed acetylene (left) and a weaker -bonded π acetylene molecule to an isolated Pd atom (right**)** [37] .

Additionally, the incorporation of a second metal into Pd structure can have an effect in blocking unselective active sites: Anderson et al [38] has shown that deposition of Bi and Pb metals over Pd metal occurs preferentially over surface defects (kinks, edges) and terraces that are linkers for -C=C- double bond migration and cis-trans isomerization steps respectively (see **Figure 1.6**) [38].

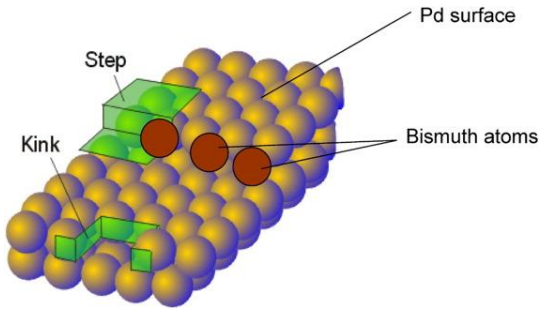

Figure 1.6: Representation of Pd surface in which Bi atoms preferentially deposits on low-coordinated step/edges sites**.** Reprinted from Ref**.** [38]. Copyright 2009, with permission from Elsevier**.**

Numerous second metals have been screened, from alkali/alkaline metals (Na, K, Mg, Ca, etc.) [39], to early and late transition metals (Nb, Ti, Cu, Ag, Au) [40,41], sp metals (Pb, Ga, Ge, etc.) [42–44] and lanthanides (*e.g.* Ce) [40,45]. Among them, the most commonly used on industrial scale are Lead, using Pd-Pb/$CaCO_3$ (Lindlar) catalyst for liquid phase fine chemicals manufacture, and Silver, using Pd-Ag/Al_2O_3 catalysts in gas phase steam reforming hydrogenation [46].

However, these approaches have had limited success and high selectivity to the target alkene remains a critical challenge. Additional modifiers (*e.g.* Zn and Bi) [11], and new catalyst synthetic routes (*e.g.* colloidal methodologies) are current strategies under consideration [47]. In addition, the combined high cost and low abundance of Pd has resulted in a search for alternative metals to promote selective alkyne hydrogenation [48].

c) **Use of Reducible Support (SMSI):** The reduction of the support impacts on the catalyst morphology (*e.g.* decrease of metal surface defects and ensemble sizes) *via* strong metal-support interaction (SMSI), which impacts in a -C=C- selectivity improvement [49,50]. **Figure 1.7** shows a schematic diagram that illustrates the SMSI effect on -C≡C- hydrogenation, in which a partial support reduction takes place by thermally treating the Pd supported catalyst under a H_2 flow. During the process, Pd active sites are covered partially or totally with a reduced oxide layer that results in a catalyst encapsulation [51]. Among all the supports chosen to induce SMSI effect, the most common in catalysis are those with a high capacity

of being reduced (*e.g.* CeO_2, TiO_2 and Fe_3O_4) [52]. In hydrogenation of unsaturated hydrocarbons, the selectivity enhancement with the use of this methodology has been recently review by several authors [52,53]

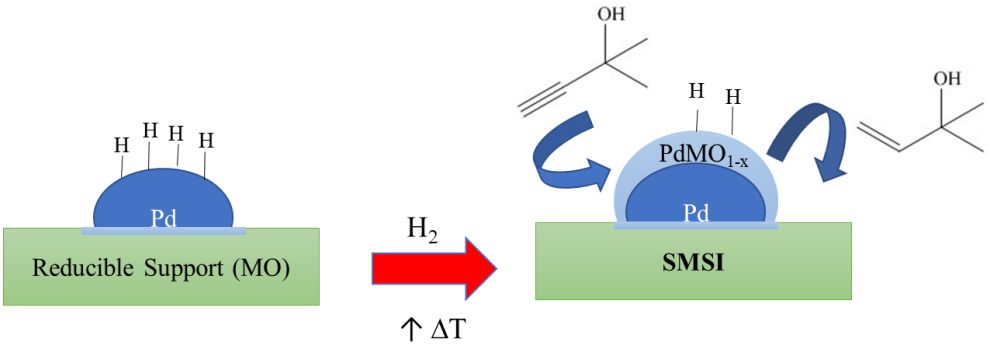

Figure 1.7: SMSI scheme applied to the selective hydrogenation of MBY.

More abundant and less expensive metals such as Fe or Cu have been considered [54], among which Ni shows promise. Hydrotalcite supported bimetallic Ni-Co and Ni-Cu catalysts delivered high olefin selectivity in the hydrogenation of acetylene at T=448 *K* and atmospheric pressure [55]. Theoretical work (DFT calculations) has suggested Zn as promising second metal [54], with NiZn exhibiting a similar -C=C-/-C≡C- adsorption strength as PdAg [56]. Further experimental work has confirmed an equivalent product distribution over γ-Ni_5Zn_{25} and PdAg alloys on acetylene hydrogenation [57]. Another research area that has emerged over the last few years is the use of alternative bulk materials, such as metal nitrides [58]. In particular, γ-Mo_2N shows promise for acetylene hydrogenation with selectivities comparable to those recorded over standard industrial catalysts ($S_{\text{Ethylene}} \geq 90\%$) [59,60], although the use of the these materials for selective hydrogenation is scarce. It is also worth mentioning the use of alternative metals such as Au and Ag which delivered high alkene selectivities but poor activity compared to Pd [61–63].

1.3 Reactor Configuration: Transition from batch to Fixed bed Plug Flow Reactor

The research of an alternative reactor in the transition from batch to continuous reactor has been developed during the last years towards a more efficient hydrogenation reaction. Batch reactors are closed systems where the reactant together with the catalysts and solvents are charged into the reactor, and remain in it for a defined reaction time under preselected H_2 pressure and temperature conditions [64]. This is an unsteady-state operation where concentration of the C≡C- reactant changes with time; where its mass balance follows this equation:

$$\left(r_{(C\equiv C}\right) = C_{(C\equiv C)0} \cdot \frac{dX_A}{dt} \quad \textbf{(1.1)}$$

Where the efficient stirring ensures uniform composition and temperatures over all the reactor volume [64,65]. For liquid phase hydrogenation of polyfunctional -C≡C- molecules (*e.g*. alkynols), a wide range of H_2 pressures (P_{H2} = 1-20 atm) and temperatures (T = 283-393 K) are used, being summarised in the work of Crespo-Quesada et.al [35]. The schematics of a batch pressurized reactor is displayed in **Figure 1.8:**

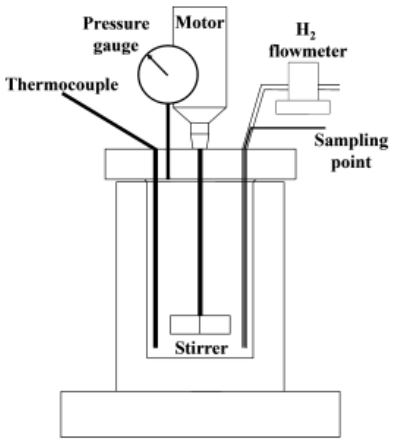

Figure 1.8: Slurry batch pressurized reactor scheme**.** Reprinted from Ref [66]**.** Copyright 2019, with permission from American Chemical Society**.**

Two major advantages that are associated with batch are namely flexibility (may be shut down easily and quickly) [65] and versatility of the equipment. However, these are counteracted with the high labour and handling cost operational procedures, with considerable shutdown time for emptying, heating and cooling of the reactor [64,65].

The switch from batch to continuous phase reactors resolves these limitations by working as an open system (the reactants are continuously introduced and the product extracted) under steady state conditions.

Several continuous reactors have been reported for selective hydrogenation reactions (capillary, packed-bed and monolithic reactors). Their performance is summarised by Marrodan et.al. [9]. In this thesis, for the selective hydrogenation of alkynols, a fixed bed plug-flow reactor is used for the first time, working in gas phase, under steady state regime and atmospheric conditions.

Apart from the simplicity and easy maintenance of a plug flow reactor [67], working under gas phase conditions allows for the removal of the liquid phase in which the alkynol is dissolved. The transition from triphasic (solid-liquid-gas) to biphasic (solid-gas) catalytic system improves the H_2 utilisation in the reaction [21] as the high H_2 pressures requirements to improve the gas solubility in the liquid solvent in batch reactors is no longer needed. At the same time, a gas-solid reaction facilitates the recovery of the solid catalysts [68] and enables control over the contact time (τ) between the solid catalyst and the gas reactants. As shown in **Equation 1.2**, the contact time between the reactant and catalysts can be easily tuned either by changing the volume of the catalysts on the bed, keeping the gas flow rate constant or *vice versa:*

$$\tau\ (s) = \frac{V_{bed}\ (cm^3)}{F\ (cm^3\ s^{-1})} \qquad \textbf{(1.2)}$$

Figure 1.9 shows a scheme of a continuous fixed-bed plug flow reactor, in which both reactants (H_2 and alkynol solution, blue and red arrow respectively in **Figure 1.9**) are continuously delivered co-axially through the top of the reactor. During the process, the gas feed (either H_2 or a mixture of N_2 and H_2) is controlled by the usage of mass flow controllers (blue arrow in **Figure 1.9**), whereas the alkynol reactant, is introduced from a calibrated infusion pump (red arrow in **Figure 1.9)**. The pressure induced by the syringe plunger into the alkynol solution, forces the falling of droplets (green arrow in **Figure 1.9**) that reaches a pre-heating zone of the reactor. In this area, it is ensured that the reactant is vaporised and diffuses through the catalysts bed where the reaction occurs. The effluents generated from the reaction are collected in a condenser (yellow arrow in **Figure 1.9**) and the sample obtained is treated *via* gas chromatography analysis.

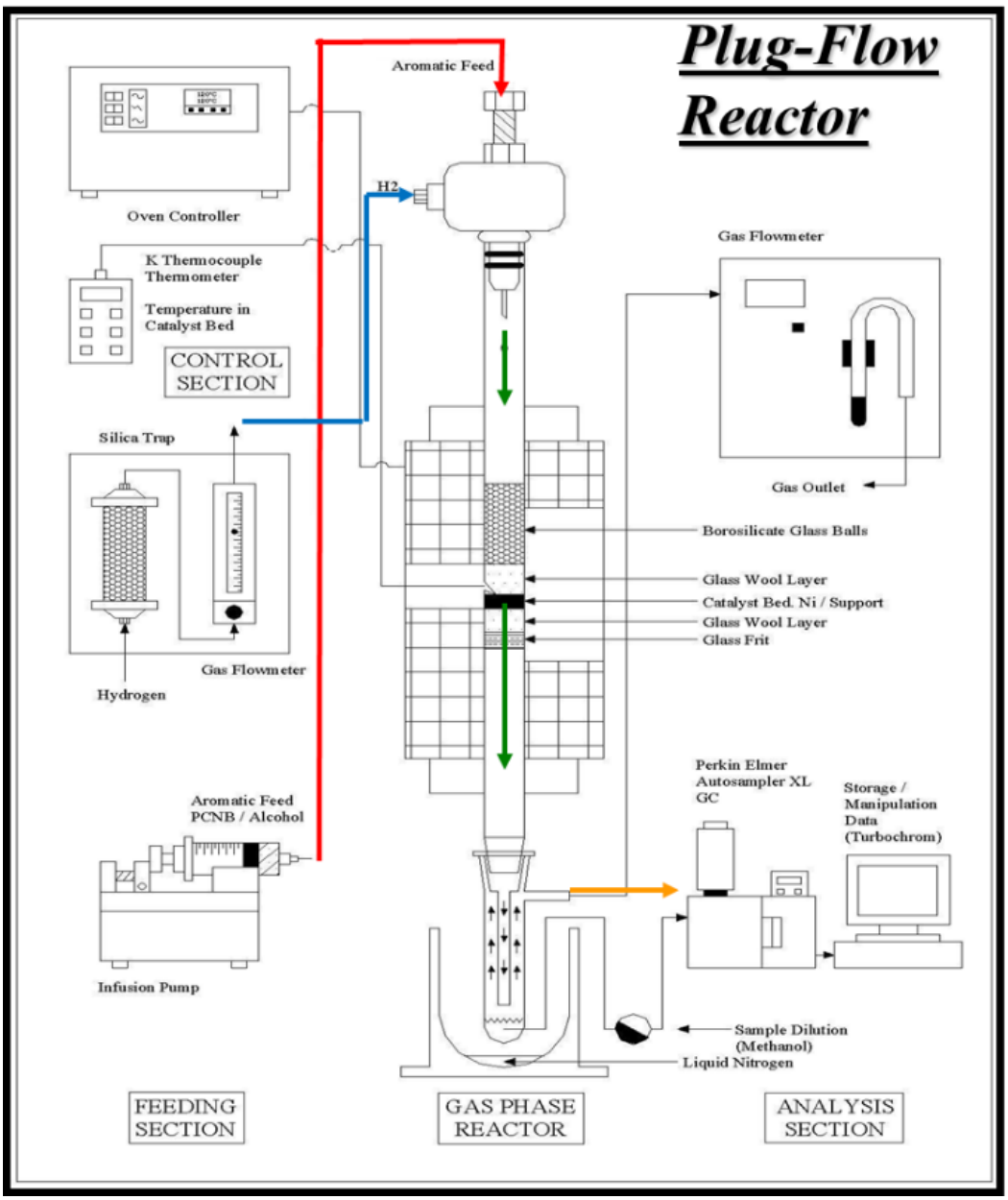

Figure 1.9: Representation of a fix-bed of a plug-flow reactor.

1.4 Characterisation Techniques used in this thesis.

The following techniques and methodologies were used in the characterisation of the different catalysts.

1.4.1.- XPS:

The X-ray photoelectron spectroscopy is an important and common method to analyse the near-surface composition of a sample [69], that requires the usage of an ultra-high vacuum (UHV) chamber for the measurements. The fundamentals of XPS is to measure the kinetic energy of electrons ejected by a material sample which was excited using X-rays beams from a specific anode (usually Mg or Al) [70]. The measurement of the kinetic energy of the electrons ejected allows the calculation of the binding energy (BE) by subtracting this parameter and the work function (φ) from the energy of the incident X-ray photons (hν):

$$BE = h\nu - KE - \varphi \qquad \textbf{(1.3)}$$

The work function (φ) is defined as the energy difference between the Fermi level and the vacuum level and varies based on the spectrometer used. From the XPS analysis, the XPS spectrum plot is obtained, that relates the intensity of the measured electrons *versus* the Binding Energy (**see Figure 1.10**). This plot allows identification of the different elements present on the sample surface as each of the elements has a distinctive binding energy emitted from different orbitals (1s,2s,2p,3d, etc.).

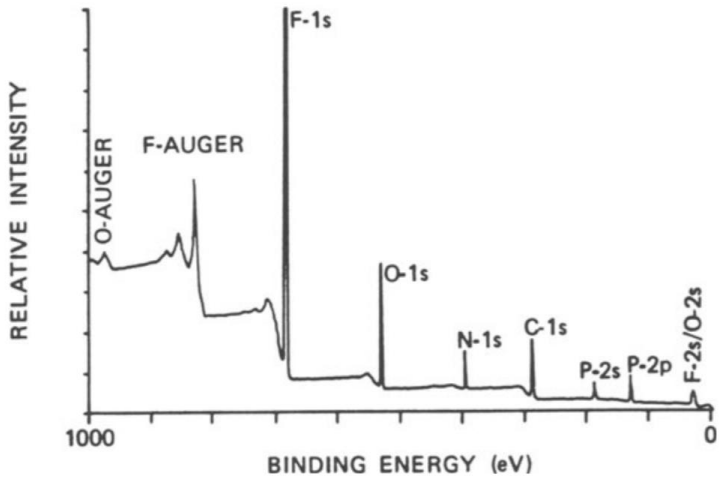

Figure 1.10: Representative (*XPS*) survey scan spectra of an elastomer with the major elemental lines identified (C, O, N, P and F). Reprinted from Ref [71]**.** Copyright 1985, with permission from Springer Nature.

The XPS analysis also allows the determination of the oxidation state of the element (*e.g.* Fe^{3+}, Fe^{2+} and Fe^{0}) [72] as well as its degree of polarization (*e.g.* $Pd^{\delta-}$ and $Pd^{\delta+}$) [73] considering the BE deviation from the standard zero-valency value of the element. The concentration of the element in the near surface region can also be determined by XPS analysis by integrating the peak element and using a tabulated sensitivity factor. Further details regarding the element concentration calculus can be found it in the following article [74].

1.4.2.- Powder X-ray powder diffraction:

Powder X-ray diffraction (XRD) is a key technique based on constructive interference that occurs between monochromatic X-rays emitted and the atomic planes of a crystalline structure. The interaction of the beam rays with the sample produce a diffraction of the X-rays (see **Figure 1.11)** with an (θ) angle, satisfying Bragg´s Law in which the wavelength of electromagnetic radiation (λ) to the diffraction angle (θ) and the lattice spacing (d) in a crystalline sample are related (see Equation 1.4) [75]

$$n \cdot \lambda = 2d \cdot sin\theta \qquad \textbf{(1.4)}$$

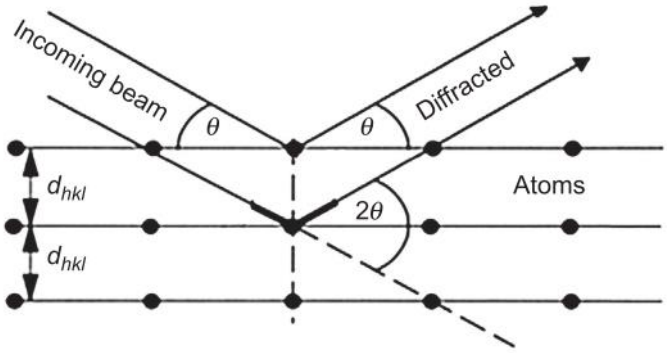

Figure 1.11: Geometrical condition for diffraction from lattice planes Reprinted from Ref**.** [75] Copyright 2016, with permission from Elsevier.

In the experiment, the monochromatic X-rays are generated in a heated cathode tube, typically of Cu, that emits an X-ray radiation with a specific wavelength (Cu K_α radiation = 1.5418Å) [76]. A detector records the diffracted signal to a count rate which is then output to a device such as a computer monitor (see **Figure 3.3**).

XRD technique allows the identification of the crystalline phases present int the catalyst sample and the quantification of the crystals mean particle size: From the

information provided by the XRD spectra, the crystal size (d_{hkl}) of the component can be calculated using the Paul Scherrer equation [77].

$$d_{hkl} = \frac{K \cdot \lambda}{\beta \cdot cos\theta} \quad \textbf{(1.5)}$$

Where β is the peak width of the diffraction peak profile at half maximum height resulting from small crystallite size in radians and K is a constant related to crystallite shape, normally taken as 0.9.

1.4.3.- Electron Microscope Technique: SEM, TEM and EDX.

The usage of electron microscopy caused a revolution in imaging technology over the last century, which overcame the resolution limitations ascribed to the light microscope on nanomaterials [78]. Resolution (R) is defined as the ability to distinguish the features of the object in the image, and is proportional to the wavelength size (λ), considering the equation proposed by Abbe [79]:

$$R = \frac{0.612 \cdot \lambda}{2 \cdot NA} \quad \textbf{(1.6)}$$

Where NA is defined as the numerical aperture. The electron microscope used the wave-particle duality physical principle, in which the shorter wavelengths of the electrons (40 pm-1 pm) compared to visible light (400-700 nm) [78] enhances the spatial resolution of the image down to less than 0.1 nm [78].

The usage of electron microscopy offers a wide variety of characterisation techniques (EELS, Auger Spectroscopy, EDX, SEM, TEM, etc.). In this thesis, scanning electron microscopy (SEM), transmission electron microscopy (TEM) and energy dispersive X-ray Spectroscopy (EDX**)** have been used. These techniques are inspired in different physical principles that occurs after the interaction between the electron beam coming from the electron microscope (primary electrons) with the sample.

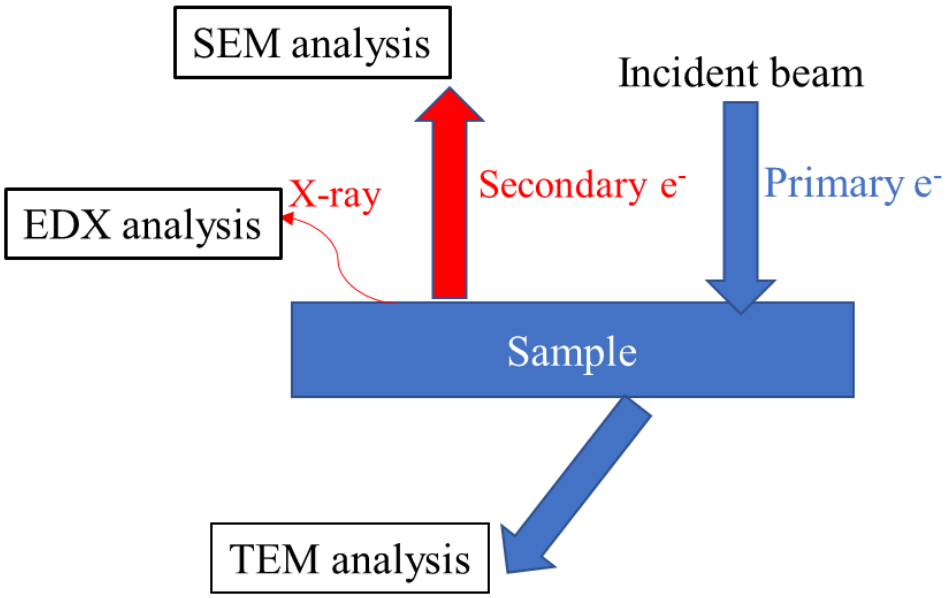

Figure 1.12: Scheme of the different interactions and analysis between the primary electrons with a sample.

As depicted in **Figure 1.12**, TEM is based on the change of the direction of the **primary electrons** after impacting with the sample [80]. SEM technique is based on the detection of electrons ejected from the inner shell of an excited element in the sample (secondary electrons emission) due to its interaction with the primary electrons (see **Figure 1.13**). The hole created from the secondary electron is occupied by an electron of an outer layer of the ionized element, releasing X-ray energy that is collected for the EDX analysis (see **Figure 1.13**).

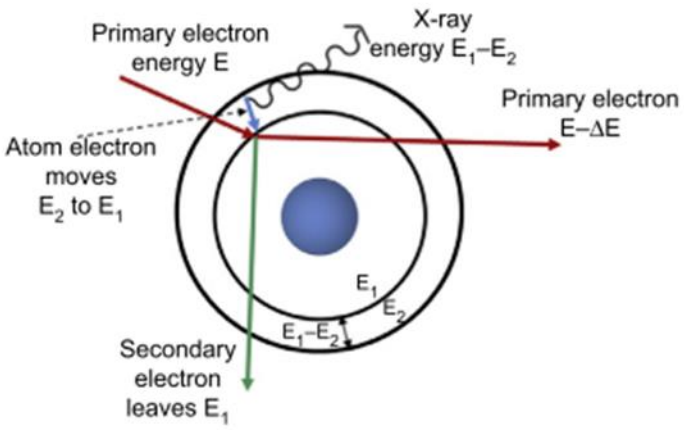

Figure 1.13: Characteristic of X-ray and secondary electron emission Reprinted from Ref. [78] Copyright 2016, with permission from Elsevier.

These techniques are used in catalysis for several purposes: While SEM provides information of the catalysts surface morphology [81] (see **Figure 3.4 (II)),** TEM technique is focused on the analysis of the catalysts internal microstructure [82], allowing measurements of nanoparticles crystallites (see **Figure 3.4 (I)),**. EDX techniques provides information on the chemical composition of the material (see **Figure7.2**) [83], as the distinctive X-ray emitted for each element allows their identification in the sample catalysts. The EDX profile is represented with the radiation recorded on (keV) and the peak intensity counts on the y-axis (see **Figure 7.2).**

1.4.4.- Quantachrome Instrument: SSA, TPR, TPD and H_2-chemisorption:

Quantachrome instrument is widely used in the characterisation of solid catalysts. In this thesis, several techniques such as specific surface area (SSA) catalyst [84], H_2-Temperature Programmed Reduction (H_2-TPR), desorption (H_2-TPD) [85] and H_2 chemisorption [84] over the different catalytic systems were carried out. All the techniques performed on Quantachrome are based on the measurement of thermo-conductivity changes of a gas mixture between the inlet/outlet of the sample cell. The gas mixture is composed of an inert gas (N_2 or a noble gas) and a gas subjected to study, having both big differences in thermo-conductivities. This instrument can measure a wide variety of gases (generally H_2, O_2, CO_2, CO and NH_3) [86] being in this thesis focused on the H_2 gas interaction with the catalysts. Quantachrome instrument is represented schematically in **Figure 1.14** in which the two gases with high purity are mixed with mass flow controllers (FC) and passes through a TCD detector (TCD R **Figure 1.14**), that measures the thermo-conductivity before entering the reactor cell.

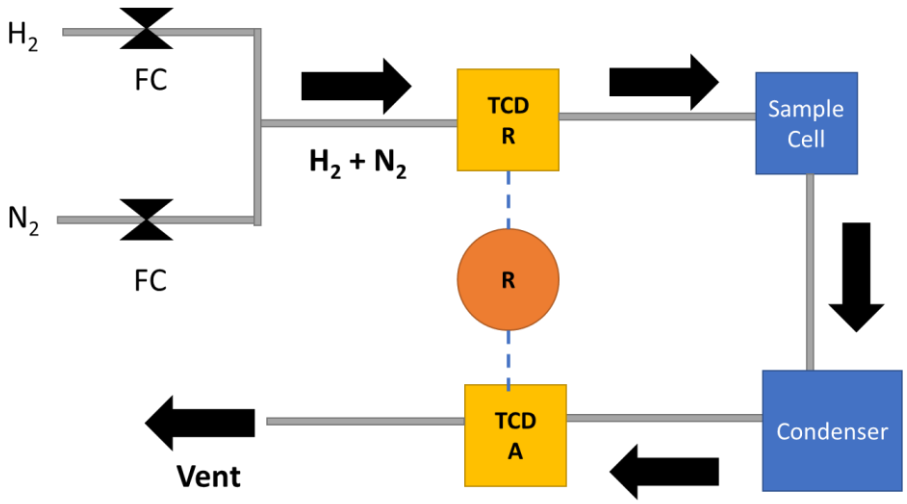

Figure 1.14: Diagram of a Quantachrome apparatus.

A cold trap is included after the gas mixture goes through the reactor with the aim to remove possible impurities (*e.g*. moisture) that can affect the reading in the second TCD (TCD A **Figure 1.14**) detector. The TCD detector is based on two sets of filaments, installed as a Wheatstone bridge circuit (R **i**n **Figure 1.14**) in which a change in the gas concentration between both filaments will unbalanced the bridge leading to an electrical signal. The changes can be quantified by making a standard external calibration that are explained in more detail in the following sections. Quantachrome apparatus can be visualized in the photo shown in **Figure 1.15** that allows a better comprehension of the equipment described.

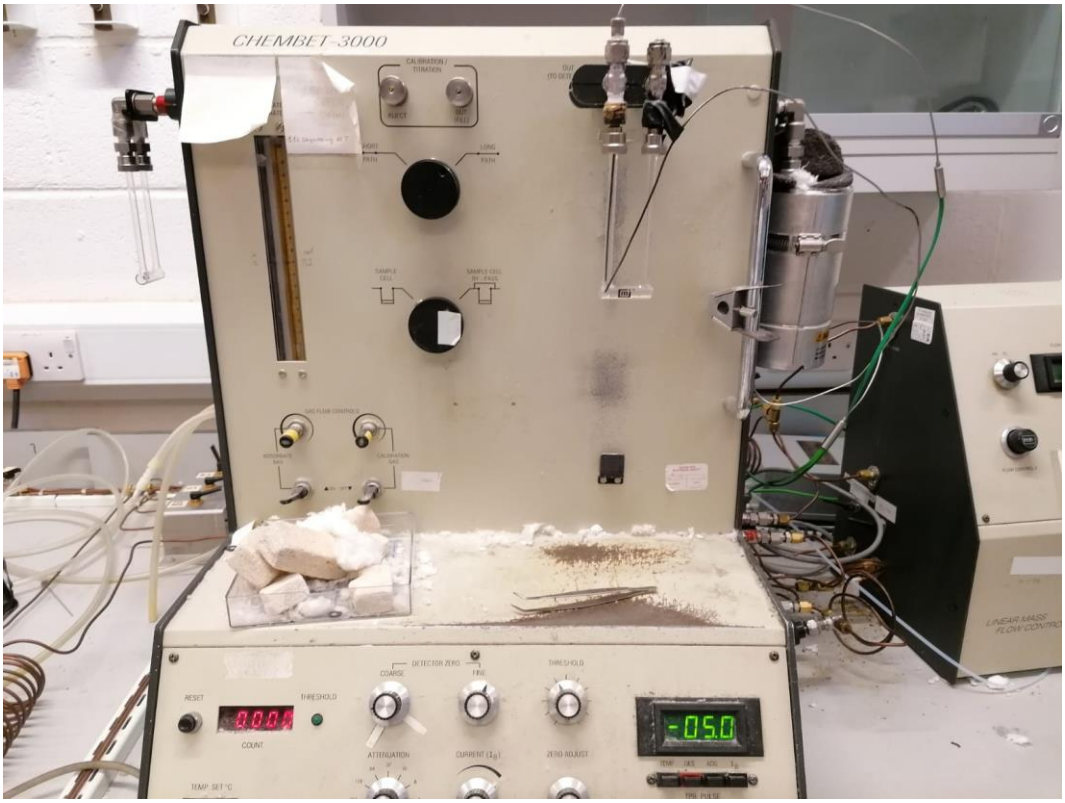

Figure 1.15: Quantachrome apparatus used for catalyst characterisation.

1.4.4.1 H_2-TPR:

In the H_2-TPR technique, a reducing gas mixture (generally H_2+N_2) [87] goes through the catalyst sample cell which is subjected to a programmed temperature linear rise [88,89]. The electrical signal coming from the TCD detector is represented *versus* time and/or temperature in a TPR spectra profile shown in **Figure 3.2.** With the temperature programmed increase, the signal fluctuates leading to the formation of several peaks with different signals, negative (H_2 release due to Pd-H decomposition, see **Figure 3.2)** and/or positive (H_2 consumption used of the metal oxidation state reduction, see **Figure 5.2**) peaks in the TPR profile. It is common to find a profile with more than one positive peak in a TPR that can be due to:

a) The stepwise reduction of an element (*e.g.* $Fe^{3+} \rightarrow Fe^{2+}$ and $Fe^{2+} \rightarrow Fe^{0}$) [90].

b) The different nature of interaction between precursor phase and support [86] (*e.g.* $Ni(NO_3)_2$ on Al_2O_3 in **Fig 5.2**).

c) The existence of different elements in the sample susceptible to be reduced (*e.g.* bimetallic Pd-Ni in **Figure 5.2** or Pd supported over a reducible support [91]).

The reduction of M_2O_x, leading to M_2O_{x-1} and H_2O product formation is controlled thermodynamically, the reaction only being feasible when the free Gibbs energy change is negative ($\Delta G < 0$), as shown in the following equation:

$$\Delta G = \Delta G^0 + RT \log \left(\frac{P_{H2O}}{P_{H2}}\right) \quad \textbf{(1.7)}$$

Where ΔG^0 represents the Gibbs standard energy and P_{H2O} and P_{H2} the gas vapour partial pressures of the reaction species. The log (P_{H20}/P_{H2}) coefficient in TPR analysis is assumed as negative as the moisture is constantly swept away from the sample cell [92]. Therefore, the stability of the oxide is linked to the temperature requirements needed for overcoming the positive ΔG^0 of the specie [93].

TPR technique is also useful for the quantification of the volumetric H_2 gas consumed during the reduction process [93] and can be determined by an external calibration. For the external calibration, injections of known H_2 volumes are made over a blank sample cell, where inert N_2 flows with the same flowrate through the apparatus at STP conditions. The different injections generate peak pulses of different areas that can be linearly correlated (see **Figure 1.16**), obtaining a correlation factor from the slope.

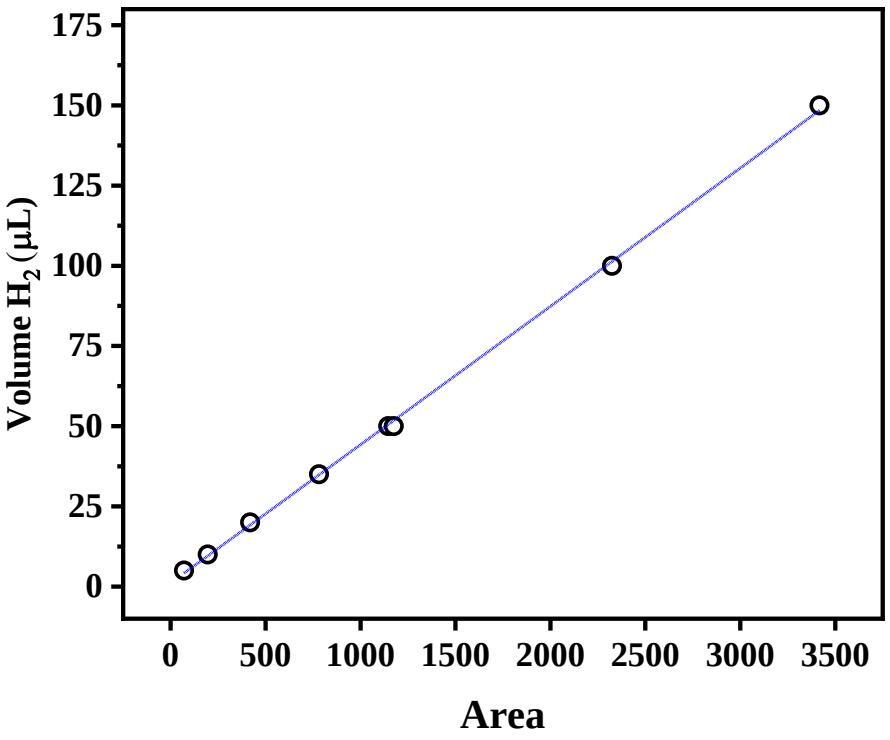

Figure 1.16: Calibration curve of a TPR experiment.

In the quantification of the H_2 consumed from TPR peaks, the reduction peak areas obtained by integration *versus* time are correlated to the volumetric of H_2 consumed by using the slope of the external calibration:

$$V_{H2}(\mu L) = Area_{peak} \cdot \frac{(\Delta V)}{(\Delta Area)} \qquad \textbf{(1.8)}$$

From the volume of hydrogen reduction, the number of moles consumed can be easily determined by applying the ideal gas law equation.

1.4.4.2 Temperature Programmed Desorption (TPD):

On H_2-TPD analysis, the sample, opportunely saturated with chemisorbed H_2 is submitted to a control temperature program, being heated at a constant heating rate (4-100 K min^{-1}) [94] up to high temperatures (1373K) [95]. With an increase in temperature, the chemisorbed H_2 is desorbed from the surface, and is swept from the sample cell using an inert flow (15-60 cm^3 min^{-1} of He, Ar or N_2) and recorded by the TCD detector outlet.

In H_2-TPD analysis it is possible to evaluate the number and different types of active sites in which H_2 chemisorbs in the sample, as well as, their bond strength. The number of different H_2 active sites in the sample can be correlated to the number of peaks that can

be visualized on a H_2-TPD diffractogram (see **Figure 7.5**). The quantification of H_2 chemisorbed from those peaks is performed by external calibration, as similarly happened with the H_2-TPR technique. On a H_2-TPD diffractogram, the H_2 desorption temperature reflects the bond strength interaction between the catalysts and the substrate, where the higher the temperature peak, the stronger the H-Catalysts bond.

1.4.4.3 Surface Chemisorption

The aim of H_2 chemisorption evaluates the amount of H_2 uptake by the catalysts sample, which is of a great help in understanding the catalytic activity and product distribution in a hydrogenation reaction [96]. This technique has been traditionally carried out on group VIII noble metal catalysts, with a great capacity on chemisorbing H_2, which is adsorbed in a dissociative form mode [50]. The procedure is based on injecting repeatedly, from an air-tight syringe, a known volume of H_2 that is mixed with the inert stream (N_2) before contacting the sample. Once the H_2 in the gas mixture contact the catalysts sample, part of it is retained on the surface in the form of chemisorbed specie and the excess will leave the sample cell, generating an electrical signal in the form of a pulse peak (see **Figure 1.17**). The total volume of H_2 adsorbed (Vt) during the analysis is given by:

$$V_t = \sum_{i=l}^{N} V_{ai} \qquad \textbf{(1.9)}$$

Where N is the number of pulses necessary to saturate the active sites and V_{ai} is the volume of gas adsorbed from the pulse. The amount of gas adsorbed for each pulse is given by the difference between the area of the peak given for the reference pulse and the area under the peak acquired during the adsorption process (see **Figure 1.17**). Once the reactive gas saturates the sample, the peaks areas acquired by the TCD (**B**, **Figure 1.17**) are equal to the reference calibration peak (**A**, **Figure 1.17**) and is an indication that the analysis is concluded [86].

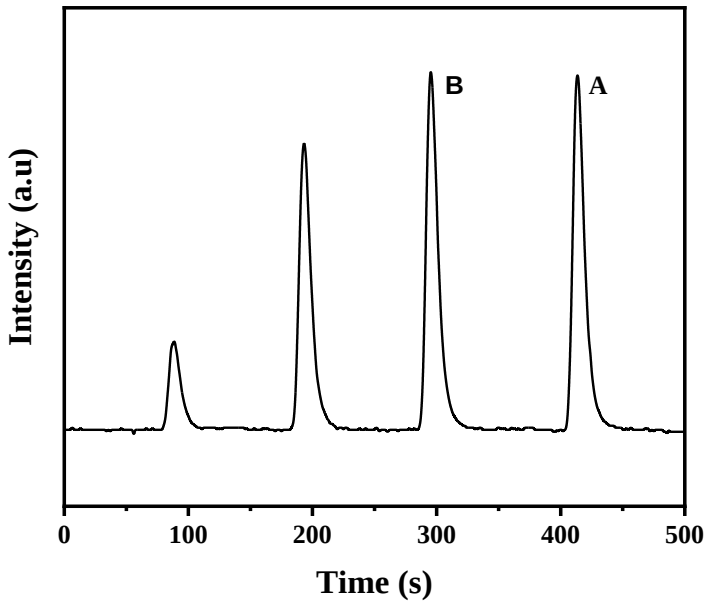

Figure 1.17: Example of a pulse chemisorption analysis using Pd/Al_2O_3 (1% wt.) catalysts.

The peaks obtained in the chromatogram, after N injections, are integrated and therefore the relation between the peak area and quantity of gas injected can be easily calculated after calibration. This technique also allows the determination of the surface transition metal exposed as well as its mean particle size determination (d_{metal}), by using the equation:

$$d_{metal} = (10^4 \cdot F)/(MSS \cdot D_m) \quad \textbf{(1.10)}$$

Where (D_m) corresponds to metal density, (F) to the shape factor (for a sphere F = 6) and MSS to metal surface area (square meters per gram of sample), that is determined by the following formula:

$$MSS = (V_m \cdot N_a)/(S_f \cdot S_d) \quad \textbf{(1.11)}$$

Where V_m is the amount of gas chemisorbed (moles per gram of sample), Na the Avogadro number, S_f the stoichiometric factor (in the case of H_2 is 2) and S_d the metal surface density (number of catalysts atoms per square meter).

1.4.4.4 Specific Surface Area (SSA):

The SSA is defined as the ratio between the total surface of a substance and its volume, and constituted a key parameter in the characterisation of porous materials [97] that can be classified as a function of their pore size range in microporous ($d_{pore} < 2$ nm), mesoporous ($2nm < d_{pore} < 50$ nm) and macroporous ($d_{pore} > 50$ nm) [98]. The SSA is determined by the usage of physical adsorption principles allowing the calculation of the total gas volume occupied on the surface catalysts [98]. In the physical adsorption, the adhesion of the gas molecules to the material takes place *via* weak Van der Waals and London dispersion forces interactions (10-40 kJ mol^{-1}) [98,99]. Among all the possible adsorbates that can be used in physical adsorption in SSA (Ar, CO, CO_2, etc.) [100], the most utilised is N_2 operating at its condensation temperature (78 K) that allows the formation of a liquid layer over the material. Prior to the SSA analysis, the catalyst sample, with the aim to remove the moisture and other volatiles, is subjected to a degasification, heating up the sample under specific temperature conditions while the carrier gas runs through the sample cell [101].

After the degasification step, a known (He + N_2) gas mixture with a fixed flowrate is set to flow over the sample cell, which is immersed in liquid N_2., generating the physical adsorption of the N_2 gas that results in a change of the signal intensity (adsorption step, peak A in **Figure 1.18**). After the maximum peak, the signal becomes stable again, suggesting that the material cannot uptake more chemisorbed N_2 (saturation point). Once the signal is stabilized, the Dewar of liquid N_2 where the sample is immersed, is replaced by one beaker of water at room temperature. The drastic changes in temperature in the sample cell forces the N_2 desorption from the catalyst leading to the formation of a negative peak (desorption step, peak B in **Figure 1.18**). The volume of N_2 physisorbed in the catalyst is calculated by injecting a known volume of N_2 after the stabilization of desorption step, correlating therefore the area obtained from the one resulting from the analysis (internal calibration step, peak C in **Figure 1.18**).

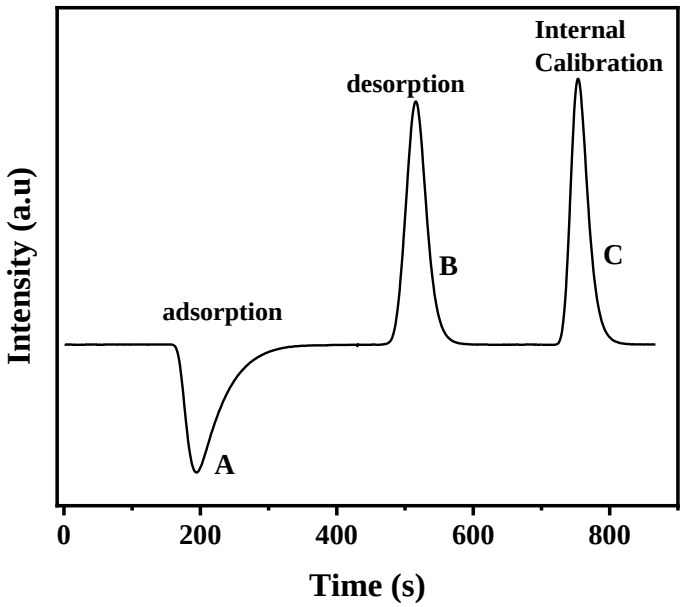

Figure 1.18: Example of N_2-Physisorption treatment using Ni/Al_2O_3 (6% wt.) catalysts as a probe.

Several theoretical descriptors are used in the characterisation of surface area (*e.g.* Langmuir, Freundlich, Polanyi, etc [102,103]), however, the most widely used is the so-called Brunauer–Emmett–Teller (BET) model. The BET model assumes several approximations with the aim to simplify the mathematical model (homogeneous surface, independent heat of adsorption with surface coverage, no interaction between adsorbates in the same layer, etc.) [97] and consider the presence of a multilayer adsorption valid for non-corrosive gases in the surface area determination [98]. The BET expression is given by the following formula:

$$\frac{x}{v\,(1-x)} = \frac{1}{v_{mon}\cdot c} + \frac{x\,(c-1)}{v_{mon}\cdot c} \qquad \textbf{(1.12)}$$

Where x is corresponds to N_2 partial pressure (controlled by instrument), v is the volume of N_2 adsorbed by the material and v_{mon} is the amount of adsorbate required to form a monolayer under standard pressure and temperature conditions and c is the Langmuir equilibrium constant. The BET equation can be simplified in cases where the c parameter is much higher than 1, leading to the single-point BET equation [104]:

$$\frac{x}{v\,(1-x)} = \frac{x}{V_{mon}} \qquad \textbf{(1.13)}$$

Therefore, the previous quantification of the volume of N_2 physisorbed by an internal calibration (see **Figure 1.18**) allows the determination of the first monolayer physisorbed by N_2. The surface area of the sample, expressed in $m^2\ g^{-1}$ is calculated using **equation 1.14**, where N is Avogadro number and A_m is the cross-sectional area of N_2 (16.2 Å) [105]

$$SSA = V_{mon} \cdot N \cdot A_m \cdot 10^{-20} \quad \textbf{(1.14)}$$

1.5 Scope and the thesis plan

The aim of this thesis is the development of an alternative hydrogenation process in continuous gas phase operation, directed at the sustainable synthesis of valuable alkenols that could lead to higher yields in comparison with the traditional batch liquid phase mode. This thesis can be structured into two main blocks, depending on the transition metal catalyst used. The first block (**chapter 2-5)** is dedicated to understanding the gas phase alkynol selective hydrogenation mechanism with the usage of Pd-based catalysts. Several operational and catalytic variables that impact in the hydrogenation process are analysed systematically, with the purpose of tailoring a suitable catalyst for the alkenol manufacture in gas phase conditions. The second part of the thesis (**chapter 5-7)** is devoted to finding alternatives to Pd catalysts by using less-scarce transition metals, such as Ni and Mo_2N catalysts, both having excellent properties in several hydrogen-mediated reactions. In these chapters, the main objective is to achieve the same range of alkenol selectivities as the ones obtained with industrial Pd catalysts. Concurrently, the alkenol yield was sought to be improved by optimizing the catalysts H_2 utilisation, with the modification of variables (*e.g.* H_2 spillover, promotion of N vacancies, etc.) that impacts in the reactivity of the process.

The work has involved catalyst synthesis and characterisation, analysis of thermodynamic and kinetics and catalyst/process optimisation. Catalyst characterisation has been based on AAS, TPR, hydrogen chemisorption at room and/or reaction temperature, H_2-TPD, BET surface area, XRD, TEM, STEM, EDX and XPS measurements.

The role of electronic effects on -C≡C- bond hydrogenation is evaluated in **chapter 2**, (publication No. 1) in the hydrogenation of several C_4 alkynols such as 2-methyl-3-butyn-2-ol (MBY), 3-butyn-2-ol (3BY) and 3-butyn-1-ol (3BYOL). The aim is to change the -C≡C- electron density with the addition of electron donating ($-CH_3$) groups to the C-OH functionality, that can decrease the C≡C- → -OH electron transfer in the molecule. The catalytic performance and product distribution formed with increasing conversion is evaluated over the three alkynols molecules using monometallic 1.2% wt. Pd/Al_2O_3 catalysts as a benchmark.

The role of Pd geometric effects in -C≡C- bond hydrogenation is considered in **chapter 3** (publication No. 2**).** The synthesis of monometallic Pd colloids, affording better control over Pd morphology (narrow particle size range), were deposited using ZnO and Al_2O_3 supports and activated over a wide activation temperature range (403-973 K)

for the catalytic hydrogenation of MBY. Under a reducing environment and depending on the activation temperature, it is known that Pd/ZnO can partially reduce the ZnO support leading to alloy phase formation (β-PdZn) followed by Pd partial encapsulation ($PdZnO_{1-x}$). The aim in this chapter is to control β-PdZn alloy formation (measured *via* XPS) by changing the activation temperature with the purpose to understand how a variation in Pd ensemble sizes (due to β-PdZn formation) impacts on MBY hydrogenation. The performance of the new Pd/ZnO catalyst formulation is demonstrated by comparing with an industrial (Pd-Lindlar) catalyst.

In **chapter 4** (publication No. 3) the issue of ($PdZnO_{1-x}$) encapsulation formation is avoided by *ex situ* preparation of PdZn colloids subsequently deposited over Al_2O_3 support with a different (Pd: Zn) molar ratio, therefore allowing the role of PdZn alloy on the reaction to be determined. The catalytic performance obtained on $PdZn/Al_2O_3$ colloids is then compared with a Pd/ZnO catalyst with a similar PdZn % alloy composition and particle size. In the same chapter, the role of H_2 in the catalytic performance on gas phase hydrogenation is determined by testing monometallic Pd/Al_2O_3 over a wide range of (H_2: alkynol) inlet molar feed ratios. Additionally, the effect of Pd electronic properties (*e.g.* $Pd^{\delta-}$ and $Pd^{\delta+}$) in the reaction process have been tested by comparing several Pd supported catalysts (Pd/MgO, Pd/C, Pd/Al_2O_3 and Pd/CeO_2) with the same morphology (mean particle size) but different acid-base properties and reducibilities.

The potential of Ni metal catalyst on selective alkynol hydrogenation is studied in **chapter 5** with the hydrogenation of 3BY. The use of Ni metal catalysts aims to block the double bond migration step, which is known to occur in 3BY hydrogenation over Pd catalysts. Therefore, with the use of Ni catalysts, we expect to simplify the product distribution, which might impact positively towards 3BE selectivity. The catalytic performance of both monometallic Ni and Pd are compared under the same reaction conditions, metal loading, and synthetic method (incipient wetness impregnation on Al_2O_3 support). The role of Ni as a co-metal catalyst is also analysed in the 3BY hydrogenation over $Pd\text{-}Ni/Al_2O_3$ catalysts. We expect that the electropositive character of Ni can induce electronic changes in Pd an electronic change that facilitates the alkenol surface displacement by tuning the (-C≡C-)/(-C=C-) adsorption strength ratio.

In chapter 6, we attempted to understand the role of Zn promoter in 3BY hydrogenation over bulk Ni catalysts. The incorporation of Zn atoms into Ni crystallographic structure leads to the formation of several NiZn alloy phases with different crystal structure (α, β, δ), In this chapter, we expect to control the Ni ensemble

sizes, responsible for undesired over-hydrogenation by modifying the Ni-Ni coordination number on the different NiZn crystallographic structures. The effect of H_2 spillover is also evaluated by comparing the catalytic response over bulk *vs*. supported α-NiZn/ZnO alloy. The main intention is to utilise the H_2 chemisorbed on ZnO support for -C≡C- reduction. (*via* spillover) with the aim to improve the catalytic activity of the process.

The potential of bulk catalytic materials is further explored in **chapter 7** by the catalytic hydrogenation of γ-Mo_2N, synthesised *via* temperature programmed reduction-nitridation of MoO_3. Changes in the reduction-nitridation set of conditions (*e.g*. H_2/N_2 ratio) have an impact on γ-Mo_2N structural properties (*e.g*. N surface vacancies) that have a direct effect in -C≡C- hydrogenations, as H_2 is known to chemisorb on N vacancies. In this chapter, the use of a Pd promoter before (γ-Mo_2N (A)) and after MoO_3 (γ-Mo_2N (B)) reduction-nitridation is suggested with the aim to enhance the H_2 uptake of the material due to structural changes (*e.g*. increase N vacancies) and/or by the ability of Pd in splitting H_2.

Chapter 2:

Gas Phase Catalytic Hydrogenation of C4 Alkynols over Pd/Al_2O_3

In this chapter, we have investigated, for the first time, the mechanism involved in the continuous gas phase hydrogenation of primary alkynol (3-butyn-1-ol, 3BYOL) over a commercial Pd/Al_2O_3 catalyst. We extend the catalyst testing to consider secondary and tertiary C4 alkynols and prove possible contributions to catalytic performance (*i.e.* alkenol production rate and selectivity) due to the position of the hydroxyl group and the number of electron donating ($-CH_3$) substituents, *i.e.* effect of -C≡C- bond electron density on catalytic performance.

2.1 Introduction

The bulk of research on -C≡C- bond hydrogenation has been focused on the transformation of acetylene (to ethylene) over Pd catalysts where the main challenge is to selectively promote semi-hydrogenation with -C=C- formation [106]. Product distribution is influenced by alkyne adsorption/activation mode [107]. Associative adsorption (through a π/σ double bond) on Pd planes [107] follows the Horiuti-Polanyi model, consistent with a stepwise alkyne → alkene → alkane transformation [22,108]. Alternatively, dissociative adsorption *via* H + three point σ bond [22] or H + π-allyl specie [24] on electron deficient edges/corners of palladium nanoparticles [109] can lead to direct alkyne → alkane hydrogenation [26] or double bond migration [27]. The electronic properties of the palladium phase and the electron density of the -C≡C- bond functionality can influence the alkyne adsorption/activation which, in turn, impact on olefin selectivity. Taking an overview of the published literature, unwanted over-hydrogenation and double migration are prevalent over electron deficient ($Pd^{\delta+}$) nanoparticles that promote strong complexation with the (electron-rich) -C≡C- bond [33,110]. The triple bond charge has also a direct role to play and can be affected by inductive effects (*i.e.* electron transfer from/to additional groups in poly-functional alkynes). The literature dealing with -C≡C- bond polarisation effects in hydrogenation of multifunctional alkynes is limited. It is, however, worth noting published work that shows increasing activity (over Pd(II) complexes [111] and Pd-Ru catalysts [112]) for hydrogenation of substituted acetylenes with electron donating (*e.g.* -R=H, $-C_6H_5$, $-CH_3$) functional groups [112]). Terasawa and *co-workers* [111], investigated the catalytic response

for a series of functionalised alkynes over polymer bounded Pd(II) complexes catalyst and concluded that -C=C- selectivity is sensitive to the nature of the substituent (*i.e.* increased olefin selectivity in the presence of electron withdrawing substituents (-Cl,-OH) *vs*. electron donating (-C_6H_6) functional groups [112]). Alkenols have found widespread applications in the manufacture of pharmaceutical (*e.g.* intermediates for vitamins E, A, K [113] and anti-cancer additives [114]) and agri-food (*e.g.* dimethyloctenol and citral [113,114]) products. Industrial synthesis involves selective hydrogenation of the correspondent substituted alkynol [5]. Alkynols can be categorised with respect to the number of carbons bonded to the carbon bearing the -OH group (C-α in **Figure 2.1**), *i.e.* primary (one C directly attached; labelled C-β_1), secondary (C-β_1 and C-β_2) and tertiary (C-β_1, C-β_2 and C-β_3).

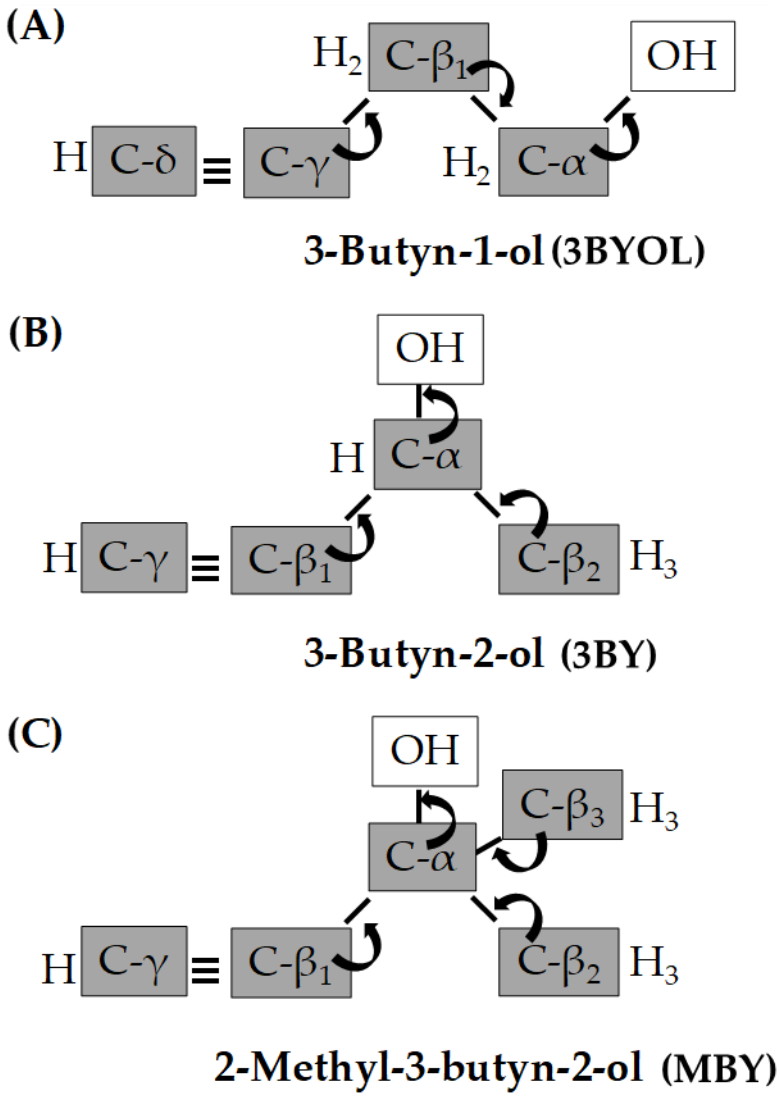

Figure 2.1: Classification of (**A**) primary, (**B**) secondary and (**C**) tertiary C4 alkynols. *Note*: Arrows represent associated charge transfer effect.

Work to date has focused on batch liquid mode hydrogenation of saturated (tertiary) alkynols (*e.g.* 3-methyl-1-pentyn-3-ol [113]) using pressurised (up to 10 atm) reactors [35] with limited research on the selective hydrogenation of primary [115,116] and secondary alkynols [66]. Gas phase continuous operation facilitates control over contact time, which can influence product selectivity [117,118]. We were unable to find any study in the open literature on gas phase hydrogenation of primary or secondary alkynols and only one published paper in the transformation of tertiary alkynols [119]. In this work, we set out to gain an understanding of the mechanism involved in the production of primary alkenols, considering continuous gas phase hydrogenation of 3BYOL over a commercial Pd/Al_2O_3 catalyst, as a model system. We extend the catalyst testing to consider secondary and tertiary butynols and prove possible contributions to catalytic performance (*i.e.* alkenol production rate and selectivity) due to the position of the hydroxyl group.

2.2 Experimental

2.2.1 Catalyst Characterisation

A commercial 1.2% wt. Pd/Al_2O_3 (Sigma-Aldrich) served as model catalyst. Prior to use, the catalyst was sieved (ATM fine test sieves) to mean particle diameter = 75 μm and activated in 60 cm^3 min^{-1} H_2 (BOC, ≥99.99%) at 2 K min^{-1} to 573 K to ensure reduction to Pd^0 [120], cooled to ambient temperature and passivated in 1% v/v O_2/He (30 cm^3 min^{-1}) for 1 h for *ex situ* characterisation. Palladium particle morphology (size and shape) was determined by STEM using a JEOL 2200FS operated at an accelerating voltage of 200 kV and employing Gatan Digital Micrograph 1.82 for data acquisition/manipulation. The sample was dispersed in acetone and deposited on a holey Cu grid (300 mesh). The number weighted mean Pd diameter (d) was determined as described elsewhere [121] from a count of 800 particles. XPS analyses were conducted on an Axis Ultra instrument (Kratos Analytical) under ultra-high vacuum conditions ($<10^{-8}$ Torr) using a monochromatic Al Kα X-ray source (1486.6 eV). The source power was maintained at 150 W and the emitted photoelectrons were sampled from a 750 × 350 μm^2 area at a take-off angle = 90°. The analyser pass energy was 80 eV for survey spectra (0–1000 eV) and 40 eV for high resolution spectra (Pd $3d_{5/2}$ and $3d_{3/2}$). The adventitious carbon 1s peak was calibrated at 284.5 eV and used as an internal standard to compensate for charging effects. Curve-fitting served to identify/quantify Pd

species with modified electronic properties using CasaXPS software in which the Pd 3*d* spectra were fitted with abstraction of the Shirley background using the Gaussian–Lorentzian function.

2.2.2 Catalytic Procedure

Reactions were carried out at 373 K at atmospheric pressure *in situ* after activation in a continuous flow fixed bed vertical tubular glass reactor (15 mm i.d.). The catalytic reactor and operating conditions were selected to ensure negligible heat/mass transport limitations. A layer of borosilicate glass beads (1 mm) served as a preheating zone where a butanolic solution of the alkynol (3BYOL + BA; 3BY +1-butanol (BOL); MBY + BOL) was vaporised and reached reaction temperature before contacting the catalyst. Isothermal conditions (±1 K) were maintained by diluting the catalyst bed with ground glass (75 μm diameter). Reaction temperature was continuously monitored by a thermocouple inserted in a thermowell within the catalyst bed. The alkynol reactant was delivered *via* a glass/teflon air-tight syringe and Teflon line using a microprocessor-controlled infusion pump (Model 100 kd Scientific) at a fixed calibrated flow rate. A co-current flow of H_2 (or H_2/N_2; P_{H_2} over the range of 5×10^{-3} – 9×10^{-2} atm) and alkynol was maintained at $GHSV = 1 \times 10^4$ h^{-1}. The flow rate was monitored using a Humonics (Model 520) digital flowmeter. Molar metal Pd (n) to inlet alkynol molar feed rate (n/F) spanned the range 3×10^{-5} – 368×10^{-4} h. In blank tests, reactions in the absence of catalyst or over the Al_2O_3 support alone did not result in any measurable conversion. The reactor effluent was condensed in an ice-bath trap for subsequent analysis, which was made on a Perkin-Elmer Auto System XL gas chromatograph equipped with a programmed split/spit-less injector and a flame ionisation detector using a Stabilwax (fused silica) 30 m × 0.32 mm i.d., 0.25 μm film thickness capillary column (RESTEK). Data acquisition/manipulation was performed using the TotalChrom Workstation Version 6.1.2 (for Windows) chromatography data system. The solvents (2-butanol (**BA**) (Alpha Aesar, 99%) and BOL (Fisher, 99.4%)), reactants 3BYOL (Aldrich, 97%), 3BY (Aldrich, 97%) and MBY (Aldrich, 98%)) and products (3-buten-1-ol (3BEOL) (Aldrich, 96%), BOL (Aldrich, 99%), crotyl alcohol (**2BEOL**) (Aldrich, 96%), butyraldehyde (**BHDE**) (Aldrich, 96%), 3-buten-2-ol (**3BE**) (Aldrich, 97%), BA (Aldrich, 99.5%), 2-butanone (**BONE**) (Aldrich, 99%), MBE (Aldrich, 98%), 2-methyl-butan-2-ol (**MBA**) (Aldrich, 99%)) were used without further purification. Reactant and product molar fractions (x_i) were obtained using detailed

calibration plots (not shown). Catalytic performance is considered in terms of conversion (X) at steady state after 3 h on-stream:

$$X(\%) = \frac{[\text{Alkynol}]_{in} - [\text{Alkynol}]_{out}}{[\text{Alkynol}]_{in}} \times 100 \quad \textbf{(2.1)}$$

while selectivity to product j (S_j) was obtained from:

$$S_j(\%) = \frac{[\text{Product}_j]_{out}}{[\text{Alkynol}]_{in} - [\text{Alkynol}]_{out}} \times 100 \quad \textbf{(2.2)}$$

The subscripts "in" and "out" refer to the inlet and outlet streams. Catalytic activity is also quantified in terms of alkynol consumption rate (R, $mol_{Alkynol}\ g_{Pd}^{-1}\ h^{-1}$) obtained following the procedure described elsewhere [122]. Repeated reactions with different samples from the same batch of catalyst delivered raw data reproducibility and a carbon mass balance within ±6%.

2.2.3 Thermodynamic Analysis

The application of thermodynamics to catalytic processes provides critical information in terms of maximum conversion/selectivity possible under a given set of reaction conditions. All the reactant and products involved in the hydrogenation of 3BYOL (as representative) were considered (3BYOL, 3BEOL, BOL, 2BEOL, BHDE and H_2). The inlet 3BYOL was set at 1 mol and product distribution determined at equilibrium where T = 373 K, P = 1 atm and H_2: Alkynol molar ratio = 2 to mimic catalytic reaction conditions. The equilibrium calculations were made using Aspen Plus [123] to obtain product distribution under conditions of minimised Gibbs free energy using the method of group contribution [124].

2.3 Results and discussion

2.3.1 Catalyst Characterisation

The Pd/Al_2O_3 catalyst used in this study bore, post- H_2-TPR to 573 K, metal nanoparticles with diameters ranging from ≤1 nm up to 6 nm (see representative STEM image (A) and histogram derived from microscopy analysis (B) in **Figure 2.2**) and a number weighted mean diameter of 3 nm. An enhanced intrinsic alkenol selectivity for palladium nanoparticles of 3 nm has been reported elsewhere in the liquid (dehydroisophytol over Pd colloids [125]) and gas phase (MBY using Pd/SiO_2 [119]) hydrogenation of alkynols. The STEM images reveal a pseudo-spherical morphology, the most thermodynamically stable configuration [109], indicative of a small area of contact at the interface between the Pd nanocrystals and the Al_2O_3 support.

XPS measurements were carried out to provide insight into the electronic character of the supported Pd phase. The resulting spectra over the Pd 3*d* BE region is shown in **Figure 2.2(C).** The XPS profile exhibits a doublet with a main Pd $3d_{5/2}$ signal at 334.9 eV, that is 0.3 eV lower than that characteristic of metallic Pd (335.2 eV, [126]), a result that suggests partial electron transfer from $OH^{\delta-}$ groups on the alumina support [127]. This is consistent with reported (electron-rich) $Pd^{\delta-}$ (4-5 nm) on Al_2O_3 [128]. The formation of butane and 2-hexene through undesired over-hydrogenation and double bond migration, respectively, has been reported in the hydrogenation of 1-butyne (over Pd/Al_2O_3) [27] and 1-hexyne (using Pd black) [110] ascribed to the presence of (electron-deficient) $Pd^{\delta+}$ nanoparticles. In addition, the profile shows a weak doublet (12%) with curve-fitted values at higher BE (Pd $3d_{5/2}$ = 337.1 eV; Pd $3d_{3/2}$ = 342.7 eV) that can be ascribed to Pd^{2+} as a result of passivation for ex situ characterisation analyses [129]. A similar (10-12%) percentage value was reported by Weissman *et al*. [130] attributed to oxygen chemisorption on Pd (111) following a passivation step.

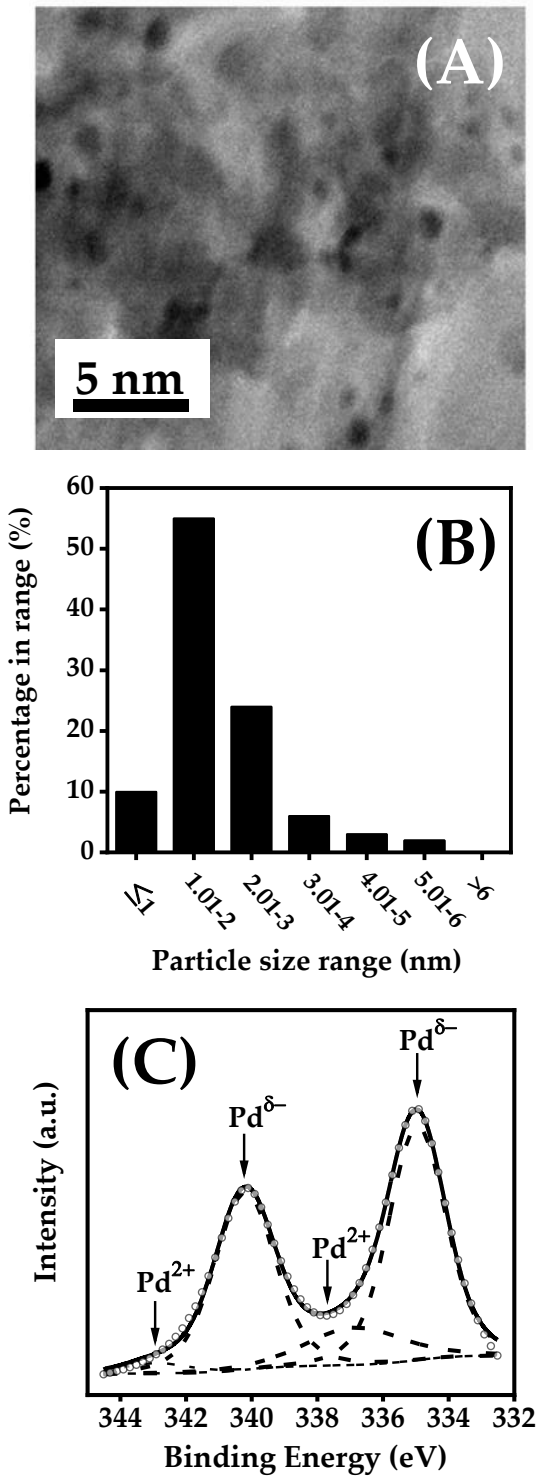

,

Figure 2.2: (**A**) Representative STEM image with (**B**) associated Pd particle size distribution and (**C**) XPS spectrum over the Pd 3*d* region for Pd/Al_2O_3. *Note*: Raw data is shown as symbols (○) while curve fitted and envelope is represented by dashed and solid lines, respectively.

2.3.2 Reaction Thermodynamics

The calculated change in Gibbs free energy of formation at 373 K for each reaction step ($\Delta G_{(I\text{-}VII)}$) are included in **Figure 2.3**. The $\Delta G_{(I\text{-}VII)}$ values serve as criteria in the evaluation of thermodynamic feasibility, where reactions can occur spontaneously when $\Delta G<0$. Each reaction step exhibits negative ΔG indicating that all products considered are thermodynamically favourable. Under our reaction conditions, a thermodynamic analysis of 3BYOL hydrogenation established full conversion predominantly to BOL (S_{BOL} > 99%) with trace amounts of BHDE. Formation of alkanol can result from -C=C- reduction in 3BEOL (**step (II)** in **Figure 2.3**) or direct alkynol hydrogenation *via* **step (III)**. Hydrogenation of the intermediates, that result from alkenol double bond migration (2BEOL (**step (IV)**) and keto-enol tautomerization (BHDE (**step (V)**), also generates BOL (**steps (VI-VII)**).

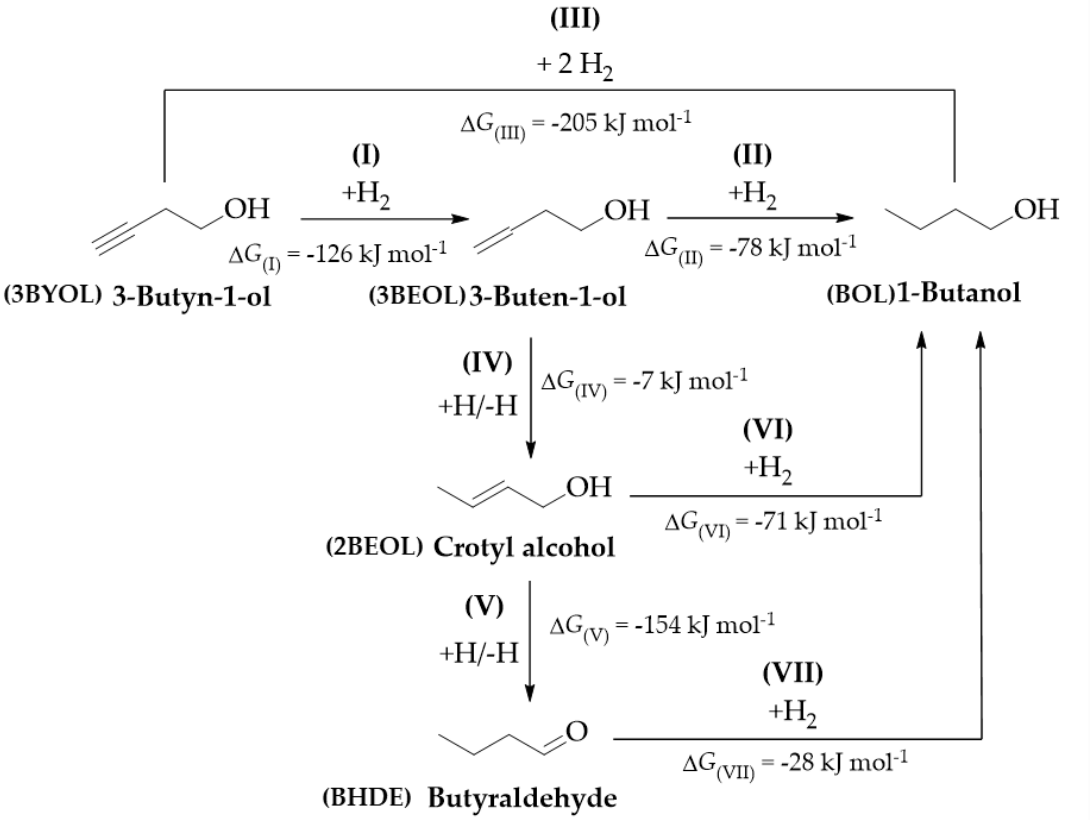

Figure 2.3: Reaction scheme with Gibbs free energies ($\Delta G_{(I\text{-}VII)}$) for each step in the hydrogenation of primary **(**3BYOL**)** alkynol: *Reaction conditions*: T = 373 K, P = 1 atm.

2.3.3 Gas Phase Hydrogenation of 3BYOL

Dependence of hydrogenation path can be effectively proved from a consideration of selectivity as a function of 3BYOL conversion; the corresponding data for reaction over Pd/Al_2O_3 is presented in **Figure 2.4**. At low conversions (<25%), product composition deviates from predominant BOL generation under thermodynamic equilibrium, indicative of operation under catalytic control. 3BEOL and BOL were the predominant products of partial and full hydrogenation, respectively, but double bond migration (to 2BEOL and BHDE) was also detected with a selectivity ≤10%. Formation of 3BEOL and BOL has been previously reported in the liquid phase (P = 1-6 atm; T = 300-348 K) hydrogenation of 3BYOL over MCM-41[131], Fe_3O_4 [132] and Fe_3O_4 coated SiO_2 [116] supported Pd Catalyst. Production of 2BEOL observed in this work can be linked to reaction temperature (373 K), where T < 353 K serve to avoid double bond migration [133].

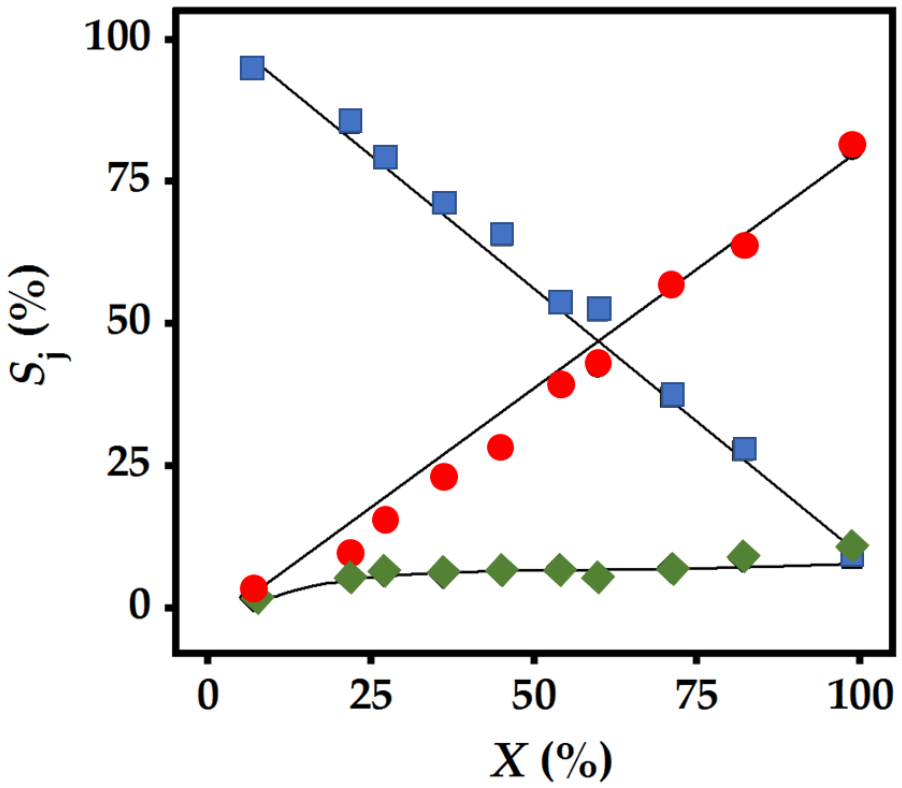

Figure 2.4: Variation of selectivity (Sj (%), j = 3BEOL (■), BOL (●), 2BEOL + BHDE (◆) with conversion (X (%)) in hydrogenation of 3BYOL *-1-ol* over Pd/Al_2O_3. *Note*: solid lines provide a guide to aid visual assessment. *Reaction conditions*: T = 373 K, P = 1 atm.

A decrease in 3BEOL selectivity was accompanied by increased formation of BOL at high conversions, indicative of a sequential hydrogenation route (*i.e.* Horiuti-Polanyi mechanism) from -C≡C- → -C=C- → -C-C-, typical for gas phase alkyne hydrogenations [39].

2.3.4 Gas Phase Hydrogenation of 3BY and MBY

Reaction pathways in the hydrogenation of secondary 3BY and tertiary (MBY) C4 alkynols are shown in **Figure 2.5**.

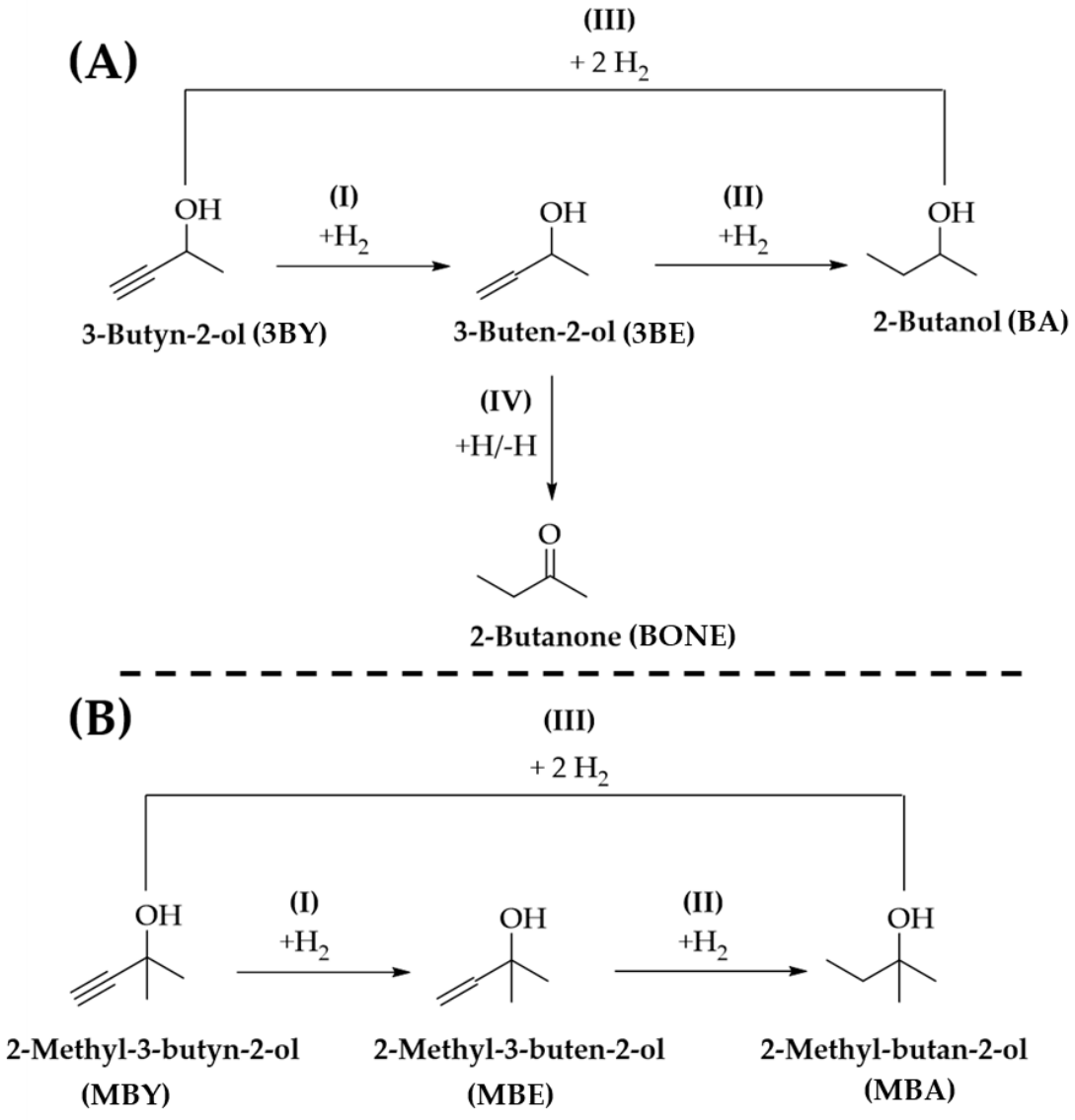

Figure 2.5: Reaction schemes for the hydrogenation of (**A**) secondary 3BY and (**B**) tertiary (MBY) alkynols.

Both alkynols can undergo sequential (alkynol → alkenol → alkanol, steps (I-II)) and direct (alkynol → alkanol, step (III)) hydrogenation. Alkenol double bond migration in the transformation of 3BY generates BONE, (step (IV) in **Figure 2.5(A))** but this step is not possible in the conversion of MBY as the C-α **(Figure 2.1)** is fully substituted. Hydrogenation rate for the three C4 alkynols is presented in **Figure 2.6(A)** where activity decreases in the order: tertiary > secondary > primary. This sequence matches that of decreasing the number of methyl substituents bonded to the C-α **(Figure 2.1**), *i.e*. MBY (C-β_1, Cβ_2 and C-β_3) > 3BY (C-β_1 and C-β_2) > 3BYOL (C-β_1). Alkyne hydrogenation has been proposed to proceed *via* an electrophilic mechanism [112,134].

Reactive hydrogen is provided by dissociative chemisorption of H_2 on Pd [135]. The hydroxyl function can serve to deactivate the triple bond for electrophilic attack through inductive effects by decreasing the overall electron density due to -C≡C- → -OH electron transfer [136,137]. The presence of (electron donating [138]) methyl substituent(s) bonded to the C-α serves to decrease the "electron-release" from the triple bond (see charge transfer in **Figure 2.1**) which favours the electrophilic attack. Our results are in line with the work of Karavanov and Gryaznov [112] who studying the liquid phase hydrogenation of functionalised tertiary alkynols over a Pd-Ru alloy membrane catalyst reported a (40%) enhanced activity as the electron donating character of the substituent increased (*i.e*. -CH_2OH < -H < -CH_3).

The results of product selectivity as a function of alkynol conversion for the three C_4 alkynols under consideration are presented in **Figure 2.6(B-C)**. The alkenol selectivity *vs*. conversion profiles (**Figure 2.6(B))** for secondary and tertiary alkynols follow a linear decrease of the intermediate concentration as conversion increases, suggesting that they follow the same consecutive hydrogenation route as the primary (steps **(I-II)** in **Figure 2.3** and **Figure 2.5(A-B)**). In each case, regardless of the degree of conversion, greater alkenol selectivity was recorded in the transformation of the primary ~ secondary > tertiary. The lower alkenol selectivity recorded for the tertiary alkynol can be ascribed to direct formation of MBA ($S_{\mathbf{MBA}}$ = 14% at X ~ 5%) following **step (III)** in **Figure 2.5(B)**). Alkynol dissociative adsorption on (low coordination) Pd sites [139] can lead to direct -C≡C- → -C-C- bond hydrogenation [26] following hydrogen attack of the surface (multi-coordinated) alkylidyne intermediate [22].

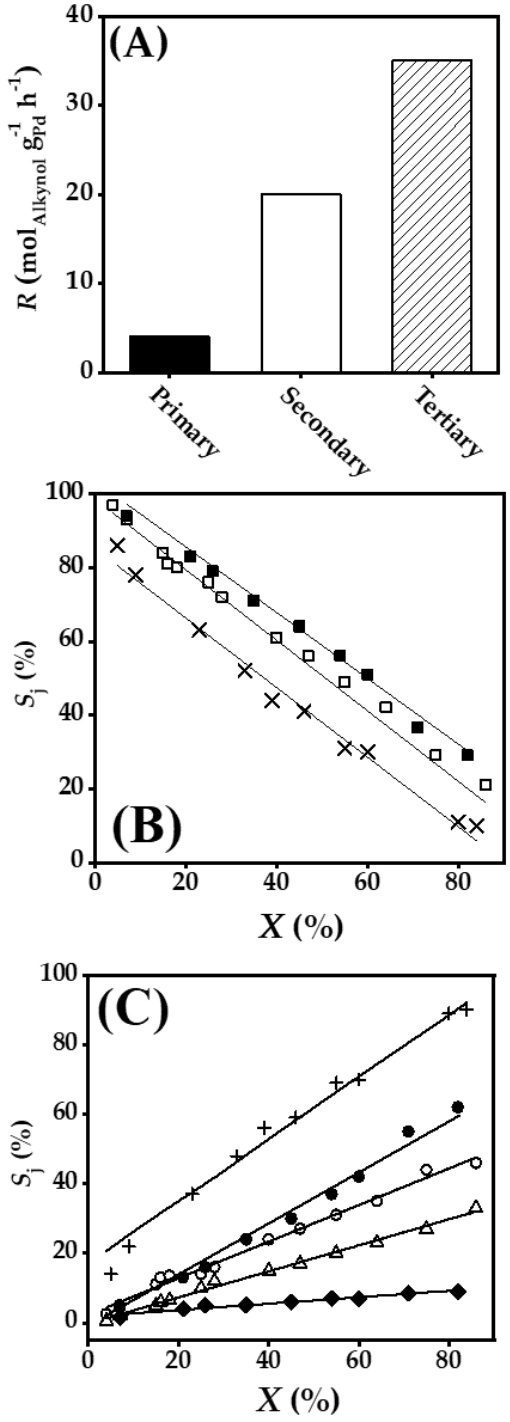

Figure 2.6: (**A**) Reaction rate and variation of selectivity (S_j, %) as a function of conversion (X, %) for products from (**B**) partial reduction and (**C**) hydrogen bond migration/reduction in the hydrogenation of primary (solid bar and solid symbols), secondary (open bar and open symbols) and tertiary (hatched bar and crossed symbols) C4 alkynols over Pd/Al_2O_3; 3BEOL (■),BOL (●), 2BEOL+ BHDE (◆), 3BE (□), BA (○), BONE (△), MBE (×) and MBA (+). *Note:* solid lines provide a guide to aid visual assessment. *Reaction conditions*: T = 373 K, P = 1 atm.

This intermediate is generated by H abstraction at the "external" carbon in the -C≡C- bond (*e.g.* C-δ in 3BYOL, **Figure 2.1**). Alternatively, double bond migration [27] with aldehyde/ketone formation (steps **(IV-V)** in **Figure 2.3** and **(IV)** in **Figure 2.5(A)**) can occur as a result of hydrogen addition to the surface π-allyl intermediate generated by hydrogen removal from the carbon bonded to the triple bond functionality (*e.g.* C-β_1 in 3BYOL) [140]. The lower activation energy for the formation of the π-allyl (*vs.* alkylidyne) intermediate [141,142] can account for the absence of direct -C≡C- → -C-C- bond hydrogenation in the conversion of 3BYOL and 3BY. In contrast, hydrogen abstraction in MBY is only possible at the (external -C≡C- carbon) C-γ (*i.e.* no C-α hydrogen) to generate **MBA**. Alkenol double bond migration (*via* hydrogen addition to the external carbon, *i.e.* C-δ in 3BYOL and C-γ in 3BY, **Figure 2.1,** of the π-allyl intermediate [24]) was promoted to a lesser extent in the transformation of 3BYOL *vs.* 3BY, *i.e.* higher selectivity to BONE relative to 2BEOL + BHDE at all conversions (**Figure 2.6(C)**). Likewise, Bianchini *et al.* [143] reported a lower isomerisation yield in the liquid phase hydrogenation of 3BEOL (relative to 3BE) over a Rh complex catalyst. We examined 2BEOL and BHDE reactivity in order to assess BOL formation *via* hydrogenation (steps **(VI)** and **(VII)**, respectively, in **Figure 2.3**) and probe selectivity responses. Under similar reaction conditions, we recorded no conversion of BHDE, a response that is consistent with the low capacity of -C=O group (*e.g.* methyl vinyl ketone and benzalacetone [144]) hydrogenation by Pd [145]. Conversion of 2BEOL generated BOL as the sole product but at an appreciable higher (by a factor of 2) rate when compared with that recorded for the 3BYOL reaction. The lower double bond migration in terms of 2BEOL + BHDE (*vs.* BONE) generation must result from a more facile transformation of the 2BEOL intermediate. Indeed, lack of activity was observed for the conversion of BONE over Pd/Al_2O_3. We acknowledge that catalytic response may not governed by inductive effect alone and the dynamics of surface interactions by the hydrogen reactant can have a major bearing. Future work will be carried out to evaluate the effect of H_2 content in the feed (*i.e.* Alkynol:H_2 molar ratio) on catalytic performance.

2.4 Conclusions

We have examined the effect of –OH group position on catalytic gas phase hydrogenation of C4 alkynols over Pd/Al_2O_3 ($Pd^{\delta-}$ nanoparticles with mean (number weighted) size = 3 nm). A correlation between the number of electron-donating ($-CH_3$) groups and catalytic activity has been established consistent with the following decreasing activity sequence: tertiary (MBY) > secondary (3BY) > primary (3BYOL). The conversion of primary and secondary alkynols follows a stepwise (alkynol → alkenol → alkanol) reaction mechanism while direct alkynol → alkanol transformation was a feature of MBY hydrogenation. Double bond migration is promoted to a greater extent in the transformation of 3BY relative to 3BYOL consistent with 2BEOL hydrogenation. The results in this work establish the role of -C≡C- polarity in determining the activity/selectivity pattern for the synthesis of valuable alkenols.

Chapter 3:

Partial Hydrogenation of MBY over Pd/ZnO: Effect of Reduction Temperature on Alloy Formation and Catalytic Response.

In this chapter, we examine the impact on catalytic performance of PdZn alloy phase relative to a standard metallic Pd phase (using Pd/Al_2O_3) in the continuous gas phase hydrogenation of MBY. The effect on catalytic response of PdZn alloy relative to PdCu (in Pd/CuO) and Pd_3Pb alloy phases (in industrial Lindlar's catalyst) has also been evaluated. Furthermore, we have also investigated the catalytic response over Au/Al_2O_3, with high selectivity in triple bond semi-hydrogenation.

3.1 Introduction

2-Methyl-3-buten-2-ol (MBE) is an important intermediate in the manufacture of vitamins A and E (30,000 tons world production [1] with an expected increasing demand [2]. Industrial synthesis of MBE involves selective hydrogenation of MBY (MBY) in pressurised (2-10 bar) batch liquid systems [3]. A transition from batch to continuous operation (at atmospheric pressure) offers clear advantages in terms of energy efficiency and increased productivity for high throughput [4]. The development of continuous systems for MBY hydrogenation is now gaining increasing attention, as shown in the review by Moreno-Marrodan *et al.* [5] The reaction network for MBY hydrogenation is presented in (**Figure 3.1**). The main challenge in MBE production is to avoid *over*-hydrogenation (to MBA) and oligomerization [6].

MBE selectivity is controlled by the relative alkenol/alkynol adsorption strength (A_{ke}/A_{ky}) on metal active sites [146] and favoured at low A_{ke}/A_{ky} [147] (*i.e.*, the alkynol reactant chemisorbs strongly on the catalyst surface and facilitates the desorption of the target MBE by displacement). Palladium has been identified as the best catalytic metal for partial hydrogenation of -C≡C- → -C=C- bond [148], which can be linked to the low A_{ke}/A_{ky} ratio ($\sim 10^{-3}$) [22] relative to other transition metals typically used in hydrogenation (*e.g.*, A_{ke}/A_{ky} on Pt $\sim 10^{-2}$) [147]. Olefin formation is structure sensitive and favoured over 3-5 nm Pd nanoparticles [149].

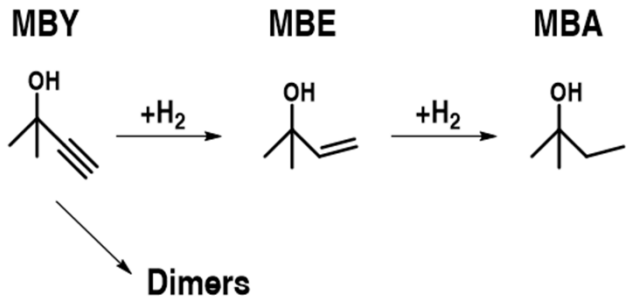

Figure 3.1: Simplified reaction scheme for the selective hydrogenation of MBY to target MBE with MBA and dimers as undesired reaction by-products from further hydrogenation/oligomerisation.

Full hydrogenation (to MBA) has been attributed to multi-coordination of MBY [149] on (i) surface defects (*e.g.*, corners and edges) of small (<3 nm) palladium nanoclusters with low electron density ($Pd^{\delta+}$) [149] and (ii) large ensembles of Pd atoms on the crystal planes of palladium nanocrystals >5 nm [30]. A number of strategies have been considered to facilitate the formation of $Pd^{\delta-}$ species and/or reduce Pd ensemble size including: use of basic supports (*e.g.*, MgO and Ga_2O_3) [150], incorporation of an external promoter with a lone pair of electrons (*e.g.*, quinoleine) [34], addition of a second (more electropositive) metal (*e.g.*, Ag, Cu, Pb) [11,22] and/or formation of a homogenous alloy [28].

Recent studies have shown the potential of a PdZn alloy phase in selective hydrogenation of CO_2 to CH_3OH [151] and semi-hydrogenation of unsaturated hydrocarbons (*e.g.*, dienes [152], alkynes [153] and alkyndiols [150]). The catalytic application of PdZn catalysts in liquid phase hydrogenation of substituted alkynes has been the subject of appreciable research [154]. However, no attempts have been made to establish a direct correlation between PdZn alloy concentration and catalytic performance, and we have failed to unearth any study in the open literature on continuous alkynol hydrogenation using a supported PdZn alloy catalyst. The synthesis of supported PdZn alloy catalysts can involve the simultaneous loading of both metal precursors on a support (*e.g.*, *co*-impregnation [155] or *co*-precipitation [156]) or loading of a Pd precursor on ZnO (*e.g.*, incipient wetness impregnation) [155] followed by high temperature (T > 473 K) activation in H_2 [157]. These methodologies suffer from poor control of particle size distribution [158] with a detrimental effect on composition/homogeneity of the PdZn alloy phase formed [159]. A strategy to avoid these issues is the synthesis of size-controlled Pd colloids that can be subsequently deposited on a ZnO support [160]. Altering the final reduction temperature impacts on

the degree of support reduction which, in turns, modifies the amount of PdZn alloy phase generated [161].

In this work, we investigate the effects on catalyst response of PdZn alloy phase in comparison with a standard metallic Pd phase (using Pd/Al_2O_3) in the continuous gas phase hydrogenation of MBY. The impact on catalytic performance of PdZn alloy relative to PdCu (using Pd/CuO) and Pd_3Pb alloy phases (in an industrial Lindlar catalyst) has also been considered. Moreover, as Au has delivered high selectivity in partial -C≡C- bond hydrogenation [162] we have also studied the catalytic response of Au/Al_2O_3.

3.2. Experimental Section

3.2.1. Catalyst Preparation and Activation

The oxide supports, ZnO, Al_2O_3 and CuO were purchased from Sigma-Aldrich and used as received. 1% wt. Pd/ZnO, Pd/Al_2O_3 and Pd/CuO were prepared by deposition of *ex-situ* synthesised monodispersed Pd nanoparticles according to a previously published procedure [163]. An aqueous solution of $PdCl_2$ (0.015 M) (Fluka, >99%) and $Na_2MoO_4 \cdot H_2O$ (Fluka, >99%) (Pd/Mo mol ratio = 1) was heated in a three neck round bottom flask at 368 K under continuous stirring (500 rpm) until complete evaporation. The solid residue was dissolved in water and contacted (at ambient temperature) with a continuous flow of H_2 (100 cm^3 min^{-1}) for 30 minutes resulting in the formation of uniform Pd nanoparticles stabilised by molybdate anions [164]. Palladium deposition was achieved *via* adsorption where the support (ZnO, Al_2O_3 or CuO; *ca.* 2 g) was immersed and stirred in the Pd colloidal solution for *ca.* 2 h, the slurry filtered and dried in air at ambient temperature. 1% wt. Au/Al_2O_3 was prepared by deposition-precipitation (DP) using urea as basification agent. An aqueous mixture of urea (100-fold excess) and $HAuCl_4$ (4.4×10^{-5} mol cm^{-3}) was added to the support (*ca.* 2 g). The suspension was continuously stirred (650 rpm) and heated at 2 K min^{-1} to 353 K, the pH progressively increased to reach *ca.* 7 after 3 h as a result of thermally induced urea decomposition [165]. The solid was separated by centrifugation, washed with deionised water (with centrifugation between each washing) until chlorine free (confirmed by $AgNO_3$ test) and dried in He (45 cm^3 min^{-1}) at 373 K (2 K min^{-1}) for 5 h. A commercial (5% wt.) $Pd(Pb)/CaCO_3$ (Lindlar catalyst; $Pd/CaCO_3$ poisoned (by impregnation) with lead acetate following a patented method) [166] was purchased from Johnson Matthey. Prior to use, the catalysts were sieved into a batch of 75 μm average diameter and thermally treated in

60 cm^3 min^{-1} H_2 at 10 K min^{-1} to 403-973 K, which was maintained for 1 h. Samples for off-line analysis were passivated in 1% v/v O_2/He at ambient temperature.

3.2.2 Catalyst Characterisation

The Pd and Au loading was measured by atomic absorption spectroscopy (AAS) using a Shimadzu AA-6650 spectrometer with an air-acetylene flame from the diluted extract in aqua regia (25% v/v HNO_3/HCl). Total SSA, TPR, and room temperature H_2 chemisorption were determined using a commercial CHEM-BET 3000 (Quantachrome) unit equipped with a thermal conductivity detector (TCD) with data acquisition/manipulation using the TPR WinTM software (Version 1.0a). Total SSA was obtained using the standard single point BET method. The samples were loaded into a U-shaped Quartz cell, outgassed at 423 K for 1 h in 60 cm^3 min^{-1} He and cooled down to room temperature. SSA values were recorded with a 50% v/v N_2/He flow (30 cm^3 min^{-1}); pure N_2 (99.9%) served as the internal standard. At least two cycles of N_2 adsorption–desorption in the flow mode were used to determine total surface area. TPR measurements involved a heating process in 17 cm^3 min^{-1} 5% v/v H_2/N_2 at 10 K min^{-1} to $403 \leq T \leq 973$ K, where the effluent gas passed through a liquid N_2 trap. *Post*-TPR, the thermally treated samples were maintained at the final temperature in a constant flow of H_2/N_2 for 1 h. After TPR, the samples were swept with a flow of N_2 for 1.5 h to remove any physisorbed hydrogen and cooled to room temperature to be subjected to H_2 chemisorption using a pulse (30 μl) titration procedure. Hydrogen pulse introduction was repeated until the signal area was constant, indicating surface saturation. SSA and H_2 uptake values were reproducible to ±5% and the values quoted in this paper are the mean. Powder X-ray diffractograms (XRD) were recorded on a Bruker/Siemens D500 incident X-ray diffractometer using Cu Kα radiation. The samples were scanned at a rate of 0.02º $step^{-1}$ over the range $20º \leq 2\theta \leq 90º$ (scan time = 5 s $step^{-1}$). Diffractograms were identified using the JCPDS-ICDD reference standard for zincite ZnO (070-8070), γ-Al_2O_3 (153-7011), Pd (046-1043) and β-PdZn (072-2936). Metal nanoparticle size and shape was examined by transmission (TEM), scanning transmission (STEM) and high resolution scanning electron microscopy (HRSEM). TEM measurements were performed using a JEOL JEM 2011 HRTEM unit with a UTW energy dispersive X-ray (EDX) detector (Oxford Instruments) operated at an accelerating voltage of 200 kV using Gatan Digital Micrograph 3.4 for data treatment. STEM analysis w conducted in a JEOL 2200FS operated at an accelerating voltage of 200 kV, employing Gatan Digital Micrograph 1.82 for data acquisition/manipulation. HRSEM measurements were carried out in a Zeiss

Merlin microscope equipped with a secondary electron detector. The acceleration voltage was 2.5 kV and the working distance was kept at 1.5 mm. Atomic number contrast (*i.e.* "Z contrast") images were obtained with a JEOL 2200FS field emission gun-equipped TEM instrument operated in scanning mode at an accelerating voltage of 200 kV with a nominal 0.5 nm probe size, employing Gatan Digital Micrograph 1.82 for data acquisition/manipulation. By using an annular dark field detector with a minimum collection semi-angle of ~100 mrad, the recorded images have intensity approximately proportional to $tZ^{1.7–2}$ (sample thickness t, average atomic number Z), facilitating a clear contrast between the heavy and lighter element components in the catalyst samples. Up to 300 individual metal particles were counted for each catalyst and the surface area weighted mean size (*d*) was calculated from:

$$d = \frac{\sum_i n_i d_i^3}{\sum_i n_i d_i^2} \qquad \textbf{(3.1)}$$

where n_i is the number of particles of diameter (*di*). XPS analyses were conducted on an Axis Ultra instrument (Kratos analytical, Manchester UK) under ultra-high vacuum condition ($<10^{-8}$ Torr) and using a monochromatic Al Kα X-ray source (1486.6 eV). The source power was maintained at 150 W and the emitted photoelectrons were sampled from a square area of 750 × 350 μm^2; the photoelectron take-off angle was 90°. The analyser pass energy was 80 eV for survey spectra (0 – 1000 eV) and 40 eV for high resolution spectra (over the Pd 3*d* core level). The carbon 1s peak was calibrated at 285.0 eV and used as an internal standard to compensate for any charging effects. Spectra curve fitting and quantification were performed with the Casa XPS software (version 2.3.17), using Shirley background and Gaussian Lorentzian curves with fixed Pd $3d_{5/2}$ position (-5.26 eV) and intensity (+1.5-fold) with respect to Pd $3d_{3/2}$ peak [167] and full width at half maximum (FWHM) of 1.4 eV and 2.4 eV to account for the difference in signal intensity [168].

3.2.3 Gas Phase Hydrogenation of MBY:

Hydrogenation of MBY (Sigma-Aldrich, 99%) was carried out at atmospheric pressure and 403 K after in situ catalyst activation in a continuous flow fixed bed tubular reactor (15 mm *i.d.*). Reactions were conducted under operating conditions that ensured negligible mass/heat transport limitations. A layer of borosilicate glass beads served as preheating zone, ensuring that the MBY reactant was vaporised and reached reaction temperature before contacting the catalyst. Isothermal conditions (±1 K) were ensured by diluting the catalyst bed with ground glass (75 μm) before insertion into the reactor. Reaction temperature was continuously monitored by a thermocouple inserted in a thermowell within the catalytic bed. Pure MBY was delivered to the reactor at a fixed calibrated flow rate (1.2 $cm^3\ h^{-1}$) *via* a glass/teflon airtight syringe and teflon line using a microprocessor-controlled infusion pump (Model 100 kd Scientific). A co-current flow of MBY and H_2 (<1% v/v organic in H_2) was maintained at a $GHSV = 2 \times 10^4\ h^{-1}$ with a molar metal (Pd or Au) to inlet reactant molar feed rate (n/F) of 4×10^{-7} - 11×10^{-6} h. The H_2 content was in excess of the stoichiometric requirement for full hydrogenation (to MBA), the flow rate was monitored using a Humonics (Model 520) digital flowmeter. In a series of blank tests, passage of MBY in a stream of H_2 through the empty reactor or over each support alone did not result in any detectable conversion. The reactor effluent was condensed in an ice-cold water trap for subsequent analysis, which was made using a Perkin-Elmer Auto System XL gas chromatograph equipped with a programmed split/split-less injector and a flame ionisation detector, employing a Stabilwax (Cross-Bond Carbowax-PEG; 30 m × 0.32 mm *i.d.*, 0.25 μm film thickness) capillary column (Restek). Data acquisition and manipulation were performed using the TurboChrom Workstation Version 6.3.2 (for Windows) chromatography data system. MBY, MBE and MBA (Sigma-Aldrich, ≥98%) were used as supplied without further purification. All the gases (O_2, H_2, N_2 and He) employed were of ultra-high purity (BOC, >99.98%). Reactant and product molar fractions (xi) were obtained using detailed calibration plots (not shown). MBY conversion (X_{MBY}) was obtained from

$$X_{MBY}(\%) = \frac{[MBY]_{in} - [MBY]_{out}}{[MBY]_{in}} \times 100 \qquad \textbf{(3.2)}$$

and selectivity in terms of MBE (S_{MBE}) as target product is given by

$$S_{\mathrm{MBE}}(\%) = \frac{[\mathrm{MBE}]_{\mathrm{out}}}{[\mathrm{MBY}]_{\mathrm{in}} - [\mathrm{MBY}]_{\mathrm{out}}} \times 100 \quad \textbf{(3.3)}$$

where the subscripts "in" and "out" refer to the inlet and outlet gas streams. Catalytic activity is also quantified in terms of MBY transformation rate (R_{MBY}, mol mol $_{\mathrm{Pd}}^{-1}$ s^{-1}) obtained from time on-stream measurements, using MBY conversion (*ca.* 5-10%) at steady-state condition:

$$R_{\mathrm{MBY}}\ (\mathrm{mol\ mol}_{\mathrm{Pd}}^{-1}\ \mathrm{s}^{-1}) = \frac{X_{\mathrm{MBY}} \cdot F}{100 \cdot n} \quad \textbf{(3.4)}$$

Turnover frequency (*TOF*, rate per active site, s^{-1}) was calculated using metal dispersion (*D*) values from microscopy analysis according to:

$$TOF\ (\mathrm{s}^{-1}) = \frac{R_{\mathrm{MBY}}}{D} \quad \textbf{(3.5)}$$

Repeated reactions with different samples from the same batch of catalyst delivered raw data reproducibility and carbon mass balances that were within ±5%.

3.3 Results and Discussion

3.3.1 Pd/ZnO vs. Pd/Al_2O_3

3.3.1.1 Catalyst Characterisation

Total SSA of the ZnO (10 m2 g^{-1}) and Al_2O_3 (173 m^2 g^{-1}) supports are in accord with values in the literature for zincite ZnO (4-10 m^2 g^{-1}) [169] and gamma-phase alumina (140-190 m^2 g^{-1}) [170]. The introduction of Pd colloids resulted in lower values of SSA (**Table 3.1**), suggesting pore blockage by the metal component [171]. The TPR profiles **(Figure 3.2)** for Pd/ZnO and Pd/Al_2O_3 show a hydrogen released (negative peak) at 335 K that can be linked to room temperature Pd β-hydride decomposition [172]; room temperature palladium precursor reduction to Pd^0 has been established elsewhere [173]

Table 3.1: Physico-chemical properties of Pd/ZnO, Pd/Al_2O_3, Au/Al_2O_3, Pd/CuO and Lindlar catalysts

		Pd/ZnO	Pd/Al_2O_3	Au/Al_2O_3	Pd/CuO	Lindlar
Metal loading (wt. %)		1.0	0.9	1.1	1.1	5.0
SSA ($m^2\ g^{-1}$)		8	157	166	20	10
TPR	T_{max} (K)[a]	*335*, 685	*335*	448	*333,525*	*340*
	H_2 consumption ($\mu mol\ g^{-1}$)	2103[b]	-	87[b]/84[c]	11300[b]	-
H_2 uptake ($\mu mol\ g_{metal}^{-1}$)[d]		167[e]/85[f]	1560[e]/1020[f]	32[e]	75[e]	217[g]
Metal particle size (nm)		6[h]/6[f]	6[h]/10[f]	4[e]	5[e]	4[g]
Metal dispersion (%)		18[h]/18[f]	18[h]/11[f]	30[e]	22[e]	27[g]

[a]T_{max} associated with negative TPR peak is given in italic.
[b]Experimental value.
[c]Theoretical H_2 consumption for $Au^{3+} \rightarrow Au^0$.
[d]Hydrogen chemisorption at room temperature.
[e]Catalyst activated in hydrogen at 573 K.
[f]Catalyst activated in hydrogen at 973 K.
[g]Catalyst activated in hydrogen at 603 K
[h]Fresh catalyst

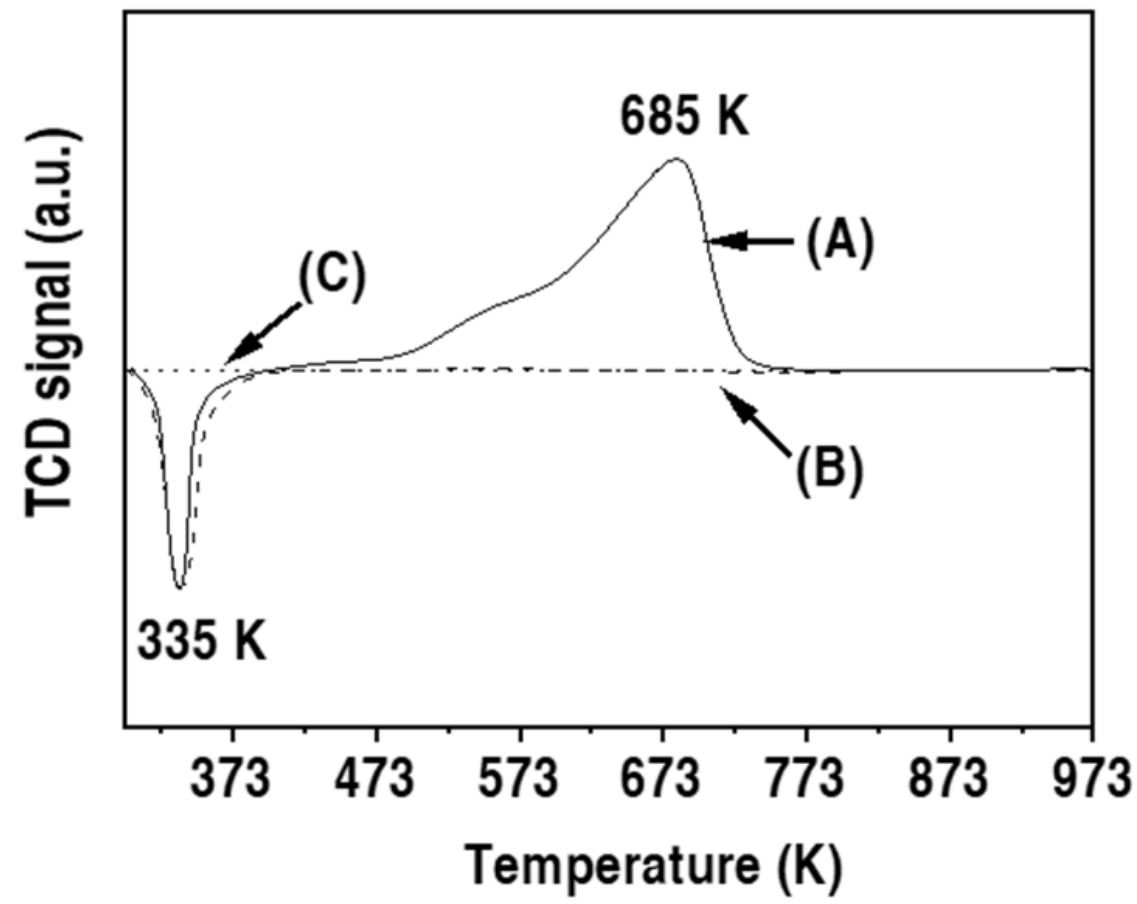

Figure 3.2: TPR profiles for (**A**) Pd/ZnO (solid line), (**B**) Pd/Al_2O_3 (dashed line) and (**C**) ZnO (dotted line).

Hydride composition in terms of H/Pd molar ratio depends on Pd nanoparticle size [174]. We observe a similar value for both catalysts (~0.20) consistent with formation of well dispersed nano-scale (4-6 nm) palladium particles [174]. TPR of Pd/ZnO (**Figure 3.2(A)**) exhibits a broad positive signal over the range 475-775 K. The amount of hydrogen associated with the single consumption peak (T_{max} at *ca*. 685 K) was significantly lower (by a factor of 6) than that required to fully reduce ZnO to metallic zinc and suggests that the presence of Pd results in "partial" ZnO → Zn reduction at the metal-support interface [175] with formation of a PdZn alloy phase [150]. The presence of Pd on ZnO surface resulted pivotal for partial support reduction, being the TPR profile recorded for bare ZnO **(Figure 3.2 (C))** featureless (*i.e*. no hydrogen consumption), as a consequence of limited H_2 splitting by ZnO.

XRD analysis was used to examine crystal properties and confirm PdZn alloy formation; results for the ZnO **(I)** and Al_2O_3 **(II)** systems are presented in **Figure 3.3** Selected areas in the diffractogram of Pd/ZnO fresh **(IB)** and post-TPR to 973 K (IC**)** have been magnified and are shown as *insets* **(a)** and **(b)**, respectively. The as-received ZnO support **(IA)** presents sharp signals at 2θ = 32.1°, 34.5°, 36.5°, 47.8°, 57.2°, 63,1°,

68.5° and 69.8° corresponding to the (1 0 0), (0 0 2), (1 0 1), (1 0 2), (2 -1 0), (1 0 3), (2 -1 2) and (2 0 1) planes of hexagonal close-packed (*hcp*) zincite **(ID).** The XRD pattern for all the Pd/ZnO samples exhibited the diffraction peaks observed in **(IA)** with an additional reflection at 2θ = 40.1° in **(IB)** (see *inset* **(a)**) due to the (1 1 1) main plane of metallic Pd **(IE)**. Post-TPR at 973 K **(IC)** the XRD reflection of Pd^0 at 2θ = 40.1° disappears while we observe the simultaneous appearance of XRD signals at 2θ = 41.2° and 44.1° (see *inset* **(b)**) characteristic of hexagonal (β-phase) PdZn alloy **(IF)**. A stable β-PdZn alloy phase can be formed at T ≥ 373 K during heating treatment in hydrogen [152,176]. The comparable intensity for the main peak in **(a)** and **(b)** observed for Pd/ZnO fresh and activated at 973 K is indicative of similar metal dispersion. This is consistent with reports in the literature that have shown absence of metal agglomeration for (2-7 nm) Cu [177], Au [178] and Pt [179] nanoparticles supported on ZnO after activation up to T = 873 K. Oxygen vacancies are surface defects generated by the loss of lattice oxygen due to high temperature chemical reduction in hydrogen (*ca*. 738 K for ZnO [180] and 550 K on Pd/ZnO [181]). The lack of metal sintering can be linked to strong interaction of Pd with surface defects on ZnO. Moreover, β-PdZn alloy at the metal-support interface [182] can also serve to anchor Pd nanoparticles inhibiting metal mobility. The XRD pattern of the as-received alumina support **(IIA)** presents a broad reflection at 2θ = 66.9° associated with the (4 4 0) main plane of cubic γ-Al_2O_3 **(IID)**. The XRD diffractograms of the fresh **(IIB)** and activated (to 973 K) Pd/Al_2O_3 **(IIC)** show an additional peak at 2θ = 40.1° (see *inset* **(c)** and **(d)**) characteristic of Pd^0 (see profile **(IIE)).** The main Pd^0 peak in Pd/ZnO (**(IB)** and *inset* **(a)**) and Pd/Al_2O_3 (**(IIB)** and *inset* **(c)**) has a similar intensity and width. In contrast, the activated Pd/Al_2O_3 exhibits a sharper peak (*i.e*. higher intensity and smaller width) suggesting Pd particle growth. A weaker interaction between (non-reducible) Al_2O_3 (vs. reducible ZnO) and Pd is consistent with the lower adhesion energy (E_{ads}, Pd-Al_2O_3 = 0.3-1.59 J m^{-2} *vs*. E_{ads}, Pd-ZnO = 2.3-2.5 J m^{-2}) [183] and can result in metal surface diffusion and particle sintering.

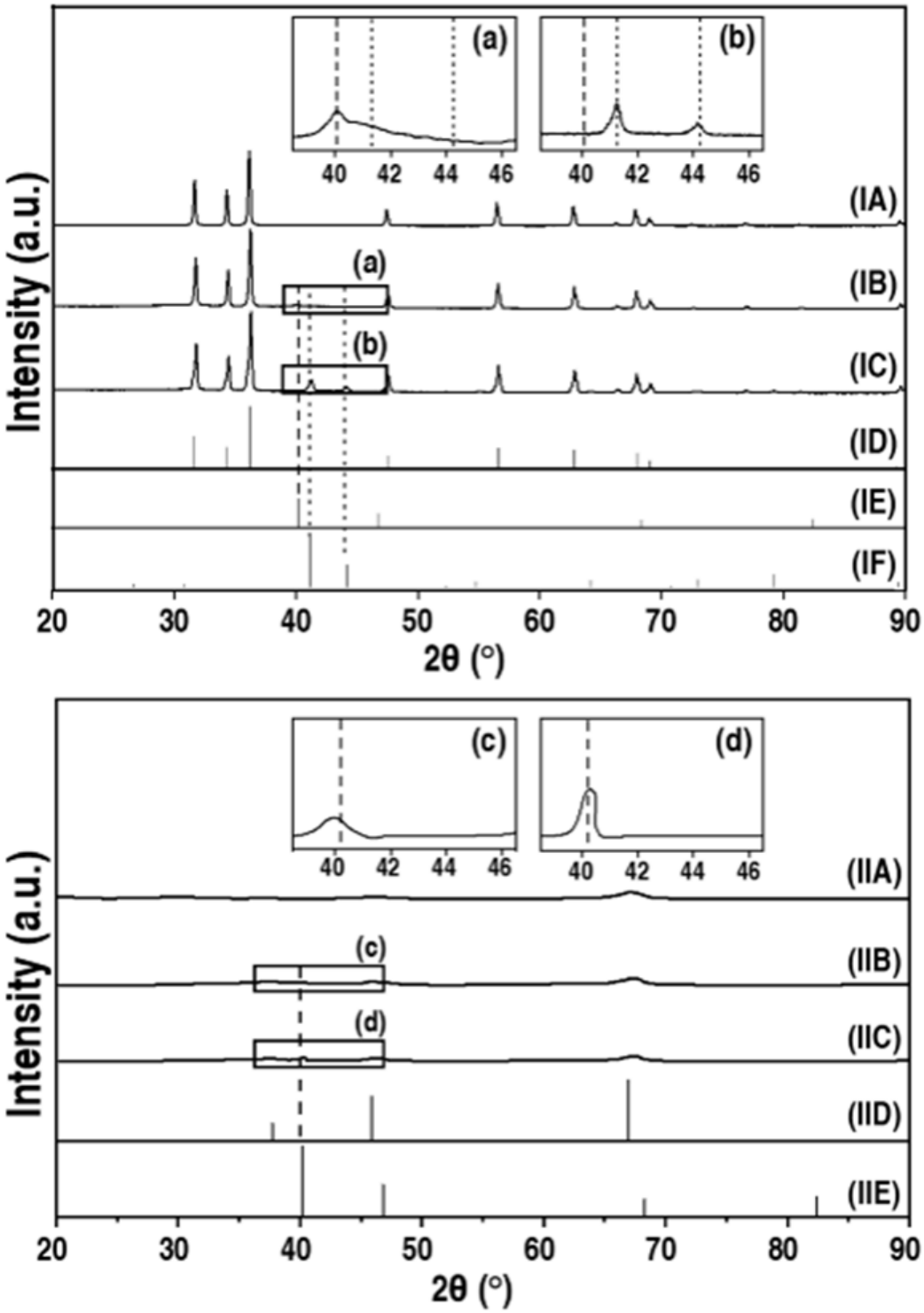

Figure 3.3: XRD patterns associated with (**I**) ZnO (**A**), Pd/ZnO fresh (**B**) and after hydrogen thermal treatment to 973 K (**C**), JCPDS-ICDD reference for (**D**) zincite-ZnO (070-8070), (**E**) Pd (046-1043) and (**F**) β-PdZn (072-2936); (**II**) Al_2O_3 (**A**), Pd/Al_2O_3 fresh (**B**) and after hydrogen thermal treatment to 973 K (**C**), JCPDS-ICDD reference for (**D**) zincite-ZnO (070-8070), (**E**) Pd (046-1043) and (**F**) β-PdZn (072-2936); (**II**) Al_2O_3 (A), Pd/Al_2O_3 fresh (**B**) and after treatment to 973 K (**C**), JCPDS-ICDD reference for (**D**) γ-Al_2O_3 (153-7011) and (**E**) Pd (046-1043). *Note*: XRD diffractogram magnifications over *ca.* 2θ = 38-46° for patterns (**IB**), (**IC**), (**IIB**) and (**IIC**) is presented as *insets* (a), (b), (c) and (d), respectively. Dashed line identifies position of the Pd^0 main peak (2θ = 40.1°) while dotted lines illustrate the position of characteristic peaks for β-PdZn (2θ = 41.2° and 44.1°)

Metal particle morphology was further examined by microscopy analyses, representative TEM, SEM and STEM images of (unsupported) Pd nanoparticles and (supported) fresh and activated to 973 K (as a representative) Pd/ZnO and Pd/Al_2O_3 are presented in **Figure 3.4**; associated metal particle size histograms are shown in **Figure 3.5.**

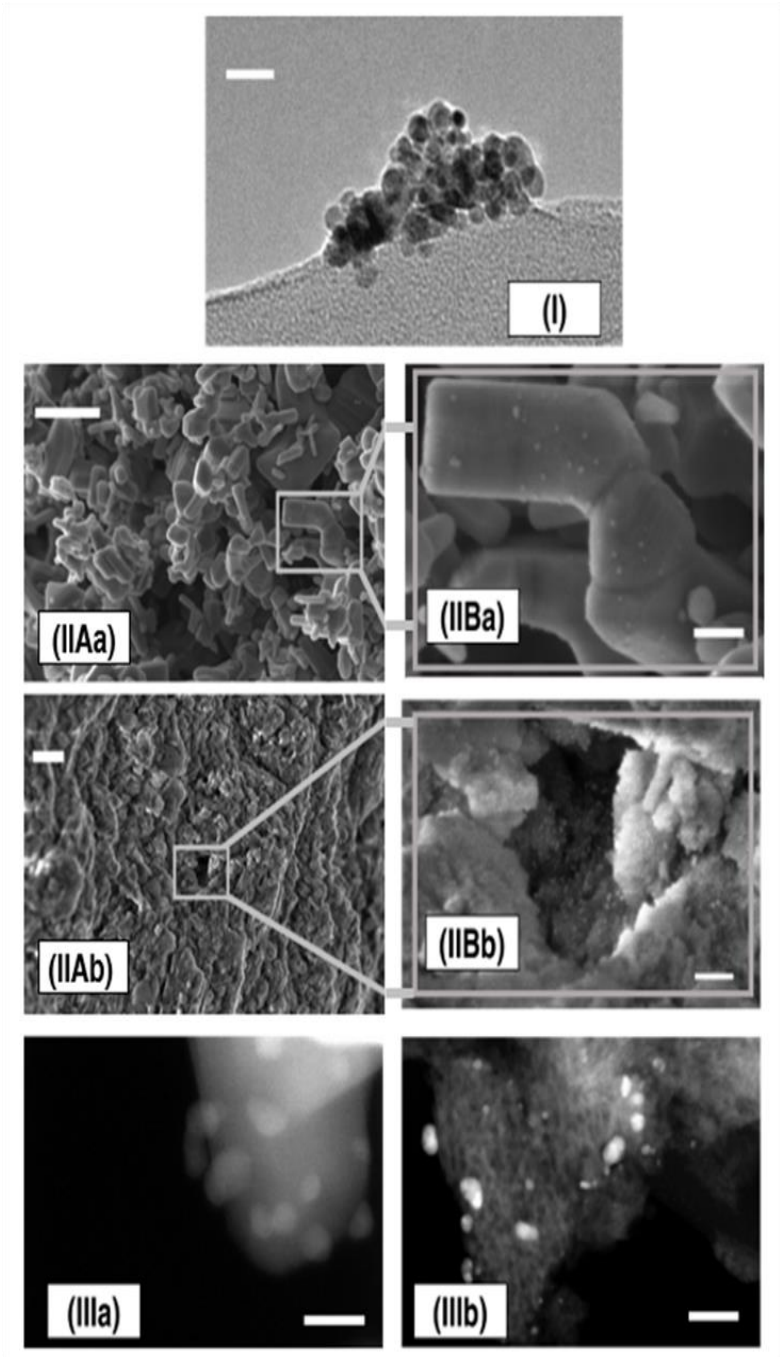

Figure 3.4: Representative (**I**) TEM image of Pd colloids (scale bar = 20 nm); (**II**) SEM micrographs at medium (**A**) (scale bar = 100 nm) and high-resolution (**B**) (scale bar = 20 nm) for fresh (a) Pd/ZnO and (b) Pd/Al_2O_3; (**III**) STEM image of (a) Pd/ZnO (scale bar = 20 nm) and (b) Pd/Al_2O_3 (scale bar = 50 nm) after H_2 treatment to 973 K.

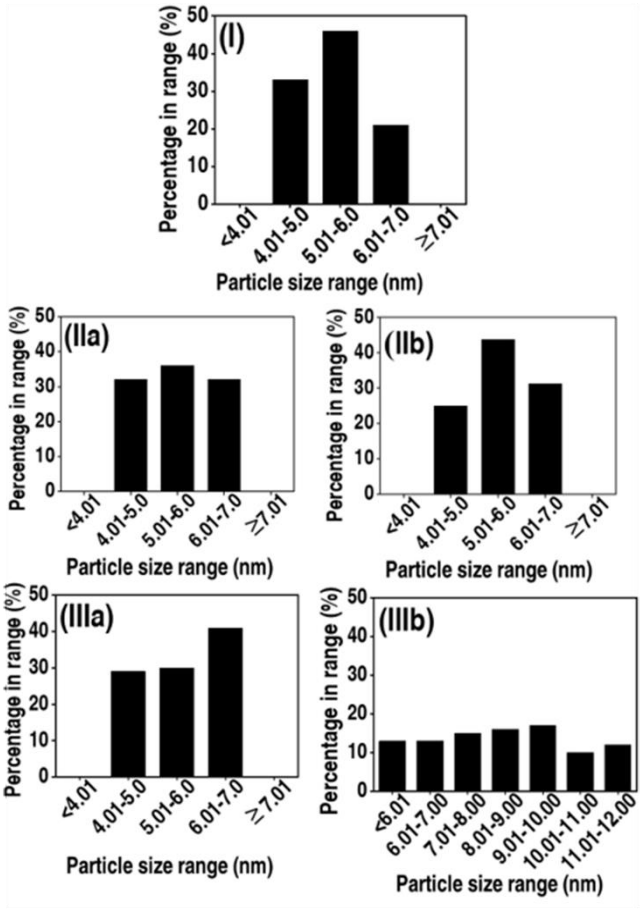

Figure 3.5: Metal particle size histograms associated with (**I**) Pd colloids, (**II**) fresh and (**III**) post-thermal treatment in H_2 to 973 K (a) Pd/ZnO and (b) Pd/Al_2O_3.

SEM analysis of Pd/ZnO (**Figure 3.4(IIa)**) shows an aggregation of small crystallites (≤40 nm) with a rod-like structure characteristic of zincite-ZnO [184]. The alumina carrier presents a more amorphous structure (**Figure 3.4(IIb)**), a result that is in line with the broad diffraction peak observed by XRD analysis (**Figure 3.3(II)**). The representative TEM image of Pd colloids (**Figure 3.4(I)**) demonstrates the formation of quasi-spherical nanoparticles with a narrow (4-7 nm; **Figure3.5 (I)**) size distribution and mean size (=5 nm). This is consistent with morphology (shape and size) reported elsewhere [163] for Pd colloids synthesised by a similar method. The SEM micrographs **(Figure 3.4(II))**, size distribution histograms **(Figure 3.5(II))** and entries in **Table 3.1** demonstrate that deposition of Pd on the ZnO and Al_2O_3 supports had little effect on palladium nanoparticle shape or size for the fresh samples. The integrity of the metal nanocrystals was maintained in Pd/ZnO with no significant changes in size/shape post-activation to 973 K (**Figure 3.4(IIIa)**, **Figure 3.5(IIIa)** and **Table 3.1**). In contrast, we observed an increase in nanoparticle size for Pd/Al_2O_3 after thermal treatment to high temperature (from 6 → 10 nm; **Figure 3.4(IIIb)**, **Figure 3.5(IIIb)** and **Table 3.1**) that is consistent with XRD measurements and reported literature showing metal sintering at T > 575 K for

Al_2O_3 supported metal catalysts [185] and Pd colloids supported on non-reducible carriers [186]. XRD provides information on bulk characteristics which can differ significantly from surface properties [187]. XPS analysis can provide critical information on surface Pd content/charge and PdZn alloy formation [188]. The fitted Pd 3*d* envelope for **(I)** Pd/ZnO and **(II)** Pd/Al_2O_3, activated in H_2 to 973 K, as representative examples, are shown in **Figure 3.6**.

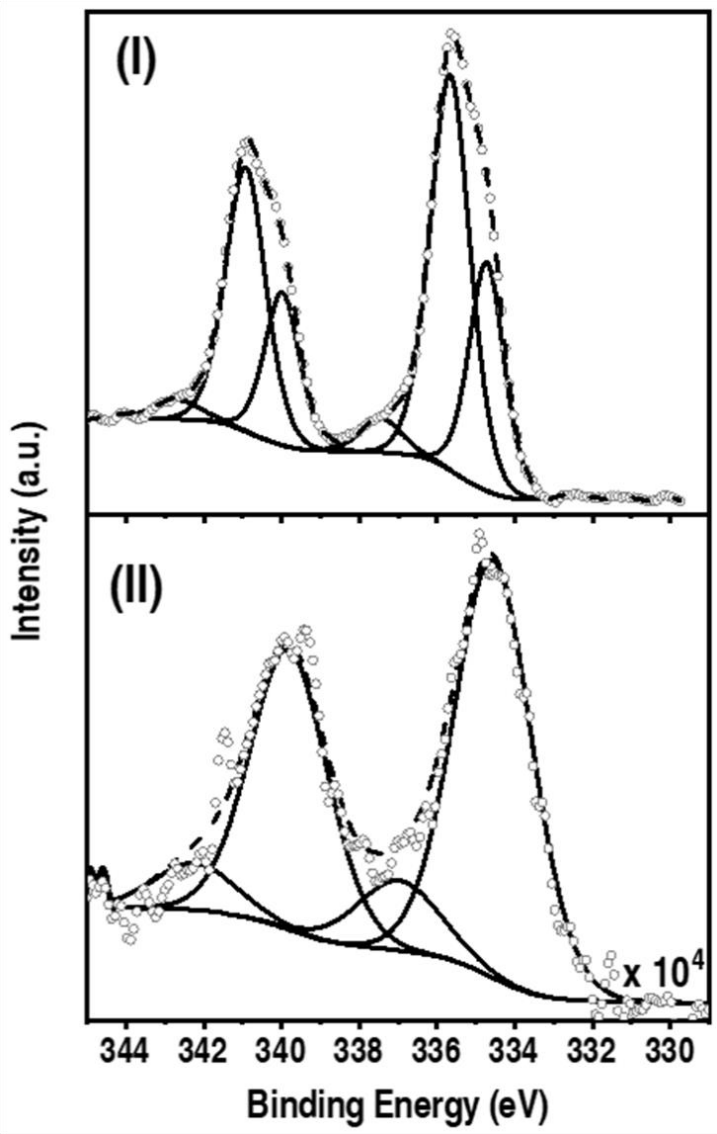

Figure 3.6: XPS profile over the Pd 3*d* region for thermally treated (to 973 K) in hydrogen (**I**) Pd/ZnO and (**II**) Pd/Al_2O_3. *Note*: Raw data are shown as open symbols (**O**) while curve fitted and envelope are represented by solid and dashed lines, respectively.

Both catalysts present an XPS spectrum characterised by a doublet with Pd $3d_{5/2}$ (BE) = 334.6 ± 0.1 eV and Pd $3d_{3/2}$ BE = 339.9 ± 0.1 eV that are *ca.* 0.5 eV lower than those characteristic of Pd^0 (Pd $3d_{5/2}$ BE = 335.1 eV and Pd $3d_{3/2}$ BE = 340.4 eV [189]). This suggests electron transfer from the carrier to Pd resulting in a partial negatively charged metal phase ($Pd^{\delta-}$). A similar downshift in BE have been previously reported for (2-10

nm) Pd nanoparticles [190] and ascribed to electron transfer from the oxide carrier [191]. The spectrum of each catalyst exhibits a doublet at higher BE (Pd $3d_{5/2}$ = 337.0 ± 0.5 eV and Pd $3d_{3/2}$ = 342.2 ± 0.5 eV) characteristic of surface Pd^{2+} species that can result from surface oxidation during the passivation step [187]. The XPS spectrum of Pd/ZnO presents an additional doublet at values of BE equal to 335.7 eV (Pd $3d_{5/2}$) and 340.9 eV (Pd $3d_{3/2}$) that is characteristic of PdZn alloy [188].

The XRD results suggest that increased activation temperature facilitates PdZn alloy formation. In order to explicitly demonstrate change(s) in the surface composition of the active sites due to thermal treatment, we have plotted the surface content of $Pd^{\delta-}$ and PdZn species (balance close with Pd^{2+} content; 5 ± 2%) obtained from XPS analysis, as a function of activation temperature and the results are presented in **Figure 3.7.**

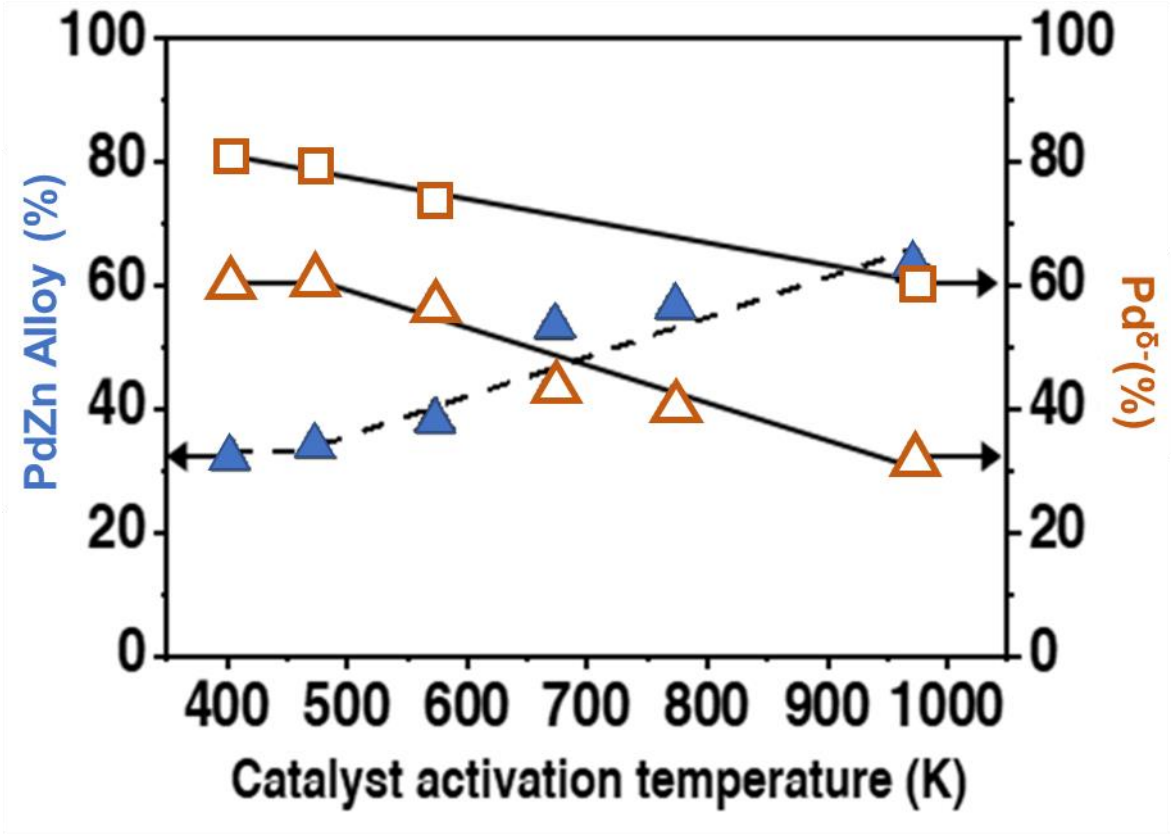

Figure 3.7: Variation in surface $Pd^{\delta-}$ (open symbol) and PdZn alloy content (solid symbols) with activation temperature for Pd/ZnO (△, ▲) and Pd/Al_2O_3 (□). *Note*: solid and dashed lines provide a guide to aid visual assessment.

We recorded a PdZn content of *ca.* 30% for Pd/ZnO activated at 403-473 K. A similar temperature requirement (≥373 K) has been shown by XANES and EXAFS for PdZn alloy phase formation [152]. A greater PdZn alloy content (30 → 63%) was accompanied by a decrease in the amount of $Pd^{\delta-}$ (from 60% to 32%) with increasing activation

temperature. Pd/Al_2O_3 exhibited a (*ca.* 25%) decrease in the surface concentration of $Pd^{\delta-}$ with activation temperature (403 K → 973 K) **(Figure 3.7)** that can be ascribed to particle sintering. Gigola *et al*. [192], observed the same temperature dependence and reached a similar conclusion for CeO_2-Pd/α-Al_2O_3. In each case, the concentration of $Pd^{\delta-}$ for Pd/Al_2O_3 was greater than that recorded for Pd/ZnO (60-80% vs. 32-60%) activated at the same temperature.

Hydrogen chemisorption analysis is of practical importance in hydrogenation applications. We recorded a total hydrogen uptake in the range 85-1560 μmol g_{Pd}^{-1} on Pd/ZnO and Pd/Al_2O_3 activated up to 973 K (**Table 3.1**) in line with reported values (234-2380 μmol g_{Pd}^{-1}) for Pd/ZnO [58] and Pd/Al_2O_3 [59] with similar metal content. We observed a decrease in uptake with increasing activation temperature, with lower values for Pd/ZnO *vs*. Pd/Al_2O_3. This is consistent with published work where β-PdZn alloy phase has exhibited limited hydrogen chemisorption capacity [58] and particles bearing a greater $Pd^{\delta-}$ content have shown to enhance H_2 adsorption/activation [60]. While the nature of the palladium phase can impact directly on hydrogen chemisorption, there is also the possibility of an indirect contribution *via* "metal encapsulation". The latter is possible through the formation of a ZnO_{1-x} layer post-H_2 treatment to $T \geq 373$ K [46] that covers partially the palladium sites and inhibits hydrogen uptake.

3.3.1.2 Catalytic Response

The effect of catalyst activation temperature on MBY hydrogenation activity **(I)** and MBE selectivity **(II)** response over Pd/ZnO and Pd/Al_2O_3 is presented in **Figure 3.8**. Both catalysts reached a pseudo stationary state after 90 minutes of reaction (see *inset*) showing a similar activity dependence characterised by a decrease in hydrogenation rate with activation temperature where greater values were observed for Pd/Al_2O_3 (*vs.* Pd/ZnO) at each activation temperature. -C≡C- bond hydrogenation over supported Pd has been proposed to follow the Horiuti-Polanyi mechanism consistent with a sequential alkyne → alkene → alkane conversion [193]. Atomic hydrogen, formed through dissociative H_2 chemisorption on palladium, acts as weak electrophilic agent and attacks (in two sequential steps) the triple bond [112]. The addition of the second H is rate limiting [194] and sensitive to hydrogen coverage on the metal Surface [108] (*i.e.* higher concentration of surface hydrogen lowers the activation energy barrier) [30]

. The greater activity over samples activated at lower temperature and Pd/Al_2O_3 (*vs*. Pd/ZnO) can be tentatively linked to an enhanced hydrogen chemisorption capacity

(**Table 3.1**) due to higher surface $Pd^{\delta-}$ content (**Figure 3.7**). Catalytic activity was insensitive to activation temperature at $T \leq 473$ K, the temperature range over which we observed an almost constant $Pd^{\delta-}$ concentration in Pd/ZnO (~60%) and Pd/Al_2O_3 (~80%) (**Figure 3.7**). Activation at $T > 473$ K resulted in a concomitant decrease in activity (R_{MBY}), $Pd^{\delta-}$ and H_2 chemisorption. This can be ascribed to β-PdZn alloy formation and (partial) metal encapsulation for Pd/ZnO and metal sintering for Pd/Al_2O_3, as demonstrated by XPS, XRD and microscopy analyses.

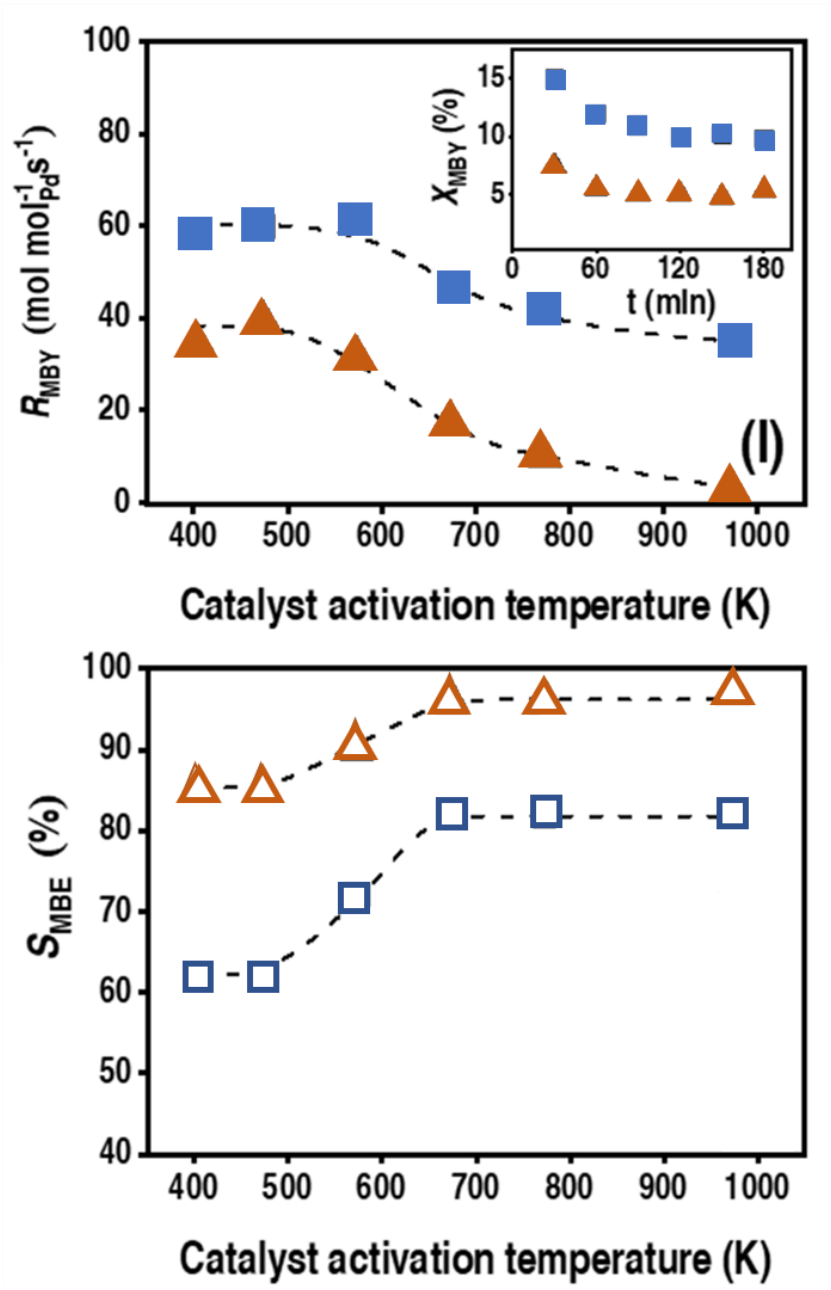

Figure 3.8: Variation of (**I**) MBY transformation rate (R_{MBY}, mol $molPd^{-1}$ s^{-1}; solid symbols) and (**II**) MBE selectivity (S_{MBE}, %; open symbols) with catalyst activation temperature over Pd/ZnO (▲,△) and Pd/Al_2O_3 (■, □). *Inset in* (**I**): Variation of MBY conversion (X_{MBY}) with time on-stream over Pd/ZnO (▲) and Pd/Al_2O_3 (■) activated at 573 K (n/F = 0.013 h), as representative samples. *Reaction conditions*: T = 403 K, P = 1 atm, X_{MBY} ~ 10%.

We conducted a series of experiments to examine the effect(s) of β-PdZn alloy formation on reaction selectivity at the same degree of conversion and the results are given in **Figure 3.8(II)**. The conversion of MBY over Pd/ZnO and Pd/Al_2O_3 generated MBE and MBA as the only products (*i.e.* $S_{MBE} + S_{MBA} = 100$). There were no detectable oligomerisation products (**Figure 3.1**), a result that deviates from -C≡C- bond gas-phase hydrogenation of alkynes (*e.g.*, acetylene) [22] over (SiO_2 and zeolite) supported Pd catalysts [195,196]. The absence of oligomer formation in this work can be the result of high H_2:Alkyne ratio [22] (*i.e.*, alkyne condensation is hampered at low surface alkyne concentrations) [197] and presence of Lewis basic sites on Al_2O_3 and ZnO [39,198] (*i.e.*, oligomerisation is promoted in the presence of metal cations of strong acid supports) [199]. We observed higher selectivity (*ca.* 25%) to the target MBE over Pd/ZnO (*vs.* Pd/Al_2O_3) at each activation temperature. Both (Al_2O_3 and ZnO supported) systems exhibit a similar S_{MBE} *vs.* activation temperature dependence characterised by three main regions: (i) low S_{MBE} (≤85%) for catalysts activated at $T \leq 473$, (ii) enhanced S_{MBE} (70-90 %) for samples reduced over $473 \leq T < 673$ K and (iii) highest S_{MBE} (up to 97%) for systems thermally treated in hydrogen at $T > 673$ K. The high selectivity achieved in this work is an important result on the light of the lower S_{MBE} values reported for MBY hydrogenation over Pd/ZnO in pressurised (3-10 bar) batch systems [200]. Pd/ZnO and Pd/Al_2O_3 bear metal particles of similar size (*ca*. 6 nm) upon activation at low temperatures (≤473 K) although the formation of β-PdZn alloy (**Figure 3.7**) can reduce the size of $Pd^{\delta-}$ ensembles on metal crystal planes (responsible for MBY multi-complexation and undesired MBA formation) [28] resulting in greater olefin selectivity. An increase in PdZn alloy concentration following activation between 473 and 673 K (**Figure 3.7**) further reduces palladium ensemble size increasing S_{MBE}. Over the same range of activation temperatures Pd/Al_2O_3 undergoes metal sintering (6 → 10 nm) which lowers the concentration of surface defects [201], responsible for over-hydrogenation [149]. The almost constant MBE selectivity for samples activated at $T > 673$ K is consistent with minor variations in PdZn alloy content (60 ± 3%, **Figure 3.7**) on Pd/ZnO and percentage of surface defects for metal particles with $d > 8$nm [202] for Pd/Al_2O_3.

3.3.2 Pd/ZnO vs. Pd/CuO vs. Au/Al_2O_3 vs. Lindlar Catalyst

3.3.2.1 Catalyst Characterisation

The SSA of Au/Al_2O_3, Lindlar and Pd/CuO are recorded in **Table 3.1**. The TPR activation profiles of the three catalysts are given in **Figure 3.9** while the temperatures associated with maximum H_2 desorption/consumption are provided in **Table 3.1**.

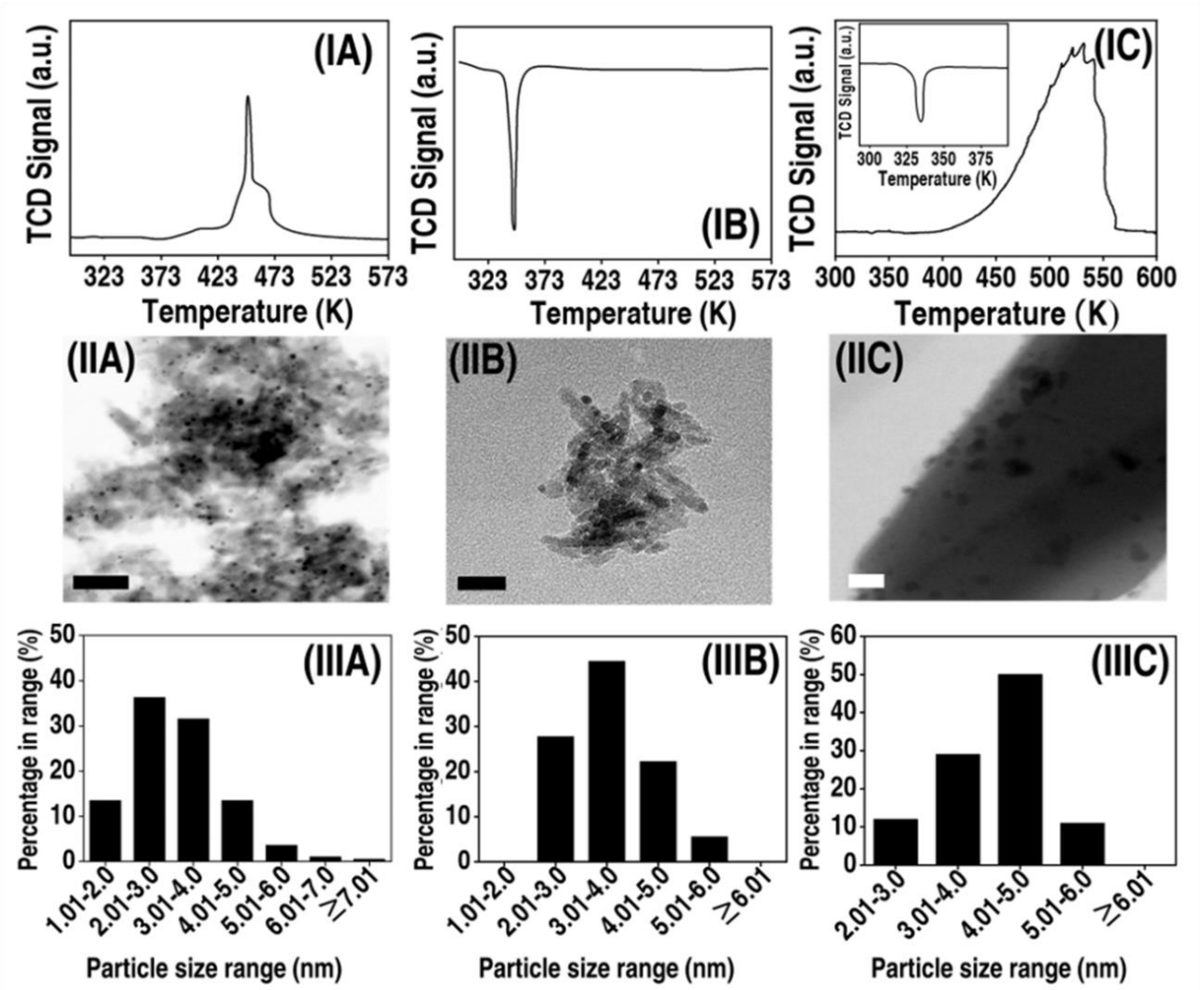

Figure 3.9: (**I**) TPR profiles and (**II**) representative TEM/STEM images (scale bar = 20 nm) with (**III**) associated metal particle size histogram for (**A**) Au/Al_2O_3, (**B**) Lindlar's and (**C**) Pd/CuO catalysts. *Note*: TPR profile magnification over *ca*. 295 K ≤ *T* ≤ 395 K for (**IC**) is included as an *inset*.

Au/Al_2O_3 **(IA)** shows a single positive peak at T_{max} = 448 K with experimental hydrogen consumption matching that required for complete Au^{3+} to Au^0 reduction [203]. Hao *et al.* [204] demonstrated (by XPS analysis) the formation of metallic gold in Au/Fe_2O_3 after thermal treatment (in H_2) to 573 K. The negative peak at 333-340 K in the TPR profiles of Lindlar **(IB)** and Pd/CuO **(IC)** catalysts can also be linked to Pd β-hydride decomposition. The equivalent H/Pd molar ratio for the Lindlar catalyst (0.17 *vs.* 0.20)

suggests a similar Pd nanoparticle size to that recorded for Pd/ZnO and Pd/Al_2O_3 (*i.e.*, 6 nm). Pd/CuO exhibited a lower H/Pd ratio (~0.05), a result that can be linked to Pd encapsulation due to the room temperature formation of $PdCuO_{1-x}$ species [205] that reduce H_2 diffusion into Pd bulk phase [206] lowering H/Pd. We observed a significantly lower surface Pd content (from XPS elemental analysis) relative to AAS loading (0.2 *vs.* 1 wt.%) for Pd/CuO which further suggests metal encapsulation by CuO. TPR of Pd/CuO shows a positive peak at *ca.* 425-560 K with a T_{max} = 525 K characteristic of $CuO \rightarrow Cu^0$ [207]. The lower band gap of CuO (1.2 eV) [208] relative to ZnO (3.3 eV) [80] results in greater reducibility [76] and can account for the downshift in the temperature requirement (by 160 K; see **Figures 3.2(A)** *vs.* **Figure 3.9(IC)**) for CuO reduction. The hydrogen uptake for Au/Al_2O_3 (32 μmol g_{Au}^{-1}) was low, in line with the high activation energy barrier of H_2 dissociative adsorption due to the filled *d* band [81]. Hydrogen chemisorption on Pd Lindlar (217 μmol g_{Pd}^{-1}) and Pd/CuO (75 μmol g_{Pd}^{-1}) was significantly lower (up to a 20-fold) than that recorded for Pd/Al_2O_3 activated at a similar temperature (**Table 3.1**), which can be linked to Pd coverage by $Pb(OAc)_2$ during catalyst synthesis [166] and PdCu alloy formation *post*-TPR at $T \geq 438$ K [209].

A representative high-resolution STEM image of Au/Al_2O_3 is given in **Figure 3. 9(IIA)** with associated nanoparticle size histogram in **Figure 3.9(IIIA)**. The catalyst exhibits pseudo-spherical Au nanoparticles in the 1–8 nm size range with a mean diameter of 4 nm (**Table 3.1**). Low-coordination surface sites (*e.g.*, corner, steps and edges) in gold nanoparticles ≤5 nm have been identified as active sites for hydrogen adsorption/activation [210] and are essential for significant activity in hydrogenations [211]. The representative STEM images of Pd Lindlar **(IIB)** and Pd/CuO **(IIC)** are shown in **Figure 3.9**. Metal particles of globular morphology in the 2- 6 nm size range are in evidence (**Figure 3.9(IIIB-IIIC)**), with a mean Pd particle size of 4 nm (Lindlar) and 5 nm (Pd/CuO) (**Table 3.1**).

3.3.2.2 Catalytic Response

In this study, catalytic performance of Pd/ZnO was compared with other well-known selective catalysts for alkyne hydrogenation including Au/Al_2O_3 and Pd alloys (Pd_3Pb in Lindlar catalyst and PdCu in Pd/CuO). We first examined the catalytic performance of Pd/ZnO *vs.* Pd/CuO *vs.* Au/Al_2O_3 under the same reaction conditions and the results obtained are presented in **Figure 3.10**.

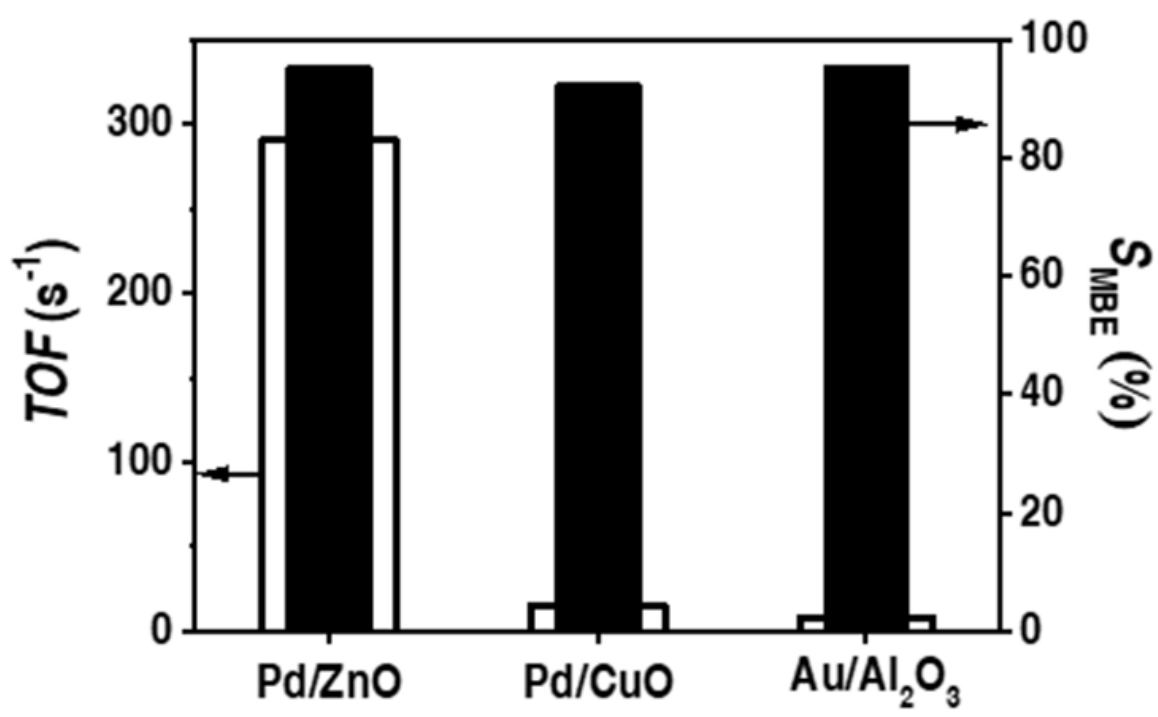

Figure 3.10: Variation of MBY transformation rate (*TOF*, s^{-1}; open bars) and MBE selectivity (S_{MBE}, %; solid bars) for reaction over Pd/ZnO, Pd/CuO and Au/Al_2O_3 activated at 573 K. *Reaction conditions*: T = 403 K, P = 1 atm, X_{MBY} ~ 10%.

Au/Al_2O_3 and Pd/CuO with lower hydrogen uptake capacity (32-75 μmol g_{metal}^{-1} *vs.* 167 μmol g_{metal}^{-1}) delivered the lowest activity. Marin-Astorga *et al.* [212] reported a similar dependence of activity with H_2 uptake in the hydrogenation of C3-C5 alkynes over Pd/SiO_2 and Pd/MCM-41. Under the same conversion degree (X_{MBY} =10%), the three catalysts delivered a similar high selectivity (*ca.* 96%) to the target MBE (S_{MBA} ~ 4%). Lin *et al.* [213] reported high S_{MBE} in liquid phase operation over Au supported on active carbon, but we provide in here the first evidence of elevated MBE production in continuous gas phase operation.

The relationship between MBY conversion (X_{MBY}) and MBE selectivity (S_{MBE}) for Pd/ZnO, Pd/Al_2O_3 and industrial Lindlar catalyst shown in **Figure 3.11** provides an overall picture of the selectivity trends; the lines are intended merely as a guide to aid visual assessment and do not possess any "fitting" significance.

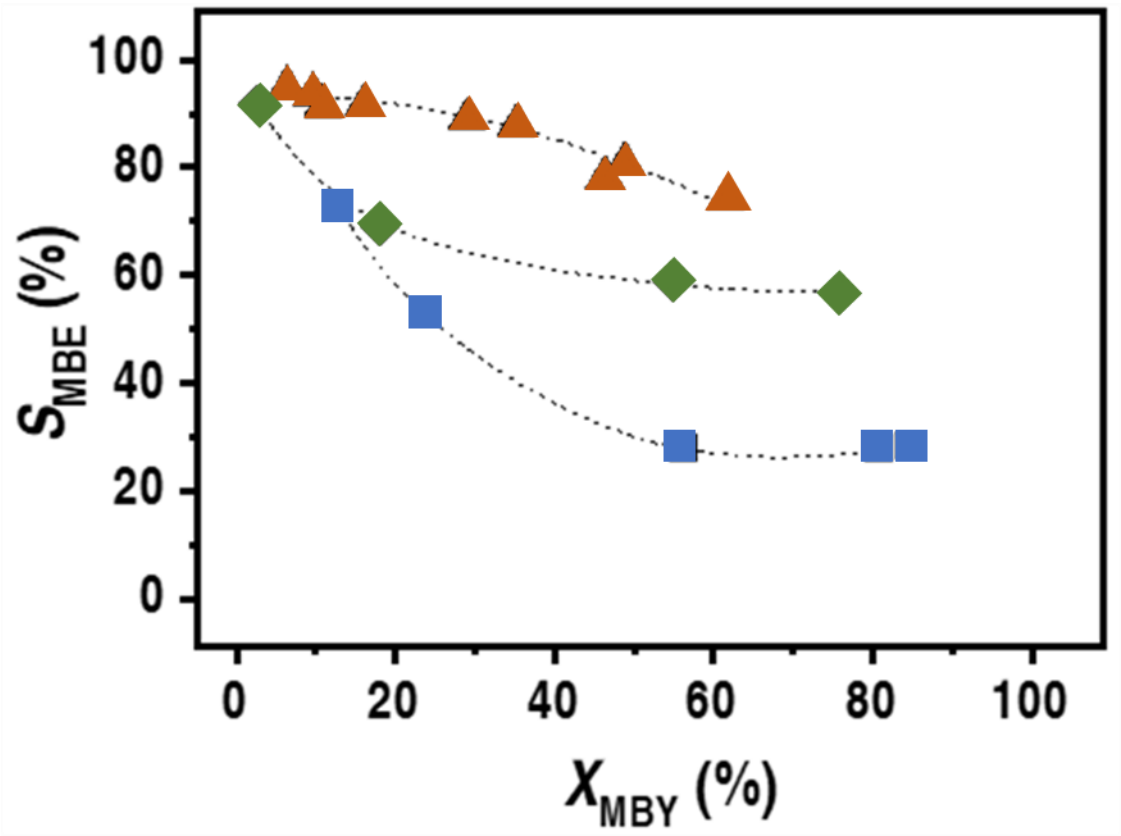

Figure 3.11: Variation of MBE selectivity (S_{MBE}, %) as a function of MBY conversion (X_{MBY}, %) for reaction over Pd/ZnO (▲), Pd/Al_2O_3 (■) and Lindlar's (◆) catalysts. *Note*: dashed lines provide a guide to aid visual assessment. *Reaction conditions*: T = 403 K, P = 1 atm.

In each case, S_{MBE} decreased (to varying degrees) as MBY conversion was increased. This anti-sympathetic correlation between X_{MBY} and S_{MBE} is to be expected in a stepwise hydrogenation scheme where total hydrogenation should be enhanced at greater X_{MBY}. We could not find any report of MBY hydrogenation promoted by supported Pd catalysts that has considered the dependence of S_{MBE} with X_{MBY}. It is, nonetheless, worth flagging the work of Kim and Moon [214] who observed a similar trend in the gas phase hydrogenation of acetylene over Pd/SiO_2. MBE selectivity over Pd/Al_2O_3 was significantly lower than that recorded for Pd/ZnO, regardless of MBY conversion. We observed an intermediate level of S_{MBE} over the Lindlar catalyst at all MBY conversions, which can be tentatively ascribed to a decrease of $Pd^{\delta-}$ ensemble size by the Pd_3Pb alloy phase [38]. The higher MBE selectivity over Pd/ZnO (vs. Lindlar) can be explained by the increased temperature requirement for the generation of Pd_3Pb relative to β-PdZn [36] which, in turn, will result in a greater surface β-PdZn content at each temperature.

3.4. Conclusions

A series of Pd/ZnO catalysts with different β-PdZn alloy content were synthesized *via* deposition of ex situ generated Pd colloids followed by thermal treatment in H_2 to 403-973 K and used in the continuous gas phase hydrogenation of MBY→MBE. Powder XRD analysis confirmed alloy formation while XPS measurements revealed the coexistence of $Pd^{\delta-}$ and β-PdZn alloy on the catalyst surface with increase PdZn/$Pd^{\delta-}$ mol ratio at higher activation temperatures. Pd/ZnO was the most selective to the target MBE while (a benchmark) Pd/Al_2O_3 delivered the highest activity, regardless of reduction temperature in H_2. Both systems showed a similar dependence with activation temperature consistent with greater MBE selectivity and lower activity over catalysts prepared at higher temperature. We attributed this response to dilution of exposed $Pd^{\delta-}$ ensembles due to alloy formation and metal encapsulation (for Pd/ZnO) or metal agglomeration (in Pd/Al_2O_3). Pd/ZnO also delivered the best combined activity/MBE selectivity relative to industrial Lindlar catalyst, Pd/CuO and Au/Al_2O_3. Our results establish a direct correlation between surface β-PdZn alloy content and catalytic performance for the continuous gas phase transformation of alkenols with multiple industrial applications.

Chapter 4:

Zn-Promoted Selective Gas Phase Hydrogenation of Tertiary and Secondary C4 Alkynols over Supported Pd

In **Chapter 3**, we have demonstrated high MBE selectivity in the continuous gas phase semi-hydrogenation of MBY over several Pd/ZnO catalysts (activated in H_2 at 403-973 K), although metal encapsulation and tuning alloy composition were decided drawbacks. In this chapter, we carry out a systematic evaluation of the key parameters (H_2: Alkynol, nature of the carrier and Pd-Zn alloy) in the production of C4 tertiary and secondary alkenols *via* alkynol semi-hydrogenation. We have analysed the dependence between alkynol hydrogenation and H_2 partial pressure using Pd/Al_2O_3, as a benchmark. We also consider the impact of the nature of the support for (carbon, CeO_2, ZnO, Al_2O_3, MgO) supported Pd catalysts and the effect of alloy composition using $Pd\text{-}Zn/Al_2O_3$ synthesised by colloidal deposition.

4.1 Introduction

The catalytic hydrogenation of alkynols is the main route to alkenols [5], widely employed as intermediates in the manufacture of fine chemicals (*e.g.* vitamins and anticarcinogenic agents) [215]. The industrial process is carried out in pressurised (2-5 bar) batch liquid phase reactors over Pd catalysts [114]. A move from batch to continuous operation reduces the number of processing steps, which improves environmental performance (E-factor reduction from ($23 \rightarrow 3$ kg $_{\text{waste generated}}$ $kg_{product}^{-1}$) [216]. Alkynols can be classified based on the number of substituents bonded to the hydroxyl C as primary, secondary and tertiary (*i.e.* one carbon, two or three, respectively). The work to date has focused on hydrogenation of tertiary alkynols [217]. The economic benefits of alkenol production are dependent on catalyst performance, where undesired condensation (to dimers), full hydrogenation (to alkanol) and double bond migration (to ketone) are difficult to fully avoid [38,218]. Hydrogen uptake/release is undoubtedly a critical factor that impacts on activity/selectivity response and is linked to metal particle size and H_2: Alkynol ratio. The formation of small (<4 nm) Pd nanoparticles is essential for significant hydrogen uptake and hydrogenation activity [219]. Control of metal dispersion is challenging using conventional catalyst preparation techniques (*e.g.* impregnation or DP)

but this can be circumvented by the synthesis of size-controlled metal colloids that are subsequently anchored onto a carrier [125]. The undesired formation of dimers and alkanols can be governed by hydrogen coverage on the catalyst surface [31] which, in turn, can be influenced by the H_2:Alkynol ratio, *i.e.* dimer generation and full hydrogenation are promoted at low (≤1.5) [31] and high ratios (≥2.5) [220], respectively. Alkynol hydrogenation reactions have been conducted where the H_2:Alkynol (stoichiometric = 1 to alkenol production) was maintained low (typically = 1×10^{-2} - 2×10^{-2}) in both, liquid and gas phase operation [221,222]. It is, however, worth flagging the work of Prestianni *et al.*[119], who examined the gas phase hydrogenation of (tertiary) MBY over unsupported Pd nanocubes using an H_2:Alkynol ratio of 3.

The electronic character of the Pd site is an additional consideration that impacts directly on the mode and strength of reactant adsorption [28]. Although this can be effectively modified by the Pd crystal size [149] or the acid-base/redox properties of the support [223], it is difficult to establish a direct correlation from the existing literature for optimum alkenol production. Surface defects (*e.g.* kinks, steps and edges) are prevalent on small (<2.5 nm) palladium nanoparticles [224] and promote undesired -C≡C- over-hydrogenation [225] and/or alkenol double bond migration [38]. On the other hand, (111) planes in larger (>6 nm) Pd^0 nanoparticles favour the formation of dimers [225]. A "support effect" has been reported in the literature for carriers with modified acid-base properties. Zakarina and *co-workers* [226] and Bönnemann [227] working with a series of oxide (SiO_2, Al_2O_3, MgO, $CaCO_3$, CeO_2) supported palladium catalysts, linked their observed increased in activity and alkenol selectivity in the liquid phase hydrogenation of MBY and 3-hexyn-1-ol to an increased basicity of the carrier that results in the formation of electron-rich Pd nanoparticles. The opposite effect has also been observed, Berguerand and *co-workers* [150] recorded a drop in activity in the 2-butyne-1,4-diol hydrogenation linked to the presence of $Pd^{\delta-}$ nanoparticles using a wide range of supports (MgO, ZnO, Ga_2O_3,Al_2O_3, ZrO_2, SnO_2, SiO_2). Alkenol selectivity over supported Pd has also been shown to be influenced by the incorporation of a second metal and ascribed to: (i) blockage of Pd surface sites at corners that promote alkanol formation, (ii) electron transfer from/to Pd sites [228] which impacts on the -C≡C-/-C=C- adsorption strength [228] and/or (iii) alloy formation that induces geometric and electronic modifications. An alloy lead-poisoned Pd/$CaCO_3$ (Lindlar's) catalyst is typically used at industrial scale [44] but there is a pressing demand for alternative formulations due to the high toxicity of Pb [229]. PdZn alloy has shown promise for alkenol production in pressurised batch liquid

systems [220]. In previous work [230], we have shown high selectivity in the continuous gas phase semi-hydrogenation of MBY over a series of Pd/ZnO catalysts (activated to different temperatures), but control of alloy composition was a decided drawback. We have extended that study to consider a series of Al_2O_3 supported Pd-Zn colloidal catalysts as a means of controlling alloy composition.

Our intended purpose in undertaken this work was to provide a systematic analysis of the critical parameters (H_2: Alkynol, nature of the support and Pd-Zn alloy) in the synthesis of tertiary and secondary alkenols through partial hydrogenation of the correspondent alkynol. We have selected MBE and 3BE, with multiple applications in the synthesis of vitamins and tocopherols [231], as model molecules. We have examined the dependence of alkynol hydrogenation on H_2 partial pressure over Pd/Al_2O_3, as a benchmark. We also address the effect of the nature of the carrier for Pd supported on a group of carbon, reducible (CeO_2 and ZnO) and *non*-reducible oxides (Al_2O_3, MgO) with modified acid-base properties as well as the effect of alloy formation for a series of $Pd-Zn/Al_2O_3$ catalysts prepared by colloidal deposition.

4.2 Experimental

4.2.1 Catalysts Preparation

MgO, CeO_2, ZnO, 1.2% wt. Pd/Al_2O_3 (denoted Pd/Al_2O_3-I in this work) and 1.0% wt. Pd/C were obtained from Sigma-Aldrich while the Al_2O_3 support was purchased from Alfa Aesar. Laboratory synthesis of Pd/MgO (0.9% wt.), Pd/CeO_2 (0.8% wt.) and Pd/ZnO (1.1% wt.) by DP using urea (Riedel-de Haën, 99%) as basification agent followed a prior procedure [232]. Briefly, an aqueous solution of urea (100-fold urea excess) and $PdCl_2$ (Sigma-Aldrich, 99%, 0.16 M, 30 cm^3) was added to MgO, CeO_2 and ZnO (Alpha Aesar, 30 g) in a three neck round bottom flask. The suspension was heated (2 K min^{-1} to 353 K) under constant stirring, where the pH progressively increased to the isoelectric point of each support (pH 7 for CeO_2 , 10 for ZnO and 11 for MgO) as a result of urea decomposition [105].

$$NH_2CONH_2 + 3H_2O \rightarrow K_2NH_4 + OH^- + CO_2 \quad (4.1)$$

The catalysts were separated by filtration, washed with distilled water until nitrate free, dried in He (45 cm^3 min^{-1}) at 373 K (2 K min^{-1}) for 5 h and sieved to 75 μm. mean particle diameter.

In addition, a series of Al_2O_3 supported colloidal catalysts (Pd/Al_2O_3-II, Zn/Al_2O_3, Pd-Zn/Al_2O_3 (Pd:Zn molar ratios = 95:5, 70:30 and 30:70)) were prepared by deposition of *ex-situ* synthesised monodispersed Pd, Zn and Pd-Zn nanoparticles prepared by a solvent (aka. Polyol) method described in detail elsewhere [233–235]. Briefly, poly-*n*-vinyl pyrrolidone (monomer: metal = 10:1) was mixed with anhydrous ethylene glycol (60 cm^3) and $ZnCl_2$ in a two-necked round-bottom flask, stirred for 1 h at 353 K and cooled to 273 K in an ice bath (*solution 1*). In a separate two-necked, round-bottom flask, palladium (II) acetate (0.03−0.07 g) was dissolved in 1,4-dioxane (20 cm^3) under vigorous stirring for 2 h (*solution 2*). Both solutions were mixed under continuous stirring to ensure homogenization where the pH of the mixture was adjusted to pH 9–10 by addition of an aqueous NaOH solution (1−2 cm^3 ,1 M). The resulting (bright yellow) solution was capped and heated at 373 K under vigorous stirring for 2 h. A change in colour took place (yellow → dark brown) indicative of colloid formation[236]. The solution was cooled to room temperature and the colloids purified (with excess acetone, ∼1000 cm^3) and redispersed (in MeOH). The nanoparticles were deposited on the Al_2O_3 support by deposition as described previously [235]. Prior to use, the catalysts were sieved into a batch of 75 μm average diameter and reduced in 60 cm^3 min^{-1} H_2 (BOC, ≥99.99%) at 2 K min^{-1} to 373-573 K in order to ensure formation of Pd^0 [237]. After activation, the samples were cooled to ambient temperature and passivated in 1% v/v O_2/He (30 cm^3 min^{-1}) for 1 h for *ex-situ* characterisation by TEM/STEM and XPS analyses.

4.2.2 Catalyst Characterisation

The Pd and Zn content was determined by inductively coupled plasma-optical emission spectroscopy (ICP-OES) using a Perkin–Elmer Optima 4300 ICP-OES spectrometer. Before analysis, the samples were treated in concentrated HNO_3 at 343 K for 12 h. SSA, H_2 chemisorption (at room temperature and/or 373 K) and hydrogen temperature-programmed desorption (H_2-TPD) were performed using the commercial CHEM-BET 3000 (Quantachrome) unit equipped with a thermal conductivity detector (TCD) with data acquisition/manipulation using the TPR Win™ software. Total SSA was obtained using the standard single point BET method. The samples were loaded into a U-shaped Quartz cell, outgassed in 60 cm^3 min^{-1} He to 373 K overnight[238] and cooled down to room temperature. SSA values were recorded with a (30 cm^3 min^{-1}) 50% v/v N_2/He flow; pure N_2 (BOC, 99.9%) served as the internal standard. At least two cycles of N_2 adsorption–desorption in the flow mode were used to determine total surface area. The samples were reduced in 17 cm^3 min^{-1}, 5% v/v H_2/N_2 at 2 K min^{-1} to 373-573 K. The

thermally treated samples were maintained at the final temperature in a constant flow of H_2/N_2 for 1 h, swept with a flow of N_2 for 1.5 h in order to remove any physisorbed hydrogen and maintained (at 373 K) or cooled (to room temperature) to be subjected to H_2 chemisorption using a pulse (30 μl) titration procedure. Samples were then thoroughly flushed (in N_2) for 30 min and H_2-TPD conducted in 60 cm^3 min^{-1} N_2 at 50 K min^{-1} to 973 K. In blank tests, there was no measurable H_2 uptake on the support alone. SSA and H_2 chemisorption/desorption values were reproducible to within ±10% and the values quoted are the mean. Metal particle size and shape was determined by transmission (TEM, JEOL JEM 2011 TEM unit) and (STEM, JEOL 2200FS field emission gun-equipped TEM unit), employing Gatan Digital Micrograph 1.82 for data acquisition/manipulation. Samples for analysis were crushed and deposited (dry) on a holey carbon/Ni grid (300 Mesh). Up to 800 individual metal particles were counted for each catalyst and the surface area-weighted metal diameter (d) was calculated from:

$$d = \frac{\sum_i n_i d_i^3}{\sum_i n_i d_i^2} \tag{4.2}$$

where n_i is the number of particles of diameter d_i. Particle size was also determined by room temperature H_2 chemisorption measurements (d_{H_2}; stoichiometric Pd:H = 1) [239]. XPS measurements were performed using a monochromatized Al anode (K_α 1486.6 eV, 10 kV, 20 mA). The source power was maintained at 3.9×10^3 W and the emitted photoelectrons were sampled from an area of 13 mm^2; the photoelectron take-off angle was normal emission (0°). The analyser pass energy was 150 eV for survey (0–1100 eV) and high-resolution spectra (over the Pd $3d_{5/2}$, Pd $3d_{3/2}$ and Pd $3p_{3/2}$ core levels). The C 1*s* peak was calibrated at 284.5 eV and used as internal standard to compensate for charging effects. Spectra curve fitting and quantification were performed with the Casa XPS software (version 2.3.17), using Shirley background and Gaussian Lorentzian curves (GL30) with band width (FWHM) ranging from 1.5-2.5 eV and fixed Pd $3d_{5/2}$ position (-5.26 eV) and intensity (+1.5-fold) relative to Pd $3d_{3/2}$ peak [240]. The same fitting procedure was employed in determining the Pd $3p_{3/2}$ position, with deconvolution of the O 1*s* peak as described in detail elsewhere [241,242].

4.2.3 Catalytic System

The hydrogenation of MBY and 3BY (Sigma-Aldrich, purity ≥97%) as a solution in BOL (Sigma-Aldrich, ≥97%) was carried out *in situ*, immediately after catalyst

activation, under atmospheric pressure at 373 K in a continuous flow fixed bed vertical glass reactor (*i.d.* = 15 mm). The catalytic reactor and operating conditions were selected to ensure negligible heat/mass transport limitations. A layer of borosilicate glass beads served as a preheating zone where the alkynol reactant was vaporised and reached reaction temperature before contacting the catalyst. Isothermal conditions (±1 K) were maintained by diluting the catalyst bed with ground glass (75 μm diameter). Reaction temperature was continuously monitored by a thermocouple inserted in a thermowell within the catalyst bed. The alkynol was delivered to the reactor at a fixed calibrated flow rate *via* a glass/teflon air-tight syringe and teflon line using a microprocessor-controlled infusion pump (Model 100 kd Scientific). A co-current flow of alkynol and H_2 or H_2/N_2 ($P_{H_2} = 4 \times 10^{-2} – 3 \times 10^{-1}$ atm) was maintained at $GHSV = 1 \times 10^4$ h^{-1}. The flow rate was monitored using a Humonics (Model 520) digital flowmeter. The molar Pd (n) to inlet alkynol molar feed rate (n/F) spanned the range $8 \times 10^{-6} – 1 \times 10^{-4}$ h. In blank tests, passage of each alkynol in a stream of H_2 through the empty reactor or over the (oxide/carbonaceous) support alone did not result in any detectable conversion. The reactor effluent was frozen in an ice-bath trap for subsequent analysis which was made using a Perkin-Elmer Auto System XL gas chromatograph equipped with a programmed split/splitless injector and a flame ionization detector using a Stabilwax (fused silica) 30 m × 0.32 mm *i.d.*, 0.25 μm film thickness capillary column (RESTEK). Data acquisition/manipulation was performed using the TotalChrom Workstation Version 6.1.2 (for Windows) chromatography data system. The products, MBE (98%), MBA (99%), 3BE (97%), BA (99.5%) and BONE (99%) were purchased from Sigma-Aldrich and used without further purification. Reactant/product molar fractions (x_i) were obtained using detailed calibration plots (not shown). Alkynol conversion (X_i) was obtained from:

$$X_i\ (\%) = \frac{[\text{Alkynol}]_{in} - [\text{Alkynol}]_{out}}{[\text{Alkynol}]_{in}} \times 100 \qquad \textbf{(4.3)}$$

where selectivity in terms of (for example) alkenol ($S_{Alkenol}$) is given by:

$$S_{Alkenol}\ (\%) = \frac{[\text{Alkenol}]_{out}}{[\text{Alkynol}]_{in} - [\text{Alkynol}]_{out}} \times 100 \qquad \textbf{(4.4)}$$

The subscripts "in" and "out" refer to the inlet and outlet streams, respectively. Catalytic activity is also quantified in terms of steady-state (after *ca.* 3 h) alkynol consumption rate (R, $mol_{Alkynol}\ g_{Pd}^{-1}\ h^{-1}$), determined from time on-stream measurements [243]. Repeated (up to three separate) catalytic runs with different samples from the same batch of catalyst delivered raw data reproducibility and carbon mass balance within ±6%.

4.3 Results and Discussion

Reaction selectivity is crucial as alkynol hydrogen treatment can result in a range of intermediates and by-products as shown in **Figure 4.1**, which presents the reaction networks for the transformation of MBY **(I)** and 3BY **(II)** based on the pathways proposed for liquid phase -C≡C- bond hydrogenation[149].

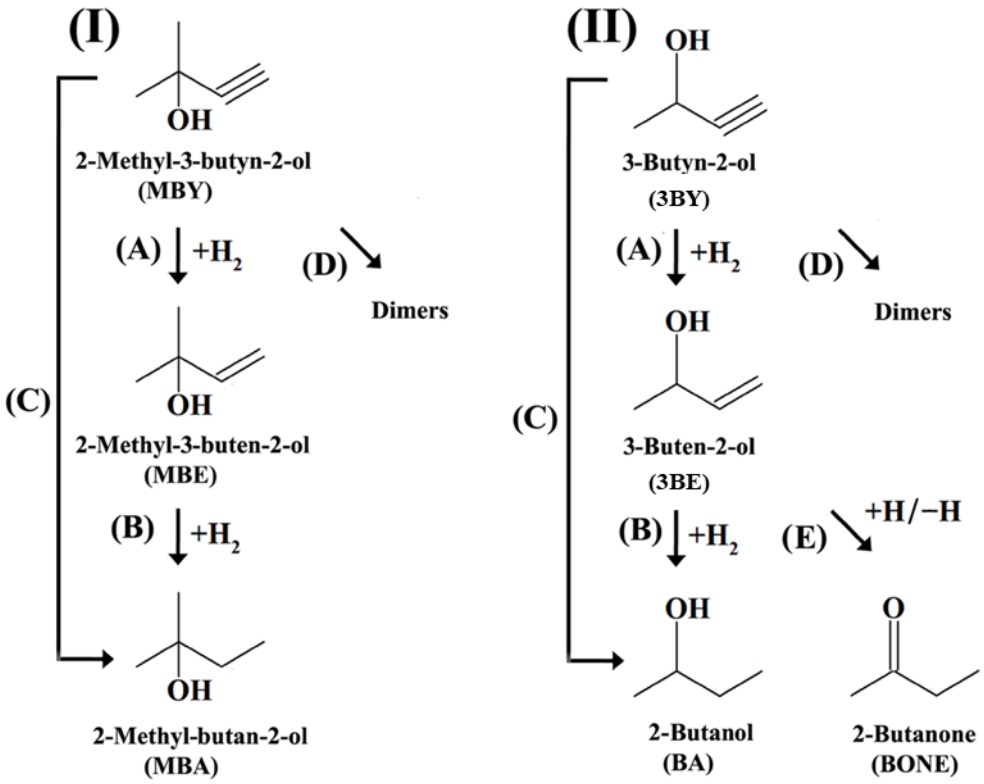

Figure 4.1: Reaction pathways in the hydrogenation of (**I**) MBY and (**II**) 3BY.

Step A represents the target -C≡C- → -C=C- alkenol semi-hydrogenation. Further hydrogenation results in alkanol formation (**Step B**), which has been ascribed to surface alkenol activation (*via* di-δ) on Pd planes [11]. Alkanol can also be generated directly from the alkynol (**Step** C) through -C≡C- dissociative adsorption on Pd surface defects [26]. The formation of dimers (Step D) can result from condensation of two semi-hydrogenated alkene species [244] and has been linked to the formation of vinyl radicals ($^{\bullet}CH=CH_2$) on surface Pd planes [245] at low H_2:-C≡C- (≤1.5) [31] and $P_{Alkynol}$ (≤0.02 kPa) [246]. BONE formation (Step E) *via* double bond migration and keto-enol tautomerization [247] is also favoured on palladium surface defects [110]. The catalysts used in this study promoted only hydrogenation (to MBE, MBA, BE and BA) and double bond migration steps (to BONE) under all reaction conditions, whereas no dimerization was observed in the transformation of MBY and 3BY unlike previous work [222].

4.3.1 Effect of Hydroxyl Group Position and Hydrogen Partial Pressure

We first examined the catalytic action of commercial Pd/Al_2O_3-I (as a benchmark) in the gas phase hydrogenation of tertiary (MBY) and secondary (BY) alkynols where the inlet hydrogen has been varied from excess (H_2: Alkynol up to 10) to lean (stoichiometric) conditions.

4.3.1.1 Catalyst Characterisation: Pd/Al_2O_3-I

The STEM analysis *post*-activation served to reveal that Pd is present in a highly dispersed form (see representative image in **Figure 4.2(I)**) with the majority of particles in the size range 1-3 nm.

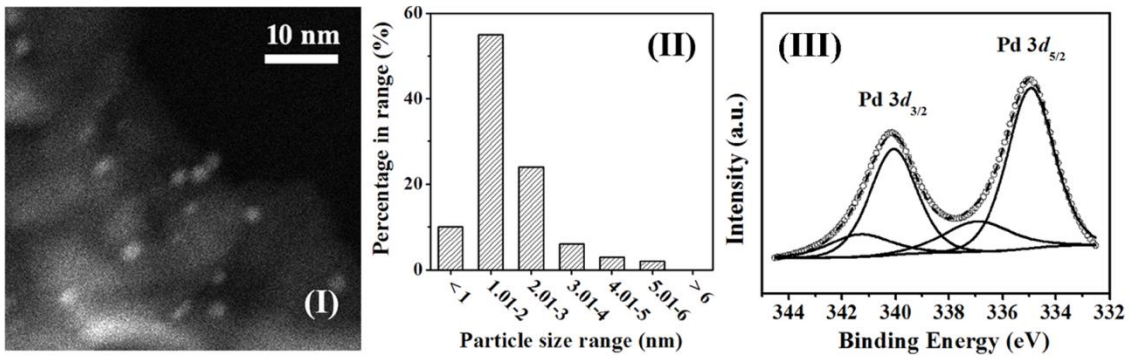

Figure 4.2: (**I**) Representative high magnification STEM image with (**II**) associated Pd particle size distribution and (**III**) XPS spectrum over the Pd 3*d* region for Pd/Al_2O_3-I. *Note*: XPS raw data is shown as open symbols (○) while curved fitted and envelope is represented by solid and dashed lines, respectively**.**

The histogram in **Figure 4.2(II)** shows metal nanoparticles with a narrow size distribution and a small mean diameter (d = 3.0 nm). A palladium particle size of d_{H_2} = 3.6 nm was calculated from H_2 chemisorption (see methodology in Experimental section) that is in good agreement with the value obtained from STEM measurements. The XPS spectrum over the Pd 3*d* BE region is shown in **Figure 4.2(III)**. A two-doublet system is in evidence for the reduced sample, spanning the range *ca.* 332-344 eV. The Pd $3d_{5/2}$ BE value for the main (79%; **Table 4.1**) doublet (334.9 eV) is lower than that characteristic of palladium bulk metal (335.1 eV) [189], suggesting the existence of electron-rich palladium particles ($Pd^{\delta-}$) as a result of electron transfer from the alumina support.[248] The appearance of the two secondary (21%) peaks with BE Pd $3d_{5/2}$ = 336.9 eV and Pd $3d_{3/2}$ = 341.2 eV can be ascribed to Pd^{2+} [249] due to formation of surface PdO during the passivation step [250].

Table 4.1: Physico-chemical characteristics of the oxide and carbon supported Pd catalysts

		Pd/Al_2O_3-I	**Pd/C**	**Pd/MgO**	**Pd/CeO_2**	**Pd/ZnO**
Pd content (%wt.)		1.2	1.0	0.9	0.8	1.1
SSA (m^2 g^{-1})		145	870	95	37	8
d^a / $d_{H_2}{}^b$ (nm)		3.0 / 3.6	2.8 / 3.0	3.0 / 3.9	3.0 / 1.0	2.9 / 5.6
H_2 chemisorption (mmol $g_{Pd}{}^{-1}$)^c		1.4	1.6	1.2	4.7	0.9
XPS Pd 3$d_{5/2}$ binding energies (eV)	Pd^0 (%)	334.9 (79)	335.8 (90)	[d]	335.4 (90)	334.7 (50)
	PdZn (%)	-	-	-	-	335.8 (28)
	Pd^{2+} (%)	336.9 (21)	337.4 (10)	[d]	337.2 (10)	336.9 (22)

[a]value obtained from STEM/TEM measurements; [b]value from room temperature H_2 chemisorption analysis; [c]hydrogen uptake at 373 K; [d]signals recorded at 530.5 eV for Pd^0 or MgO.[189]

4.3.1.2 Catalytic Response over Pd/Al_2O_3-I

Catalytic activity (R; $mol_{Alkynol}\ g_{Pd}^{-1}\ h^{-1}$) and selectivity ($S_j$; %) in the hydrogenation of MBY **(I)** and 3BY **(II)** at the same degree of conversion ($X_{Alkynol} \sim 25\%$) is illustrated as a function of H_2: Alkynol molar ratio in **Figure 4.3**. The experimentally determined hydrogenation rate of the two alkynols increased linearly with increasing H_2 content in the feed. The non-competitive nature of reactive alkyne/hydrogen adsorption has been established theoretically for (liquid phase) 1-butyne hydrogenation over Pd/Al_2O_3 [251] and is consistent with experimental work that has demonstrated a first order dependence in hydrogen coverage for the (gas phase) hydrogenation of acetylene[252] but we provide here, for the first time, catalytic data for continuous gas phase operation using functionalised alkynes (alkynols). The hydrogenation rate of the tertiary alkynol (MBY) was (*ca.* 2-fold) greater than that of the secondary (BY) over the entire H_2: Alkynol interval that was examined. Although we could find no comparable published catalytic study for the gas phase hydrogenation of alkynols, Aramendia *et al.*[253] reported a similar two-fold greater hydrogenation rate in the liquid phase (P = 4 bar, T = 306 K) transformation of MBY (compared to BY) over Pd/Sepiolite. The hydrogenation of alkynes has been suggested to proceed through an electrophilic mechanism [112] where the presence of an additional (electron donor) methyl substituent on the -OH carbon (in MBY *vs.* BY) increases electron density at the -C≡C- bond (positive inductive effect)[137] favouring the hydrogen attack.

We observe the formation of products from partial (MBE and BE) and full hydrogenation (MBA and BA) in the transformation of MBY and 3BY while BONE formation from double bond migration was recorded in the conversion of BY. The hydrogen content in the feed did not influence the selectivity response in the conversion of MBY or 3BY and a similar product distribution was maintained at each H_2:Alkynol (MBY → S_{MBE} = 62 ± 3%, S_{MBA} = 38 ± 3%; 3BY → S_{BE} = 69 ± 3%, S_{BA} = 19 ± 3%, S_{BONE} = 12 ± 2%).

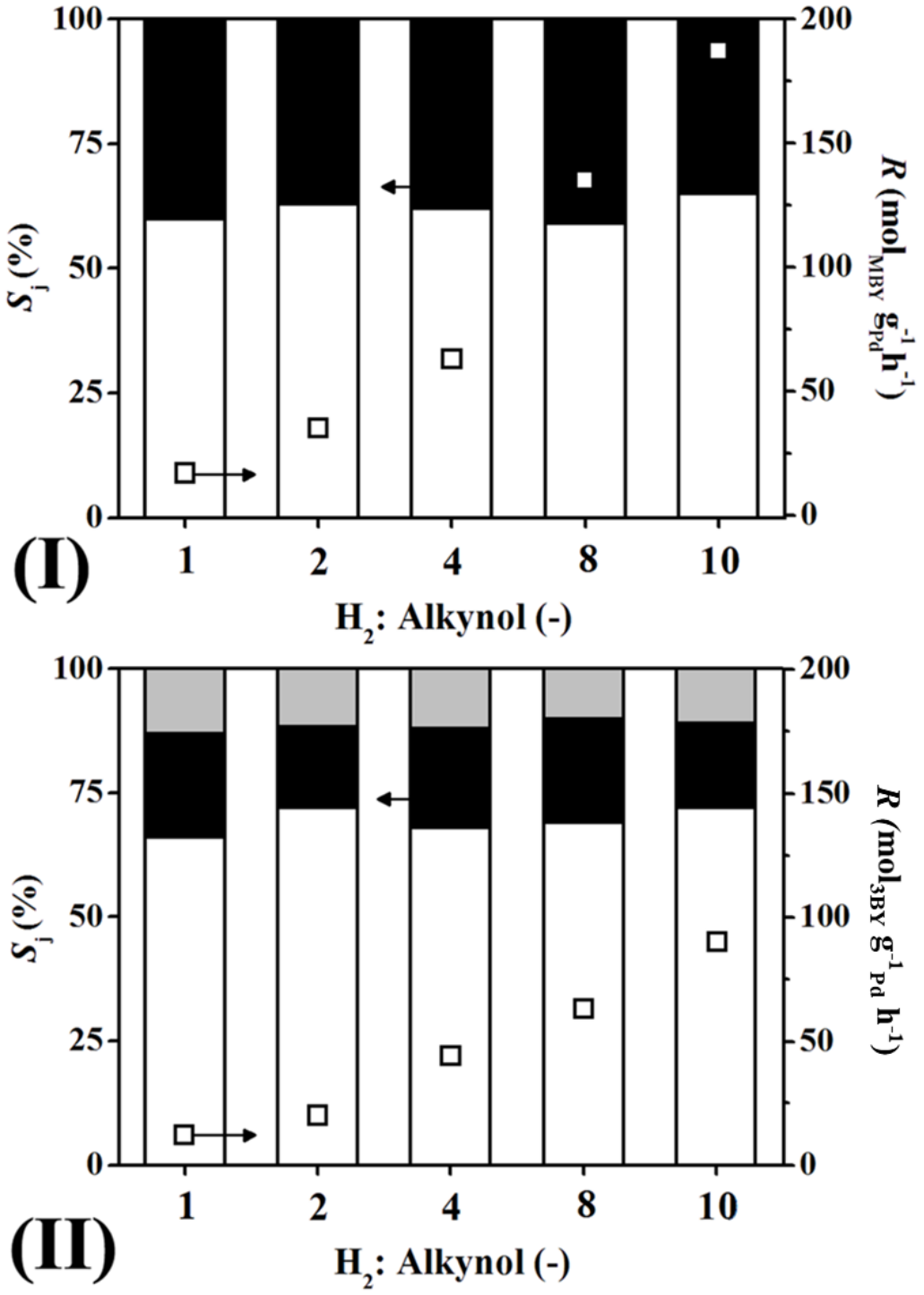

Figure 4.3: Variation of selectivity (*S*j, bars) and alkynol transformation rate (*R*, □) with H_2:Alkynol molar inlet ratio in the hydrogenation of (**I**) MBY to MBE (open bars) and MBA (solid bars) and (**II**) 3BY to BE (open bars), BA (solid bars) and BONE (grey bars) over Pd/Al_2O_3-I. *Reaction conditions*: P = 1 atm, T = 373 K, $X_{Alkynol}$ ~ 25%.

Our results are in line with published work showing a similar selectivity for the gas phase hydrogenation of isoprene over a hydrotalcite supported Cu catalyst under conditions of modified hydrogen content (H_2:Reactant = 1-11) in the feed [254]. We observe a lower selectivity to the target alkenol in the hydrogenation of tertiary MBY (S_{MBE} ~60%) relative to 3BY (S_{BE} ~70%). This can be ascribed to differences in the alkynol/alkenol adsorption strength ($K_{Alkynol/Alkenol}$), *i.e.* a stronger adsorption of the -C≡C- functionality (relative to -C=C-) on the Pd surface for 3BY compared to MBY ($K_{MBY/MBE}$ = 19 *vs.* $K_{BY/BE}$ = 35) [253] favours the desorption of the alkenol intermediate by displacement. The formation of BA (S_{BA} = 19 ± 3%) was greater than BONE generation (S_{BONE} = 12 ± 2%), *i.e.* preferential hydrogenation (**Steps B**+**C** in **Figure 1(II)**) relative to double bond migration (**Step E**), which can be linked to the inhibited formation of the π-allyl intermediate involved in the formation of BONE [24]. The results in this section clearly demonstrate that the hydrogen content in the feed had little effect on reaction selectivity in the hydrogenation of tertiary (MBY) and secondary (BY) alkynols. We focus our attention then on the role of the carrier.

4.3.2 Effect of the Support

The acid-base and/or redox properties of the carrier can induce electron transfer [255] from/to the support to the Pd phase resulting in the formation of negatively (electron-enriched) or positively charged palladium nanoparticles [255] which can impact on reactant adsorption/activation [256] and catalytic performance in hydrogenations [257]. In this section we examine the hydrogenation of MBY and 3BY over Pd supported on reducible and *non*-reducible supports with modified acidity. We consider a series of catalysts with similar Pd loading (0.8-1.2% wt.; **Table 4.1**) that facilitates a direct comparison to determine the role of the carrier.

4.3.2.1 Catalyst Characterisation: Oxide and Carbon Supported Pd Catalysts

The main physico-chemical properties of the oxide and carbon supported Pd catalysts are presented in **Table 4.1**. STEM analysis of commercial and laboratory synthesised Pd supported systems demonstrates a similar mean particle size of 2.9 ± 0.1 nm (**Table 4.1**)**.** Consistent (mean) nanoparticle sizes determined from STEM and H_2 chemisorption were obtained for Pd supported on *non*-reducible oxides and carbon (*i.e.* Pd/Al_2O_3-I (3.3 ± 0.3 nm), Pd/C (2.9 ± 0.1 nm) and Pd/MgO (3.5 ± 0.5 nm)). A similar metal dispersion (7-10% error) was reported by Mustard and Bartholomew [258] using microscopy and H_2 chemisorption measurements in the analysis of *non*-reducible (Al_2O_3 and SiO_2) supported

Ni catalysts. There are discrepancies in the results generated with both techniques for the remaining two Pd supported on reducible oxide (*i.e.* CeO_2 and ZnO) catalysts, a response that suggests some involvement of the carrier which influences hydrogen uptake. Metal encapsulation and alloy formation are two possible sources that can inhibit uptake, resulting in an over-estimation of metal particle size [258]. The term "encapsulation" can be defined as a partial/total blockage of the catalytic active (metal) sites by a thin layer of reduced oxide support [259] and is a documented feature of Pd supported on ZnO *post*-activation (in H_2) to 423 K [260]. Moreover, the incorporation of Au[261] and Pb[262] to Pd/Al_2O_3 resulted in a reduction in H_2 uptake attributed to alloy formation. The generation of a supported PdZn alloy phase in Pd/ZnO can occur following partial reduction of the ZnO support by hydrogen generated on Pd^0 during thermal treatment in H_2 to $T \geq 373$ K [152]. The positive deviation on the particle size determination on Pd/ZnO can be tentatively linked to partial encapsulation by the ZnO carrier and/or PdZn alloy formation that lowers hydrogen chemisorption capacity. Under-estimation of metal size can be the result of H_2 consumption by the support. Indeed, there is reported evidence that have shown room temperature hydrogen spillover for Pd/CeO_2 that results in "partial" reduction of ceria [263]. The application of electron microscopy for the determination of metal nanoparticle size has certain limitations that can result in inaccurate size estimation, *e.g.* poor contrast between the metal crystallites and the carrier that results in an over-estimation of the mean particle size and difficulties in the detection of metal particles with sizes <1 nm [240]. Although both (microscopy and chemisorption) techniques should complement each other, our results suggest that the titration analysis for the reducible oxide supported catalysts does not provide a reliable measure of palladium size, STEM gives the more accurate metal size. Hydrogen chemisorption is, however, a key consideration in hydrogenation processes. Hydrogen uptake under reaction conditions (373 K) was significantly lower than that recorded at ambient temperature for all the catalysts, which can be linked to the exothermic nature of hydrogen chemisorption over Pd metal, making the process less favourable as temperature increases [264]. Hydrogen chemisorption on Pd/Al_2O_3-I, Pd/C and Pd/MgO (1.4 ± 0.2 mmol g_{Pd}^{-1}) was equivalent and in line with values reported elsewhere (0.7-2.4 mmol g_{Pd}^{-1}) [265] for supported Pd catalysts with the same metal content. Pd/CeO_2 and Pd/ZnO exhibit the lowest (0.9 mmol g_{Pd}^{-1}) and highest hydrogen chemisorption values (4.7 mmol g_{Pd}^{-1}), respectively, displaying the same trend as previously obtained at room temperature.

We examined the electronic properties of the palladium phase by XPS analysis over the Pd 3*d* BE region with peak deconvolution, as presented in **Figure 4.4** for Pd/ZnO, as representative; the results for the Pd $3d_{5/2}$ peaks are shown in **Table 4.1**.

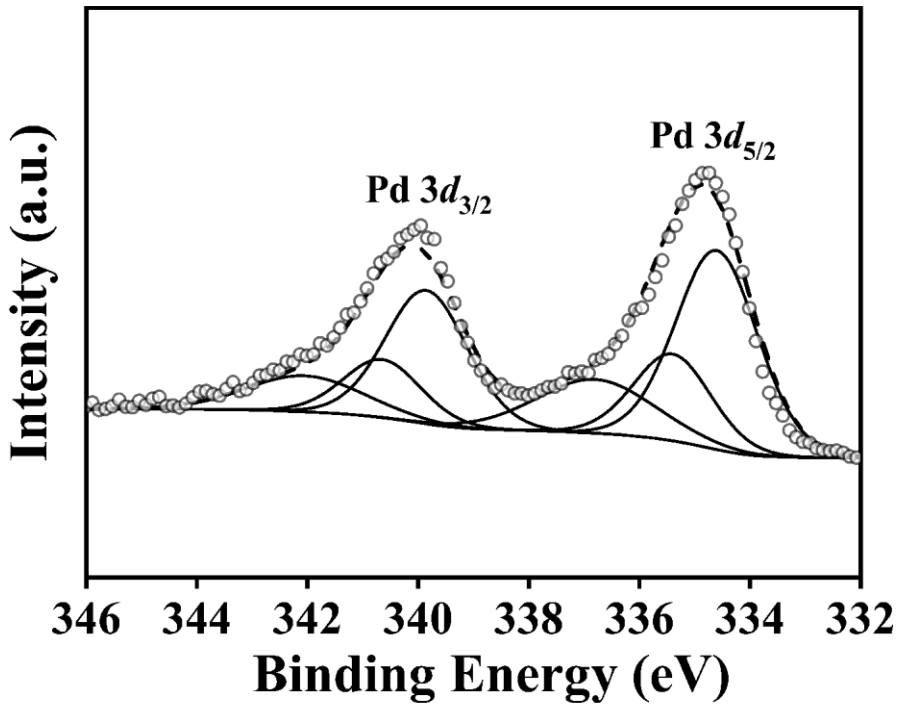

Figure 4.4: XPS spectrum over the Pd 3*d* region for Pd/ZnO catalyst. *Note*: Raw data is shown as open symbols (○) while curve fitted and envelope is represented by solid and dashed lines, respectively**.**

In this region of the $3d_{5/2}$ signals Pd/C, Pd/CeO_2 and Pd/ZnO exhibit a main (50-90%) component with BE (334.7-335.8 eV) close to Pd^0 (335.1 eV) [189] and a secondary (10-22%) peak (BE = 336.9-337.4 eV) that can be ascribed to Pd^{2+} from passivation [266]. The BE associated with the principal Pd $3d_{5/2}$ signal shows a clear dependence on the carrier. Previous studies have reported a positive shift to higher (+0.6 eV) binding energies with a decrease in metal particle size (from 8 nm to <1 nm) [267] ascribed to a decrease on the electron density of Pd that affects its *d* band [268]. In this study, all the catalysts exhibit an equivalent particle size which suggests that this effect alone cannot account for the modification of the main Pd $3d_{5/2}$ peak BE. A shift of BE to lower/higher values can also be the result of interactions with the carrier. Pd/ZnO exhibits a BE (334.7 eV) that is *ca.* 0.4 eV lower than metallic palladium indicative of electron-rich ($Pd^{\delta-}$) active sites which are ascribed to the electron donating character of the basic carrier [269]. The presence of $Pd^{\delta+}$ on C and CeO_2 follows from the recorded (0.3-0.7 eV) higher BE (compared to Pd^0) that can be linked to Pd → carrier electron transfer [270,271]. The

occurrence of the MgKL_1L_{23} peak originating from the catalyst support lies in the region of the $3d_{5/2}$ signal of Pd^0 (335.1 eV [189]) and Pd^{2+} (336.3 eV)[189]. Consequently, the electronic properties of the palladium component in Pd/MgO were examined by analysing the BE of Pd $3p_{3/2}$[242], which offers an alternative to the use of a *non*-monochromatized MgKα (1253.6 eV) radiation [272]. Pd/MgO exhibits a Pd $3p_{3/2}$ BE of 530.5 eV which is lower than that characteristic of Pd^0 (531.4 eV) [273], consistent with the presence of $Pd^{\delta-}$. The Pd/ZnO spectrum (**Figure 4.4**) presents an additional signal at Pd $3d_{5/2}$ of 335.8 eV (**Table 4.1**) that can be attributed to the occurrence of a PdZn alloy phase[274]. Tew *et al.*[152], demonstrated (by XRD and XAS) formation of PdZn alloy (at 373 K) on the Pd surface of Pd/ZnO that progresses into the bulk with increasing the temperature.

The characterisation measurements demonstrate formation of nanoscale Pd particles with similar mean size (2.9 ± 0.1 nm) but different electronic properties and hydrogen uptake capacities.

4.3.2.2 Catalytic Response over Oxide and Carbon Supported Pd Catalysts

The effect of the support on alkynol hydrogenation rate (*R*) and selectivity response is shown in **Figure 4.5**. A similar hydrogenation rate was obtained in the hydrogenation of MBY (62 ± 5 $mol_{MBY}\ g_{Pd}^{-1}\ h^{-1}$) and 3BY (36 ± 6 $mol_{3BY}\ g_{Pd}^{-1}\ h^{-1}$) over Pd/$Al_2O_3$-I, Pd/C and Pd/MgO while Pd/ZnO, with the lowest hydrogen uptake (**Table 4.1**), delivered the lowest MBY (35 $mol_{MBY}\ g_{Pd}^{-1}\ h^{-1}$) and 3BY (20 $mol_{3BY}\ g_{Pd}^{-1}\ h^{-1}$) transformation rate. This result suggests that the nature of the carrier does not impact significantly on hydrogenation rate, which is governed by the hydrogen uptake. Bragina and *co-workers* [275], working with a series of oxide supported Pd catalysts, associated their observed increase in diphenylacetylene hydrogenation to higher hydrogen concentration where the nature of the support did not affect the activity/selectivity response. The opposite effect has also been reported, where a greater activity over Pd/$CaCO_3$ (*vs.* Pd/Al_2O_3, Pd/Charcoal and Pd/CeO_2) was recorded by Bönnemann and *co-workers*[227] and attributed to the presence of $Pd^{\delta-}$, that lowers the strength of alkyne interaction with palladium sites[139]. Pd/CeO_2 with greater hydrogen chemisorption (**Table 4.1**) delivered equivalent activity, which further confirms that the additional chemisorbed hydrogen is consumed by the support and does not contribute to hydrogenation activity under the reaction conditions applied.

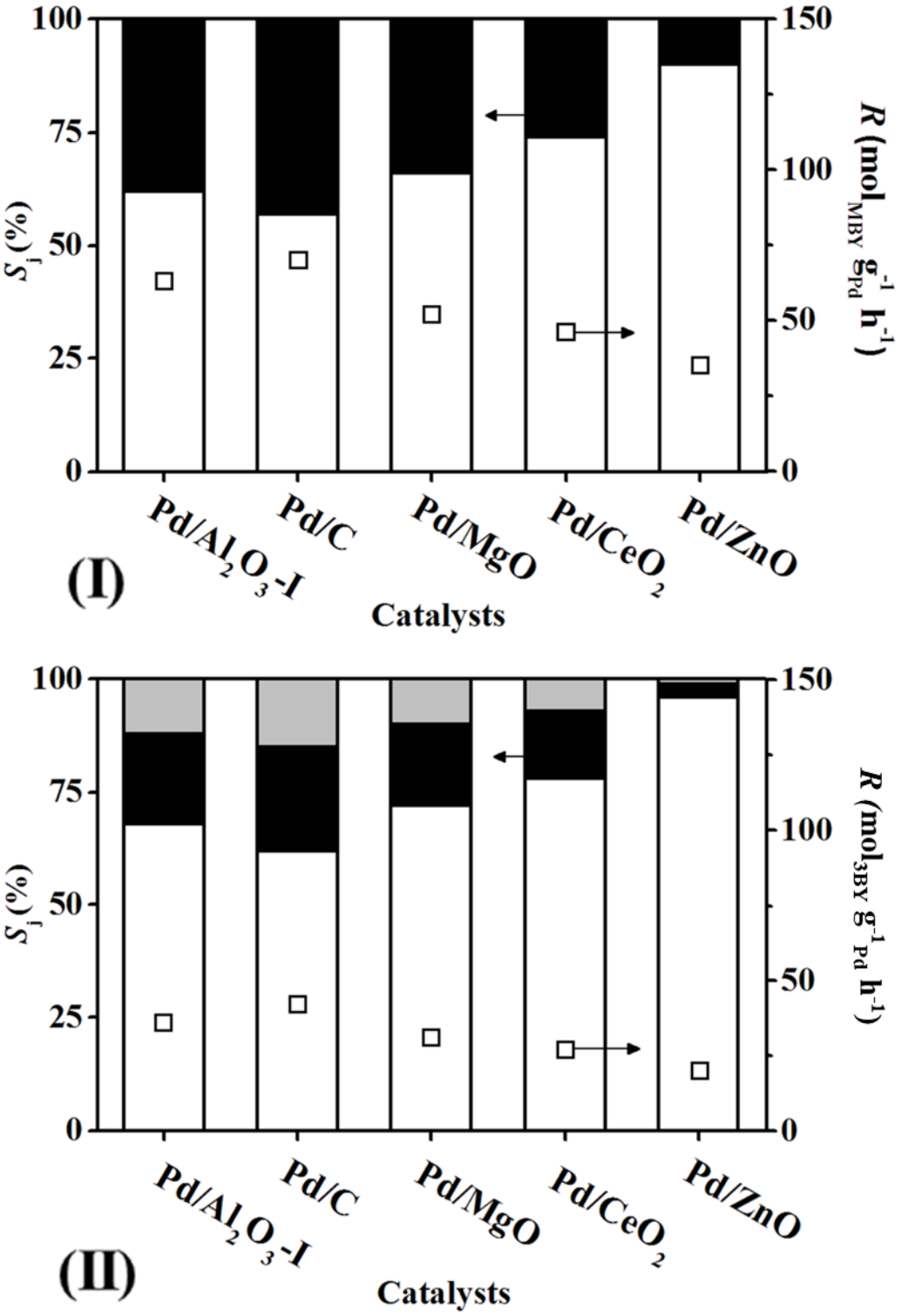

Figure 4.5: Variation of selectivity (*S*j, bars) and transformation rate (*R*, □) in the hydrogenation of (**I**) MBY to MBE (open bars) and MBA (solid bars) and (**II**) 3BY to BE (open bars), BA (solid bars) and BONE (grey bars) over a series of oxide and carbon supported Pd catalysts. *Reaction conditions*: P = 1 atm, T = 373 K, H_2: Alkynol molar inlet ratio = 4, $X_{Alkynol}$ ~25%.

With respect to product distribution, it can be seen the modified catalytic performance of Pd/ZnO with a significant greater alkenol selectivity (S_{MBE} = 90%; S_{BE} = 96%) in comparison with the rest of the systems. This suggests that the electronic modifications on Pd catalyst linked to the interactions with the support are playing a minor role where the increased olefin selectivity over the Pd/ZnO catalyst can be tentatively attributed to PdZn alloy formation and partial encapsulation that serves to decrease Pd ensemble size and (partially) cover palladium defect sites [182].

4.3.3 Promoting Effect of Zn in Pd for Pd-Zn Colloids Supported on Al_2O_3

We evaluated in this section the possibility of Zn promotion over Pd by deposition (on Al_2O_3) of a series of bimetallic colloids with varying Pd: Zn molar ratios ((95:5), (70:30) and (30:70)). We compare the results with those obtained over two monometallic (colloidal) Pd/Al_2O_3-II and Zn/Al_2O_3 and examined the effect of PdZn alloy formation for alkynol hydrogenation (using MBY and BY) in catalytic systems with Pd, Zn and PdZn active sites, evaluating individually the contribution of each of them. The catalytic action of three physical mixtures (Pd/Al_2O_3-II+Zn/Al_2O_3) was also considered for comparison purposes.

4.3.3.1 Catalyst Characterisation: Colloidal Pd and Pd-Zn Supported on Al_2O_3

Physico-chemical properties of the colloidal catalysts in this study are given in **Table 4.2**. Representative medium **(I)** and higher (*inset* in **(I)**) magnification TEM images of Pd-Zn/Al_2O_3 (95:5 **(A)**, 70:30 **(B)**, 30:70 **(C)**) are presented in **Figure 4.6** and serve to illustrate the nature of metal particle size and shape for the four Pd-containing colloidal systems. The catalysts present *pseudo*-spherical metal particles, a typical shape for PVP stabilised Zn[276] and Pd[277] colloids, with similar size distribution (size range 1–6 nm, **Figure 4.6(II)**) and mean (2.7 ± 0.2 nm; **Table 4.2**). XPS analysis was conducted to provide some insight into Pd–Zn surface interactions. The results for Pd/Al_2O_3-II (profile **(I)**) and Pd-Zn/Al_2O_3 (30:70) **(II)**, as representatives, are presented in **Figure 4.7**; the Pd $3d_{5/2}$ BE are given in **Table 4.2**

Table 4.2: Physico-chemical characteristics of the Al_2O_3 supported colloidal Pd, Zn and Pd-Zn catalysts

		Pd/Al_2O_3-II	**Zn/Al_2O_3**	**$Pd\text{-}Zn/Al_2O_3$ (95:5)**	**$Pd\text{-}Zn/Al_2O_3$ (70:30)**	**$Pd\text{-}Zn/Al_2O_3$ (30:70)**
Pd content (% wt.)		0.7	-	1.0	0.8	0.6
Pd: Zn molar ratio		-	0	95:5	70:30	30:70
SSA ($m^2\ g^{-1}$)		50	41	42	42	42
H_2 chemisorption (mmol g_{Pd}^{-1})[a]		0.4	[b]	0.5	0.6	0.5
Metal size range (nm)[c]		1-5	-	1-5	1-5	1-6
***d* (nm)[c]**		2.5	-	2.5	2.6	2.9
XPS Pd $3d_{5/2}$ BE (eV)	Pd^0 (%)	335.0 (80)	-	334.7 (65)	335.0 (39)	334.9 (37)
	PdZn (%)	-	-	335.5 (5)	335.7 (31)	335.8 (36)
	Pd^{2+} (%)	337.1 (20)	-	336.7 (30)	336.8 (30)	336.7 (27)

[a]hydrogen uptake at 373 K; [b]absence of hydrogen uptake; [c]value obtained from STEM/TEM measurements.

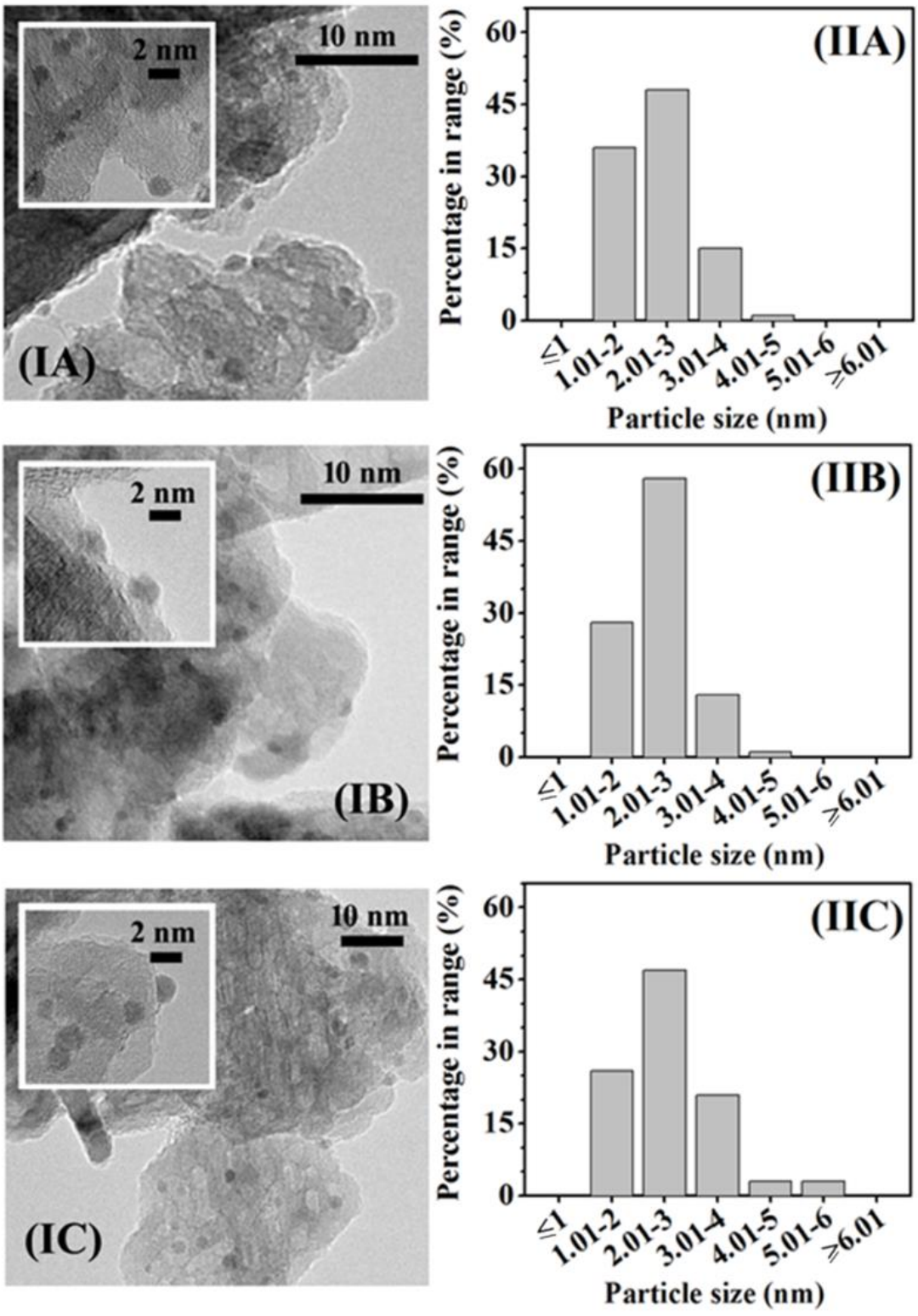

Figure 4.6: (**I**) Representative medium and high (*inset*) TEM images with (**II**) associated metal particle size distribution for the activated colloidal bimetallic (**A**) Pd-Zn/Al_2O_3 (95:5), (**B**) Pd-Zn/Al_2O_3 (70:30) and (**C**) Pd-Zn/Al_2O_3 (30:70) catalysts.

After deconvolution, the Pd 3$d_{5/2}$ spectra for the four Pd-containing systems present two peaks characteristic of $Pd^{\delta-}$ (334.8 ± 0.2 eV) and Pd^{2+} (336.9 ± 0.2 eV), similar to those recorded for Pd/Al_2O_3-I (**Figure 4.2(III)** and **Table 4.1**) with equivalent metal dispersion, suggesting similar particle size and metal-support interaction that is independent of the preparation method. Pd-Zn/Al_2O_3 presented and additional peak at higher (335.6 ± 0.2 eV) BE characteristic of PdZn alloy [278] with a concomitant decrease in $Pd^{\delta-}$ and increase in PdZn with enhanced Zn content. Hydrogen pulse titration measurements at reaction temperature demonstrate a significantly lower H_2 chemisorption for Pd/Al_2O_3-II relative to Pd/Al_2O_3-I, which can be linked to an adsorption site coverage by the PVP stabiliser in the colloidal system [279]. We observed an equivalent (0.5 ± 0.1 mmol g_{Pd}^{-1}) H_2 uptake for the monometallic Pd/Al_2O_3-II and bimetallic Pd-Zn/Al_2O_3 catalytic systems, indicative of hydrogen uptake by the PdZn alloy, in agreement with published work [280].

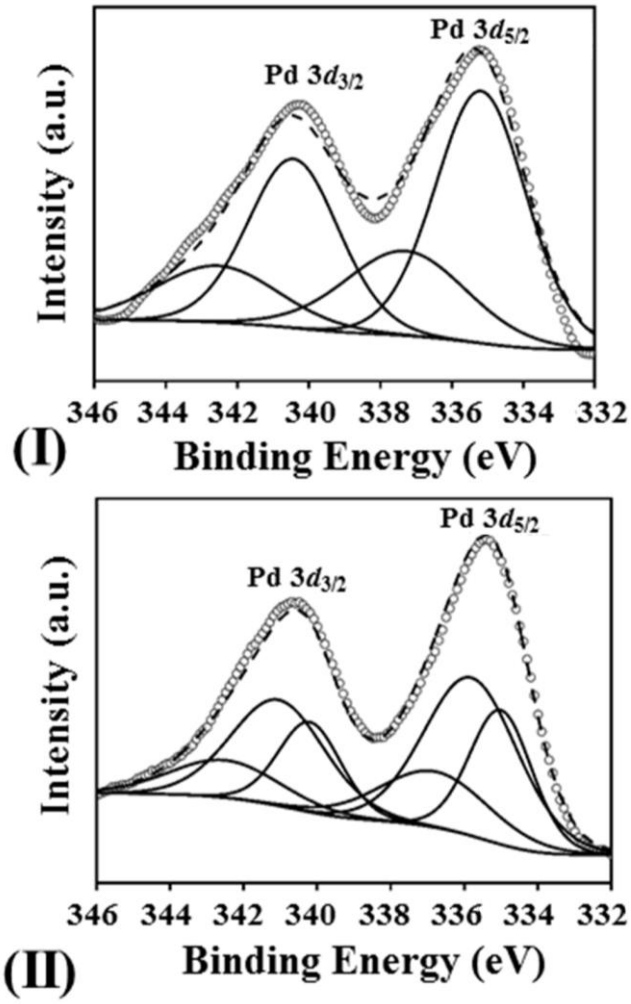

Figure 4.7: XPS spectra over the Pd 3*d* region for colloidal (**I**) Pd/Al_2O_3-II and (**II**) Pd-Zn/Al_2O_3 (30:70). *Note:* Raw data is shown as open symbols (○) while curve fitted and envelope is represented by solid and dashed lines, respectively.

. 4.3.3.2 Catalytic Response over Colloidal Pd and Pd-Zn Supported on Al_2O_3

Monometallic Pd/Al_2O_3-II delivers a similar catalytic response than Pd/Al_2O_3-I and exhibits the lowest alkenol selectivity (S_{MBE} = 64%; S_{BE} = 66%) among all the colloidal catalysts subjected to study. Under the same reaction conditions Zn/Al_2O_3 was inactive, which can be attributed to the incapacity of Zinc for hydrogen adsorption/activation[281], consistent with the absence of hydrogen uptake at reaction temperature (**Table 4.2**). The catalytic response recorded for the Pd/Al_2O_3-II+Zn/Al_2O_3 physical mixtures was demonstrated under reaction conditions where the Pd content was kept constant in the catalyst bed and the Pd:Zn mol ratio varied (95:5, 70:30 and 30:70) by the addition of different amounts of the Zn/Al_2O_3 catalyst. The results shown in **Figure 4.8** for the hydrogenation of MBY **(I)** and 3BY **(II)** demonstrate that, for this operational window, the activity over the three Pd/Al_2O_3-II+Zn/Al_2O_3 combinations coincide with that recorded over Pd/Al_2O_3-II (*i.e.* 124 ± 7 mol_{MBY} g_{Pd}^{-1} h^{-1}; 66 ± 4 mol_{3BY} g_{Pd}^{-1} h^{-1}). Moreover, product distribution over the three physical mixtures was also similar to that observed for Pd/Al_2O_3-II (*i.e.* S_{MBE} = 63 ± 2%, S_{MBA} = 37 ± 1%; S_{BE} = 68 ± 2%, S_{BA} = 20 ± 1%, S_{BONE} = 13 ± 1%). This suggests that incorporation of Zn/Al_2O_3, as a physical mixture with Pd/Al_2O_3-II, does not impact on catalytic response, which is governed by the Pd component. The three (bimetallic) Pd-Zn/Al_2O_3 catalysts were tested under similar reaction conditions (*i.e.* constant Pd content in the bed). The results in **Figure 4.8** show a similar alkynol consumption rate for Pd-Zn/Al_2O_3, Pd/Al_2O_3-II+Zn/Al_2O_3 and Pd/Al_2O_3-II, a result that is consistent with the equivalent hydrogen chemisorption under reaction conditions (0.5 ± 0.1 mmol g_{Pd}^{-1}; **Table 4.2**). In contrast, the selectivity response is remarkable, in that the three Pd-Zn/Al_2O_3 catalysts promoted a greater selectivity (up to S_{MBE} = 86% and S_{BE} = 92%) to the target alkynol whereas Pd/Al_2O_3-II and Pd/Al_2O_3-II+Zn/Al_2O_3 promoted over-hydrogenation (to alkanol; steps **B** and **C** in **Figure 4.1**) and double bond migration (to butanone; step **E**) to a significantly greater extent ($S_{MBE} \leq 64\%$ and $S_{BE} \leq 69\%$); full hydrogenation and double bond migration inhibition was a feature of increasing Zn content. The switch in catalytic response from over-hydrogenation/double bond migration (Pd/Al_2O_3-II and physical mixtures) to preferential partial hydrogenation (Pd-Zn/Al_2O_3) is indicative of differences in alkynol interaction where preferential -C≡C- → -C=C- occurs on the supported bimetallic.

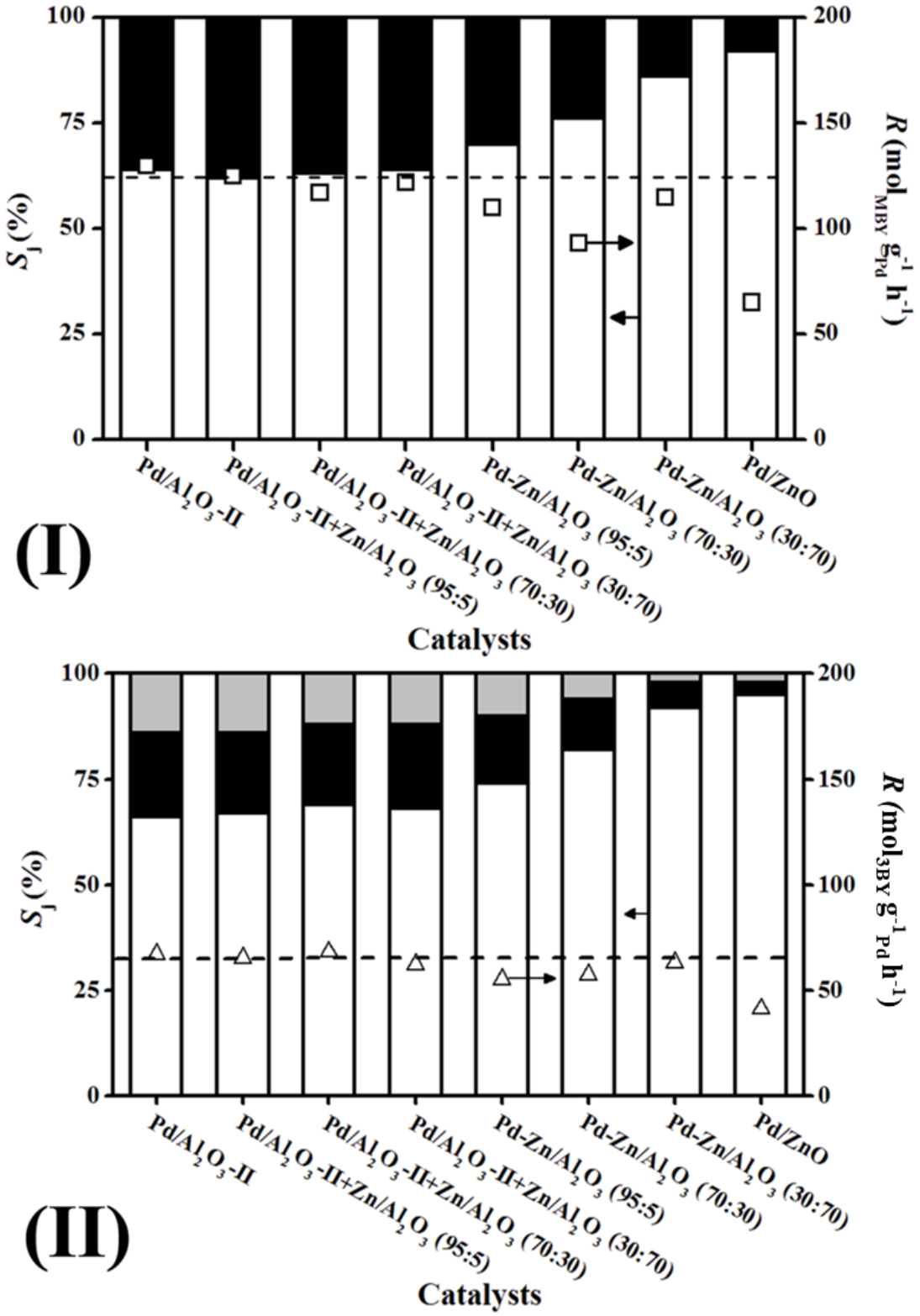

Figure 4.8: Variation of selectivity (S_j, bars) and transformation rate (R) in the hydrogenation of (**I**) MBY (□) to MBE (open bars) and MBA (solid bars) and (**II**) 3BY (△) to BE (open bars), BA (solid bars) and BONE (grey bars) over colloidal Pd/Al_2O_3-II and a series of bimetallic $Pd\text{-}Zn/Al_2O_3$ and (physical mixtures) Pd/Al_2O_3-II+Zn/Al_2O_3 catalysts. *Note*: dashed lines provide a guide to aid visual assessment. *Reaction conditions*: P = 1 atm, T = 373 K, H_2: Alkynol molar inlet ratio = 10, $X_{Alkynol}$ ~25%.

The incorporation of a second metal in bimetallic Pd-containing catalysts can result in geometric and/or electronic modifications [28], which impacts on catalytic (activity/selectivity) performance. A Ag →Pd electron donation generates palladium nanoparticles with a partial negative charge ($Pd^{\delta-}$), increasing the rate of triple bond hydrogenation while decreasing the rate of double bond hydrogenation [282]. Moreover, incorporation of Cu has been reported to induce geometrical changes on the Pd active sites leading to a partial blockage of low-coordination metal atoms and/or a decrease in Pd ensemble size, active sites for over-hydrogenation and/or double bond migration[283]. The increase in alkenol production that we observe can be tentatively ascribed to a reduction of $Pd^{\delta-}$ surface concentration (from 80% to 37%, **Table 4.2**) due to PdZn alloy that decreases the number of palladium atoms on surface ensembles responsible for unselective reactions. We cannot discount a partial coverage of (unselective) low-coordinated Pd kinks and corner sites by the Zn component [284] due to its lower surface tension (0.99 J m^{-2}) relative to Pd (2.03 J m^{-2}) [285]. Indeed, at 373 K, Zn atoms can diffuse to the surface and interact with Pd to form a thermodynamically stable PdZn alloy (ΔH = -100.4 kJ mol^{-1}) [286] on Pd planes and/or defects sites.[287] Wang *et al.*[283], investigated the liquid phase hydrogenation of phenylacetylene over a series of Al_2O_3 supported Pd-Zn catalysts (Zn:Pd molar ratios 91:9 - 86:14) and reported the highest yield to the target olefin ($Y_{Ethylbenzene}$ ~ 90%) at full conversion over the bimetallic system with the highest Zn content ascribed to Pd Zn electron transfer and PdZn alloy formation that blocks unselective active sites. We provide here, for the first time, the results over a highly active and selective Pd-Zn catalyst for continuous production of secondary and tertiary alkenols.

Catalytic properties of PdZn are sensitive to changes on the support. A similar alkenol selectivity (S_{MBE} = 89 ± 3% and S_{BE} = 94 ± 2%) was observed over Pd/ZnO and Pd-Zn/Al_2O_3 (30:70) with equivalent PdZn alloy content (32 ± 4%). However, a (2-fold) lower hydrogenation rate was obtained over Pd/ZnO compared to the colloidal catalyst albeit a similar hydrogen uptake for both catalysts (0.7 ± 0.2 mmol g_{Pd}^{-1}; **Tables 4.1** and **4.2**). The hydrogenation of -C≡C- bond-containing chemicals can be elevated by contributions due to spillover hydrogen, *i.e.* atomic hydrogen produced by dissociative adsorption of H_2 on supported metal sites that can migrate to the carrier. H_2-TPD is a practical measurement that can serve to quantify the degree of hydrogen spillover; the H_2 TPD profiles for Pd/ZnO **(I)** and Pd-Zn/Al_2O_3 (30:70) **(II)** are presented in **Figure 4.9**.

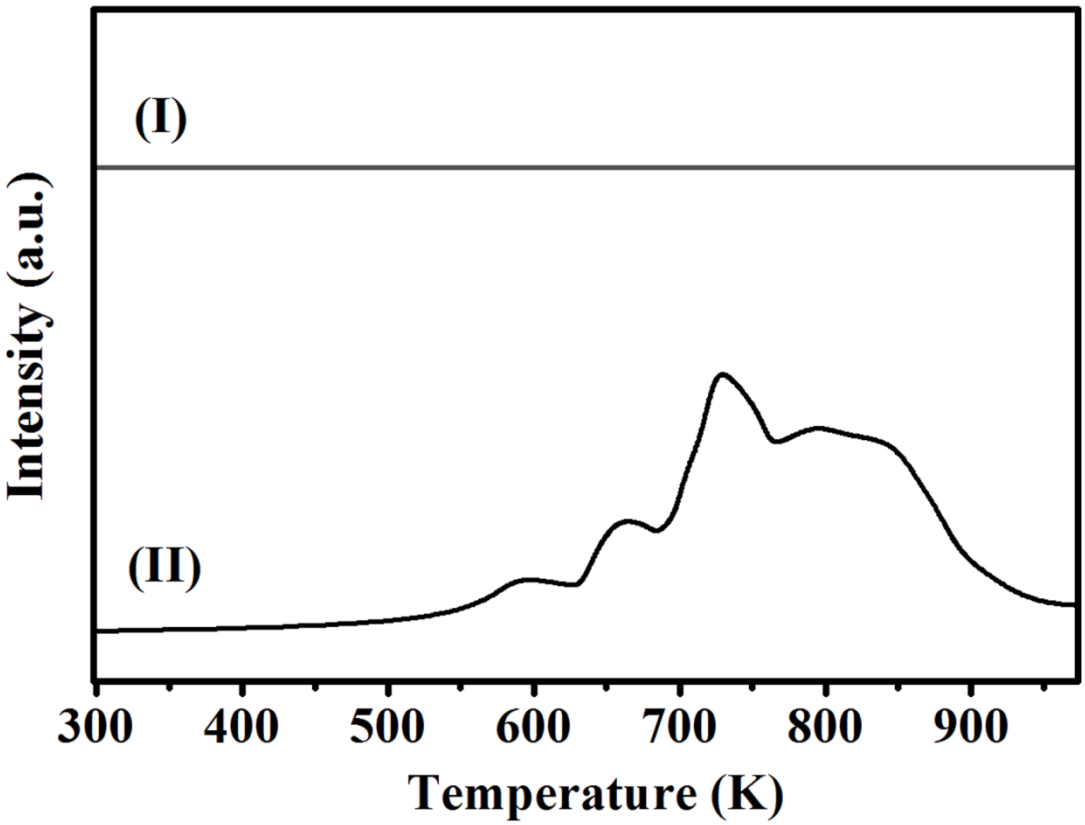

Figure 4.9: Hydrogen temperature programmed desorption (H_2-TPD) profiles for (**I**) Pd/ZnO and (**II**) Pd-Zn/Al_2O_3 (30:70).

The profile obtained for Pd/ZnO was featureless, indicative of hydrogen consumption by the ZnO support during TPR and consistent with the recorded hydrogen chemisorption measurements, *i.e.* atomic hydrogen spills from the Pd sites to the carrier resulting in "partial" ZnO → ZnO_{1-x} reduction at the metal-support interface with generation of a PdZn alloy phase [288], [180]. In contrast, over the same temperature range, the Pd-Zn/Al_2O_3 (30:70) catalyst exhibited a broad positive signal (H_2 released) at T > 503 K where the total amount desorbed that was significantly greater (by a factor of 13) than that taken up in the titration step. This response is a strong indication that the hydrogen released from the Pd-Zn/Al_2O_3 (30:70) sample is predominately spillover hydrogen generated during the activation step by H_2-TPR [289]. The elevated rate recorded in this work over Pd-Zn/Al_2O_3 (30:70) can be correlated with surface available reactive hydrogen where H_2-TPD is related to alkynol consumption rate. A similar effect has been reported elsewhere [289] in the hydrogenation of acetylene over a series of Pd-Ag/Al_2O_3 catalysts with a different Ag content, where an increase in the amount of hydrogen desorbed (based on TPD measurements) resulted in greater catalytic activity.

4.4 Conclusions

We have established that the formation of a Pd-Zn alloy phase can influence catalytic performance in Pd promoted gas phase hydrogenation of tertiary (MBY) and secondary (BY) alkynols. Catalyst characterisation of Pd nanoparticle size by (room temperature) H_2 chemisorption and TEM/STEM was carried out where the latter is shown to provide the most reliable results. Hydrogen titration leads to erroneous results due to metal encapsulation, alloy formation and/or consumption by the carrier. Alkynol consumption rate correlates with H_2 chemisorption capacity. An increase in H_2: Alkynol was accompanied by enhanced hydrogenation rate in the conversion of MBY and 3BY, albeit a similar product composition. The nature of the carrier (carbon, Al_2O_3, MgO, CeO_2) affects the electronic properties of the Pd phase (proved by XPS) but did not influence significantly catalytic activity or selectivity for a series of catalysts with similar metal nanoparticle size. In total contrast, Pd/ZnO delivered a significantly greater selectivity to the target olefin, which is attributed to the generation of a PdZn alloy (based on XPS). The beneficial role of spillover hydrogen has been established where increase surface hydrogen content enhances alkenol production over Pd-Zn/Al_2O_3 (30:70) compared to Pd/ZnO with similar PdZn alloy content.

Chapter 5:

Selective Gas Phase Hydrogenation of 3BY over Pd-Ni/Al_2O_3

Nickel is a well-established metal for hydrogenation but its application in triple bond transformation is limited, albeit a reported low isomerisation activity. The introduction of a second electropositive metal, such as Ni, in bimetallic Pd-Ni systems can modify the Pd electronic properties and/or surface ensemble size, with a direct impact on catalytic performance. In this chapter, we study the continuous gas phase hydrogenation of 3BY over bimetallic Pd-Ni/Al_2O_3. For comparison purposes, we also evaluate the catalytic response over Pd/Al_2O_3, Ni/Al_2O_3 and a physical mixture of Pd/Al_2O_3+Ni/Al_2O_3.

5.1 Introduction

Alkenols are important intermediates employed in the manufacture of vitamins and agri-food products [5]. The standard industrial synthesis route has involved the hydrogenation of alkynols over Pd catalysts [114]. The existing literature on alkynol hydrogenation has focused on tertiary alkynols, notably MBY [290]. The only reported transformation of secondary alkynols involved liquid phase conversion of 3BY using Pd/Al_2O_3 in pressurised (oscillatory baffled *vs*. stirred tank) reactors [66]. We have recently reported the formation of BA and BONE as by-products in the continuous hydrogenation of 3BY over a commercial Pd/Al_2O_3 catalyst [291]. Four possible reaction pathways are associated with the hydrogenation of 3BY [66], as shown in **Figure 5.1**. *Path A* involves partial hydrogenation to the target product, 3BE. BA formation can occur either *via* further conversion of 3BE (*Path B*) or through direct hydrogenation of the 3BY reactant (*Path C*). In *Path D*, 3BE undergoes isomerisation (*via* double bond migration) to BONE. Our main goal in this work is to direct the reaction along *Path A*, increasing the level of 3BE formation in continuous flow operation.

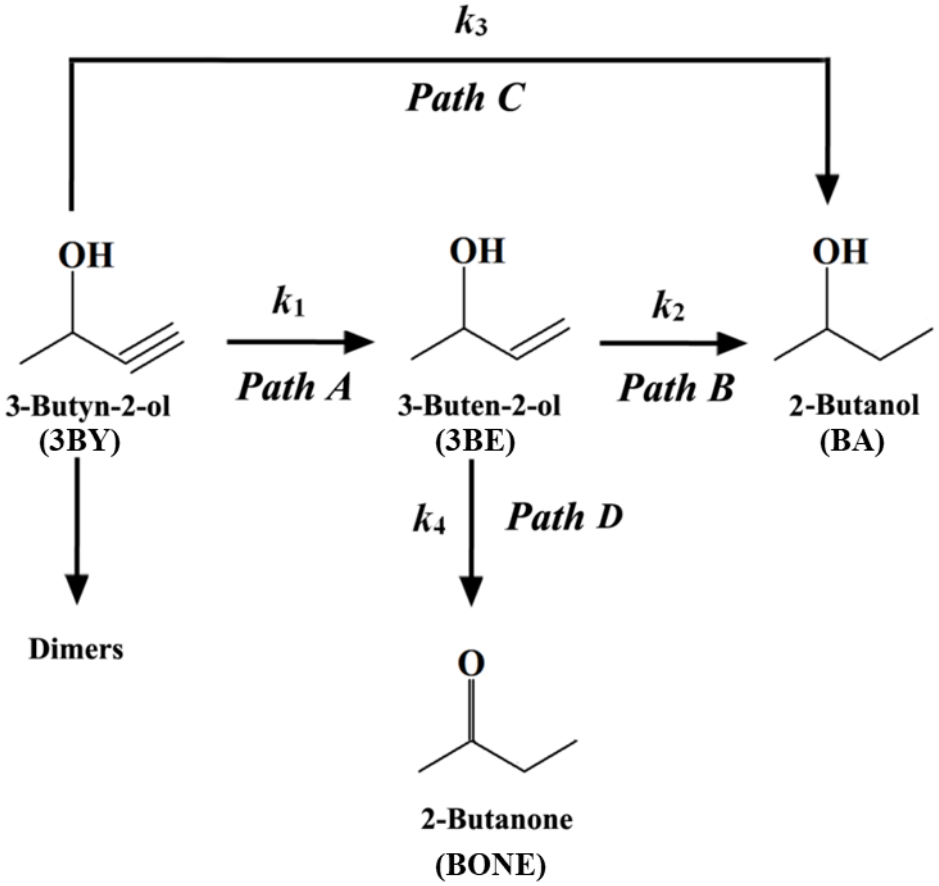

Figure 5.1: Reaction scheme in the hydrogenation of 3BY.

Triple bond hydrogenation is strongly influenced by the electronic and geometric properties of the active metal sites [283]. Negatively charged Pd nanoparticles favour partial (-C≡C-→-C=C-) reduction (*Path A* in **Figure 5.1**) [292] while low-coordination sites ($Pd^{\delta+}$) in small (<3 nm) nanoparticles promote -C=C- bond conversion, *Paths B* and *D* [38,39]. 3BY multi-coordination on large (surface) Pd ensembles of ≥5 nm metal nanoparticles [106] also leads to undesired alkanol generation (*Paths B* and *C*) [22,293]. The incorporation of a second electropositive metal (*e.g.* nickel) can alter the Palladium (i) electronic character (through Ni→Pd electron donation) and (ii) size of surface ensembles [42]. Although nickel is a well-known metal for hydrogenation, there is limited work dealing with its application in -C≡C- bond hydrogenation and we could find no reports in the literature on alkynol hydrogenation. Nonetheless, in liquid phase operation, it was shown that for a series of SiO_2 supported (Pd, Ni, Pt, Ru, Rh and Ir) catalysts nickel inhibits isomerisation in the hydrogenation of *cis*-2-butene-1,4-diol, a response that was attributed to a lower electron density in the *d* band [294]. In this study we consider the catalytic action of Pd-Ni bimetallic as a means of controlling -C=C- bond formation while achieving high activities. The promoting effect of Bi [295] Ag [228] and Cu [228] on

supported Pd catalysts for liquid phase MBY hydrogenation has been previously considered but the authors have been unable to find any published study on alkynol hydrogenation over Pd-Ni catalysts. Nevertheless, higher activity and -C=C- bond selectivity has been reported over supported (γ-Al_2O_3, zeolites) and unsupported Pd-Ni (*vs.* Pd) in the hydrogenation of 3-hexyne [296] and phenylacetylene [233] attributed to electronic/geometric modifications of the Pd phase. Increased activity in the liquid phase hydrogen treatment of hexachlorobenzene over Pd-Ni/C (*vs*. Pd/C) was observed by Simagina and *co-workers* [297], ascribed to segregation of surface palladium. Hou *et al.* [298] recorded inhibited double bond migration in the hydrogenation of butadiene over Pd-Ni/SiO_2 (relative to Pd/SiO_2 and Ni/SiO_2) which they linked to differences in 1-butene adsorption strength. In this work we report, for the first time, the gas phase hydrogenation of 3BY over Pd-Ni/Al_2O_3. We also consider catalytic performance of laboratory synthesised Pd/Al_2O_3, Ni/Al_2O_3 and a Pd/Al_2O_3+Ni/Al_2O_3 physical mixture for comparison purposes; catalytic response is linked to critical structural characteristics.

5.2 Experimental

All the gases (H_2, N_2, He and O_2) employed in this work were of ultra-high purity (BOC, >99.98%).

5.2.1 Materials and Catalysts Preparation

The Al_2O_3 support (Puralox) was purchased from Condea Vista Co. and used as received. Al_2O_3 supported Pd (6.9% wt.), Ni (6.1% wt.) and Pd–Ni (Pd: Ni mol ratio 1:1; total metal content 7.1% wt.) were synthesised by incipient wetness impregnation. Aqueous solutions (0.6 $cm^3\ g^{-1}$) of Pd $(NO_3)_2$ (1.4 mol dm^{-3}) and/or Ni $(NO_3)_2$ (2.3 mol dm^{-3}) were added dropwise (at 353K) to the Al_2O_3 carrier with constant agitation (*ca.* 500 rpm). The impregnated solid samples were oven dried (at 383K for 16 h) and sieved (ATM fine test sieves) into a batch of particles in the 62–75 μm size range. A physical mixture of Pd/Al_2O_3+Ni/Al_2O_3 (Pd: Ni mol ratio 1:1, denoted Pd+Ni in this work) was also investigated for comparison purposes. The catalysts were activated in 60 $cm^3\ min^{-1}$ H_2 at 10 K min^{-1} to 723 K, cooled to room temperature and passivated (30 $cm^3\ min^{-1}$, 1% v/v O_2/He, Brooks mass flow controlled, 1 h) for *ex situ* characterisation.

5.2.2 Catalyst Characterisation

Palladium and nickel metal content was determined by inductively coupled plasma-optical emission spectrometry (ICP-OES, Varian Vista-PRO) from the diluted extract in

HF. SSA, H_2-TPR and (ambient temperature) H_2 chemisorption measurements were performed using the commercial CHEMBET 3000 (Quantachrome Instruments) unit equipped with a thermal conductivity detector (TCD) with data acquisition/manipulation using the TPR Win^{TM} software (version 1.0a). Total SSA was obtained using the standard single point BET method. The catalysts were loaded into a U-shaped Pyrex glass cell (3.76 mm i.d.), outgassed by heating treatment (60 cm^3 min^{-1} He to 423 K overnight) and cooled to room temperature. SSA values were recorded with a (30 cm^3 min^{-1}) 50% v/v N_2/He flow; pure N_2 served as the internal standard. At least three cycles of N_2 adsorption-desorption in the flow mode were used to determine total surface area. TPR involved heating treatment (17 cm^3 min^{-1}, 5% v/v H_2/N_2) to 723K at 10 K min^{-1} where the effluent gas passed through a liquid N_2 trap. The hydrogen treated samples were swept (65 cm^3 min^{-1}, N_2) for 1.5 h, cooled to ambient temperature and subjected to H_2 chemisorption using a pulse (50 μL) titration procedure. Hydrogen pulse introduction was repeated until the signal area was constant, indicating surface saturation. In a series of blank tests, there was no measurable hydrogen uptake on the Al_2O_3 support alone. SSA and H_2 chemisorption values were reproducible to within ±5% and the values quoted in this paper are the mean. Powder X-ray diffractograms (XRD) were recorded on a Bruker/Siemens D500 incident X-ray diffractometer using Cu Kα radiation. The samples were scanned at a rate of 0.02º $step^{-1}$ over the range $20º \leq 2\theta \leq 90º$. Diffractograms were identified using the JCPDS-ICDD reference standards, *i.e.* γ-Al_2O_3 (10-0425), Pd (05-0681) and Ni (04-0850). Metal particle size and shape was examined by TEM using a JEOL JEM 2011 HRTEM unit with a UTW detector (EDX) detector (Oxford Instruments) operated at an accelerating voltage of 200 kV and using Gatan Digital Micrograph 3.4 for data acquisition/manipulation. Samples for analysis were prepared by dispersion in acetone with deposition on a holey Cu grid (300 mesh). Up to 600 individual metal particles were counted for each catalyst and the surface area-weighted metal diameter (d_{TEM}) was calculated from:

$$d_{TEM} = \frac{\sum_i n_i \cdot d_i^3}{\sum_i n_i \cdot d_i^2} \qquad \textbf{(5.1)}$$

where n_i is the number of particles of diameter d_i. XPS analyses were conducted on an Axis Ultra instrument (Kratos Analytical) under ultrahigh vacuum conditions ($<10^{-8}$ Torr) using a monochromatic Al Kα X-ray source (1486.6 eV). The source power was maintained at 150 W, and the emitted photoelectrons were sampled from a 750 × 350 μm^2

area at a take-off angle of 90°. The analyser pass energy was 80 eV for survey spectra (0−1000 eV) and 40 eV for high-resolution spectra (Pd $3d_{5/2}$, Pd $3d_{3/2}$, Ni $2p_{3/2}$ and Ni $2p_{1/2}$). The oxygen 1*s* peak was calibrated at 531.0 eV and used as an internal standard to compensate for any charging effects. XPS analysis was employed to assess the formation of bimetallic Pd-Ni nanoparticles by measuring the satellite intensities for the 2*p* levels of nickel with respect to the Ni $2p_{3/2}$ (denoted ΔNi $2p_{3/2}$) and Ni $2p_{1/2}$ lines (ΔNi $2p_{1/2}$) [299].

5.2.3 Catalytic Procedure

Reactions were carried out at 373 K and atmospheric pressure in situ after activation in a continuous flow fixed bed vertical tubular glass reactor (15 mm i.d.). The catalytic reactor and operating conditions were selected to ensure negligible heat/mass transport limitations. A layer of borosilicate glass beads (1 mm) served as a preheating zone and the alkynol reactant was vaporised and reached reaction temperature before contacting the catalyst. Isothermal conditions (±1 K) were maintained by diluting the catalyst bed with ground glass (75 μm). Reaction temperature was continuously monitored by a thermocouple inserted in a thermowell within the catalyst bed. 3BY (Sigma-Aldrich, ≥97%) was delivered in a butanolic (BOL; Aldrich, 99%) solution *via* a glass/teflon air-tight syringe and Teflon line using a microprocessor controlled infusion pump (Model 100 kd Scientific) at a fixed calibrated flow rate (1.2 $cm^3\,h^{-1}$). A co-current flow of H_2 (or H_2/N_2; P_{H_2} over the range $5 \times 10^{-3} – 90 \times 10^{-2}$ atm) and alkynol was maintained at *GHSV* = 1×10^4 h^{-1}. The flow rate was monitored using a Humonics (Model 520) digital flowmeter. The molar metal (n_{metal}) to inlet alkynol molar feed rate (n_{metal}/F) spanned the range $0.3 \times 10^{-4} – 368 \times 10^{-4}$ h. In blank tests, reactions in the absence of catalyst or over the support alone did not result in any measurable conversion. The reactor effluent was frozen in a liquid nitrogen trap for subsequent analysis which was made using a Perkin-Elmer Auto System XL gas chromatograph equipped with a programmed split/splitless injector and a flame ionisation detector using a Stabilwax (fused silica) 30 m × 0.32 mm i.d., 0.25 μm film thickness capillary column (RESTEK). Data acquisition/manipulation was performed using the TotalChrom Workstation Version 6.1.2 (for Windows) chromatography data system and reactant/product molar fractions (x_i) were obtained using detailed calibration plots (not shown). Hydrogenation activity is expressed in terms of conversion of 3BY (*X*):

$$X(\%) = \frac{[3BY]_{in} - [3BY]_{out}}{[3BY]_{in}} \cdot 100 \quad \textbf{(5.2)}$$

where [3BY] is the concentration of 3BY; the subscripts "in" and "out" refer to the inlet and outlet streams. Selectivity in terms of (*e.g.*) 3BE (S_{3BE}) is given by:

$$S_{3BE}(\%) = \frac{[3BE]_{out}}{[3BY]_{in} - [3BY]_{out}} \cdot 100 \quad \textbf{(5.3)}$$

Catalytic activity is also quantified in terms of stationary state alkynol consumption rate (R, $mol_{3BY}\ g_{metal}^{-1}\ h^{-1}$), determined from time on-stream measurements as described elsewhere [122]. Repeated reactions with different samples from the same batch of catalyst delivered raw data reproducibility and a carbon mass balance within ±6%.

5.3 Results and Discussion

5.3.1 Catalyst Characterisation

Critical catalyst properties are given in **Table 5.1**. The three systems have a similar metal content (6.6 ± 0.5% wt.), which enables a direct comparison. The SSA (166-173 $m^2\ g^{-1}$) are within the range (123-205 $m^2\ g^{-1}$) reported elsewhere [300] for γ-Al_2O_3 supported metal catalysts. We recorded a (9-13%) decrease in SSA for each catalyst relative to the starting Al_2O_3 carrier (190 $m^2\ g^{-1}$) that can be attributed to a partial blockage by the metal phase [301]. The H_2-TPR profiles for Pd/Al_2O_3 **(I)**, Ni/Al_2O_3 **(II)** and Pd-Ni/Al_2O_3 **(III)** are shown in **Figure 5.2**, and the T_{max} values associated with the predominant peak(s) in each profile are given in **Table 5.1**; the H_2-TPR conditions matched those employed for catalyst activation before hydrogenation (see section 5.2.1 Materials and Catalysts Preparation). Over the same temperature range (*i.e.* up to 723 K), the TPR response for the alumina carrier was featureless, *i.e.* lack of hydrogen uptake/release, an expected result that is in line with reported literature showing a higher temperature requirement (≥1373 K) for the reduction of γ-Al_2O_3 [302]. The TPR profile for Pd/Al_2O_3 exhibits a single negative (H_2 released) peak with a T_{max} at 387 K. It is well known that palladium can absorb hydrogen at room temperature to generate the β-Pd hydride phase where H_2 partial pressure exceeds 0.02 atm [303]; 0.06 atm in this work. The decomposition of the β-Pd hydride has been associated with the appearance of a hydrogen release during H_2-TPR in the temperature range 360-473 K [304,305]. Hydride composition (H/Pd) is dependent on palladium nanoparticle size [306]. The value recorded in this work (0.20 $\mu mol_H\ \mu mol_{Pd}^{-1}$) is significantly smaller than that

characteristic of bulk Pd (0.7 $\mu mol_H\ \mu mol_{Pd}^{-1}$) [307], indicative of palladium particles at the nano-scale. Indeed, Aduriz *et al.*[308], reported an average palladium particle size of *ca.* 12 nm (from TEM) for Pd/Al_2O_3 with an associated H/Pd = 0.20. In addition to hydride decomposition, the TPR profile for Pd/Al_2O_3 also exhibited two positive peaks, a main H_2 consumption at 560 K and a (lower intensity) ill-defined signal at 723 K, indicative of oxide-Pd precursor interactions that serve to stabilise the metal phase requiring a greater reduction temperature [257,309]. Otto *and co-workers* [310] observed the presence of unreduced PdO (based on XPS analysis) in activated (to 573 K) Pd/Al_2O_3, ascribed to carrier-metal electron transfer that serves to stabilise the metal oxide, increasing the reduction temperature requirements.

Table 5.1: Physico-chemical properties of the Al_2O_3 supported Pd, Ni and (bimetallic) Pd-Ni catalysts.

		Pd	Ni	Pd-Ni
Metal loading (% wt.)		6.9	6.1	7.1
SSA (m^2 g^{-1})		173	166	168
TPR T_{max} (K)[a]		387[b], *560*, 723	*715*	354[b], *429*, 723
d_{TEM} (nm)		20	30	27
Pd/Ni surface atomic ratio		-	-	0.7-24
XPS binding energies (eV)	**Pd $3d_{5/2}$**	335.0	-	335.5
	Pd $3d_{3/2}$	340.2	-	340.7
	Ni $2p_{3/2}$	-	856.1	854.9
	ΔNi $2p_{3/2}$		5.2	5.6
	Ni $2p_{1/2}$	-	873.3	872.1
	ΔNi $2p_{1/2}$		6.4	6.8

[a]main positive (H_2 consumption) TPR peak is given in italic; [b]negative TPR peak associated with Pd hydride decomposition;

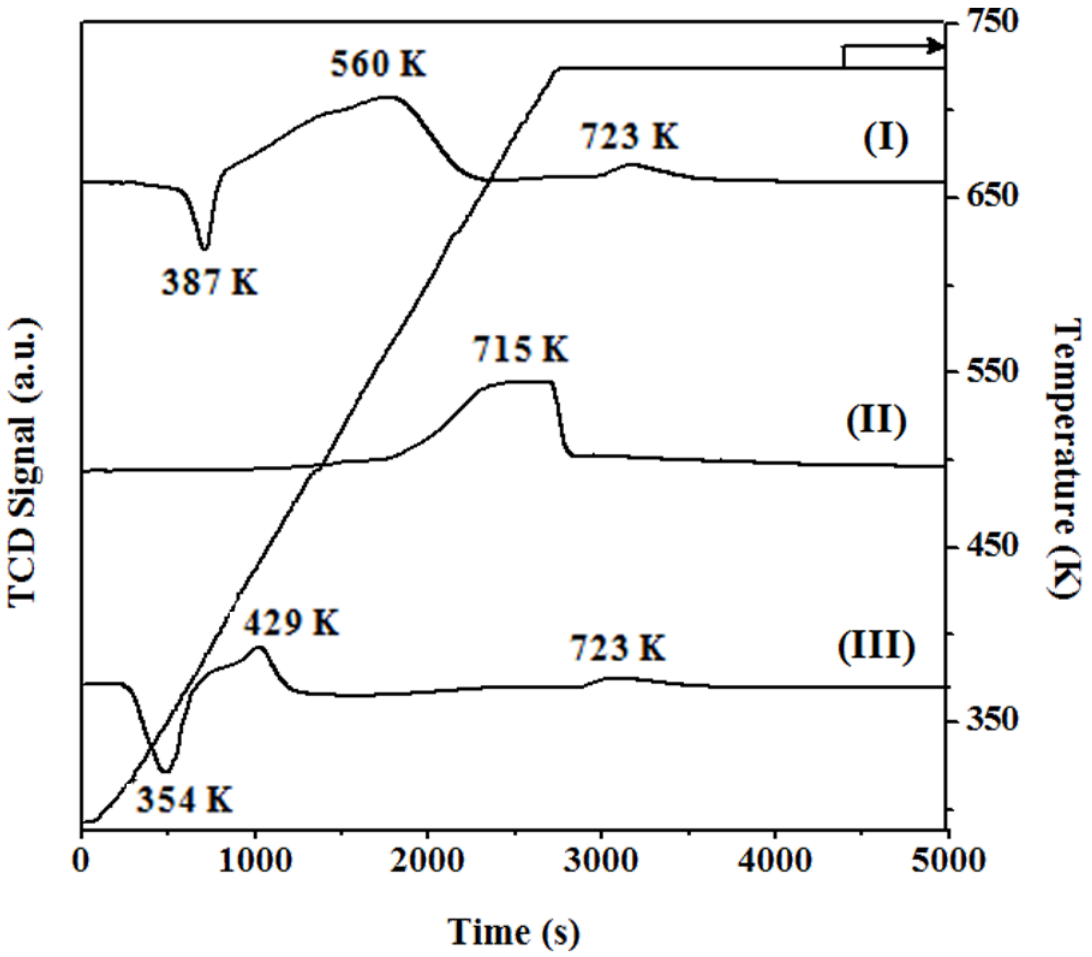

Figure 5.2: TPR profiles for Al_2O_3 supported (**I**) Pd, (**II**)Ni and (**III**) bimetallic Pd-Ni

In contrast, a single positive peak (T_{max} = 715 K) was recorded during the reduction of Ni/Al_2O_3, that can be associated with the reduction of Ni^{2+} to metallic nickel [311]. The broadness of the signal suggests the reduction of several surface nickel species. This is consistent with a stepwise decomposition of nickel nitrate to nickel oxide where $T \sim 573\ K$ [312,313], with subsequent reduction to metallic nickel at 673-773 K [313]. The TPR profile for the bimetallic $Pd–Ni/Al_2O_3$ (**Figure 5.2(III)**) differs significantly from that resulting from the combination of those recorded for Pd/Al_2O_3 **(I)** and Ni/Al_2O_3 **(II)**, indicative of an interaction between nickel and palladium that impacts on reduction behaviour. Differences relative to the monometallic Pd catalyst are in evidence in terms of the hydride composition; we observed a reduction (0.20 → 0.11 $\mu mol_H\ \mu mol_{Pd}^{-1}$) of H/Pd mol ratio. The lower H/Pd can be attributed to a smaller number of octahedral cavities in Pd due to a decrease in nanoparticle size [306] and/or generation of bimetallic by incorporation of nickel in the palladium lattice [314]. Moreover, we recorded a (*ca.* 33 K) displacement to lower temperatures in the palladium hydride decomposition peak

which can be due to the formation of bimetallic clusters [306]. Indeed, a shift in the temperature of hydride decomposition has been reported for Pd-Ag/TiO_2 [315] and Pd-In/SiO_2 [316] attributed to the generation of bimetallic nanocrystals. A hydrogen consumption peak at T_{max} = 429 K was also in evidence in the TPR profile of Pd–Ni/Al_2O_3, which can be ascribed to the combined reduction of both metal precursors where the presence of Pd and Ni impacts on overall activation, resulting in a more facile reduction, *i.e.* hydrogen spillover from dissociative adsorption on Pd^0 (formed at room temperature) facilitates Ni^{2+} reduction [304] lowering the temperature requirement for this step [317]. In support to this, P. Mierczynski *et al.* [318] concluded that incorporation of Pd with Ni (on Pd-Ni/CeO_2-Al_2O_3) serves to decrease the reduction temperature of nickel by *ca.* 30-60 K.

The XRD patterns presented in **Figure 5.3** for the γ-Al_2O_3 carrier **(I)** and the supported Pd **(II)**, Ni **(III)** and bimetallic Pd-Ni **(IV)** systems provide important bulk structural properties. The diffractogram pattern associated with the oxide support show signals at 2θ = 45.9° and 66.9°, corresponding to the (4 0 0) and (4 4 0) planes of cubic γ-Al_2O_3, the broadness of the peaks suggests a short range order [319]. In addition, reflections at 2θ = 40.1°, 46.7° and 68.1° for Pd/Al_2O_3 can be assigned to the (1 1 1), (2 0 0) and (2 2 0) planes of Pd^0 with a cubic symmetry. The peak at 2θ = 44.5° for Ni/Al_2O_3 matches the (1 1 1) plane of cubic metallic nickel. By comparison with the XRD pattern generated for Pd/Al_2O_3, the Pd–Ni catalyst exhibits a 0.6° (positive) displacement of the Pd (1 1 1) plane (dashed line). Such effect has been reported previously and attributed to the formation of a bimetallic Pd–Ni phase [320]. Lu *et al.* [321] examined (unsupported) Ni-Pd nanoparticles and reported a similar (0.6°) shift in the Pd (1 1 1) main plane attributed to a contraction of the lattice spacing (0.228 → 0.204 nm) due to Ni incorporation in the crystal structure of Pd.

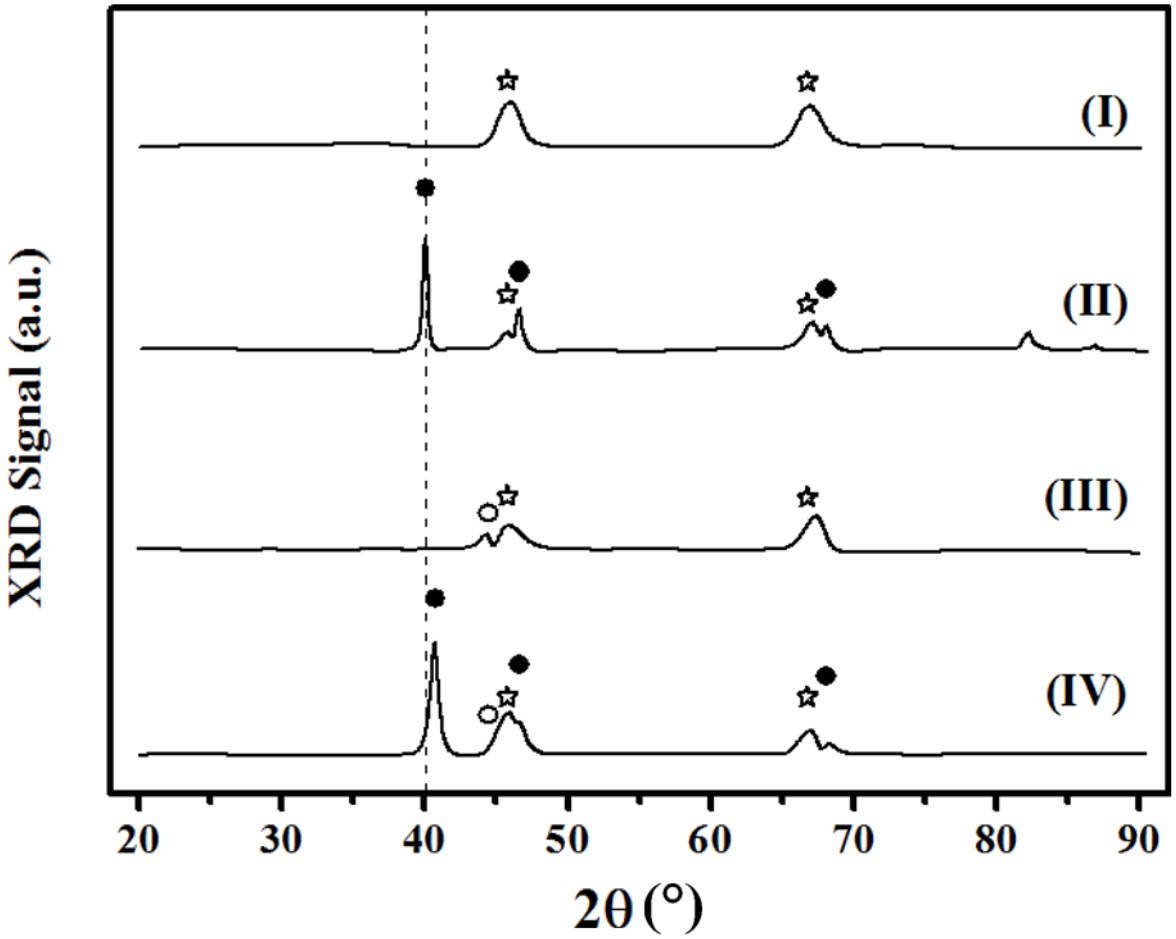

Figure 5.3: XRD patterns associated with (**I**) Al_2O_3 carried and supported (**II**) Pd, (**III**) Ni and (**IV**) bimetallic Pd-Ni. *Note* peak assignments based on JCPDS-ICDD references data: (☆) γ-Al_2O_3 (10-0425); (●) Pd (05-0681); (○) Ni (04-0850). Dashed line serves to illustrate the position of the main reflection (2θ = 40.1°) corresponding to the (111) plane of metallic Pd.

Metal nanoparticle size distribution from TEM analysis for supported Pd **(I)**, Ni **(II)** and Pd-Ni **(III)** can be compared in **Figure 5.4** and **Table 5.1**. The metal size range and mean nanoparticle size of Ni/Al_2O_3 and Pd-Ni/Al_2O_3 coincided (1-60 nm; d_{TEM} = 28 ± 2 nm) with no obvious modifications due to *co*-impregnation with both metal precursors. The broad metal size range is consistent with literature dealing with oxide (SiO_2 and Al_2O_3) supported Ni prepared by impregnation with similar metal content (~8% wt.) [289]. On the other hand, palladium on Al_2O_3 is characterised by a narrower distribution of smaller Pd nanoparticles (1-40 nm; d_{TEM} = 20 nm). The ultimate particle size distribution is sensitive to metal-support interactions which is dependent on the charge density of the metal precursor. The greater charge density of palladium in $Pd(NO_3)_2$ (1.01×10^3 *e* nm^{-3} *vs.* 0.83×10^3 *e* nm^{-3} for nickel in $Ni(NO_3)_2$ [322]) favours interaction with tetrahedral/octahedral sites on Al_2O_3 [323] which, in turn, results in a narrow size distribution of smaller palladium particles.

Representative TEM images of Pd/Al_2O_3 (IA), Ni/Al_2O_3 (IB) and $Pd\text{-}Ni/Al_2O_3$ (IC) in **Figure 5.5** revealed a similar pseudo-spherical shape morphology for the three catalysts, diagnostic of limited metal/carrier interactions in catalysts prepared by impregnation [324].

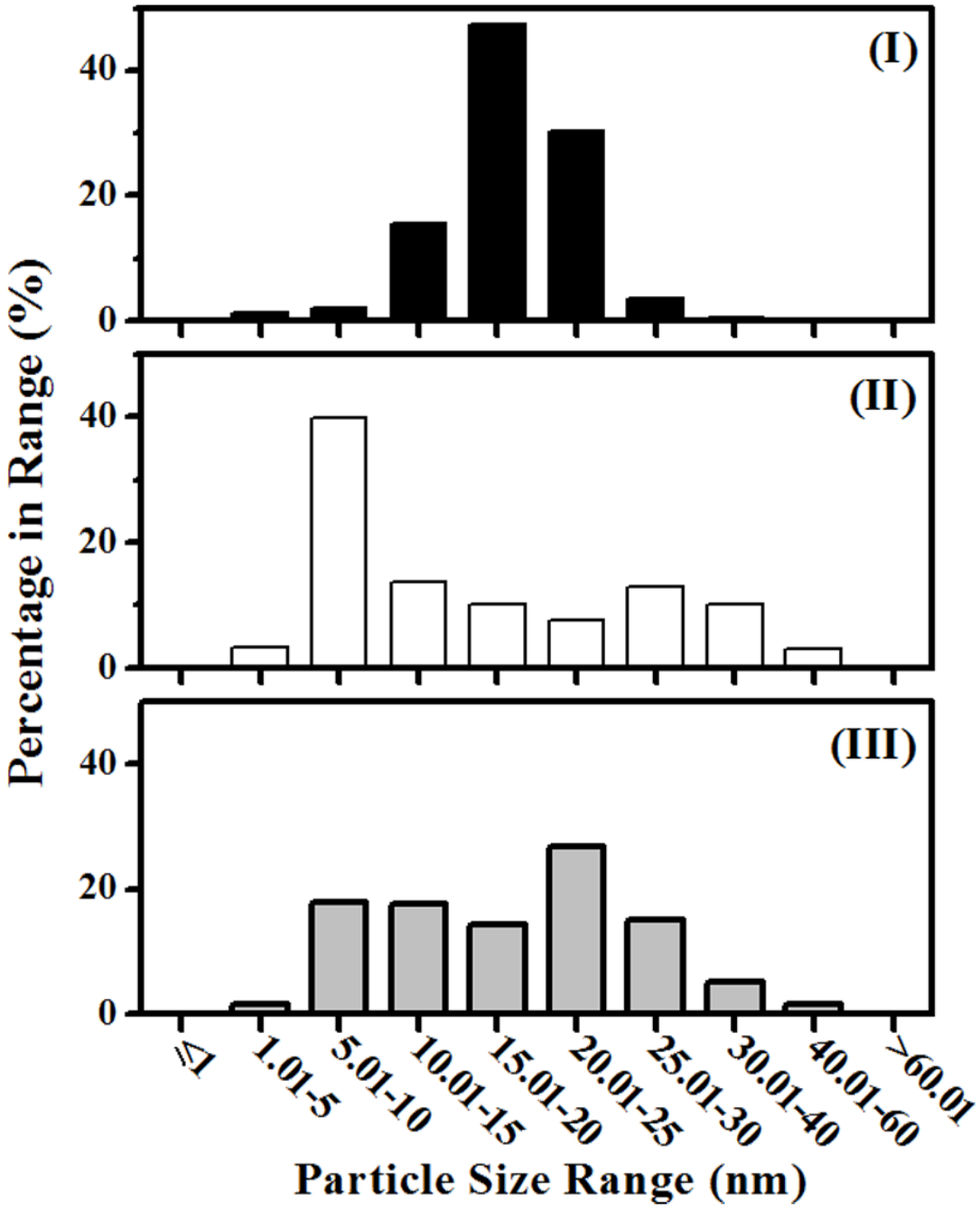

Figure 5.4: Metal particle size distribution for Al_2O_3 supported (**I**) Pd (solid bars), (**II**) Ni (open bars) and (**III**) bimetallic Pd-Ni (grey bars).

The TEM-EDX quantitative analysis of multiple isolated metal particles in Pd-Ni/Al_2O_3 revealed a *non*-uniform distribution of both metals on the catalyst surface albeit no evidence of segregated clusters of pure Pd or Ni. The extracted range of surface Pd/Ni atomic ratios (see **Table 5.1**; representative EDX spectra for single metal nanoparticle in **Figure 5.5(II)**) is consistent with a palladium surface enrichment. Our results find support in previous studies that have demonstrated (by XPS) surface segregation with palladium enrichment for carbon [325] and SiO_2 [326] supported Pd-Ni catalysts. Segregation in bimetallic is dependent on the surface free energy which, in turn, can be affected by the surface tension of the two metals [327]. The diffusion (from the bulk) of Pd with the lowest surface tension (1.6 J m^{-2} *vs.* 2.3 J m^{-2} for Ni [328,329]) lowers the free energy, resulting in surface enrichment.

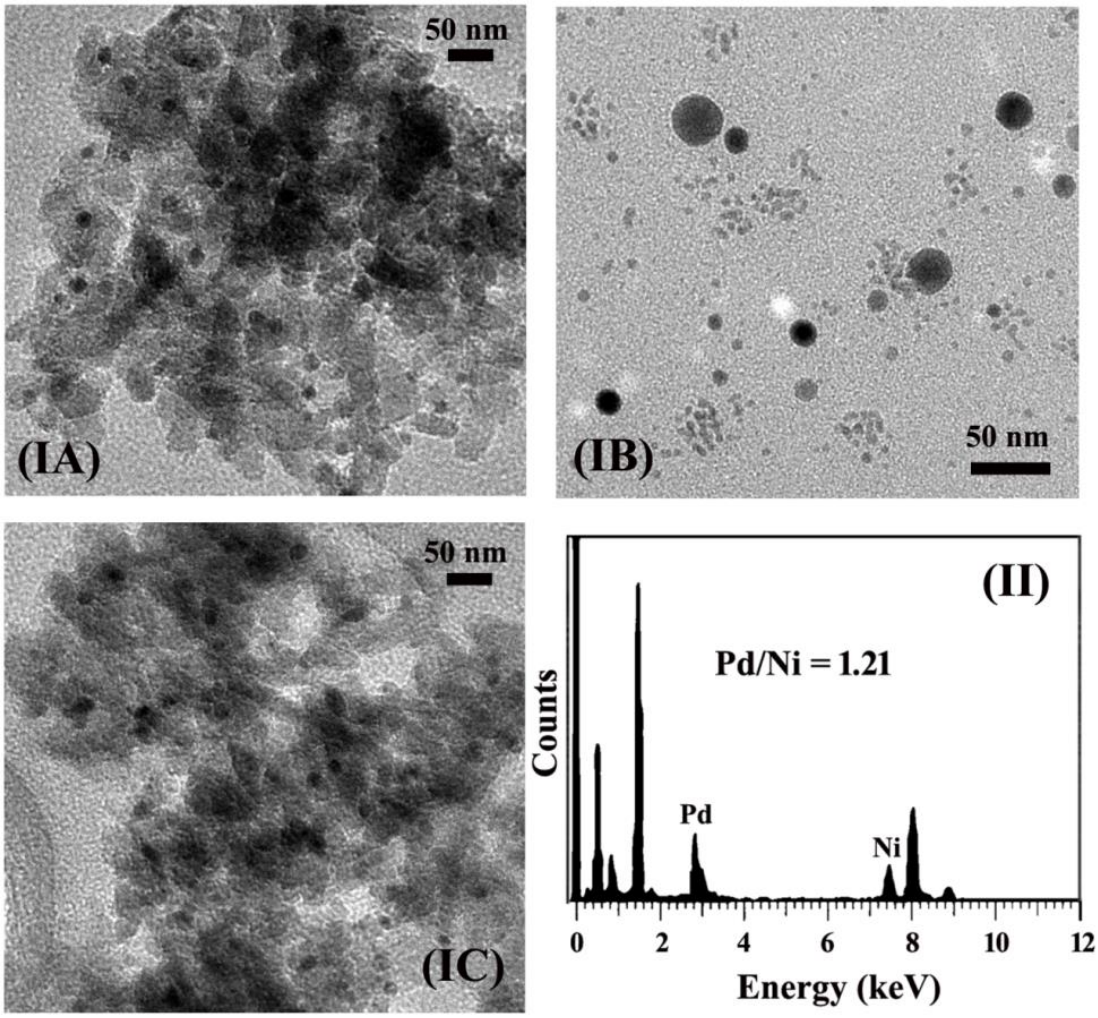

Figure 5.5: (**I**) Representative TEM images for Al_2O_3 supported (**A**) Pd, (**B**) Ni and (**C**) bimetallic Pd-Ni and (**II**) EDX spectrum of an individual metal particle in bimetallic Pd-Ni/Al_2O_3..

X-ray photo-electron spectroscopic (XPS) analysis can provide critical information in terms of changes to the electronic properties of surface Pd sites as a result of Ni incorporation. The XPS spectra over the Pd 3*d* and Ni 2*p* BE regions for Pd/Al_2O_3 **(IA)** Ni/Al_2O_3 **(IB)** and $Pd–Ni/Al_2O_3$ (**(IC)** and **(IIC)**) are shown in **Figure 5.6**; the associated Pd $3d_{5/2}$, Pd $3d_{3/2}$, Ni $2p_{3/2}$ and Ni $2p_{1/2}$ BE are compared in **Table 5.1.** The XPS for Pd/Al_2O_3 exhibits a BE maximum at 335.0 eV for Pd $3d_{5/2}$ with a secondary peak at higher BE (= 340.2 eV) for Pd $3d_{3/2}$ that are within the 335.2 ± 0.3 eV and 340.5. ± 0.2 eV of Pd^0 [330,331]. $Pd-Ni/Al_2O_3$ also presented two peaks but at higher (by 0.5 eV) BE, a response indicative of a Pd electronic modification by the inclusion of Ni component in its crystallographic structure that is consistent with an electronic re-hybridisation of Pd orbitals, *i.e.* electron transfer from the inner (*d*) orbital to the outer (*s*) orbital that results in a reduction of electrostatic repulsion shifting the Pd core-levels to higher BE [332]

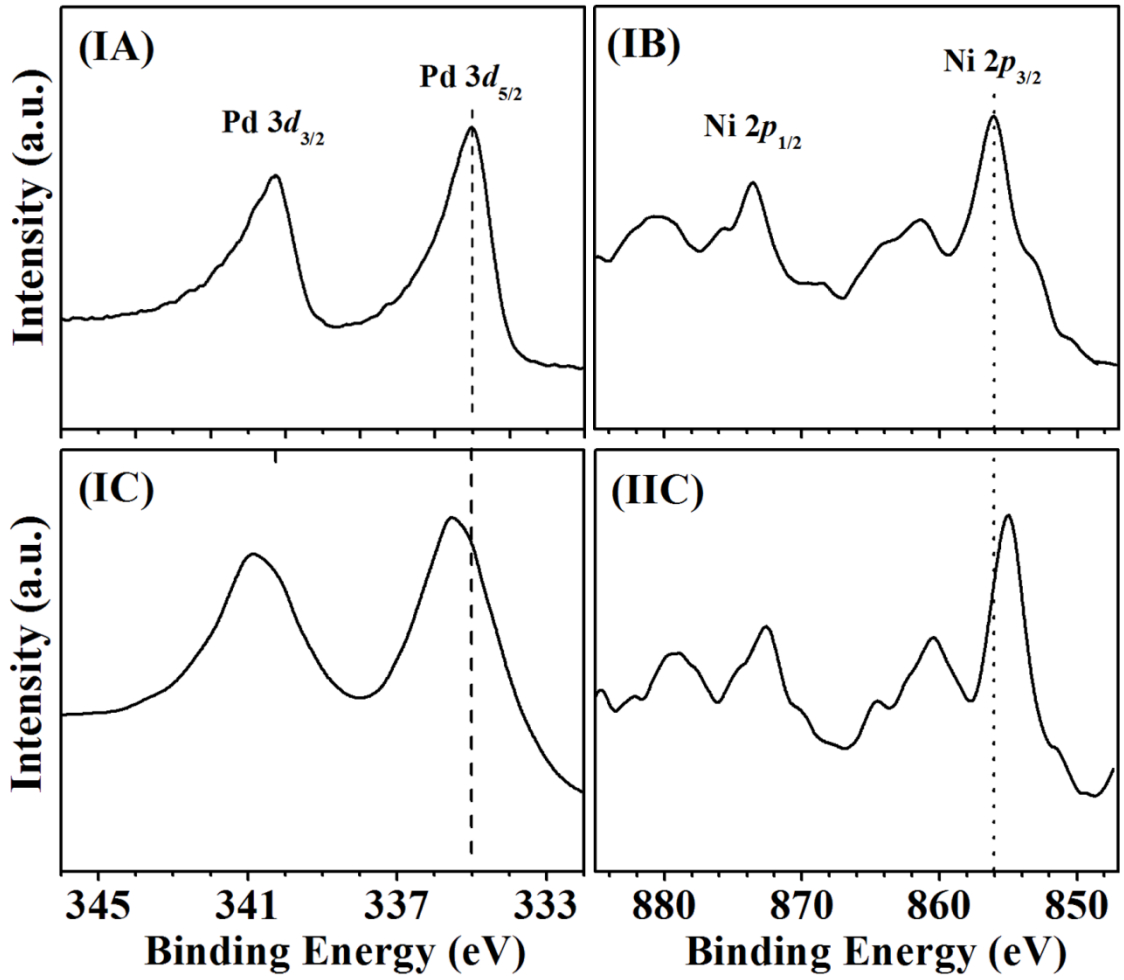

Figure 5.6: XPS spectra for Al_2O_3 supported (**A**) Pd, (**B**) Ni and (**C**) bimetallic Pd-Ni over the (**I**) Pd 3*d* and (**II**) Ni 2*p* regions. *Note*: Dashed line in (**IA**) and (**IC**) illustrate the position of the core level binding energies (BE) for Pd $3d_{5/2}$ while dotted lines in (**IB**) and (**IIC**) denote the BE for Ni $2p_{3/2}$ of Ni^0.

Bertolini *et al.* [333,334] recorded a similar 0.4-0.8 eV shift in the Pd 3*d* BE of bulk Pd-Ni attributed to formation of a bimetallic phase. The Ni 2*p* spectra for Ni/Al_2O_3 **(IB)** exhibited two peaks with BE = 856.1 and 873.3 eV for Ni $2p_{3/2}$ and Ni $2p_{1/2}$, respectively. The reference BE values for Ni^0 are 852.7 and 869.9 eV) [335], although it has been reported elsewhere [336] that nickel-alumina interactions can result in a displacement to higher BE values. The shift in the BE of Ni 2*p* suggests the generation of $Ni^{\delta+}$ nanoparticles through electron transfer to Al_2O_3 [337]. Moreover, overlap of Ni 3*d* and O 2*p* orbitals on adjacent atoms can result in the generation of a covalent polar bond where nickel atoms (on alumina) exhibit a "partial" electron charge [338]. For the $Pd\text{-}Ni/Al_2O_3$ catalyst, a 1.2 eV decrease in the BE associated with Ni 2*p* (*vs*. Ni/Al_2O_3, **Table 5.1**) is in evidence, suggesting formation of bimetallic nanoparticles, which is in line with XPS the results in the Pd 3*d* region [339]. Moreover, the formation of bimetallic Pd-Ni nanoparticles can also be attested by the changes in the relative distance between the main and satellite peaks in the Ni 2*p* regions for Ni/Al_2O_3 and $Pd\text{-}Ni/Al_2O_3$ (ΔNi $2p_{X/2}$, **Table 5.1**), where an increase, by 0.4 eV, is observed for the bimetallic catalyst. Such increase can be related to the introduction of Pd with higher electronegativity (2.2 *vs.* 1.9 for Ni) that impacts on surface plasmon losses from the Ni $3d^9\,4s^1$ valence band [299]. The same conclusion was reached by Hillebrecht *et al.* [299] who recorded a 0.4 eV increase in the in ΔNi $2p_{3/2}$ and ΔNi $2p_{1/2}$ of unsupported Ni *vs.* PdNi. The Pd/Ni atomic ratio from XPS analysis (=6.1) exceeded the bulk value, which confirms the Pd surface enrichment from EDX analysis. TPR, XRD and XPS analyses suggest the generation of the bimetallic phase with a palladium surface enrichment (from TEM-EDX and XPS) in $Pd\text{-}Ni/Al_2O_3$.

5.3.2 Catalytic Performance

The hydrogenation of 3BY over all the catalysts generated 3BE, BA and BONE with no evidence of condensation (to dimers). The high H_2/-C≡C- molar ratio in this work (=8) can account for the observed absence of dimer generation which is favoured at ≤1.5 ratios [22]. The temporal variation of 3BY conversion (*X*) is shown in the *inset* to **Figure 5.7** for $Pd\text{-}Ni/Al_2O_3$, as a representative. We observe an initial drop in activity to reach a pseudo-stationary state after *ca.* 2 h on-stream. The absence of dimer formation and attainment of stationary state activity is an important result given reports in the literature that have shown a continuous decline of time on-stream activity in the hydrogenation of -C≡C- compounds over Cu/SiO_2 [340] and $Pd\text{-}Ag/Al_2O_3$ [341] attributed to coke formation and/or deposition of oligomers.

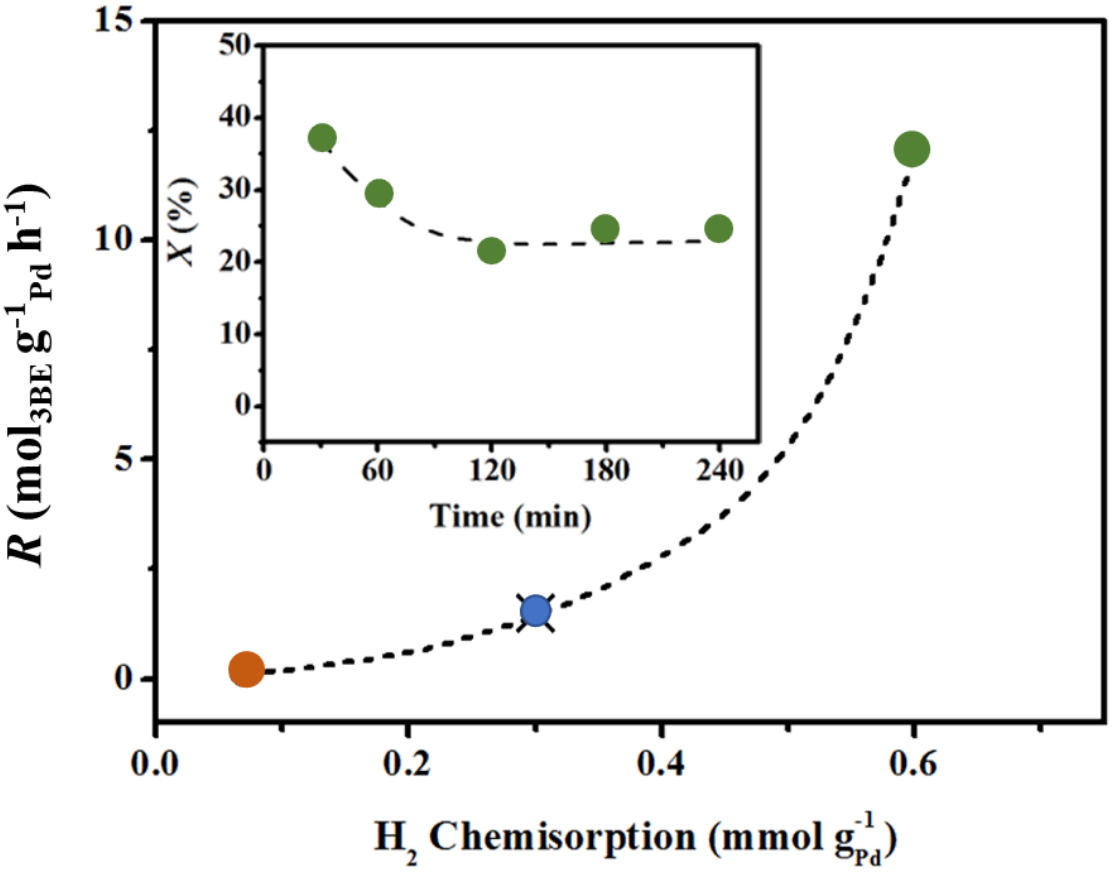

Figure 5.7: Variations in 3BY consumption rate (*R*, $mol_{3BY}\ g_{Pd}^{-1}\ h^{-1}$) with hydrogen chemisorption at ambient temperature for Al_2O_3 supported Pd (●), Ni (●), physical mixture Pd+Ni (✕) and bimetallic Pd-Ni (●). *Inset*: Variation of 3BY conversion (*X*, %) with time on-stream over Pd-Ni/Al_2O_3. *Note*: Raw data is shown as symbols (●,●,✕,●) while (dashed) trend lines serve to guide the eye. *Reaction conditions*: *T* = 373 K, *P* = 1 atm, H_2:Alkynol mol ratio = 2.

Dissociative adsorption of H_2 is a key controlling step in -C≡C- bond hydrogenation [194] and is dependent on the nature [342] and particle size [343] of the supported metal. Room temperature hydrogen chemisorption is a practical approach to quantify metal hydrogen dissociation capacity [344]. Hydrogen uptake was measured and is presented as a function of alkyne transformation rate (*R*) in **Figure 5.7**, where there is a clear increase in *R* with increasing hydrogen chemisorption. This tendency is in line with published work showing enhanced catalytic activity over catalysts with greater hydrogen uptake capacity in phenol hydrogenation [345] and methanol steam reforming [346]. Hydrogenation activity was low over Ni with the lowest hydrogen uptake capacity, which can be linked to the presence of electrons in the 4*s* orbital [347], resulting in a high activation energy barrier for dissociative hydrogen adsorption, *i.e.* 432 kJ mol^{-1} on Ni *vs.* 420 kJ mol^{-1} on Pd [348]. The introduction of Ni/Al_2O_3 as a physical mixture had not a significant effect on neither H_2 uptake capacity nor alkynol consumption rate with a similar response to that recorded over Pd/Al_2O_3, a result suggesting that the catalytic

performance is driven by palladium active sites. We observe a significantly greater hydrogenation rate over Pd-Ni/Al_2O_3 relative to the monometallic Pd and Ni catalysts. The enhanced hydrogen uptake over the Pd-Ni catalyst suggests a more efficient H_2 cleavage over bimetallic nanoparticles. Maccarrone *et al.* [296] quoted differences in hydrogen chemisorption for Pd-Ni/Al_2O_3 compared to Pd/Al_2O_3, while computational work [349] has shown an increase in hydrogen uptake capacity for PdNi *vs.* Pd accounted for on the basis of a lower associated H_2 dissociation energy over the former [349]. Variations in catalytic activity and/or selectivity [350] in hydrogenation reactions over mono- and bi-metallic catalysts have been observed previously. Lederhos *et al.* [351] and Domínguez-Domínguez and *co-workers* [233] studying the hydrogenation of 1-heptyne and phenylacetylene over Pd-Ni/Al_2O_3 and a series of (bulk) Pd-X catalysts (X = Ni, Fe and Mg) reported enhanced activity/olefin selectivity attributed to the bimetallic character of the Pd-X nanoparticles linked to modifications in active site geometric properties and electron density. Dependence of hydrogenation pathway over the four Al_2O_3 supported catalysts (Ni, Pd, Pd+Ni and Pd-Ni) can be effectively proved from a consideration of 3BE selectivity (S_{3BE}) as a function of 3BY conversion (X); the corresponding data for the different catalysts is shown in **Figure 5.8**.

At the same degree of conversion (*e.g.* 44±2%), the activity selectivity profiles for Pd/Al_2O_3 and Pd/Al_2O_3+Ni/Al_2O_3 overlapped, which indicates that incorporation of nickel as a physical mixture does not contribute to the reaction pathway which is governed by palladium. However, the S_{3BE} *vs.* X profiles for Pd/Al_2O_3, Ni/Al_2O_3 and Pd-Ni/Al_2O_3 do not coincide, suggesting that the presence of Pd and Ni in the bimetallic system can impact on the reaction network, *i.e.* parallel (k_3, **Figure 5.1**) *vs.* stepwise (k_1, k_2) hydrogenation *vs*. double bond migration (k_4). In order to relate the catalytic response of the three catalysts (Pd/Al_2O_3, Ni/Al_2O_3 and Pd-Ni/Al_2O_3) in terms of hydrogenation pathway (see **Figure 5.1** and **Eqns. (5.4)-(5.7)**), the mass balance for each compound was applied assuming pseudo-first order kinetic behaviour, as previously established for catalytic hydrogenation of phenyl-acetylene and styrene [352], for each individual step working under H_2:Alkynol in excess (by a factor of 16) of the stoichiometric requirement for the generation of the alkenol intermediate, which gives **Eqns. (5.8)- (5.11)**.

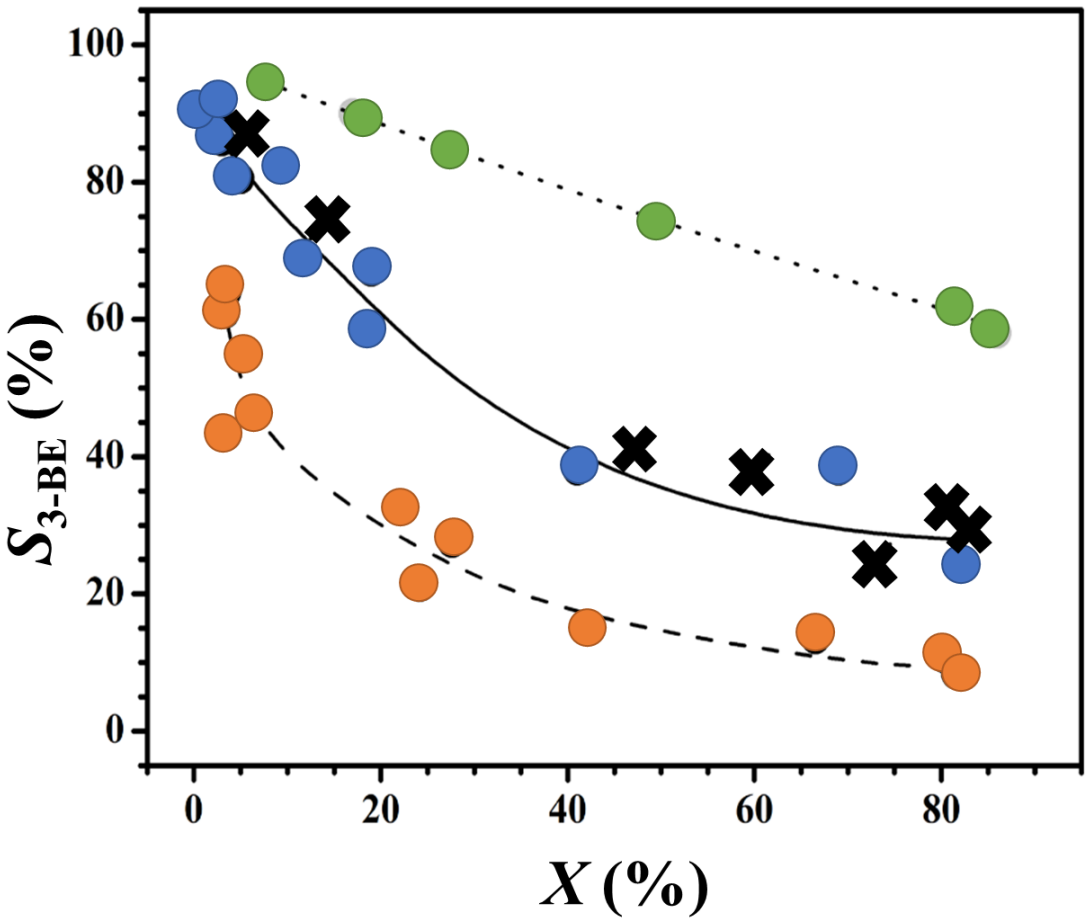

Figure 5.8: Variations in 3BE selectivity ($S_{3BE,}$ %) with conversion (X, %) in hydrogenation of 3BY over Al_2O_3 supported Pd (●, solid line), Ni (●, dashed line), physical mixture Pd+Ni (✕, solid line) and bimetallic Pd-Ni (●, dotted line). *Note*: Raw data is shown as symbols (●,●,✖,●) while trend lines (solid, dashed and dotted) serve to guide the eye. *Reaction conditions*: T = 373 K, P = 1 atm**.**

$$3BY + H_2 \xrightarrow{k_1} 3BE \quad \textbf{(5.4)}$$

$$3BE + H_2 \xrightarrow{k_2} BA \quad \textbf{(5.5)}$$

$$3BY + 2H_2 \xrightarrow{k_3} BA \quad \textbf{(5.6)}$$

$$3BE \xrightarrow{k_4} BONE \quad \textbf{(5.7)}$$

and

$$\frac{d_{x_{3BY}}}{d(n/F)} = -(k_1 + k_3) \cdot x_{3BY} \quad \textbf{(5.8)}$$

$$\frac{d_{x_{3BE}}}{d(n/F)} = k_1 \cdot x_{3BY} - (k_2 + k_4) \cdot x_{3BE} \quad \textbf{(5.9)}$$

$$\frac{d_{x_{BA}}}{d(n/F)} = k_2 \cdot x_{3BE} + k_3 \cdot x_{3BY} \quad \textbf{(5.10)}$$

$$\frac{d_{x_{BONE}}}{d(n/F)} = k_4 \cdot x_{3BE} \quad \textbf{(5.11)}$$

where k_i is the pseudo-first order kinetic rate constant for step i and $(n_{metal})/F$ has the physical meaning of contact time. The results of a *non*-linear regression of the experimental data to the kinetic model using the Berkeley Madonna software are presented in **Figure 5.9** while the resulting k_3/k_1, k_2/k_1 and k_2/k_4 are given in **Table 5.2**; which reveals a good fitting of experimental data (mole fractions) with the model with an error deviation of <5 %.

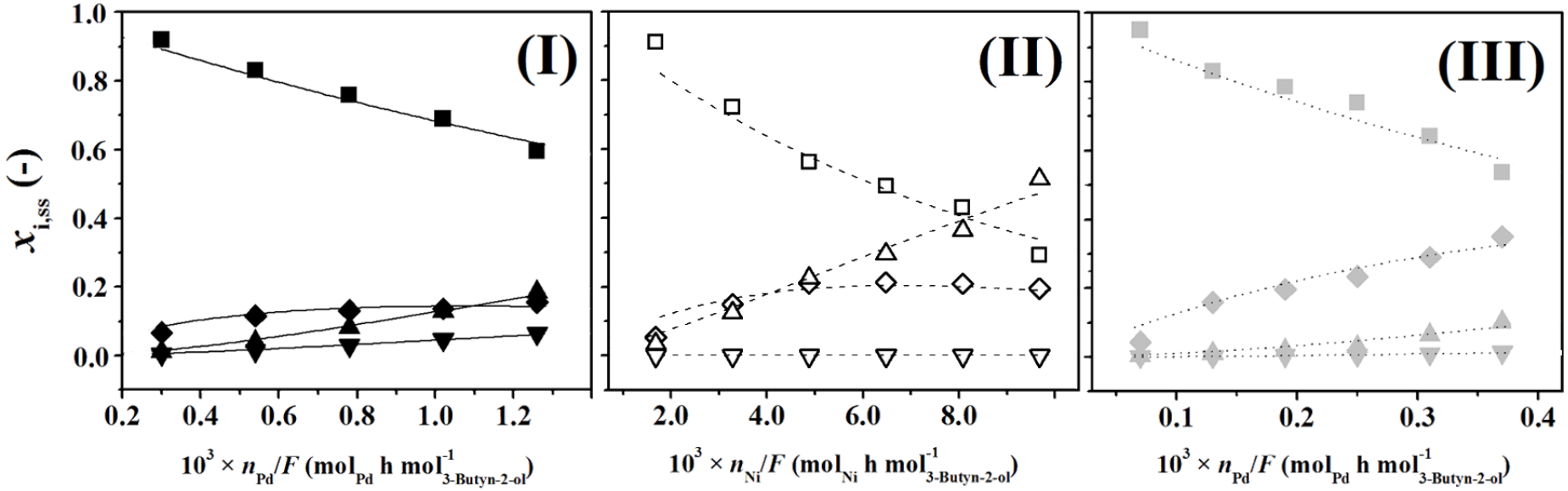

Figure 5.9: Molar fractions at steady state ($x_{i,ss}$) of 3BY (■,□,■), 3BE (◆,◇,◆), BA (▲,△,▲) and BONE (▼,▽,▼) as a function of contact time (n/F, $mol_{Pd\ or\ Ni}\ h^{-1}\ mol_{3BY}$) for reaction over Al_2O_3 supported (**I**) Pd (solid symbols, solid lines), (**II**) Ni (open symbols, dashed lines) and (**III**) (bimetallic) Pd-Ni (grey symbols, dotted lines). *Note*: dashed lines represent fit to eqns. (5.8- 5.11).

.

Table 5.2: Values of the rate constant ratios k_3/k_1, k_2/k_1 and k_2/k_4 for the 3BY → 3BE (k_1), 3BE → BA (k_2), 3BY → BA (k_3) and 3BE → BONE (k_4), steps.

	Pd	**Ni**	**Pd-Ni**
$\boldsymbol{k_3/k_1}$	0.2	0.5	0.0
$\boldsymbol{k_2/k_1}$	0.8	2.1	0.4
$\boldsymbol{k_2/k_4}$	1.3	-	4.7

The hydrogenation of 3BY over all the catalysts proceeded through a preferentially consecutive mechanism (*i.e.* $k_3/k_1 \leq 1$) that is typical of triple bond hydrogenation in gas phase over supported Pd [353] and Ni [354] catalysts. Double bond migration occurs as a result of hydrogen addition to the surface π-allyl intermediate formed by hydrogen removal from the carbon bonded to the triple bond functionality [27]. Butanone formation was not observed over Ni/Al_2O_3, although isomerisation was promoted over both Pd/Al_2O_3 and $Pd\text{-}Ni/Al_2O_3$ where the k_2/k_4 ratio (>1, **Table 5.2**) is indicative of preferential over-hydrogenation (to BA). The k_2/k_1 ratio (≤ 1) over Pd/Al_2O_3 and $Pd\text{-}Ni/Al_2O_3$ is consistent with an electrophilic mechanism, characteristic of alkyne hydrogenation [112], where the conversion of the alkenol intermediate proceeded at a lower rate than that of 3BY as a result of the greater electron density of the -C≡C- (*vs.* -C=C-) bond [18]. Cherkasov *et al.* [295], observed the same trend (*i.e.* $k_1 > k_2$) for the liquid phase hydrogenation MBY over Pd/SiO_2 $Pd\text{-}Bi/SiO_2$ and Pd-Lindlar, although the authors did not elaborate further. In this mechanism, hydrogen generated by dissociative adsorption on Pd sites attacks sequentially the chemisorbed -C≡C- and -C=C- species, where the latter is rate limiting [119]. Reaction over Pd-Ni favoured 3BE hydrogenation ($k_1 >>> k_2$) leading to increase 3BE selectivity (**Figure 5.9** and **Table 5.2**). The bimetallic particles in $Pd\text{-}Ni/Al_2O_3$ have a lower electron withdrawing character than palladium in Pd/Al_2O_3 due to a lower $\pi \rightarrow d$ electron donation (by up to 0.14 e^-) [339], with a consequent weaker interaction of (electron rich) -C=C- bond with PdNi that must favour the displacement of 3BE from the surface by 3BY. This is consistent with computational work (DFT calculations) [355] that has demonstrated a greater alkene displacement from the surface of Pd-Ni (*vs.* Pd) by an alkyne molecule [355]. The opposite trend (*i.e.* $k_2/k_1 > 1$) is observed over Ni/Al_2O_3, a result that we tentatively attribute to 3BY rate inhibition

due to strong -C≡C- bond interaction that serves to stabilize the reactant, rendering it less susceptible to hydrogen attack. Our premise is in line with the reported greater alkynol-metal adsorption strength on Ni (189 kJ mol^{-1}) compared to Pd (91 kJ mol^{-1}) [87].

5.4 Conclusions

The synthesis of monometallic Pd/Al_2O_3 by incipient wetness impregnation followed by hydrogen TPR activation delivered a narrow distribution of metal nanoparticles (mean = 20 nm). Preparation of monometallic Ni/Al_2O_3 following the same procedure and bimetallic $Pd\text{-}Ni/Al_2O_3$ (by co-impregnation) generated larger metal nanocrystals (mean = 28 ± 2 nm). Powder XRD, TEM-EDX and XPS measurements have revealed a bimetallic PdNi phase enriched with palladium on the surface in $Pd\text{-}Ni/Al_2O_3$, a consequence of which is an enhanced H_2 uptake capacity relative to Pd/Al_2O_3. Hydrogenation over Ni/Al_2O_3 resulted in low catalytic activity to promote partial (to 3BE) and full hydrogenation (BA) with no detectable BONE generation. In contrast, Pd/Al_2O_3 and Pd/Al_2O_3+Ni/Al_2O_3 delivered a similar (greater) transformation rate and promoted a coupled hydrogenation/isomerisation with the formation of 3BE, BA and BONE. Reaction over $Pd\text{-}Ni/Al_2O_3$ resulted in an increase rate (up to 12 mol_{3BY} g_{Pd}^{-1} h^{-1}) and the highest selectivity to 3BE (up to 95%). We attribute the distinct catalytic performance over $Pd\text{-}Ni/Al_2O_3$ to electronic modifications induced by the addition of Ni in agreement with XPS and TPR results. Our results proved the potential of Ni-promotion for Pd-based catalysts directed and the selective production of alkenols with multiple industrial applications.

Chapter 6:

Gas Phase Hydrogenation of 3BY over Unsupported and Supported Ni-Zn Alloys.

Nickel promotes lower isomerisation activity compared to palladium, while the results in **Chapters 3** and **4** have demonstrated the beneficial effect of Zn as a modifier to inhibit full hydrogenation (to alkanol). In this chapter, we have evaluated the continuous production of 3BE through the gas phase hydrogenation on 3BY using a series of bulk and supported NiZn alloys with different crystallographic phase (*i.e.* α-, β- and δ-).

6.1 Introduction

Partial hydrogenation of alkynols to alkenols is a topic that is currently attracting appreciable research activity. However, a search through the open literature revealed only one study that considered the hydrogenation of secondary alkynols (over Pd/Al_2O_3) [66]. 3BE is a valuable intermediate in the manufacture of butadiene (13,000,000 tonnes per year worldwide [358]. The hydrogenation of 3BY can follow several pathways, as shown in **Figure 6.1**.

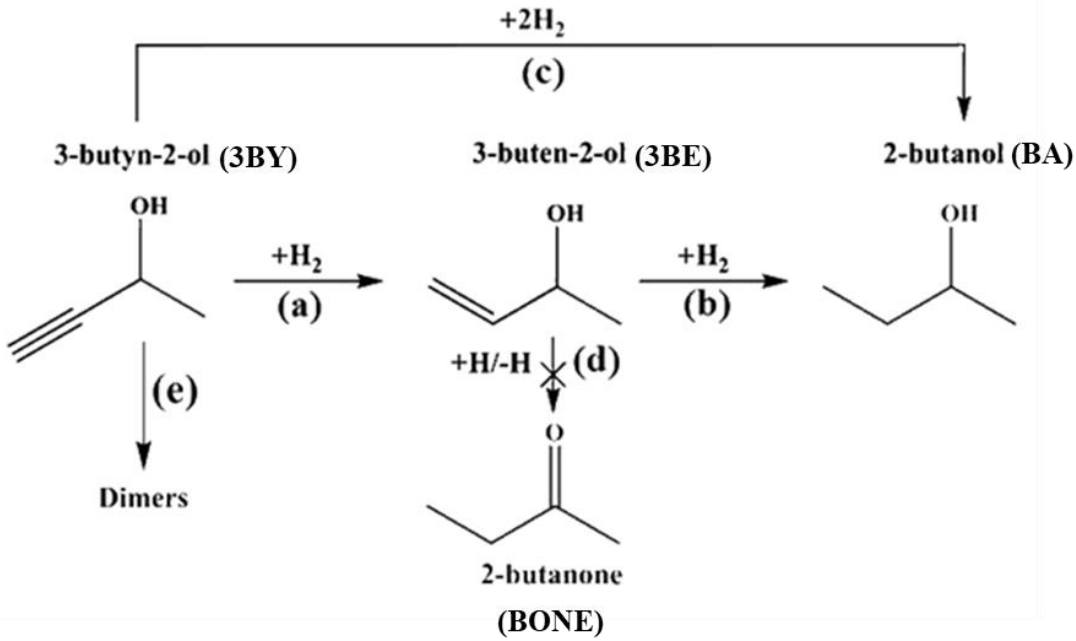

Figure 6.1: Reaction pathway in the hydrogenation of 3BY.

Step a involves partial hydrogenation to target 3BE, which can be further hydrogenated to BA (**step b**). In **step c**, 3BY is directly converted to BA while 3BE is isomerised to BONE in **step d** *via* double bond migration and keto-enol tautomerization. The formation of dimers (**step e**) can result from condensation involving 3BY [57].Existing industrial routes have involved the use of Pd catalysts [359] that suffer from the generation of by-products from undesired oligomerisation, double bond migration and over-hydrogenation [110]. In addition to the selectivity issue, palladium is a *non*-abundant metal (6×10^{-4} ppm in the Earth's crust [48]) with a high associated cost (~10^3 USD kg^{-1}, [56]).

Nickel promotes lower isomerisation activity relative to palladium, a response that has been attributed to electronic effects from differences in the bandwidth on both metals that impact on reactant adsorption/activation [294]. Moreover, Ni is available in higher concentrations (90 ppm) and at a lower cost (10 USD kg^{-1}, [48,294]). Nickel catalysts have been successfully employed in hydrogen mediated reactions such as conversion of aldehydes, carboxylic acids, CO_2, alkenes and alkynes [360]. However, we have failed to unearth any study in the literature using nickel catalysts in the gas phase hydrogenation of alkynols. It is, however, worth flagging the work of Trimm *et al.* [354,361], who examined acetylene hydrogenation over Ni/SiO_2 and reported good stability with time on-stream but poor alkene selectivity (S_{ethene}= 45%) due to extensive oligomerisation and over-hydrogenation to ethane.

We have reported recently [362] the results of the gas phase hydrogenation of 3BY over a series carbon/oxide supported Pd catalysts. In that work, we demonstrated that incorporation of Zn results in the formation of a PdZn alloy phase that inhibits generation of BA but an appreciable isomerisation to BONE. We have extended that study to consider the catalytic action of NiZn bimetallic as a means of controlling selectivity (*i.e.* inhibit isomerisation using Ni (**step d** in **Figure 6.1**) and hinder BA generation by incorporation of Zn (**steps b** and **c**)) while attaining high conversions through alloy formation. High temperature (973-1173 K) reaction of the cubic (α-NiZn; Zn content = <1-27%), tetragonal (β-NiZn; 45-53%), brass type (γ-NiZn; 75-85%) and monoclinic (δ-NiZn; 90-92%) structures [363]. There is a dearth of literature dealing with the catalytic implications of NiZn alloys, which is the focus of this work. Nevertheless, Al_2O_3 supported α- and β-NiZn catalysts have been successfully employed in the steam reforming of ethanol [364] and deoxygenation of methyl laurate [365]. Of particular relevance to this study, Spanjers *et al.* examined the hydrogenation of acetylene+ ethylene

over (bulk) α-, β- and γ-NiZn alloys [57] and Ni/ZnO [366], concluding a decrease in oligomer formation and greater olefin selectivity with increasing Zn content. In this study we have investigated the continuous gas phase hydrogenation on 3BY over unsupported (bulk) and supported NiZn alloys, linking catalytic performance with critical catalyst characterisation measurements. To the best of our knowledge, this is the first reported explicit comparison of α-, β- and δ-NiZn in hydrogenation.

6.2 Experimental

6.2.1 Catalyst Preparation

The metal precursors (Ni $(NO_3)_2 \cdot 6H_2O$ and Zn $(NO_3)_2 \cdot 6H_2O$), ZnO and δ-NiZn alloy were obtained from Sigma-Aldrich. The (unsupported) bulk catalysts were prepared by DP using Na_2CO_3 as a basification agent following a method described in detail elsewhere [367]. Briefly, 100 cm^3 of an aqueous (0.1 M) solution of $Ni(NO_3)_2 \cdot 6H_2O$ + $Zn(NO_3)_2 \cdot 6H_2O$ (Ni: Zn molar ratios = 90:10 and 50:50) was stirred (600 rpm) at 353 K for 1 h. An aqueous Na_2CO_3 solution (1 M) was then added dropwise to the suspension until pH = 9.0, and aged under vigorous stirring for 2 h to generate a cake from the precipitated nickel and zinc carbonate salts [368]. The solid obtained was separated by filtration, washed with deionized water until pH = 7 and dried at 373 K in static air. The dried sample was calcined in static air (5 K min^{-1} to 773 K for 4 h) in order to form ONi_xZn_{100-x} solid solution [369]. A Ni bulk catalyst was prepared for comparison purposes following an identical synthesis route with Ni $(NO_3)_2 \cdot 6H_2O$. Using the same procedure (nickel precursor, basification agent, stirring rate and temperature), we also synthesised a 13 mol% Ni/ZnO by DP until the pH reaches the isoelectric point of ZnO (pH= 10), *post*-treatment as above. The catalyst precursors were sieved (ATM fine test sieves) into a batch of 75 μm average particle diameter. Prior to reaction, the samples were activated in 60 cm^3 min^{-1} H_2 (BOC, ≥99.99%) at 4 K min^{-1} to 1073 K, which was maintained for 48 h, and cooled to room temperature in a N_2 flow (52 cm^3 min^{-1}, BOC, ≥ 99.99%) at 4-10 K min^{-1} for 24-48 h to ensure reduction of nickel and zinc with generation of an alloy phase [57]. Samples were passivated at ambient temperature in 1% v/v O_2/He (30 cm^3 min^{-1}, BOC, 99.9%) for 1 h for *ex-situ* characterisation.

6.2.2 Catalyst Characterisation

The Ni and Zn content were measured by AAS using a Shimadzu AA-6650 spectrometer with an air-acetylene flame from the diluted extract in aqua regia (25% v/v HNO_3/HCl). H_2-TPR, H_2 chemisorption (at reaction temperature = 373 K) and hydrogen temperature programmed desorption (TPD) were determined using the commercial CHEM-BET 3000 (Quantachrome) unit equipped with a thermal conductivity detector (TCD) with data acquisition/manipulation using the TPR Win^{TM} software. The samples were loaded in a U-shaped quartz cell, contacted with 5% v/v H_2/N_2 (17 cm^3 min^{-1}) and activated at 4 K min^{-1} to 1073 K. The effluent gas passed through a liquid N_2 trap to ensure removal of released water. After TPR, the reduced samples were maintained at the final temperature in a constant flow of H_2/N_2 for 1 h and swept with a (50 cm^3 min^{-1}) flow of N_2 for 1.5 h in order to remove any physisorbed hydrogen. The samples were then cooled to 373 K and subjected to an undiluted H_2 chemisorption pulse (30 μL) titration procedure. Pulses were repeated until the signal area was constant, indicative of surface saturation. In blank tests, there was no measurable H_2 uptake on ZnO alone. Samples were then thoroughly flushed (in N_2; 50 cm^3 min^{-1} for 1 h) and TPD conducted at 50 K min^{-1} to 873 K. At least three cycles of TPR, hydrogen chemisorption and TPD were carried out where the results were reproducible to within ±10% and the values quoted in this paper are the mean.

Powder X-ray diffractograms (XRD) were recorded on a Bruker/Siemens D500 incident X-ray diffractometer using Cu Kα radiation. The samples were scanned at a rate of 0.02º $step^{-1}$ over the range $20º \leq 2\theta \leq 90º$ (scan time = 5 s $step^{-1}$). Diffractograms were identified against JCPDS-ICDD reference standards (ZnO (210-7059), NiO (043-1049), Ni (003-1051), $ONi_{90}Zn_{10}$ (230-0284), α-NiZn (153-8880), $ONi_{70}Zn_{30}$ (152-6386), β-NiZn (153-8139) and δ-NiZn (152-3421)). Crystal particle size (d_{hkl}) was estimated using the Scherrer equation:

$$d_{hkl} = \frac{K \times \lambda}{\beta \times \cos\theta} \qquad \textbf{(6.1)}$$

where $K = 0.9$, λ is the incident radiation wavelength (1.5056 Å), β is the peak width at half the maximum intensity and θ represents the diffraction angle corresponding to the main plane associated with NiO ($2\theta = 43.4°$), Ni ($2\theta = 44.6°$), $ONi_{90}Zn_{10}$ ($2\theta = 43.2°$), α-NiZn ($2\theta = 44.2°$), $ONi_{70}Zn_{30}$ ($2\theta = 43.1°$), β-NiZn ($2\theta = 46.6°$) and δ-NiZn ($2\theta = 43.0°$).

6.2.3 Catalytic Performance in the Hydrogenation of 3BY

The hydrogenation of 3BY (Sigma-Aldrich, purity ≥97%) as a solution in BOL (Sigma-Aldrich, ≥97%) was carried out *in situ*, immediately after catalyst activation, under atmospheric pressure at 373 K in a continuous flow fixed bed vertical glass reactor (*i.d.* = 15 mm). The catalytic reactor and operating conditions were selected to ensure negligible heat/mass transport limitations. A layer of borosilicate glass beads (diameter = 3 mm) served as a preheating zone where the alkynol reactant was vaporised and reached reaction temperature before contacting the catalyst bed. Isothermal conditions (±1 K) were maintained by diluting the catalyst bed with ground glass (75 μm diameter). Reaction temperature was continuously monitored by a thermocouple inserted in a thermowell within the catalyst bed. The alkynol reactant was delivered to the reactor *via* a glass/teflon air-tight syringe and teflon line using a microprocessor-controlled infusion pump (Model 100 kd Scientific) with an inlet molar flow = 1.5-3.1 mmol h^{-1}. A co-current flow of alkynol and H_2 or H_2/N_2 (P_{H_2} = 9 × 10^{-2} - 100 × 10^{-2} atm) was maintained at *GHSV* = 1 × 10^4 - 3 × 10^4 h^{-1}, the flow rate of which was monitored using a Humonics (Model 520) digital flowmeter. The molar Ni (*n*) to inlet alkynol molar feed rate (*n/F*) spanned the range 36 × 10^{-5} – 33 × 10^{-2} h. In blank tests, passage of 3BY in a stream of H_2 through the empty reactor or over the ZnO support alone, *i.e.* in the absence of catalyst, did not result in any detectable conversion. The reactor effluent was frozen in an ice-bath trap for subsequent analysis which was made using a Perkin-Elmer Auto System XL gas chromatograph equipped with a programmed split/split-less injector and a flame ionization detector using a Stabilwax (fused silica) 30 m × 0.32 mm *i.d.*, 0.25 μm film thickness capillary column (RESTEK). Data acquisition/manipulation was performed using the TotalChrom Workstation Version 6.1.2 (for Windows) chromatography data system. The products, 3BE (97%), BA (99%) and BONE (99%) were purchased from Sigma-Aldrich and used without further purification. Reactant/product molar fractions (x_i) were obtained using detailed calibration plots (not shown). 3BY conversion (*X*) was obtained from:

$$X(\%) = \frac{[3BY]_{in} - [3BY]_{out}}{[3BY]_{in}} \times 100 \qquad \textbf{(6.2)}$$

where selectivity in terms of (for example) 3BE (S_{3BE}) is given by:

$$S_{3BE}(\%) = \frac{[3BE]_{out}}{[3BY]_{in} - [3BY]_{out}} \times 100 \qquad \textbf{(6.3)}$$

The subscripts "in" and "out" refer to the inlet and outlet streams. Catalytic activity is also quantified in terms of initial 3BY transformation rate (R, mol g_{Ni}^{-1} h^{-1}), determine from time on-stream measurements as described elsewhere [243] and T*OF* (rate per active site, h^{-1}) calculated using metal particle size from XRD analysis [370] . Repeated (up to three separate) catalytic runs with different samples from the same batch of catalyst delivered raw data reproducibility and carbon mass balance within ±6%.

6.3 Results and Discussion

6.3.1 Bulk Ni and NiZn Alloys

6.3.1.1 Catalyst Characterisation

Powder XRD patterns of the fresh/calcined bulk catalysts before **(A)** and after activation **(C)** are presented in **Figure 6.2**; the TPR profiles recorded during the hydrogen treatment step are shown in **Figure 6.2(B)**. The X-ray diffractogram pattern of the fresh (**Figure 6.2(IA)**) and hydrogen treated (**(IC)**) ZnO are identical and show peaks at 2θ = 31.8º, 34.6º, 36.4º, 47.7º, 56.8º, 63.1º, 66.6º, 68.2º, 69.3º, 72.9º, 77.2º and 81.7º that can be associated, respectively, with the (100), (002), (101), (102), (110), (103), (200), (112), (201), (004), (202) and (104) main planes of *hcp* ZnO. The similar XRD patterns is consistent with the negligible H_2 uptake during TPR (**Figure 6.2(IB)**), a response that was expected and in agreement with reported literature where reduction of ZnO requires $T > 1225$ K [371].

The diffractogram for the calcined Ni catalyst precursor (**Figure 6.2(IIA)**) presents signals at 2θ = 37.3º, 43.4º, 63.0º, 75.6º and 79.6º corresponding to the (111), (200), (220), (311), and (222) planes of NiO (JCPDS-ICDD 043-1049). Standard X-ray line broadening based on the Debye-Scherrer formula using the main diffraction peak (at 2θ = 43.4º) yielded an average particle size of 13 nm.

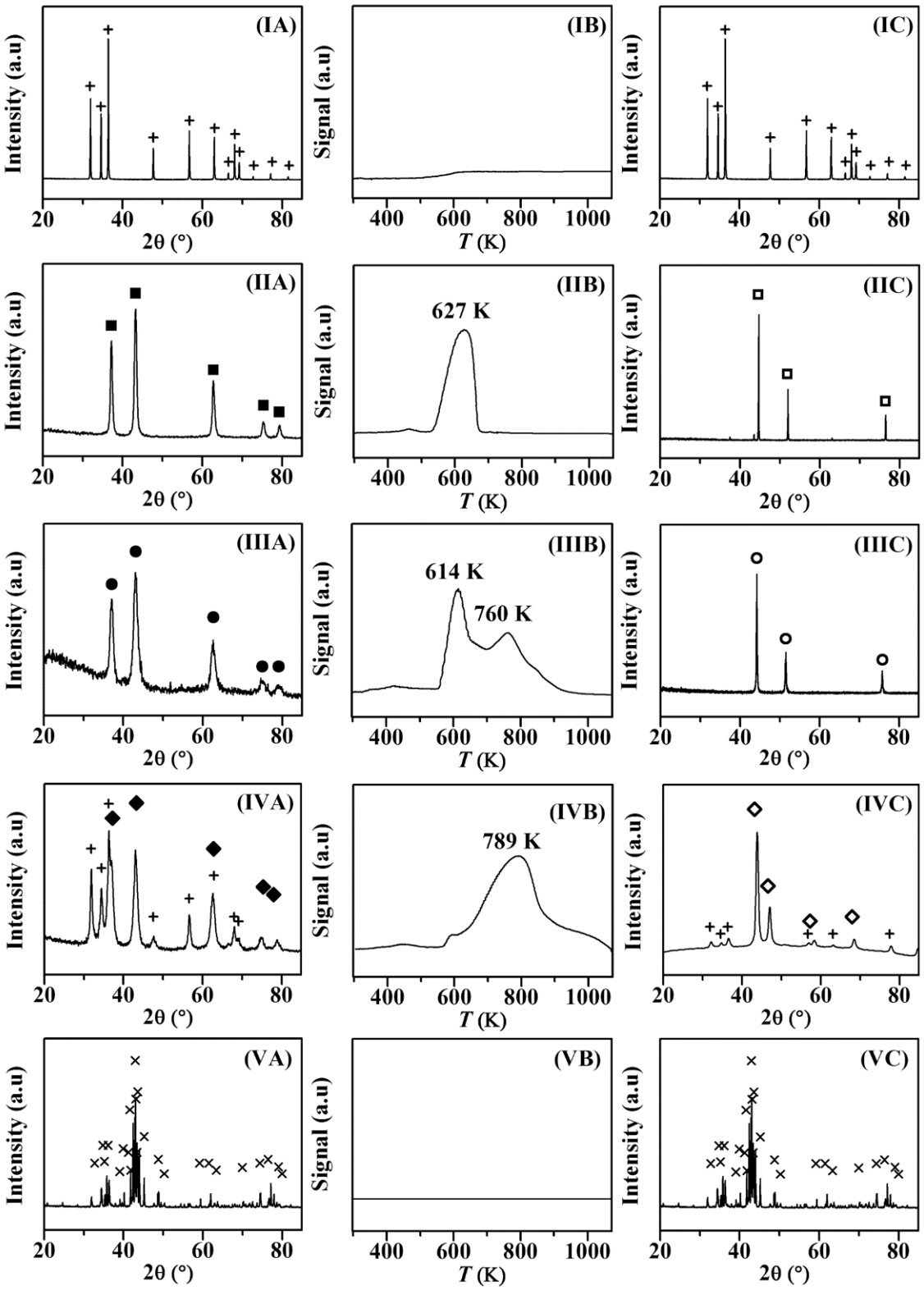

Figure 6.2: XRD patterns associated with (**A**) fresh/calcined and (**C**) reduced samples and (**B**) TPR profiles for (**I**) ZnO and (unsupported) bulk (**II**) Ni, (**III**) α-NiZn (**IV**) β-NiZn and (**V**) δ-NiZn. *Note*: Peak assignments based on JCPDS-ICDD reference data for ZnO (210-7059, ✚), NiO (043-1049, ■), Ni (003-1051, ◘)$ONi_{90}Zn_{10}$ (230-0284, ●), α-NiZn (153-8880, ○), $ONi_{70}Zn_{30}$ (152-6386, ◆), β-NiZn (153-8139. ◇) and δ-NiZn (152-3421, ✕).

This mean size is in good agreement with the value (8 nm) reported by Li *et al.* [372] for NiO prepared by a similar precipitation method with nickel acetate and sodium carbonate. The TPR profile generated for bulk NiO is presented in **Figure 6.2(IIB)**. Hydrogen consumption matched (±5%) that required for the reduction of $Ni^{2+} \rightarrow Ni^{0}$. The profile is characterised by a sharp positive signal (H_2 consumption peak) at T_{max} = 627 K. A single stage reduction with associated T_{max} in the 600-685 K temperature range has been reported in the literature [372] during TPR of bulk NiO and ascribed to the reduction to metallic nickel. Differences in reduction temperature for unsupported NiO can be accounted for in terms of metal particle size where a shift in T_{max} to higher values is indicative of larger nickel nanoparticles [373]. The T_{max} for maximum H_2 consumption was close to the value (643 K) recorded elsewhere [173] for bulk NiO with an associated particle size (obtained from XRD) of 17 nm, indicative of a similar metal dispersion to the catalyst in this work. The XRD diffractogram pattern of the activated bulk catalyst (**Figure 6.2(IIC)**) presents peaks at 2θ = 44.6°, 51.9°, and 76.5° that correspond, respectively, to the (1 1 1), (2 0 0) and (2 2 2) planes of (cubic) metallic Ni; mean particle size based on main (2θ = 44.6°) = 85 nm. This result suggests that thermal treatment in hydrogen to 1073 K served to increase metal crystallite size. Richardson and *co-workers* [374] reported a crystal size increase from 2.5 nm (for as prepared NiO) to 45 nm (reduced at 573 K). Sehested *et al.* [375] noted that crystal size grew drastically (by 27%) for activation at $T \geq 973$ K and ascribed this to agglomeration of Ni crystallites formed on the surface of Ni^{2+} during reduction.

The diffractogram of the calcined α-NiZn catalyst **(IIIA)** exhibits peaks at 2θ = 37.1°, 43.2°, 62.7°, 75.2° and 79.1° that match the (111), (200), (220), (311) and (222) of $ONi_{90}Zn_{10}$ solid solution (JCPDS-ICDD 230-0284); mean size = 7 nm. It is important to note that there were no detectable signals due to NiO or ZnO, a result that confirms complete transformation to $ONi_{90}Zn_{10}$. By comparison with the diffractogram pattern of NiO (**Figure 6.2(IIA)**), we observe a 2θ = 0.2-0.5° shift to lower values. This can be attributed to substitution of Ni^{2+} by Zn^{2+} in the crystal structure where the greater radii of the latter (0.074 nm *vs.* 0.069 nm [369]) serves to increase the lattice parameter [369], inversely proportional to the XRD diffraction angle (θ) following the Bragg's law [376]. The TPR profile of the calcined α-NiZn (**Figure 6.2(IIIB)**) is characterised by a broad hydrogen consumption with a main positive peak at T_{max} at 614 K and a secondary uptake at 760 K, that can be attributed to the concurrent reduction of Ni^{2+} and Zn^{2+} in $ONi_{90}Zn_{10}$. The overall hydrogen uptake during TPR matched the requirement for precursor reduction to

zero valent Ni and Zn. While we could not find any directly comparable published TPR analysis of ONi_xZn_{100-x} solid solutions, we can draw on the findings of some pertinent catalyst characterisation reports. Wang and *co-workers* [377] recorded a similar response for a physical mixture of NiO+ZnO, where the TPR profile exhibited a main consumption at *ca.* 623 K with a (weak) broad reduction peak at $T > 653$ K. Velu *et al.* [378] working with $Cu_{100-x}Ni_xZn$Al-mixed metal oxide catalysts associated the broad TPR peak at 573-673 K to the reduction of Ni^{2+} and/or Zn^{2+}. Jafarbegloo *et al.* [379], studying $Ni_xMg_{100-x}O$ solid solutions reported the appearance of two peaks at 573-773 K and 1098 K during TPR that they attributed to the reduction of Ni^{2+} on the surface and bulk of the catalyst, respectively. After activation, α-NiZn (**Figure 6.2(IIIC)**) exhibits three peaks at 2θ = 44.2°, 51.5°, and 75.8°, characteristic of (111), (200) and (220), main planes of a *fcc* alpha- phase NiZn alloy (JCPDS 153-8880); mean size = 35 nm. A similar (~ 6-fold) increase in crystal size was observed in the reduction of → Ni and $ONi_{90}Zn_{10}$ → α-NiZn.

Peak assignments for calcined β-NiZn (**Figure (IVA)**, 2θ = 37.0º, 43.1º, 62.6º, 75.0º and 78.9º) are consistent with the (003), (10-2), (2-10), (2-13) and (006) planes associated with $ONi_{70}Zn_{30}$ solid solution (JCPDS 152-6386); mean size = 8 nm. The increased Zn content in the Ni lattice resulted in a further (2θ = 0.1-0.2º) shift relative to $ONi_{90}Zn_{10}$. In addition to the solid solution peaks, a response due to ZnO is in evidence. In support of this, Rubio-Marcos *et al.* [369] showed that, for Zn concentrations above 30%, the samples undergo phase-separation into ZnO and $ONi_{70}O_{30}$. Mean particle size (8 nm) was equivalent to that obtained for $ONi_{90}Zn_{10}$. The TPR of calcined β-NiZn **(IVB)** shows a broad peak with a T_{max} at 789 K, which can be linked to the reduction of $ONi_{90}Zn_{10}$ and ZnO. The quantity of hydrogen associated with the single hydrogen consumption exceeded the amount required for the $Ni^{2+} \rightarrow Ni^0$ conversion but was lower than that necessary to fully reduce Zn^{2+} to metallic Zn. A comparison of the TPR response of $ONi_{90}Zn_{10}$ with that of $ONi_{70}Zn_{30}$ suggests an increase in reduction temperature for ONi_xZn_{100-x} solid solutions with greater zinc content. This observation is in line with the study of García *et al.*[380], who working with NiO-MgO system recorded a (*ca.* 35 K) shift to higher reduction temperature for the hydrogen consumption during TPR for samples with increase Mg content. We tentatively linked the displacement towards higher reduction temperatures to a zinc surface enrichment due to the higher surface tension of Zn^{2+} (1.8 N m^{-1} *vs.* 0.8 N m^{-1} for Ni^{2+} [381]), and higher temperature requirement for the reduction of Ni^+ in the bulk of the solid solution. Indeed, a zinc-rich surface has been demonstrated (by XPS) for $Ni/ZnO/Al_2O_3$ catalysts with a Ni Zn ratio = 48:52 [367].

Moreover, Parmaliana *et al*. [382], working with a series of mixed phase of $Ni_xMg_{100-x}O$ calcined at 973 K at different final isothermal hold times, recorded an increase in intensity and shift to higher temperatures (from 613 to 788 K) for the TPR peak linked to the reduction of Ni^{2+} ions in the subsurface of the MgO, which they ascribed to enhanced nickel diffusion into the subsurface at extended calcination times. The XRD pattern of the hydrogen treated β-NiZn is presented in **Figure 6.2(IVC**), with reflections at 43.2°, 46.6° 57.7° and 68.0° corresponding to the (111), (200), (002) and (220) planes of a tetragonal β-phase NiZn alloy (JCPDS-ICDD 153-8139); mean particle size 13 nm. The smaller (2-fold) increase in crystal size observed during the $ONi_{70}Zn_{30}$ → β-NiZn transition (*vs*. $ONi_{90}Zn_{10}$ → α-NiZn) can be tentatively ascribed to the formation of an intermediate α-$ONi_{70}Zn_{30}$ alloy phase that induces partial recrystallization in the bulk structure. A similar rationale has been provided by Murzinova *et al.* [383] in their study of TiAlMoZr alloys to account for the variations in grain size associated with the α- *vs*. β-alloy phases.

The X-ray diffractogram pattern of the fresh (**Figure 6.2(VA)**) and hydrogen treated (**(VC)**) δ-NiZn are the same and show the main diffraction peaks at 2θ = 32.7º, 33.2º, 34.8º, 35.2º, 35.4º, 35.6º, 36.1º, 36.8º, 37.6º, 38.1º, 39.0º, 39.8º, 41.2º, 41.6º, 41.8º, 42.3º, 42.9º, 43.0º, 43.1º, 43.4º, 43.6º, 43.7º, 45.1º, 45.2º, 48.5º, 48.7º, 48.8º, 50.2º, 59.1º, 59.3º, 61.5º, 62.2º, 63.4º, 70.0º, 70.2º, 74.3º, 74.3º, 76.4º, 76.5º, 77.2º, 77.7º, 77.8º, 79.0º, 80.0º corresponding to (221), (202), (022), (20-3), (401), (51-1), (42-1), (130), (420), (13-1), (31-3), (131), (222), (60-2), (33-1), (330), (22-3), (113), (421), (13-2), (600), (51-3), (402), (023), (62-2), (040), (40-4), (620), (711), (800), (24-3), (423), (82-3), (731), (115), (93-2), (40-6), (060), (60-6), (153), (55-3), (443), (713), (642) planes characteristic of a monoclinic δ-NiZn alloy phase (JCPDS-ICDD 152-3421); mean size = 75 nm. The TPR of the commercial δ-NiZn catalyst (**Figure 6.2(VB)**) was featureless, a response consistent with the identical XRD patterns *pre*- and *post*-TPR.

Hydrogen uptake (**Table 6.1**) on all bulk catalysts was low (≤1 μmol g_{Ni}^{-1}). We could not find any other study in the literature that provides a measure of H_2 chemisorption at 373 K for comparable bulk Ni systems. However, our recorded hydrogen chemisorption values are of the same order of magnitude than those recorded at room temperature for bulk Ni and supported Ni-Au alloy (2-4 μmol g_{Ni}^{-1}) [384,385]. Hydrogen adsorption on nickel is dependent on chemisorption temperature and Ni coordination number. Smeds *et al*. [386] demonstrated enhanced chemisorbed hydrogen (by up to a 2-fold) with an

increase in titration temperature (298 → 423 K). In terms of Ni nanoparticle size dependence, the consensus that emerges from the literature is of a greater hydrogen uptake on smaller nanocrystals [384], *i.e.* greater Ni surface area. We observe a decrease in hydrogen chemisorption for Ni > α-NiZn > β-NiZn > δ-NiZn (see **Table 6.1**). This result is consistent with reported literature [365] showing a (15%) lower hydrogen uptake for a $Ni_{70}Zn_{30}Al$ alloy with a greater amount of zinc relative to $Ni_{80}Zn_{20}Al$. The decrease in hydrogen chemisorption for the Ni-containing catalysts with increase Zn content can be linked to zinc migration through diffusion effects that results in a concomitant decrease in surface nickel and hydrogen uptake.

Table 6.1: Characterisation and catalytic results over bulk catalytic systems. *Catalyst characterisation* results: catalyst source or preparation method (for laboratory synthesised samples), zinc content, nominal Ni:Zn content and crystal structure, hydrogen uptake and Ni size. *Catalysis results*: hydrogenation rate (*R*) and *TOF* for hydrogenation of 3BY . *Reaction conditions*: T = 373 K, P = 1 atm, (H_2:Alkynol) mol ratio = 114, X ~ 25%.

Catalyst		**ZnO**	**Ni**	**α-NiZn**	**β-NiZn**	**δ-NiZn**
Catalyst source/Synthesis		Commercial	DP[a]	DP	DP	Commercial
Zn content (mol%)		-	-	11	48	89
Nominal Ni:Zn Content (Crystal structure)		(*hcp*[b])	(*fcc*[c])	90:10 (*fcc* solid solution)	50:50 (tetragonal)	10:90 (monoclinic)
H_2 uptake (μmol g_{Ni}^{-1})[d]		-	1.0	0.3	0.1	<0.1
d_{hkl} (nm)[e]	**Calcined[f]**	-	13	7	8	-
	Reduced[g]	-	85	35	13	72
10^2 × R (mol g_{Ni}^{-1} h^{-1})		-	7	6[h]/11[i]	4	5×10^{-2}
TOF **(h^{-1})**		-	356	124[h]/230[i]	31	2

[a]DP = deposition-precipitation; [b]*hcp* =hexagonal close-packed; [c]*fcc* = face-centred cubic; [d]at reaction temperature (373 K); [e]from XRD measurements; [f]in air to 773 K; [g]in H_2 to 1073 K; [h]for reaction over α-NiZn; [i]for reaction over a physical mixture of α-NiZn+ZnO (Ni:Zn = 1:15).

6.3.1.2 Catalytic Response

We first examined the catalytic action of the NiZn alloy systems in the gas phase hydrogenation of 3BY; catalytic activity and conversion *vs.* 3BE selectivity (S_{3BE}) dependence is shown in **Table 6.1** and **Figure 6.3**, respectively, where 3BE was the main product (up to 98%). BA was formed as by-product with no detected generation of BONE or oligomers.

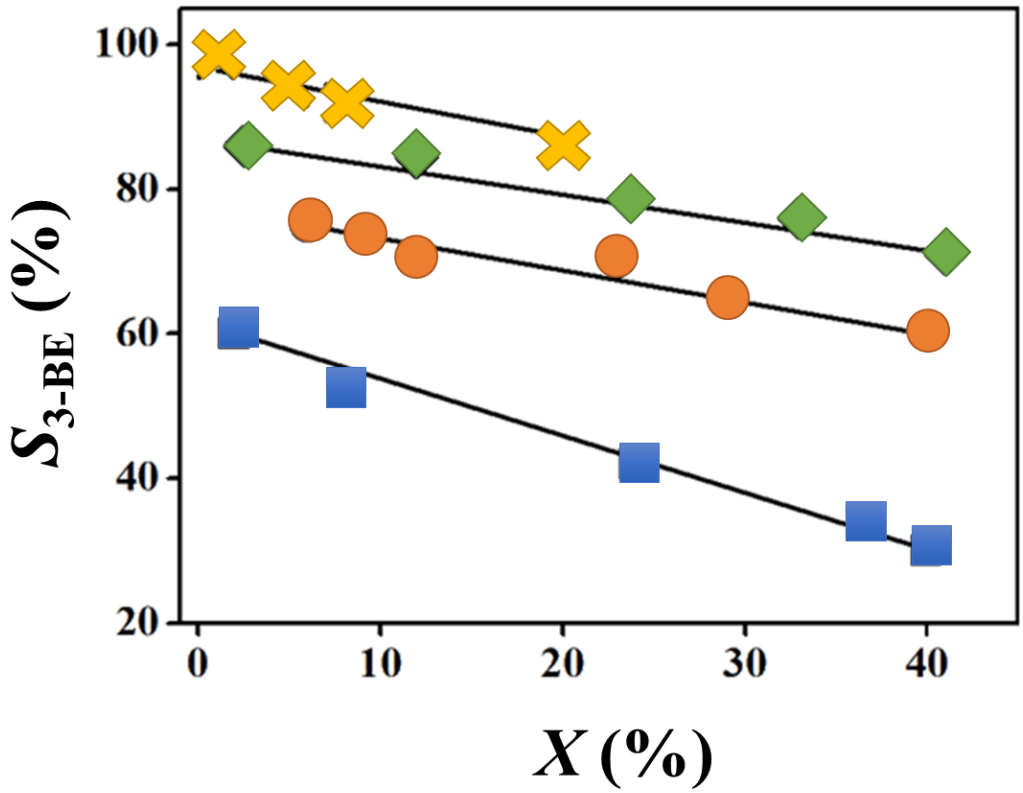

Figure 6.3: Variation of 3BE selectivity (S_{3BE}, %) with initial 3BY conversion (X, %) for reaction over activated (unsupported) bulk Ni (■), α-NiZn (●), β-NiZn (◆) and δ-NiZn (✖) catalysts. *Reaction conditions*: T = 373 K, P = 1 atm, (n/F) = 4×10^{-4} - 15×10^{-2} h. *Note:* solid lines provide a guide to aid visual assessment.

There is evidence in the literature suggesting that oligomerization over Ni catalysts is sensitive to H_2:-C≡C- molar ratio and consistent with a decrease in oligomerisation rate with increased hydrogen content [387]. The absence of oligomerisation in this work can be linked to the high H_2:-C≡C- (= 54-114), well above the experimental values (6-10) used when oligomer formation has been promoted [361,366]. The results presented in **Table 6.1** demonstrate a decrease in activity (R) with increasing Zn content following the order Ni > α-NiZn > β-NiZn > δ-NiZn. Analysis of possible contributions to catalytic activity in bulk Ni and NiZn alloys bearing different metal particle sizes is only

meaningful in terms of specific activity (*TOF*, see **Experimental** section). The similar decrease in *TOF* and *R* over catalysts with increasing Zn content demonstrate that metal dispersion had little impact on catalytic activity in the case of unsupported Ni and NiZn mixed phases, which is governed by the zinc content in the catalyst. Trimm *et al.* [361] and Spanjers and *co-workers* [366] working in the catalytic hydrogenation of acetylene over ($MgAl_2O_4$ and ZnO) supported Ni *vs.* NiZn alloys reported elevated activity over the former and for α- (*vs.* β-NiZn with greater Zn content) that they attributed to the presence of surface Zn/ZnO that inhibits hydrogen/acetylene adsorption lowering the rate. The modified activity over the catalytic systems can be linked to hydrogen uptake capacity as shown in **Table 6.1** where the activity decreased sequence matches that of decreasing hydrogen uptake, *i.e.* the decrease in hydrogen chemisorption that results from incorporation of Zn with Ni was accompanied by a lower hydrogenation rate. This is consistent with reports in the literature showing enhanced activity in the hydrogenation of phenyl-alkynes (propyne, butyne and pentyne) over Pd/MCM relative to Pd/SiO_2 with greater hydrogen uptake capacity [212].

Alkenol selectivity increased over the samples with enhanced Zn content, S_{3BE} Ni < α-NiZn < β-NiZn < δ–NiZn. The lower 3BE selectivity over bulk Ni can be ascribed to a contribution of the parallel (**step c** in **Figure 6.1**) and sequential (**step b** in **Figure 6.1**) reaction pathways due to -C≡C- multi-coordination on large surface nickel ensembles [388], to generate ethylidyne (**step c**) and ethylidene intermediates (**step b**) [31,389]. Each of these systems bears a unique Ni coordination environment, where the number of nearest nickel neighbours decrease in the order: Ni (12) > α-NiZn (9.6) > β-NiZn (4.0) > δ-NiZn (0; only Zn neighbours) [57]. Moreover, there is reported literature [365] that has demonstrated (by magnetic hysteresis) a decrease on the size of surface nickel ensembles with increasing zinc for NiZn alloys. Consequently, an increase in zinc content will serve to decrease the population of large nickel-atom ensembles, responsible for BA formation. While the size of surface Ni-atom aggregates can impact on product distribution through the reactant adsorption mode, the adsorption/activation of the alkynol can also be affected by electronic modifications in the Ni phase (*post*-Zn incorporation). Indeed, the inclusion of Zn in the NiZn alloy induces a reduction in the *d* bandwidth as a result of $d \rightarrow (s,p)$ orbital electronic rehybridization, weakening the electronic interaction with the -C=C- bond [390], facilitating its desorption [57] and increasing selectivity to 3BE. This finds agreement with theoretical work that has demonstrated a lower -C=C- bond adsorption stability for NiZn alloys relative to Ni [54].

The results in this section suggest a positive effect in alkenol selectivity with the progressive increase of Zn content that we link to geometric/electronic effects that impact on reactant adsorption/activation. The highest alkenol production (*TOF* = 100 h^{-1}) was attained over the alpha-phase NiZn alloy. Hydrogenation rate in the transformation of CO, toluene and NO_x [391–393] can be increased by contributions due to spillover hydrogen. Spillover hydrogen is formed through H_2 dissociative chemisorption on metal sites, followed by migration of atomic hydrogen to the support [384]. The occurrence of hydrogen spillover has been suggested to be influenced by the addition of support as a physical mixture [384]. In order to evaluate the possible spillover effects in the hydrogenation of 3BY we have assessed in the next section the action of bulk and supported α-NiZn and consider a contribution due to spillover hydrogen by examination of physical mixtures with added (ZnO) carrier.

6.3.2 ZnO Supported α-NiZn Alloy

6.3.2.1 Catalyst Characterisation

A 13 mol% Ni/ZnO catalyst was prepared to compare with the bulk α-NiZn alloy, introducing as an external factor the hydrogen spillover that takes place from ZnO support species; critical characteristics are presented in **Table 6.2**

Table 6.2: Characterisation and catalytic results over the Ni/ZnO catalyst. *Catalyst characterisation* results: nickel loading, temperature maxima (T_{max}) and H_2 consumption/desorption during activation by TPR and TPD, hydrogen uptake and Ni size. *Catalysis results*: hydrogenation rate (*R*) and *TOF* for hydrogenation of 3BY. *Reaction conditions*: *T* = 373 K, *P* = 1 atm, (H_2: Alkynol) mol ratio = 114, *X* ~ 25%.

Catalyst		**Ni/ZnO**
Ni loading (mol%)		13
TPR	T_{max} **(K)**	602
	H_2 uptake (μmol g^{-1})	2.4×10^3 [a]/1.4×10^3 [b]
H_2 uptake (μmol g_{Ni}^{-1})[c]		3.4
TPD	T_{max} **(K)**	733[d], 756[e]
	H_2 released (μmol g_{Ni}^{-1})	37[d]/460[e]
d_{Ni} **(nm)**[f]		12
10^2 × *R* (mol g_{Ni}^{-1} h^{-1})		26[d]/43[e]
TOF **(h^{-1})**		190[d]/314[e]

[a]experimental value; [b]required for the $Ni^{2+} \rightarrow Ni^0$ reduction step; [c]at reaction temperature (373 K); [d]for Ni/ZnO, [e]for a physical mixture of Ni/ZnO+ZnO (NiZn = 1:15); [f]from XRD measurements.

The recorded TPR profile is shown in **Figure 6.4** and presents a principal peak at 602 K with a shoulder at 468 K. The main peak can be ascribed to the reduction of Ni^{2+} to zero valent metal [394].

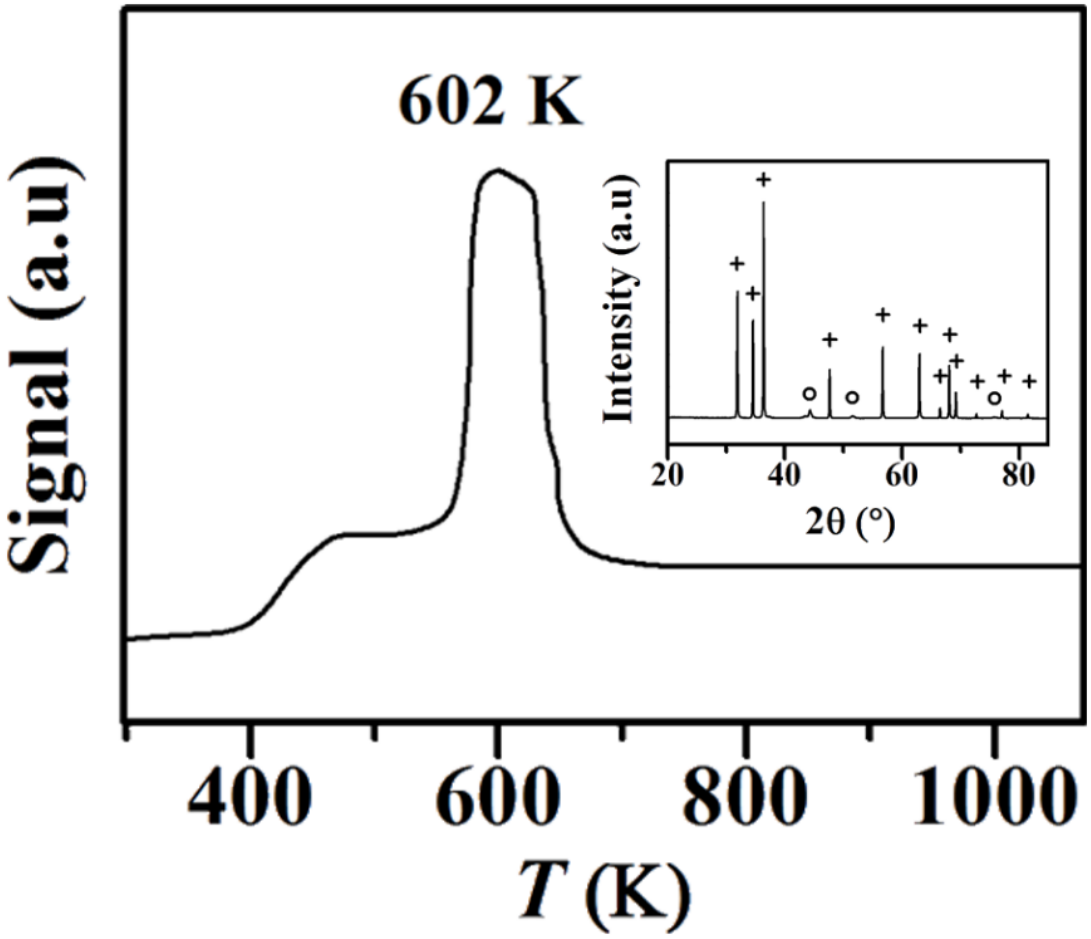

Figure 6.4: TCD response for the (hydrogen) temperature programmed treatment of Ni/ZnO to 1073 K. *Inset*: XRD pattern for passivated catalyst *post*-thermal (TPR) treatment. *Note*: Peak assignments based on JCPDS-ICDD reference data for ZnO (210-7059, ✚) and α-NiZn (153-8880, ○).

The secondary peak can be attributed to reduction of a NiO_x surface phase [395] formed during the drying step [396]. The quantity of hydrogen consumed during TPR (2.4×10^3 μmol g^{-1}) exceeded (by a factor of 2) the amount required to reduce the Ni precursor to the metallic form but was significantly lower (by a ten-fold) than that necessary to fully transform ZnO to Zn. This suggests a partial reduction of the zinc oxide support at 602 K promoted by Ni, which can result in the formation of an NiZn alloy phase [366]. The formation of intermetallic alloy after TPR was examined by XRD. The diffractogram generated is presented as an *inset* to **Figure 6.4.**

In addition to reflections characteristic of ZnO ($2\theta = 31.8^o$, 34.6^o, 36.4^o, 47.7^o, 56.8^o, 63.1^o, 66.6^o, 68.2^o, 69.3^o, 72.9^o, 77.2^o and 81.7^o), peaks at 44.2^o, 51.5^o, 75.8^o can be assigned to (111), (200) and (220) planes of α-NiZn. A metal particle size of *ca.* 12 nm was calculated from XRD measurements. Hydrogen chemisorption *post*-activation for Ni/ZnO (3.4 μmol g_{Ni}^{-1}, **Table 6.2**) was significantly greater (by a factor of 11) relative

to the value recorded for the bulk α-NiZn sample. An increase in uptake with decreasing α-NiZn particle size in the supported catalyst (35 *vs.* 12 nm) is consistent with reported enhanced hydrogen chemisorption for smaller Ni nanoparticles [384]. Hydrogen temperature programmed desorption (TPD) were conducted to evaluate total surface hydrogen [391]. In the case of NiZn alloys, it has been established [390] that decomposition (Zn_{gas}+Ni_{solid}) is possible in the temperature range 650-850 K under ultrahigh vacuum conditions (2×10^{-10} Torr). A decrease in Zn content as a result of alloy decomposition will alter the Ni_xZn_{100-x} composition and should result in a modification of the XRD diffractogram pattern.

Exclusive hydrogen desorption during TPD was confirmed by XRD analysis (see insets to **Figure 6.5**), where no changes in composition and/or particle size were observed *pre*- and *post*-thermal treatment. Ni/ZnO with inclusion of additional support should exhibit different amounts of spillover hydrogen, therefore, we consider the TPD response of Ni/ZnO **(A)** and Ni/ZnO+ ZnO **(B)** and the TPD profiles (*post*-TPR) are given in **Figure 6.5**; hydrogen release from bulk α-NiZn was negligible and close to detection limits. It is important to note that we recorded an equivalent hydrogen chemisorption value for the Ni/ZnO system with or without addition of the support (3.4 ± 0.05 μmol g_{Ni}^{-1}), which demonstrates that H_2 chemisorption was only associated with the supported α-NiZn component.

The profile for the Ni/ZnO catalyst (**Figure 6.5(A)**) showed a positive (hydrogen release) peak at $T > 730$ K where associated amount of hydrogen released well exceeded (by a factor of 10, **Table 6.2**) that taken up in the chemisorption step, indicative of spillover hydrogen generated during TPR from the support [397]. Indeed, desorption at $T \geq 593$ K have been reported in the literature for ZnO supported Ni [398] and Pd [399] and Zn-based Cu [400] catalysts and linked to spillover hydrogen. The profile obtained for the catalyst carrier mixture is like that corresponding to the catalyst alone but with a significant (12-fold) increase in the amount of hydrogen desorbed (**Table 6.2**). A similar effect has been reported elsewhere [401] attributed to an enhanced spillover hydrogen.

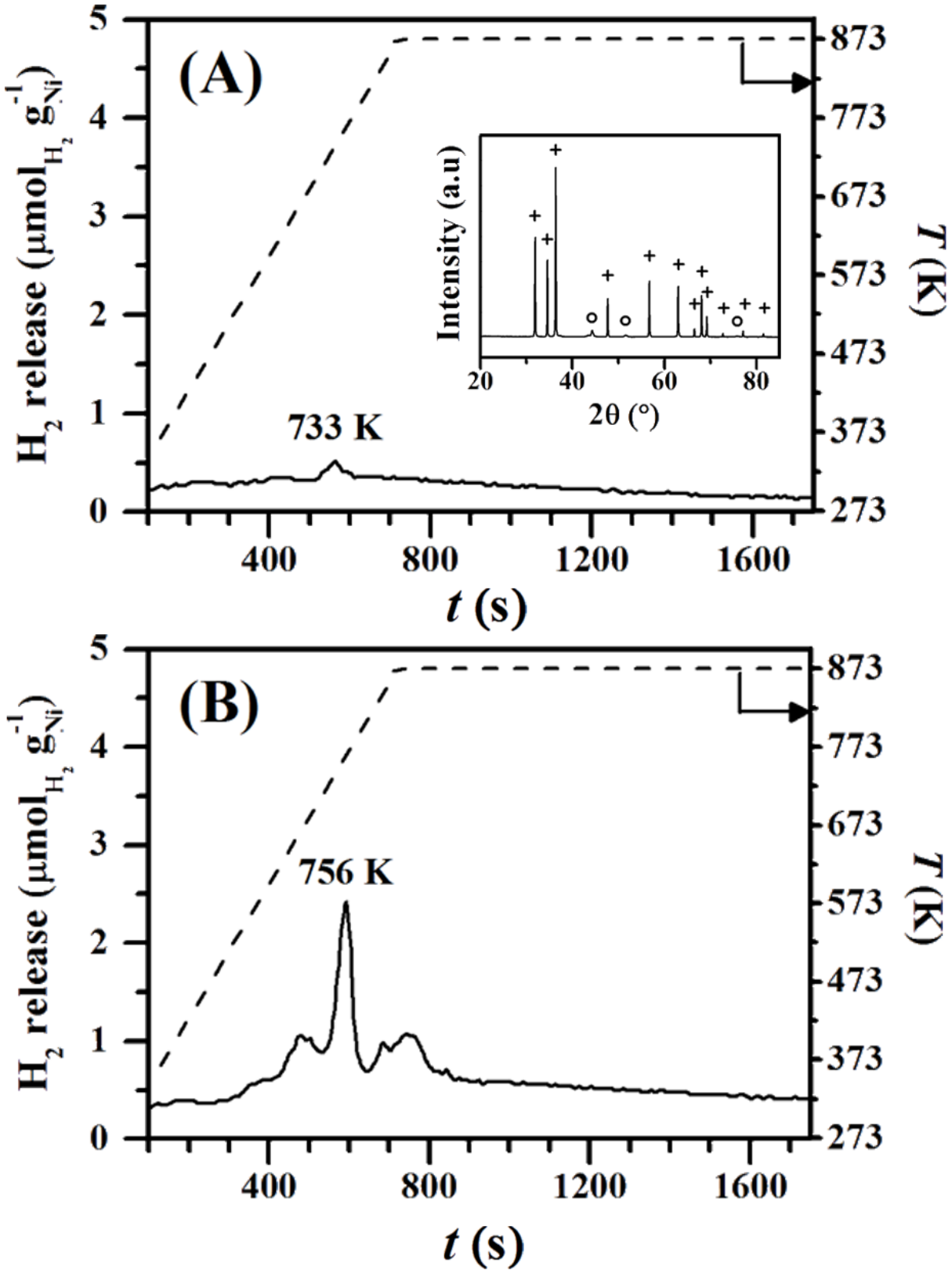

Figure 6.5: H_2-TPD response (solid line) with temperature ramp (dashed line) for: (**A**) Ni/ZnO and (**B**) Ni/ZnO+ZnO. *Inset to* (**A**): XRD pattern for passivated Ni/ZnO *post*-thermal (TPD) treatment. *Note*: Peak assignments based on JCPDS-ICDD reference data for ZnO(210-7059, +) and α-NiZn (153-8880, O).

6.3.2.2 Catalytic Response

In order to fully evaluate the performance of α-NiZn we compared the catalytic response of the bulk and supported catalyst under the same reaction conditions. In terms of specific activity, hydrogenation rate was greater (2-fold) for Ni/ZnO, which can tentatively link to the higher surface hydrogen (hydrogen chemisorption + TPD) on the supported system. This is in line with reported literature [402] that has identified hydrogen addition as the rate-determining step in -C≡C- → -C=C- hydrogenation over Ni-based catalysts. Moreover, Burch *et al.* [403] suggested that ZnO can act as a reservoir of hydrogen in the hydrogenation of CO in methanol steam reforming over Cu/ZnO. Considering the TPD results, the use of physical (or mechanical) mixtures of the support (ZnO) with the catalysts (α-NiZn and Ni/ZnO; Catalyst: ZnO mol ratio = 1:15) can provide an explicit assignment of spillover contribution to hydrogenation performance. The inclusion of ZnO led to a (2-fold) increase specific hydrogenation rate, which can be taken as confirmation of the participation of spillover hydrogen in hydrogenation over Ni/ZnO. Both catalysts bearing the same (alpha-phase) NiZn alloy phase display the same product distribution, a result that suggests that 3BE selectivity is controlled by the NiZn molar ratio in the alloy. Since catalytic activity is evaluated as specific rate (*TOF*), the differences must be linked to variations in surface hydrogen content (hydrogen chemisorption and spillover hydrogen).

6.4 Conclusions

Bulk and (ZnO) supported Ni and NiZn alloy catalysts with different Zn content and crystallographic phase (*i.e.* α-NiZn (NiZn = 90:10), β-NiZn (50:50) and δ-NiZn (10:90)) exhibit quite distinct behaviour in the continuous gas phase hydrogenation of 3BY. Powder XRD analysis confirmed alloy formation where incorporation of Zn served to suppress H_2 chemisorption. While double bond migration (to BONE) was fully avoided over all the catalysts, we observed lower H_2 uptake and specific activity (up to a 70-fold) but increased alkenol selectivity (up to 98%) over the bulk alloys with increasing Zn content. We can associate the differences in the observed catalytic performance to variations in reactant adsorption/activation over the different Ni-based catalysts. α-NiZn delivered the highest alkenol activity/selectivity. The synthesis of a ZnO supported α-NiZn catalyst served to maintain the same alkenol selectivity but increase activity (by a factor of 2), which is linked to the participation of spillover hydrogen (based on TPD analyses). Our results demonstrate the potential of NiZn alloys for the continuous production of valuable alkenols.

Chapter 7:

Pd-Promoted Selective Gas Phase Hydrogenation of Alkynes over γ-Mo_2N

Standard heterogeneous catalysts based on supported transition metals suffer from the complexity and high cost associated with their synthesis. Bulk molybdenum nitrides can uptake hydrogen and exhibit catalytic properties similar to those of noble metals, although its application in selective hydrogenation has been considered to a limited extent. In this chapter, we investigate the application of gamma-phase Mo nitride to promote the selective gas phase hydrogenation of acetylene, phenylacetylene and MBY. We also evaluate the effect of Pd, introduced in trace amounts, as a promoter.

7.1 Introduction

Molybdenum nitrides exhibit catalytic properties similar to those of noble metals (*e.g.* Pd, Pt) [404]. A switch from classic heterogeneous catalysts based on supported transition metals to bulk materials offers clear advantages in terms of less complex and expensive production. Molybdenum nitrides have been employed successfully in several hydrogen-mediated reactions (*e.g.* hydrodesulfurisation of dibenzothiophene, hydrodeoxygenation of phenol and hydrodechlorination of 1,3-dichlorobenzene) [405]. However, their application in selective hydrogenation has been considered to a lesser extent. Hydrogenation over molybdenum nitrides is limited by hydrogen adsorption/activation [406] although they exhibit a different selectivity response compared with "conventional" Group VIII metal catalysts [407] that has yet untapped potential.

Molybdenum nitrides can adopt several Mo_xN_y phases, including cubic (γ-Mo_2N), tetragonal (β-Mo_2N) and hexagonal (δ-MoN) crystal structures [408]. The three allotropic forms have shown distinct catalytic properties, where the application of γ-Mo_2N in chemoselective hydrogenation show promise [409]. Synthesis by temperature programmed reduction-nitridation of MoO_3 with H_2+N_2 [59] generates γ-Mo_2N with SSA and surface N/Mo molar ratio in the range 45-132 m^2 g^{-1} [59] and 0.3-1.2 [404,410], respectively. Gamma-phase Mo nitride generation follows a topotactic pathway (*i.e.* maintenance of reactant morphology), with a stepwise (MoO_3 → H_xMoO_3 → MoO_yN_{1-y} → γ-Mo_2N) transformation that involves the formation of molybdenum bronzes (H_xMoO_3) and oxynitrides (MoO_yN_{1-y}) [411]. Changes in stabilisation of the

intermediates influences (SSA) and/or N/Mo, which impacts on reactant/catalyst surface interactions and catalytic performance.

Palladium is a well- known catalytic metal for hydrogenation with a high capacity to dissociate H_2 [174]. It is possible to deposit trace amounts of Pd on the MoO_3 precursor, which, with reduction/nitridation generates γ-Mo_2N [59]. Variations in surface hydrogen from palladium deposition can impact on the composition and structural properties of the H_xMoO_3 and/or MoO_yN_{1-y} [412] which, in turn, affects SSA and/or surface N/Mo [413]. Moreover, the increase in surface hydrogen from the incorporation of Pd with gamma-phase Mo nitride should result in enhanced catalytic performance. These are the premises on which this work has been based. Prior research has focused on the promoting effect of Mo_2N in chemoselective hydrogenation over transition metal supported catalysts. This is the case with Mo_2N-promoted Pt/SBA-15 in the hydrogenation of cinnamaldehyde [414] or the liquid phase reduction of *p*-nitrophenol over Mo_2N-Pd/ SBA-15 [415]. It is, however, worth flagging the work of Zaman *et al.*, who investigated the promoting effect of K [416] and alkali metals (Cs and Li) [417] on the hydrogenation of CO over γ-Mo_2N. In terms of hydrogenation, the focus of this work, gamma-phase Mo_2N has been employed to promote the transformation of crotonaldehyde [418], CO [416,417], acetylene [419] and aromatic nitrocompounds [420]. However, a search through the open literature has failed to unearth any reported study on hydrogenation of alkynols over Mo nitride.

Styrene and 2-methyl-3-buten-2ol (MBE) are commercially important chemicals in the manufacture of synthetic rubbers [421] and nutraceuticals (*e.g.* vitamins A and E) [422], while selective semi-hydrogenation of acetylene (to ethene) is key in the synthesis of polyethylene (49×10^6 tons $year^{-1}$ [423]). In this contribution, we provide the first reported application of Pd-promoted gas phase hydrogenation of acetylene, phenylacetylene and MBY over γ-Mo_2N.

7.2 Experimental

7.2.1 Materials and Analytical Methods

All the gases used in this work (Ar, N_2, H_2, O_2, He and C_2H_2) were of ultra- high purity (>99.7%, BOC). The (phenylacetylene (Aldrich, ≥ 99.9%) and MBY (Aldrich, 98%)) reactants and solvent (ethanol, Riedel-de Häen, ≥ 99.5%) were purchased and used without further purification. The composition of the reaction/product mixtures was determined using a Perkin-Elmer Auto System XL chromatograph equipped with a programmed split/split-less injector and a flame ionization detector, employing a Stabilwax (Cross-bond Carbowax-PEG, Restek, USA) or Carboxen 1010 (Supelco, Fluka Holding AG) capillary column. Data acquisition and manipulation were performed using the TotalChrom Workstation (Version 6.3.2 for Windows) chromatography data system. Reactant and product molar fractions (x_i) were obtained using detailed calibration plots (not shown) where the total mass balance in the mixture (based on GC analysis) was analysed for every extracted sample. The extent of hydrogenation can be represented by the reactant conversion where, taking acetylene ($X_{\text{Acetylene}}$) as representative reactant.

$$X_{\text{Acetylene}}(\%) = \frac{n_{\text{Acetylene, in}} - n_{\text{Acetylene, out}}}{n_{\text{Acetylene, in}}} \times 100 \qquad \textbf{(7.1)}$$

where "$n_{\text{Acetylene}}$" represents the number of moles of acetylene; subscripts “in” and “out” refer to the inlet and outlet streams, respectively. The selectivity of *e.g.* ethylene (S_{Ethylene}) as the target product in the transformation of acetylene, is given by:

$$S_{\text{Ethylene}}(\%) = \frac{n_{\text{Ethylene,out}}}{n_{\text{Acetylene,in}} - n_{\text{Acetylene,out}}} \times 100 \qquad \textbf{(7.2)}$$

while selectivity to green oil ($S_{\text{Green oil}}$) was calculated from the mass balance [359]

$$S_{\text{Green oil}}(\%) = 100 - (S_{\text{Ethylene}} + S_{\text{Ethane}}) \qquad \textbf{(7.3)}$$

Catalytic activity is quantified in terms of stationary state specific (per total surface area of the catalyst (SSA), m^2) alkyne consumption rate (R, μmol m^{-2} h^{-1}), following the procedure described elsewhere [59].

$$R\left(\mu\text{mol m}^{-2}\text{h}^{-1}\right)=\frac{F_{\text{in}}\times X_{\text{Alkyne}}}{\text{SSA}\times \text{m}\times 100} \qquad \textbf{(7.4)}$$

where "F_{in}" is the organic reactant (acetylene/phenylacetylene/MBY, μmol h^{-1}) inlet molar flow of and "m" the mass of catalyst (g). Repeated reactions with different samples from the same batch of catalyst delivered raw data reproducibility and a carbon mass balance within ±7%.

7.2.2 Catalyst Preparation

Bulk γ-Mo_2N was synthesised by temperature programmed reduction-nitridation following a method described in detail elsewhere [59]. Briefly, MoO_3 (130 mg, 99.9995%, Alfa Aesar) was placed in a horizontally mounted quartz reactor (13 mm *i.d.*), flushed with dry He 400 cm^3 min^{-1} (Bronkhorst mass flow controlled) for 4 h (*GHSV* = 24000 h^{-1}) and heated (at 5 K min^{-1}) to 623 K to ensure removal of physisorbed water [424]. A (400 cm^3 min^{-1}) flow of 10% v/v N_2/H_2 was then introduced and the temperature raised at 0.15 K min^{-1} to 933 K and maintained for 8 h. At the end of the temperature programmed treatment, the sample was quenched by switching to He (60 cm^3 min^{-1}), cooled (at *ca.* 50 K min^{-1}) to ambient temperature for 1 h with sample passivation in 1% v/v O_2/N_2 (100 cm^3 min^{-1}) for 2 h to avoid autothermal oxidation upon contact with air [404]. Two Pd/γ-Mo_2N with a nominal metal content of 0.1% wt. were prepared by deposition of monodispersed Pd nanoparticles on γ-Mo_2N (denoted γ-Mo_2N-Pd(A) in this work) and MoO_3 (γ-Mo_2N-Pd(B)), where the latter underwent a reduction-nitridation process as above. An aqueous solution of $PdCl_2$ (0.015 M) (Fluka, >99%) and $Na_2MoO_4{\cdot}H_2O$ (Fluka, >99%) (Pd/Mo mol ratio = 1.2) was heated at 368 K under continuous stirring (500 rpm) until the solution underwent a colour change (from light to dark brown), indicative of Pd-polyoxometallate formation [164]. An aliquot of aqueous Pd-polyoxometallate (50 cm^3, 1×10^{-4} M) and (100 mg) MoO_3 (γ–Mo_2N-Pd(B)) or γ-Mo_2N (γ–Mo_2N-Pd(A)) was mixed and contacted (at ambient temperature) with a continuous flow of H_2 (100 cm^3 min^{-1}) for 30 min and kept for *ca.* 2 h resulting in the formation of uniform Pd nanocrystals stabilised by molybdate anions ≤ 1.5 nm [164] and deposition (*via* adsorption) on MoO_3/γ-Mo_2N [164], the slurry was then filtered and dried

in air at ambient temperature. The samples were sieved (ATM fine test sieves) into a batch of 75 μm average diameter. Prior to use in catalysis, the samples were activated in 60 cm^3 min^{-1} H_2 at 5 K min^{-1} to 700 K and maintained at the final isothermal hold for 1h.

7.2.3 Catalyst Characterisation

The Pd loading was measured by AAS using a Shimadzu AA-6650 spectrometer with an air-acetylene flame from the diluted extract in aqua regia (25% v/v HNO_3/HCl). Temperature programmed reduction (TPR), total SSA and temperature programmed desorption (TPD) were determined using a commercial CHEM-BET 3000 (Quantachrome) unit equipped with a thermal conductivity detector (TCD) with data acquisition/manipulation software (TPR WinTM, Version 1.0a). TPR measurements were conducted by heating the samples in 17 cm^3 min^{-1} 5% v/v H_2/N_2 at 5 K min^{-1} to 700 K, where the effluent gas passed through a liquid N_2 trap. The reduced samples were maintained at the final temperature for 1 h. The samples were then swept with 52 cm^3 min^{-1} N_2 for 1 h, to remove physisorbed hydrogen, and cooled to room temperature.

Hydrogen TPD was conducted in a N_2 flow (52 cm^3 min^{-1}) at 50 K min^{-1} to 900 K with a final isothermal hold until the signal returned to the baseline. Total SSA was obtained using the standard single point BET method. SSA values were recorded with a 50% v/v N_2/He flow using pure N_2 as internal standard. At least two cycles of N_2 adsorption–desorption in the flow mode were used to determine total surface area. SSA, TPR and TPD values were reproducible to ±5% and the values quoted in this paper are the mean.

Powder X-ray diffractograms (XRD) were recorded on a Bruker/Siemens D500 incident X-ray diffractometer using Cu Kα radiation. The samples were scanned at a rate of 0.02º $step^{-1}$ over the range $15º \leq 2\theta \leq 85º$ (scan time = 5 s $step^{-1}$). Diffractograms were identified using the JCPDS-ICDD reference standard for γ-Mo_2N (25-1366) and Pd (046-1043). Surface N/Mo mol ratio and Pd content was extracted from XPS measurements, performed on a Scientia ESCA 300 spectrometer using a monochromatic Al anode (K_α 1486.6 eV, 10 kV, 20 mA). The source power was maintained at 3900 W and the emitted photoelectrons were sampled from an area of 13 mm^2; the photoelectron take-off angle was normal emission (0°). The analyser pass energy was 150 eV for full range survey (0–1100 eV) and high-resolution spectra (over the Mo $3d_{3/2}$ and Mo $3d_{5/2}$ BE range, 227-239 eV). The adventitious C 1s peak was calibrated at 284.5 eV and used as internal standard to compensate for any charging effects. Spectral curve fitting and quantification

employed the CasaXPS software, using relative sensitivity factors provided by Kratos. Analysis by scanning electron microscopy (SEM) was conducted using a Philips FEI XL30-FEG equipped with an Everhart-Thornley secondary-electron (SE) detector operated at an accelerating voltage of 10-15 kV and using a NORAN System SIX version 1.6 for data acquisition/manipulation. Before analysis, the samples underwent hydrocarbon decontamination using a plasma cleaner (EVACTRON). STEM probe corrected measurements were conducted using a JEOL ARM 200CF unit equipped with an (EDX) detector operated at an accelerating voltage of 200 kV. The scanned images were collected using either Gatan 806 High Angle Annular Dark Field, Gatan 805 Annular Dark Field/Bright field or JEOL ADF1detectors under the control of a Gatan Digi-Scan II, employing Gatan Digital Micro-graph software (version 2.31) for data acquisition/manipulation. Samples were prepared for analysis by dry deposition on a holey carbon/Cu grid (300 Mesh).

7.2.4 Alkyne Hydrogenation

Reactions were carried out at T = 453 K and P = 1 atm, in situ immediately after activation (in flowing H_2 at 5 K min^{-1} to 700 K) under operating conditions that ensured negligible heat/mass transport limitations. A layer of borosilicate glass beads served as preheating/mixing zone, ensuring that the reactants reached reaction temperature before contacting the catalyst. Isothermal conditions (±1 K) were maintained by mixing the catalyst with ground glass (75 μm). Reaction temperature was continuously monitored by a thermocouple inserted in a thermowell within the catalyst bed. The hydrogenation of acetylene was conducted in a (*i.d.* = 12 mm) jacketed tubular reactor equipped with a Juvo thermostat (Type 500, K. K. Juchheim Laborgeräte GmbH, Bernkastel-Kues, Germany). The gas reactant (200 - 1000 cm^3 min^{-1}, Brooks mass flow controlled) mixture (1%/20%/79% v/v C_2H_2/H_2/Ar) was introduced and samples taken for analysis every 10 min on-stream using an extraction valve. The gas phase hydrogenation of phenylacetylene and MBY were carried out in a fixed bed vertical glass reactor (*i.d.* = 13 mm). The organic reactant was delivered to the reactor at a fixed calibrated flow rate range (2×10^{-2} cm^3 min^{-1} (phenylacetylene) and 1.2×10^{-2} cm^3 min^{-1} (MBY)) *via* a glass/teflon air-tight syringe and teflon line using a microprocessor-controlled infusion pump (Model 100 kd Scientific). A co-current flow of the organic and ultra-pure H_2 (<1% v/v organic in H_2) was maintained at $GHSV$ = 4200 h^{-1} and the ratio of catalyst mass to inlet organic molar feed rate (W/F_{in}) in the range 16-42 g mol^{-1} h. In a series of blank tests, passage of each

reactant (acetylene, phenylacetylene or MBY) in a stream of H_2 through the empty reactor did not result in any detectable conversion**.**

7.3 Results and Discussions

7.3.1 Catalyst Characterisation

The XRD diffractogram patterns for the γ-Mo_2N **(I)**, γ-Mo_2N-Pd(B) **(II)** and γ-Mo_2N-Pd(A) **(III)** systems are shown in **Figure 7.1.** The three catalysts present diffraction peaks over the range 2θ= 15-85^0 at 37.4^0, 43.5^0, 63.1^0, 75.7^0 and 79.8^0 corresponding to the (111), (200), (220), (311) and (222) planes of (cubic) γ-phase Mo_2N (JCPDS-ICDD card number 25-1366)).

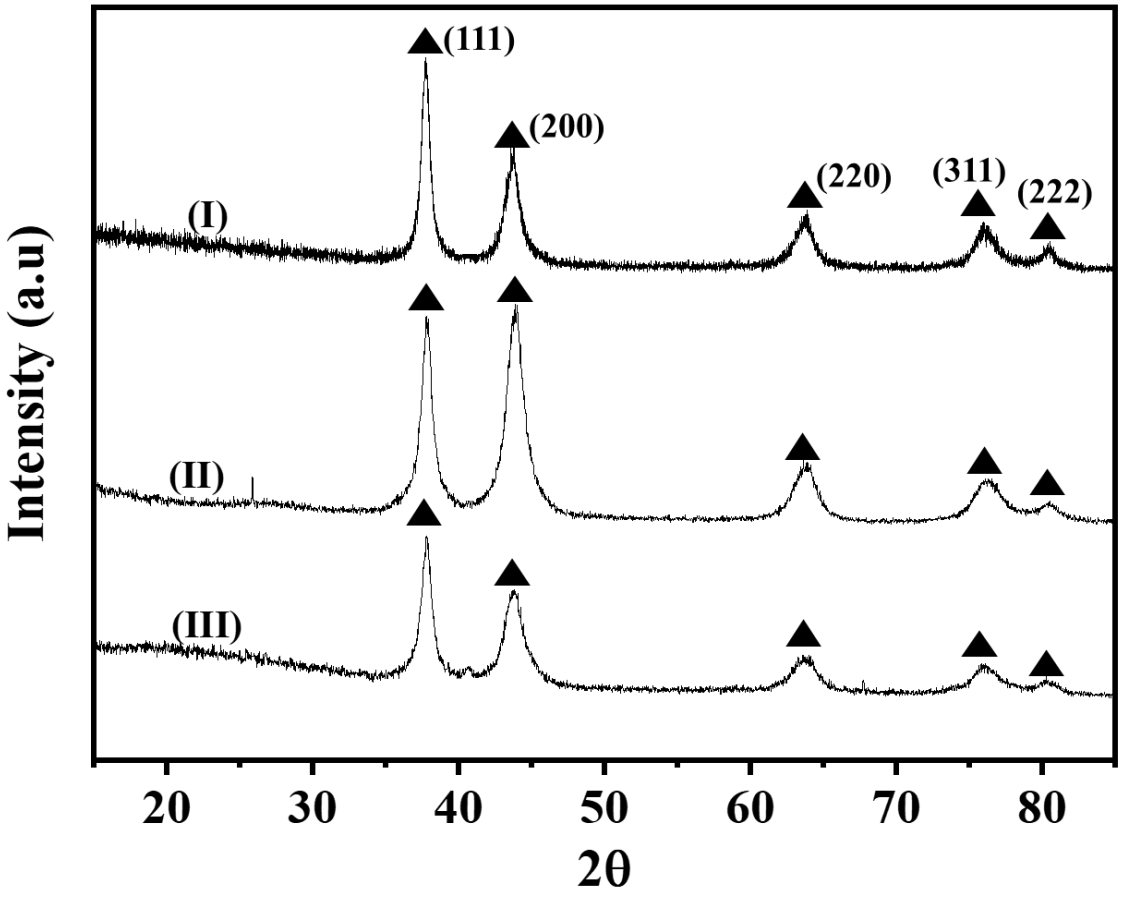

Figure 7.1: XRD patterns with crystallographic plane characteristic of each peak associated with (**I**) γ-Mo_2N, (**II**) γ-Mo_2N-Pd(B) and (**III**) γ-Mo_2N-Pd(A). XRD peak assignments based on JCPDS-ICDD reference data: (▲) γ–Mo_2N (Card No. 25-1366).

There were no reflections characteristic of bulk oxides (*e.g.* MoO_3, MoO_2) in the reduced-nitridised samples. This is consistent with the complete transformation of the MoO_3 precursor to γ-Mo_2N where the passivation step results in the generation of a surface (*vs.* bulk) protective oxide layer. It should be noted, that there were no detectable signals due to palladium in the XRD of γ-Mo_2N-Pd(B) **(II)** or γ-Mo_2N-Pd(A) **(III)**, which can be attributed to the low metal content and/or the presence of small (≤2 nm) Pd nanoparticles [425].

A low Pd content (Pd/Mo ≤ 0.0010) in γ-Mo_2N-Pd(B) **(a)** and γ-Mo_2N-Pd(A) **(b)** was also confirmed by STEM-EDX surface analysis (**Figure 7.2(I-II)**) and XPS measurements, albeit it was appreciable (2-fold) greater for γ-Mo_2N-Pd(A).

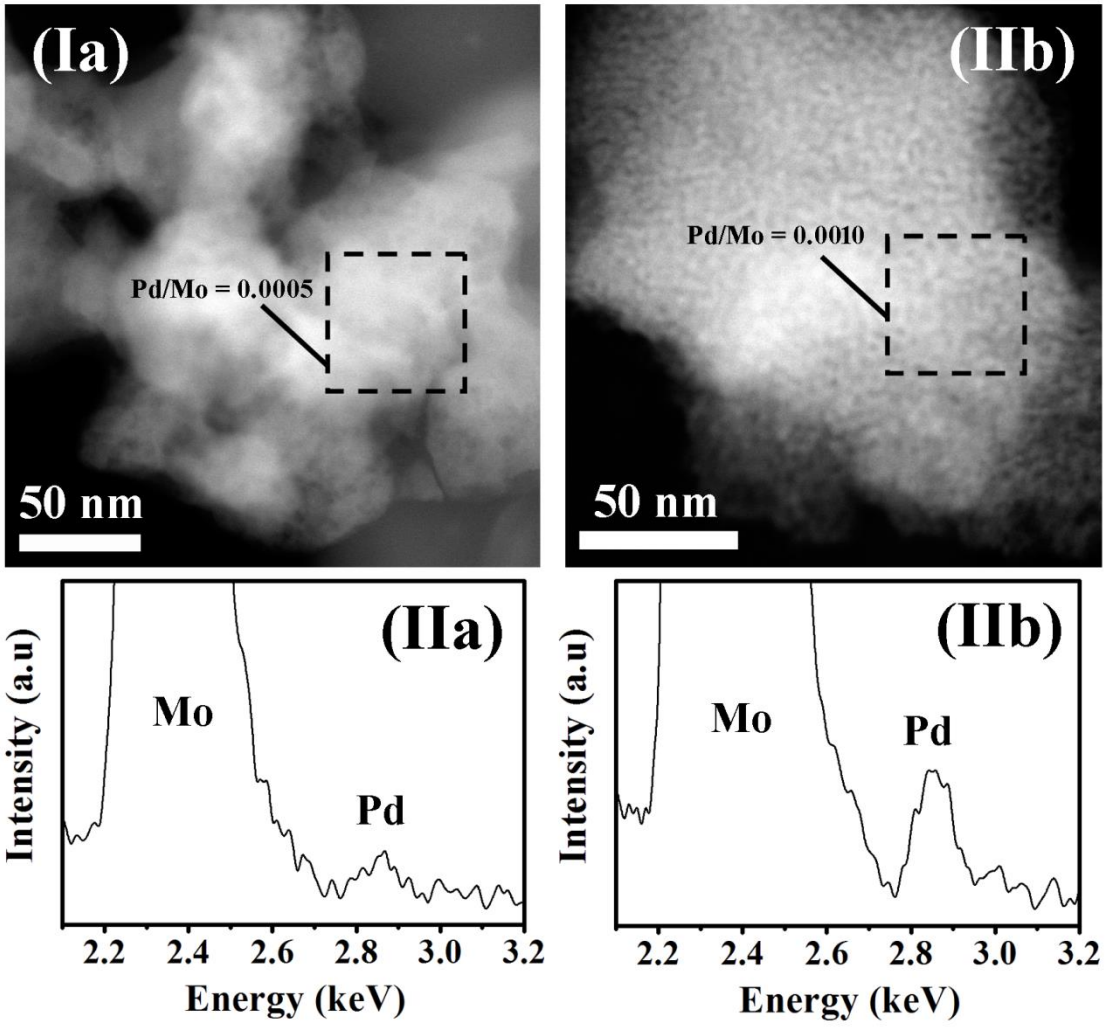

Figure 7.2: Representative (**I**) STEM images with EDX analysis and (**II**) spectra over framed areas for (**a**) γ–Mo_2N-Pd(B) and (**b**) γ–Mo_2N-Pd(A).

The migration of suboxide species on top of metal nanoparticles, termed "encapsulation", is a documented feature of Pd on oxide supports (*e.g.* Fe_2O_3) during H_2 thermal treatment at $T \geq 523$ K [426]. The low surface Pd/Mo content in γ-Mo_2N-Pd(B) suggests that this effect extends to Pd/MoO_3. The three gamma-phase Mo nitrides exhibit a similar crystallite size (9.9 ± 0.9 nm, **Table 7.1**) that is consistent with reported values (7.7-14.2 nm) [427]. The SSA recorded for the three nitrides (**Table 7.1**) is similar (85 $m^2\ g^{-1}$) to that recorded by McKay *et al.* [428] for γ-Mo_2N prepared by thermal treatment, where the following sequence is established:γ-Mo_2N-Pd ~ γ- Mo_2N(A)<γ-Mo_2N-Pd(B).

Table 7.1: Physicochemical properties of γ–Mo_2N and (0.1 %wt.) Pd-promoted (introduced before (B) and after (A) nitride preparation) γ–Mo_2N.

Catalysts	XRD analysis		SSA ($m^2\ g^{-1}$)	H_2 uptake (μmol g^{-1})	TPD (μmol m^{-2})	Surface N/Mo[a]
	d_{hkl} (nm)	$I_{(111)}/I_{(200)}$				
γ-Mo_2N	10.8	1.5	63	498	11	0.7
γ-Mo_2N-Pd(B)	9.0	0.9	90	619	78	0.3
γ-Mo_2N-Pd(A)	10.2	1.6	60	1384	98 (33[a]/65[b])	0.4

[a]from XPS measurements; [b]hydrogen released associated with peak at T_{max} *ca.* 700 K; [c] hydrogen desorption associated with peak at T_{max} *ca.* 800 K.

This sequence matches that of decreasing the intensity ratio of the (111)/(200) XRD peaks ($I_{(111)}/I_{(200)}$, **Table 7.1**) and there is evidence in the literature that variations in textural features result in changes in SSA and the $I_{(111)}/I_{(200)}$ [58]. Hydrogen molybdenum bronze (H_xMoO_3), is generated during the formation of γ-Mo_2N by incorporation of hydrogen in MoO_6 octahedra [429,430]. Dissociative chemisorption of hydrogen on palladium increases surface hydrogen content [174]. This can affect the structure/composition of the H_xMoO_3, which must influence the textural properties of the nitride. Such premise is consistent with the work of Sakagami *et al.* [431], who concluded a simultaneous increase in the amount of hydrogen in the molybdenum bronze ($H_{0.8}MoO_3$ → $H_{1.6}MoO_3$) and SSA (from *ca.* 75 to 180 $m^2\ g^{-1}$) for MoO_3 reduced at 773 K. Zhang *et al.* [432] observed, during the synthesis of γ-Mo_2N by heating treatment of MoO_3 with NH_3+N_2, that an increase in NH_3:N_2 *GHSV* (14000 → 88000 h^{-1}) was accompanied by lower $I_{(111)}/I_{(200)}$ (1.4 → 0.4) ratios and an increase in surface area (13 → 140 $m^2\ g^{-1}$).Representative SEM images for γ-Mo_2N **(I)**, γ-Mo_2N-Pd(B) **(II)** and γ-Mo_2N-Pd(A)

(III) are presented in **Figure 7.3**, where it can be seen that the three nitrides are comprised of predominantly large platelets (*ca.* 12 × 11 × 0.5 μm) with secondary small rod-like crystallites (*ca.* 2.5 × 1.5 × 0.2 μm). The similar structure of the γ-Mo_2N samples and the starting MoO_3 (see *inset* to **Figure 7.3(I)**) confirms the topotactic molybdenum trioxide transformation [433]**.**

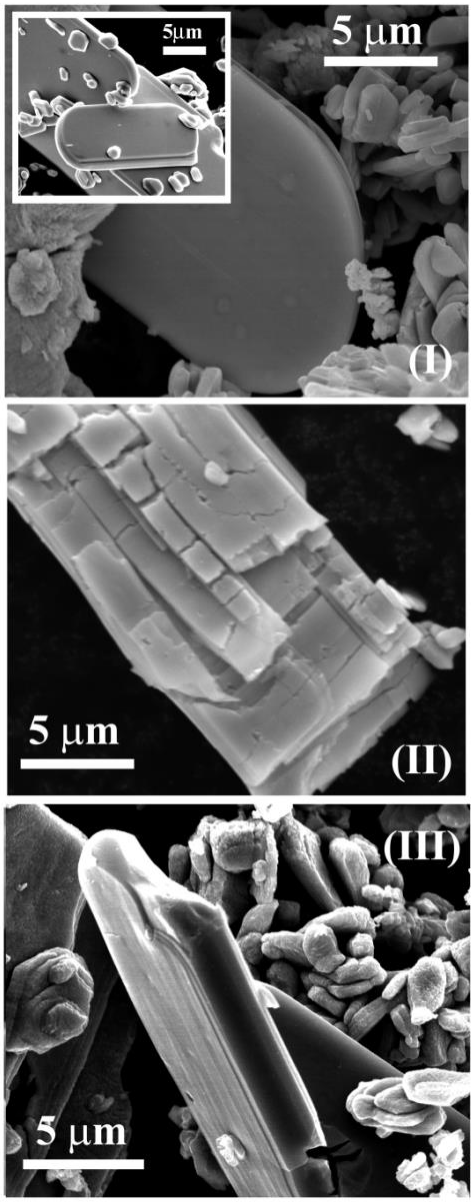

Figure 7.3: Representative SEM micrographs for (**I**) γ–Mo_2N, (**II**) γ–Mo_2N-Pd(B) and (**III**) γ–Mo_2NPd(A). *Note*: *Inset* in (**I**) shows representative SEM image for MoO_3 precursor.

The surface morphology of γ-Mo_2N-Pd(B) is different and the platelet show greater surface irregularities (cracks), which contribute to an increase in the surface area. This can be attributed to the presence of Pd that serves to elevate surface hydrogen, resulting in a greater and faster H_2O release during the formation of the oxynitride intermediate [59].

The TPR profiles (up to 700 K) generated for γ-Mo_2N **(I)**, γ-Mo_2N-Pd(B) **(II)** and γ-Mo_2N-Pd(A) **(III)** are shown in **Figure 7.4**. The TPR response for γ-Mo_2N is characterised by two (hydrogen consumption) positive signals, a principal peak at 591 K with a shoulder at 700 K.

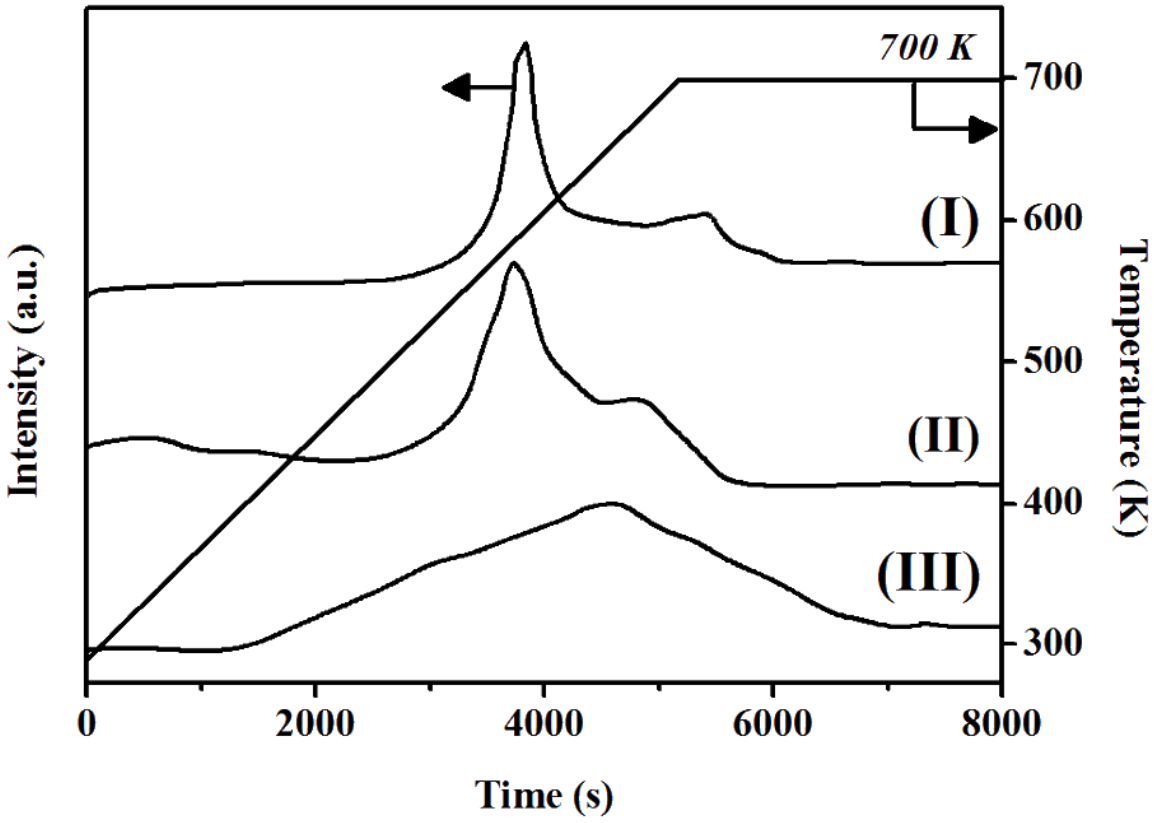

Figure 7.4: TPR profiles for (**I**) γ-Mo_2N, (**II**) γ-Mo_2N-Pd(B) and (**III**) γ-Mo_2N-Pd(A).

The hydrogen consumed during the TPR analysis can be linked to (i) removal of the passivating layer, (ii) reaction with N and the occurrence of nitrogen vacancies and/or (iii) surface adsorption of hydrogen, which can migrate to sub-layers. Indeed, Ozkan *et al.* [434] working with passivated γ-Mo_2N, reported the appearance of two peaks at very similar temperatures (*ca.* 403-573 K and 603-695 *K*) which they ascribed to the removal of oxygen and nitrogen, respectively [434]. The introduction of palladium resulted in a

displacement in the reduction temperature to a lower value (by *ca.* 15 K) for γ-Mo_2N-Pd(B). An equivalent effect has been recorded for reducible oxides (*e.g.* CeO_2 [91], TiO_2 [435] *post*-incorporation of Pd with a decrease in the temperature requirements (up to 225 K) for the partial reduction of the carrier. This can be linked to a contribution from reactive hydrogen dissociated on palladium [174], which spills over onto the γ-Mo_2N and participates on its superficial reduction. The TPR response for γ-Mo_2N-Pd(A) was quite distinct, with a broad single peak with a maximum at *ca. T* = 648 K which can be linked to the concomitant reaction with N and O.

XPS measurements can provide crucial information on surface nitrogen content [427] where N vacancies have been identified as active sites in hydrogenation over Mo nitrides [60]. The surface N/Mo extracted from XPS analysis (**Table 7.1**) is comparable with values (0.3-1.2) [404,410] recorded for γ-Mo_2N prepared through thermal treatment in N_2+H_2.. We observed decreasing N/Mo for γ-Mo_2N > γ-Mo_2N-Pd(A) > γ-Mo_2N-Pd(B). A decrease in N/Mo as a result of nitrogen removal is accompanied by the formation of surface cracks and craters, which can contribute to elevate SSA [427]. The lowest N/Mo content for γ-Mo_2N-Pd(B) is consistent with SEM (**Figure 7.3**) and SSA measurements (**Table 7.1**).

Hydrogen TPD generated the profiles for **(I)** γ–Mo_2N**, (II)** γ–Mo_2N-Pd(B) and **(III)** γ–Mo_2N-Pd(A) presented in **Figure 7.5**. The three samples exhibit a H_2 desorption over a broad temperature interval with a main peak at T_{max} *ca*. 800 K. Hydrogen released at *T* > 500 K have been attributed to loss of H_2 from bulk (*vs*. surface) γ-Mo_2N [436]. The diffusion hydrogen from the surface to γ-Mo_2N sub-layers has been suggested, which results in strong interactions that necessitate high temperatures for release [437]. The TPD profile for γ–Mo_2N-Pd(A) exhibits a secondary peak at *ca*. 700 K, which coincide with that reported elsewhere (680-725 K) for hydrogen desorption from Pd [438].

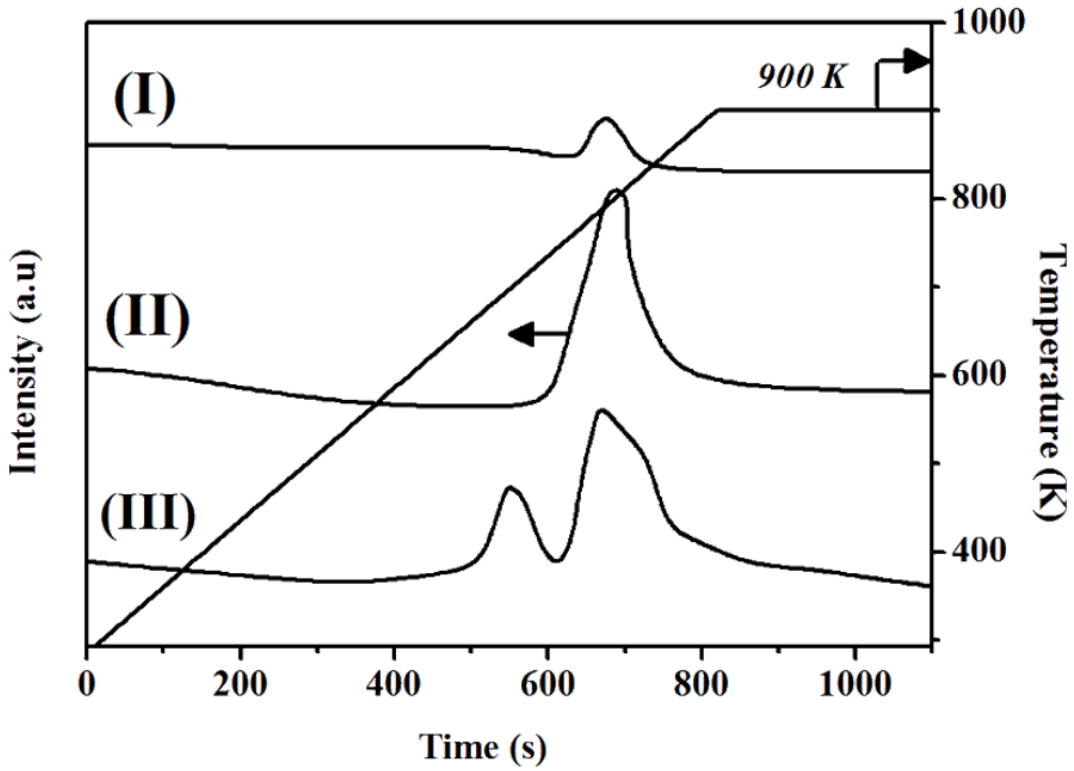

Figure 7.5: TPD profiles for **(I)** γ-Mo_2N, **(II)** γ-Mo_2N-Pd(B) and **(III)** γ-Mo_2N-Pd(A**)**

The absence of low temperature hydrogen desorption peak for γ–Mo_2N-Pd(B) suggests Pd encapsulation, in agreement with STEM-EDX measurements. Taking the three nitrides, the specific (per SSA) volume of H_2 desorbed (**Table 7.1**) was up to *ca.* 650 times greater than hydrogen chemisorption values recorded for γ-Mo_2N with similar SSA [420], and must result from hydrogen uptake during TPR. Taking the H_2 desorbed from the Mo nitride (*i.e.* associated with the peak at T_{max} *ca.* 800 K), the specific volume of hydrogen released decreased in the following order: γ–Mo_2N-Pd(B) (78 μmol m^{-2}) > γ–Mo_2N-Pd(A) (65 μmol m^{-2}) > γ–Mo_2N (11 μmol m^{-2}). This sequence mimics that of increasing N/Mo and there is evidence in the literature that nitrogen vacancies in Mo nitrides can accommodate hydrogen [439]. The higher concentration of nitrogen vacancies (*i.e.* lower N/Mo) can explain the greater hydrogen desorption from the Mo nitrides.

7.3.2 Catalytic Response

Reaction selectivity is crucial in acetylene **(I)**, phenylacetylene **(II)** and MBY **(III)** hydrogenation, where several intermediates and by-products can be generated [9], as shown in **Figure 7.6.** Ethylene, styrene and MBE were the main products in the hydrogenation of acetylene, phenylacetylene and MBY, respectively, over the three Mo nitrides (S = 82-93%) with ethane, green oil, ethylbenzene and MBA formed as secondary products (**Table 7.1**).

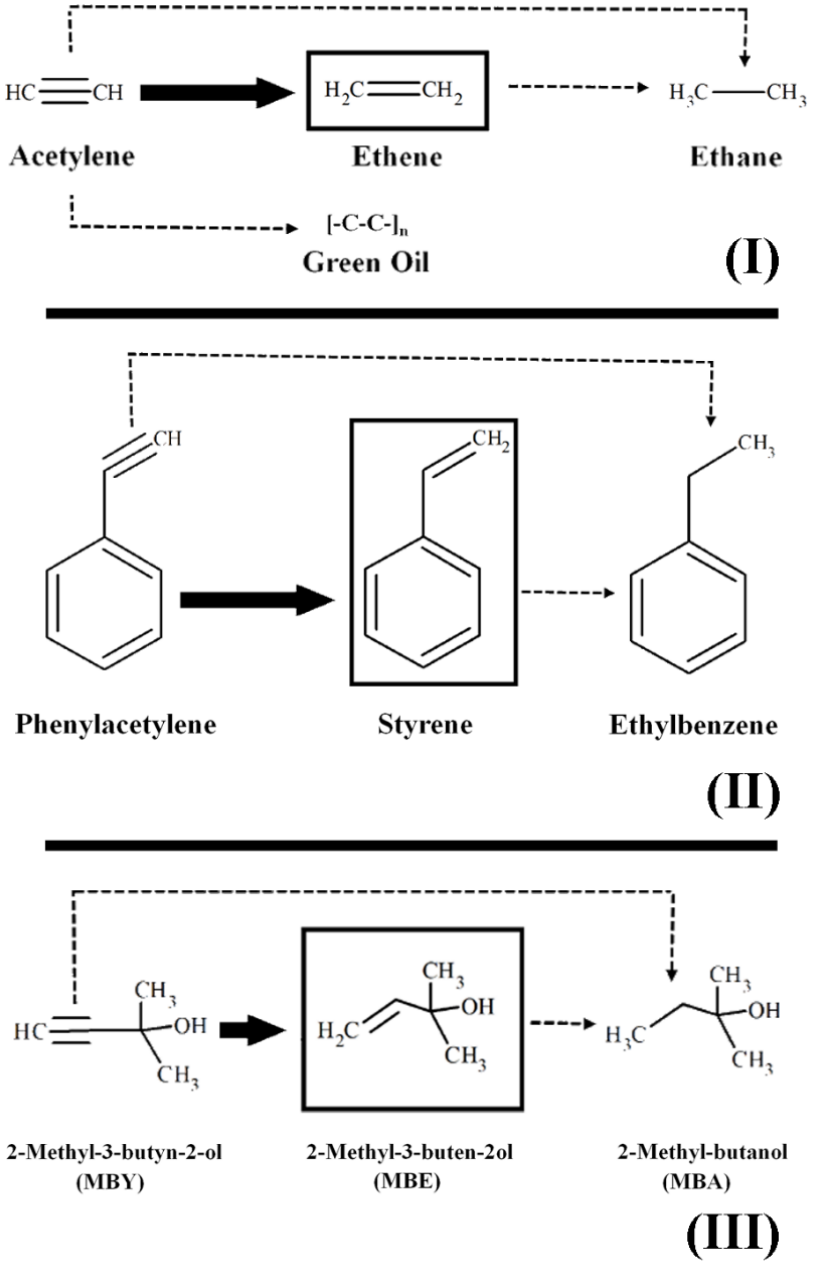

Figure 7.6: Reaction scheme illustrating the pathways for hydrogenation of (**I**) acetylene, (**II**) phenylacetylene and (**III**) MBY. *Note*: solid arrow denotes pathway to target (framed) product from partial hydrogenation while dashed arrows indicate routes to undesired by-products from -C≡C- bond full-hydrogenation and/or oligomerisation.

It is important to stress that the alkene selectivity achieve in this work is equivalent to that reported for reactions at industrial scale over Pd-based catalysts [440], which demonstrates that Mo nitrides could represent a suitable replacement. Hao and *co-workers* [419] reported high selectivity to ethylene (40-85%) in the selective hydrogenation of acetylene over γ-Mo_2N but we could not find any report in the open literature for the conversion of alkynols using Mo nitrides. Hydrogenation of -C≡C- over γ–Mo_2N, follows the Horiuti-Polanyi mechanism, *i.e.* sequential -C≡C- → -C=C- → -C-C- conversion [60]. The high selectivity to the target alkene/alkenol can be linked to the surface displacement of the chemisorbed partial hydrogenated product by the alkyne reactant as a result of the differences in adsorption energy on γ-Mo_2N (-51.6 for -C≡C- *vs* -15.4 Kcal mol^{-1} -C=C-) [60]. Product distribution was equivalent in the conversion of three alkynes over all the Mo nitrides ($S_{Alkene/Alkenol}$ = 87 ± 5%, $S_{Alkane/Alkanol}$ = 11 ± 4%, $S_{Green\ oil}$ = 7 ± 4%), albeit formation of green oil in small quantities was only promoted in the conversion of acetylene. Green oil formation occurs *via* alkene+alknyne condensation and is inhibited at increasing surface H_2 coverage [245], *i.e.* high acetylene surface concentration limits H_2 coverage and inhibits hydrogenation. The generation of green oil results in catalyst deactivation due to occlusion of active sites and it is a common feature of processes at both industrial and laboratory scale with reported selectivities in the range 15-97% [441–443]. We recorded a largely minimised green oil formation over the three Mo nitrides in this work (3-11 %), a result that can be tentatively linked to the high hydrogen to alkyne mol ratio (H_2:C≡C-≥ 20).

Table 7.2: Reaction rate (R) with product selectivities (S_i) at the same conversion ($X_{Reactant}$ ~ 20%) for the hydrogenation of acetylene, phenyl-acetylene and MBY over γ–Mo_2N and (0.1% wt.) Pd-promoted (introduced before (B) and after (A) nitride preparation) γ–Mo_2N. (*Reaction conditions*: P = 1 atm, T = 453K).

Catalysts	**Reactants**					
	Acetylene		**Phenylacetylene**		**MBY**	
	R **(μmol m^{-2} h^{-1})**	**Products (% S_i)**	***R*** **(μmol m^{-2} h^{-1})**	**Products (% S_i)**	***R*** **(μmol m^{-2} h^{-1})**	**Products (% S_i)**
γ–Mo_2N	72	C_2H_4 (90) Green oil (3) C_2H_6 (7)	0.4	Styrene (93) Ethylbenzene (7)	1.3	MBE (92) MBA (8)
γ–Mo_2N-Pd(B)	236	C_2H_4 (82) Green oil (11) C_2H_6 (7)	0.9	Styrene (90) Ethylbenzene (10)	10.4	MBE (87) MBA (13)
γ–Mo_2N-Pd(A)	380	C_2H_4 (83) Green oil (10) C_2H_6 (7)	1.3	Styrene (88) Ethylbenzene (12)	14.2	MBE (86) MBA (14)

In terms of activity, the extracted specific (per SSA) reaction rates are given in **Table 7.2**. The promoting effect of Pd is probed by the significantly increase hydrogenation rate over γ–Mo_2N-Pd(B) and γ–Mo_2N-Pd(A) relative to γ–Mo_2N. Zaman and *co-workers* [416,417] observed increased activity in CO hydrogenation (to alcohol) for alkali metals (Li, K, and Na) promoted γ–Mo_2N but we demonstrate in here, for the first time, the Pd-promoting effect in -C≡C- bond hydrogenation over γ-Mo_2N. The greater rate recorded in this work can be attributed to elevated surface available hydrogen for the Pd-promoted samples (**Table 7.1**), *i.e.* the enhanced surface hydrogen that results from incorporation of Pd with γ-phase Mo_2N was accompanied by an increased hydrogenation rate. Moreover, reaction rate over the three nitride catalysts decreased in the order: $R_{\text{Acetylene}} > R_{\text{MBY}} > R_{\text{Phenylacetylene}}$, a result that can be tentatively linked to (i) steric constrains due to the aromatic ring in phenylacetylene and (ii) the deactivating effect of (electron withdrawing) -OH in MBY, which is consistent with an electrophilic mechanism, as demonstrated previously [112]. S. Shimazu *et al.* [444] observed that hydrogenation of acetylene proceed at a (36-fold) higher rate than that of phenylacetylene for reaction over Pd(II) complexes and ascribed this rate inhibition to steric hindrance in the case of the latter. Moreover, Terasawa *et al.* [111] investigated the hydrogenation of functionalised alkynes over Pd catalysts and observed lower activity in the transformation of reactants with electron withdrawing (*e.g.* -Cl, -OH) substituents.

7.4 Conclusions

Thermal treatment of MoO_3 in N_2+H_2 generated γ-Mo_2N with high SSA (60 m^2 g^{-1}). Incorporation of Pd before (on MoO_3; denoted γ–Mo_2N-Pd(B)) and after (γ-Mo_2N; γ–Mo_2N-Pd(A)) reduction/nitridation generated an equivalent particle size (9.9 ± 0.9 nm) but elevated specific (per SSA) surface hydrogen (based on TPD measurements) and lower N/Mo (from XPS), with higher specific hydrogenation rate in the conversion of acetylene, phenylacetylene and MBY. TPD analysis suggests Pd encapsulation for γ–Mo_2N-Pd (B) where STEM-EDX mapping has establish a low Pd/Mo surface content. The target alkene/alkenol was the main product (*S* = 82-93%) in the hydrogenation of acetylene, phenylacetylene and MBY over the three Mo nitrides with green oil generation in trace amounts (≤11%) in the conversion of acetylene. Increased -C≡C- bond hydrogenation rate in the transformation of acetylene > MBY > phenylacetylene is associated to steric constrains and the deactivating effect of the -OH functional group. Our results demonstrate the promoting effect of Pd for selective hydrogenation of alkyne/alkynols over Mo nitrides.

Chapter 8:

Summary and Future Work

The goal of this PhD was to demonstrate the feasibility of an alternative gas phase catalytic process for the selective hydrogenation of alkynols to alkenols. The results presented demonstrate the viability of tuning the electronic and structural properties of Pd and Ni through interactions with the support and/or incorporation of a second metal to control catalytic performance. A number of strategies have been suggested to enhance alkenol production. The work has established the potential of bimetallic Pd-Ni, Pd-Zn, Ni-Zn and bulk γ-Mo_2N catalysts for the selective production of valuable alkenols in a continuous catalytic system operated under mild reaction conditions.

8.1 General conclusions.

The results in this thesis have established the suitability of selective gas phase -C≡C- bond partial hydrogenation of C4 primary, secondary and tertiary alkynols over oxide/carbonaceous supported Pd, Pd-Zn, Ni, Pd-Ni, Ni-Zn and bulk γ-Mo_2N catalysts. The catalytic performance on gas phase hydrogenation using Pd-based bimetallic catalysts leads into alkenol selectivities better than the ones given for industrial Lindlar catalysts. The use of alternative transition metal catalysts such as Ni-Zn and bulk β-Mo_2N, shows promising -C=C- selectivities values albeit further work must be done in optimizing the alkenol yield production in order to be considered as feasible Pd-based catalyst substitutes.

In **chapter 2,** it has been proved that the polarity of the -C≡C- bond is affected by the position of the -OH group functionality and the number of (electron-donating) -CH_3 groups in primary (3BYOL), secondary (3BY) and tertiary (MBY) C4 alkynols which, in turn, determines the activity/selectivity response in the gas phase production of alkenols over Pd/Al_2O_3. The catalytic response shows a catalytic activity increase with increasing -C≡C- electron density, consistent with an electrophilic mechanism. A wide product distribution is observed on three alkynols due to over-hydrogenation and double bond migration side of reaction, attributed to Pd ensembles and surface defects.

In **chapter 3,** Pd/ZnO has been proven to be more selective and less active than Pd/Al_2O_3, under all activation temperature ranges, and is ascribed to β-PdZn alloy and $PdZnO_{1-x}$ surface phases formation, that limits the hydrogen uptake capacity of the catalyst. An increase of the activation temperature enhances a β-PdZn alloy surface

enrichment on Pd/ZnO whereas a Pd particle size growth due to particle sintering is experienced on Pd/Al_2O_3, resulting in an MBE selectivity improvement due to the dilution of $Pd^{\delta-}$ ensembles and surface defects respectively. The quality of Pd/ZnO catalytic performance has been shown by its comparison with industrial Lindlar catalysts, delivering greater alkenol selectivity. However, the role of surface β-PdZn and $PdZnO_{1-x}$ species on catalytic hydrogenation are still to be determined.

In chapter 4, the PdZn alloy formation was proven to be controlled by deposition of (Pd: Zn) colloids with different mol ratio over Al_2O_3 support. A decrease in (Pd: Zn) mol ratio results in a greater PdZn alloy formation (measured by XPS) and a higher alkenol enhancement. Under similar PdZn (%) alloy mol content, bimetallic $Pd-Zn/Al_2O_3$ (30:70) display a 2-fold time rate increase with similar alkenol selectivities than Pd/ZnO due to metal encapsulation circumvention. The higher H_2 spillover capacity of Al_2O_3 support compared to ZnO (measured by H_2-TPD) also accounted for the higher activity response. Alkynol gas phase hydrogenation over 1-10 (H_2: Alkynol) molar feed range, has shown a first order dependence in H_2 coverage. A competitive character does not exist between reactants. We demonstrate that alkynol consumption rate correlates with surface hydrogen (H_2 chemisorption/TPD) where the nature of the support (carbon, Al_2O_3, MgO, CeO_2) affects the electronic properties of the Pd phase (from XPS) but does not significantly influence catalytic performance.

In chapter 5, The undesired formation of BONE (*via* 3BE isomerisation) in the hydrogenation of 3-butyn-2-ol is fully circumvented over Ni/Al_2O_3 albeit low conversions and extensive over-hydrogenation was recorded. A higher activity is recorded over Pd/Al_2O_3, but an appreciable ketone formation was recorded as double bond migration was promoted. The role of Ni as a co-metal has been proved successful for the selective hydrogenation process. The electronic modifications on Pd core shell induced by Ni incorporation on $Pd-Ni/Al_2O_3$ catalysts (from XPS and TPR results) results in a hydrogen uptake enhancement and in a concomitant improvement in the catalytic activity and 3-buten-2-ol selectivity.

In chapter 6, bulk and (ZnO) supported Ni and NiZn alloy catalysts with different Zn content and crystallographic phase (*i.e.* α-NiZn, β-NiZn and δ-NiZn) exhibit distinct behaviour in the continuous gas phase hydrogenation of 3BE, attributed to variations in reactant adsorption/activation that inhibits C≡C- multi-coordination on surface Ni. A decrease in the Ni-Ni coordination in the crystalline structure on the different NiZn alloys

structures results in a higher 3BE selectivity albeit a decrease in the 3BY rate of transformation is observed. Among the different alloy phases, α-NiZn delivered the highest alkenol production rate, with an increase in activity over α-NiZn/ZnO linked to a contribution of spillover hydrogen.

We demonstrate the potential of bulk γ-Mo_2N as a suitable replacement for selective -C≡C- bond hydrogenation in **chapter 7**, delivering high selectivity to the target alkene/alkenol in the hydrogenation of different -C≡C- molecules, such as acetylene, phenylacetylene and MBY. The incorporation of Pd as a promoter before and after MoO_3 nitridation serves to increase surface H_2 content (measured by H_2-TPD) which is ascribed to surface modifications γ-Mo_2N crystal structure and/or the exceptional properties of Pd in chemisorbing in H_2. The increase in the hydrogen uptake of the material results on Pd promoted γ-Mo_2N resulting in a higher -C=C- production.

8.2 Future Directions

8.2.1 Enhanced Alkenol Production over Supported NiZn Alloys

The results presented in **Chapter 6** have established selective hydrogenation of 3BY to 3BE over bulk and supported NiZn alloys, but low activity attributed to the limited hydrogen uptake capacity of the alloy. Further work should target higher activity with full selectivity to the target alkenol. Several strategies are considered for increasing the C≡C- hydrogenation rate. The use of low SSA ZnO support on NiZn alloy has shown an improvement in the alkenol production. The swap from ZnO to other oxide/carbonaceous supports with a considerable higher surface area, can enhance the H_2 chemisorption on the support [445] which improves the hydrogenation rates achieved (see **Chapter 6**)

A second strategy will be directed to promoted the formation of $Ni^{\delta+}$ as it is known to promote the H_2 adsorption/activation [446] to a higher extent. A suitable means for changing Ni electronic structure is with the use of acidic supports (*e.g.* TiO_2, ZrO_2) in which metal ↔ support interactions [447] takes place. The utilisation of reducible supports with acidic properties are recommended considering the high temperature requirements (≥ 602 *K*, **chapter 7**) for NiZn alloy formation. Therefore, NiZn alloy sintering can be avoided by using reducible carriers *e.g.* (CeO_2, TiO_2, La_2O_3) that anchors the transition metal to the support. [448,449]. Furthermore, reducible supports are also able to uptake hydrogen [450], which should further elevate catalytic activity. Another way to induce $Ni^{\delta+}$ is by the addition of a second co-metal which is more electronegative, (*e.g.* Au) which have recently given promising results in -C≡C- hydrogenation [451]

The production of other valuable alkenols (*e.g.* 3-hexyn-1-ol and isophytol) with applications in the synthesis of leaf alcohol and Vitamin A and E [5,452] through selective alkynol hydrogenation should also be considered to demonstrate the versatility of the new catalyst formulations.

Furthermore, the utilisation of NiZn metal catalyst in the hydrogenation of internal -C≡C- bond (3-hexyn-1-ol) would be interesting to analyse from the mechanistic point of view due to the impossibility of forming some surface intermediates responsible for over-hydrogenation (*e.g*. ethylidyne) on internal -C≡C-, and to the poor capacity of Ni in promoting double bond migration.

8.2.2 Alkynol Hydrogenation over Bulk/Supported Molybdenum Nitrides

The work presented in **Chapter 7** demonstrates the potential of γ-Mo_2N for selective alkynol hydrogenation in the conversion of phenylacetylene and 2-methyl-3-butyn-2-ol with limitations in activity. Hydrogenation of molybdenum nitrides occurs on uncoordinated $Mo^{\delta+}$ active sites linked to N vacancies occurring at high reduction temperatures (T_{max} = 650-700 *K*).

To shed some light on N vacancies formation, it is suggested to perform a study that systematically evaluates how the activation conditions parameters (*e.g.* H_2 partial pressure, final temperature) impacts on the topotactic bronze H_xMoO_3 formation that conditioned the N vacancies density and catalytic activity.

On the other hand, N vacancies can also be promoted by causing textural changes (*e.g*. surface irregularities) during MoO_3 reduction-nitridation with the addition of Pd promoter (see **Chapter 7**). A further investigation focused on determining Pd role γ-Mo_2N structure could be performed by testing, under the same reaction and activation conditions, Pd/ γ-Mo_2N catalysts with different Pd loadings. Additionally, the role of other promoters typically used on γ-Mo_2N catalysis (*e.g.* Pt, K) [453] should be considered for alkynol hydrogenation.

Along the same lines, a transition from γ-Mo_2N bulk to supported γ-Mo_2N crystallites in a high surface area support can be considered by deposition and further reduction/nitridation of $(NH_4)_6Mo_7O_{24}\cdot 4H_2O$ precursor deposits [418]. The switch to supported systems affords: i) the formation of smaller nanoparticles with a higher concentration of surface defects and ii) the presence chemisorbed hydrogen in the support might enhance the transformation rate.

References

[1] Wernet, G.; Mutel, C.; Hellweg, S.; Hungerbühler, K. *J. Ind. Ecol.* **2011**, *15*, 96–107.

[2] García, V.; Pongrácz, E.; Keiski, R. In *Proceedings of the Waste Minimization and Resources Use Optimization Conference, Oulu, Finland*; 2004; pp 93–106.

[3] Lancaster, M. Green Chemistry: An Introductory Text; Royal Society of Chemistry: Croydon, 2010.

[4] Sulman, E.; Nikoshvili, L.; Matveeva, V.; Tyamina, I.; Sidorov, A.; Bykov, A.; Demidenko, G.; Stein, B.; Bronstein, L. *Top. Catal.* **2012**, *55*, 492–497.

[5] Bonrath, W.; Eggersdorfer, M.; Netscher, T. *Catal. Today* **2007**, *121*, 45–57.

[6] Wüstenberg, B.; Stemmler, R. T.; Létinois, U.; Bonrath, W.; Hugentobler, M.; Netscher, T. *Chim. Int. J. Chem.* **2011**, *65*, 420–428.

[7] Sheldon, R. A. *Pure Appl. Chem.* **2000**, *72*, 1233–1246.

[8] Barreiro, C.; Barredo, J.-L. Carotenoids Production: A Healthy and Profitable Industry. In *Microbial Carotenoids*; Humana Press: New York, 2018; pp 45–55.

[9] Moreno-Marrodan, C.; Liguori, F.; Barbaro, P. *J. Org. Chem.* **2017**, *13*, 734–754.

[10] Cherkasov, N.; Denissenko, P.; Deshmukh, S.; Rebrov, E. V. *Chem. Eng. J.* **2020**, *379*, 122292–122301.

[11] López, N.; Vargas-Fuentes, C. *Chem. Commun.* **2012**, *48*, 1379–1391.

[12] Vernuccio, S. Selective Hydrogenation of Alkynes for Vitamin Production, ETH Zurich, 2017.

[13] Siegel, S. *Adv. Catal.* **1966**, *16*, 123–177.

[14] Lindlar, H. *Helv. Chim. Acta* **1952**, *35*, 446–450.

[15] Arnold, H.; Dobert, F.; Gaube, J.; Ertl, G.; Knozinger, H.; Weitkempl, J. *Handbook of Heterogeneous Catalysis*; VCH: Weinheim, 2008.

[16] Ravanchi, M. T.; Sahebdelfar, S. *Palladium as a Catalyst for Selective*

Hydrogenation: Fundamentals and Applications; Lap Lambert Academic Publishing: Saarbrücken, 2015.

[17] Nakatsuji, H.; Hada, M.; Yonezawa, T. *J. Am. Chem. Soc.* **1987**, *109*, 1902–1912.

[18] Bond, G. C. *Platin. Met. Rev.* **2000**, *44*, 146–155.

[19] Chan, C. W. A. Ultraselective Nanocatalysts in Fine Chemical and Pharmaceutical Synthesis, University of Oxford, **2012**.

[20] Vilé, G.; Almora-Barrios, N.; Mitchell, S.; López, N.; Pérez-Ramírez, J. *Chemistry* **2014**, *20*, 5926–5937.

[21] Chalk, A. J.; Rylander, P. N.; Greenfield, H.; Augustine, R. L. *Catalysis of Organic Reactions*; New York, **1988**.

[22] Molnár, Á.; Sárkány, A.; Varga, M. *J. Mol. Catal. A Chem.* **2001**, *173*, 185–221.

[23] Zhang, Q.; Li, J.; Liu, X.; Zhu, Q. *Appl. Catal. A Gen.* **2000**, *197*, 221–228.

[24] Karpiński, Z. Catalysis by Supported, Unsupported, and Electron-Deficient Palladium. In *Advances in catalysis*; Academic Press: Warsaw, 1990; Vol. 37, pp. 45–100.

[25] Bond, G. C. *J. Mol. Catal. A Chem.* **2000**, *156*, 1–20.

[26] Sárkány, A.; Weiss, A. H.; Guczi, L. *J. Catal.* **1986**, *98*, 550–553.

[27] Hub, S.; Touroude, R. *J. Catal.* **1988**, *114*, 411–421.

[28] Coq, B.; Figueras, F. *J. Mol. Catal. A Chem.* **2001**, *173*, 117–134.

[29] Edvinsson, R. K.; Holmgren, A. M.; Irandoust, S. *Ind. Eng. Chem. Res.* **1995**, *34*, 94–100.

[30] Mei, D.; Neurock, M.; Smith, C. M. *J. Catal.* **2009**, *268*, 181–195.

[31] Bos, A. N. R.; Westerterp, K. R. *Chem. Eng. Process. Process Intensif.* **1993**, *32*, 1–7.

[32] Leviness, S.; Nair, V.; Weiss, A. H.; Schay, Z.; Guczi, L. *J. Mol. Catal.* **1984**, *25*, 131–140.

[33] Boitiaux, J. P.; Cosyns, J.; Vasudevan, S. *Appl. Catal.* **1985**, *15*, 317–326.

[34] Nijhuis, T. A.; van Koten, G.; Moulijn, J. A. *Appl. Catal. A Gen.* **2003**, *238*, 259–271.

[35] Crespo-Quesada, M.; Cárdenas-Lizana, F.; Dessimoz, A. L.; Kiwi-Minsker, L. *ACS Catal.* **2012**, *2*, 1773–1786.

[36] Furukawa, S.; Komatsu, T. *ACS Catal.* **2016**, *6*, 2121–2125.

[37] Osswald, J. Active-Site Isolation for the Selective Hydrogenation of Acetylene: The Pd-Ga and Pd-Sn Intermetallic Compounds, Technische Universität Berlin, **2005**.

[38] Anderson, J.; Mellor, J.; Wells, R. *J. Catal.* **2009**, *261*, 208–216.

[39] Nikolaev, S. A.; Zanaveskin, L. N.; Smirnov, V. V.; Averyanov, V. A.; Zanaveskin, K. L. *Russ. Chem. Rev.* **2009**, *78*, 231–247.

[40] Kang, J. H.; Shin, E. W.; Kim, W. J.; Park, J. D.; Moon, S. H. *Catal. Today* **2000**, *63*, 183–188

[41] Huang, W.; Li, A.; Lobo, R. F.; Chen, J. G. *Catal. Lett.* **2009**, *130*, 380–385.

[42] Kovnir, K.; Armbrüster, M.; Teschner, D.; Venkov, T. V.; Szentmiklósi, L.; Jentoft, F. C.; Knop-Gericke, A.; Grin, Y.; Schlögl, R. *Surf. Sci.* **2009**, *603*, 1784–1792.

[43] Li, R.; Yue, Y.; Chen, Z.; Chen, X.; Wang, S.; Jiang, Z.; Wang, B.; Xu, Q.; Han, D.; Zhao, J. *Appl. Catal. B Environ.* **2020**, 119348–119359.

[44] García-Mota, M.; Gómez-Díaz, J.; Novell-Leruth, G.; Vargas-Fuentes, C.; Bellarosa, L.; Bridier, B.; Pérez-Ramírez, J.; López, N. *Theor. Chem. Acc.* **2011**, *128*, 663–673.

[45] Vilé, G.; Bridier, B.; Wichert, J.; Pérez-Ramírez, J. *Angew. Chemie Int. Ed.* **2012**, *51*, 8620–8623.

[46] Zea, H.; Lester, K.; Datye, A. K.; Rightor, E.; Gulotty, R.; Waterman, W.; Smith, M. *Appl. Catal. A Gen.* **2005**, *282*, 237–245.

[47] Jia, C.-J.; Schuth, F. S. *Phys. Chem. Chem. Phys.* **2011**, *13*, 2457–2487.

[48] Anderson, L. D. Chemical Composition of the Mantle. In *Theory of the Earth*; Blackwell Scientific Publications: Boston, 1989; pp 147–175.

[49] Goodman, D. W. *Catal. Lett.* **2005**, *99*, 1–4.

[50] Haller, G. L.; Resasco, D. E. Metal–Support Interaction: Group VIII Metals and Reducible Oxides. In *Advances in catalysis*; Elsevier, **1989**; Vol. 36, pp 173–235.

[51] Liu, J. J. *ChemCatChem* **2011**, *3*, 934–948.

[52] Pan, C.-J.; Tsai, M.-C.; Su, W.-N.; Rick, J.; Akalework, N. G.; Agegnehu, A. K.; Cheng, S.-Y.; Hwang, B.-J. *J. Taiwan Inst. Chem. Eng.* **2017**, *74*, 154–186.

[53] McCue, A.; Anderson, J. *Front. Chem. Sci. Eng.* **2015**, *9*, 142–153.

[54] Studt, F.; Abild-Pedersen, F.; Bligaard, T.; Sørensen, R. Z.; Christensen, C. H.; Nørskov, J. K. *Science* **2008**, *320*, 1320–1322.

[55] Rodríguez, J. C.; Marchi, A. J.; Borgna, A.; Romeo, E.; Monzón, A. *Stud. Surf. Sci. Catal.* **2001**, *139*, 37–44.

[56] Nørskov, J. K.; Bligaard, T.; Rossmeisl, J.; Christensen, C. H. *Nat. Chem.* **2009**, *1*, 37–46.

[57] Spanjers, C. S.; Held, J. T.; Jones, M. J.; Stanley, D. D.; Sim, R. S.; Janik, M. J.; Rioux, R. M. *J. Catal.* **2014**, *316*, 164–173.

[58] Furimsky, E. *Appl. Catal. A Gen.* **2003**, *240*, 1–28.

[59] Cárdenas-Lizana, F.; Lamey, D.; Kiwi-Minsker, L.; Keane, M. A. *J. Mater. Sci.* **2018**, *53*, 6707–6718.

[60] Jaf, Z. N.; Altarawneh, M.; Miran, H. A.; Jiang, Z.-T.; Dlugogorski, B. Z. *Catal. Sci. Technol.* **2017**, *7*, 943–960.

[61] Jia, J.; Haraki, K.; Kondo, J. N.; Domen, K.; Tamaru, K. *J. Phys. Chem. B* **2000**, *104*, 11153–11156.

[62] Gluhoi, A. C.; Bakker, J. W.; Nieuwenhuys, B. E. *Catal. Today* **2010**, *154*, 13–

20.

[63] Vilé, G.; Baudouin, D.; Remediakis, I. N.; Copéret, C.; López, N.; Pérez-Ramírez, J. *ChemCatChem* **2013**, *5*, 3750–3759.

[64] Beller, M.; Renken, A.; van Santen, R. A. *Catalysis: From Principles to Applications*; Wiley-VCH Verlag, 2012.

[65] Levenspiel, O. *Chemical Reaction Engineering*; Wiley Online Library: New York, 2000.

[66] Navarro-Fuentes, F.; Keane, M.; Ni, X.-W. *Org. Process Res. Dev.* **2019**, *23*, 38–44.

[67] Escudié, R.; Conte, T.; Steyer, J. P.; Delgenès, J. P. *Process Biochem.* **2005**, *40*, 2311–2323.

[68] Khokarale, S. G.; Garcia-Suarez, E. J.; Fehrmann, R.; Riisager, A. *ChemCatChem* **2017**, *9*, 1824–1829.

[69] Rameshan, C.; Stadlmayr, W.; Penner, S.; Lorenz, H.; Mayr, L.; Hävecker, M.; Blume, R.; Rocha, T.; Teschner, D.; Knop-Gericke, A. *J. Catal.* **2012**, *290*, 126–137.

[70] Watts, J. F.; Wolstenholme, J. Electron Spectrometer Design. In *An Introduction to Surface Analysis by XPS and AES*; Wiley: Hoboken, 2019; pp 22–23.

[71] Andrade, J. D. X-Ray Photoelectron Spectroscopy [XPS]. In *Surface and interfacial aspects of biomedical polymers*; Springer, NewYork, 1985; pp 105–195.

[72] Descostes, M.; Mercier, F.; Thromat, N.; Beaucaire, C.; Gautier-Soyer, M. *Appl. Surf. Sci.* **2000**, *165*, 288–302.

[73] Mojet, B. L.; Kappers, M. J.; Muijsers, J. C.; Niemantsverdriet, J. W.; Miller, J. T.; Modica, F. S.; Koningsberger, D. C. *Stud. Surf. Sci. Catal.* **1994**, *84*, 909–916.

[74] Mohai, M. *Surf. Interf. Anal.* **2004**, *36*, 828–832.

[75] Epp, J. X-Ray Diffraction [XRD] Techniques for Materials Characterization. In *Materials Characterization Using Nondestructive Evaluation [NDE] Methods*; Woodhead Publishing, 2016; pp 81–124

[76] Cullity, B. D. *Elements of X-Ray Diffraction*; Addison-Wesley Publishing, Boston, 1956.

[77] Monshi, A.; Foroughi, M. R.; Monshi, M. R. *World J. Nano Sci. Eng.* **2012**, *2*, 154–160.

[78] Inkson, B. J. Scanning Electron Microscopy [SEM] and Transmission Electron Microscopy [TEM] for Materials Characterization. In *Materials characterization using nondestructive evaluation [NDE] methods*; Elsevier, Sheffield, United Kingdom **2016**; pp 17–43.

[79] Kuno, M. *Introductory Nanoscience: Physical and Chemical Concepts*; CRC Press: New York, 2011.

[80] Carter, C. B.; Williams, D. B. *Transmission Electron Microscopy: Diffraction, Imaging, and Spectrometry*; Springer: New York, 2016.

[81] Parker, S. C.; Lawrence, P. J.; Freeman, C. M.; Levine, S. M.; Newsam, J. M. *Catal. Letters* **1992**, *15*, 123–131.

[82] Pyrz, W. D.; Buttrey, D. J. *Langmuir* **2008**, *24*, 11350–11360.

[83] Veisi, H.; Tamoradi, T.; Karmakar, B.; Mohammadi, P.; Hemmati, S. *Mater. Sci. Eng. C* **2019**, *104*, 109919–109928.

[84] Ross, J. R. H. Surfaces and Adsorption. In *Contemporary Catalysis*; Elsevier, Amsterdam, 2019; pp 39–68.

[85] Tanksale, A.; Beltramini, J. N.; Dumesic, J. A.; Lu, G. Q. *J. Catal.* **2008**, *258*, 366–377.

[86] Fadoni, M.; Lucarelli, L. *Stud. Surf. Sci. Catal.* **1999**, *120*, 177–225.

[87] Kapteijn, F.; Moulijn, J. A.; Tarfaoui, A. *Stud. Surf. Sci. Catal.* **1993**, *79*, 401.

[88] Zhu, H.; Qin, Z.; Shan, W.; Shen, W.; Wang, J. *J. Catal.* **2004**, *225*, 267–277.

[89] Kanervo, J. M.; Harlin, M. E.; Krause, A. O. I.; Bañares, M. A. *Catal. Today* **2003**, *78*, 171–180.

[90] Ma, L.; Han, D.; Ma, H.; Liu, L.; Guo, H. *Catalysts* **2018**, *8*, 635.

[91] Wang, X.; Liu, D.; Li, J.; Zhen, J.; Wang, F.; Zhang, H. *Chem. Sci.* **2015**, *6*, 2877–2884.

[92] Hurst, N. W.; Gentry, S. J.; Jones, A.; McNicol, B. D. *Catal. Rev.* **1982**, *24*, 233–309.

[93] Jones, A. *Temperature-Programmed Reduction for Solid Materials Characterization*; CRC Press: New York, **1986**.

[94] Alnot, M.; Cassuto, A. *Surf. Sci.* **1981**, *112*, 325–342.

[95] Britten, J. A.; Falconer, J. L.; Brown, L. F. *Carbon* **1985**, *23*, 627–633.

[96] McEwan, L.; Julius, M.; Roberts, S.; Fletcher, J. C. Q. *Gold Bull.* **2010**, *43*, 298–306.

[97] Gibson, N.; Kuchenbecker, P.; Rasmussen, K.; Rauscher, H. Volume-Specific Surface Area by Gas Adsorption Analysis with the BET Method. In *Characterization of Nanoparticles*; Elsevier, Amsterdam, 2020; pp 265–294.

[98] Shaji, A. Surface Area Analysis of Nanomaterials. In *Thermal and Rheological Measurement Techniques for Nanomaterials Characterization*; Elsevier, 2017; pp 197–231.

[99] Pilko, E.; Hensen, E. Adsorption Methods for Characterization of Pororus Materials. In *Catalysis: from principles to applications*; Beller, M., Renken, A., van Santen, R. A., Eds.; Wiley-VCH Verlag: Eindhoven, 2012; pp 514–534.

[100] Leddy, N. In *CMA Analytical Workshop*; 2012; pp 1–28.

[101] Qi, L.; Tang, X.; Wang, Z.; Peng, X. *Int. J. Min. Sci. Technol.* **2017**, *27*, 371–377.

[102] Thomas, J. M.; Thomas, W. J. *Principles and Practice of Heterogeneous Catalysis*; John Wiley & Sons, Weinheim, 2014.

[103] Lowell, S.; Shields, J. E.; Thomas, M. A.; Thommes, M. Surface Area Analysis from the Langmuir and Bet Theories. In *Characterization of Porous Solids and Powders: Surface Area, Pore Size and Density*; Springer, New York, 2004; pp 58–8.

[104] Dollimore, D.; Spooner, P. *J. Appl. Chem. Biotechnol.* **2007**, *24*, 35–41.

[105] Augustine, R. L. *Heterogeneous Catalysis for the Synthetic Chemist*; Chemical Industries; Taylor & Francis: New York, 1995

[106] Delgado, J. A.; Benkirane, O.; Claver, C.; Curulla-Ferré, D.; Godard, C. *Dalt. Trans.* **2017**, *46*, 12381–12403.

[107] Rajaram, J.; Narula, A. P. S.; Chawla, H. P. S.; Dev, S. *Tetrahedron* **1983**, *39*, 2315–2322.

[108] Mei, D.; Sheth, P.; Neurock, M.; Smith, C. *J. Catal.* **2006**, *242*, 1–15.

[109] Semagina, N.; Kiwi-Minsker, L. *Catal. Rev.* **2009**, *51*, 147–217.

[110] Semagina, N.; Renken, A.; Kiwi-Minsker, L. *J. Phys. Chem. C* **2007**, *111*, 13933–13937.

[111] Terasawa, M.; Yamamoto, H.; Kaneda, K.; Imanaka, T.; Teranishi, S. *J. Catal.* **1979**, *57*, 315–325.

[112] Karavanov, A. N.; Gryaznov, V. M. *Bull. Acad. Sci. USSR, Div. Chem. Sci.* **1989**, *38*, 1593–1596.

[113] Bonrath, W.; Netscher, T. *Appl. Catal. A Gen.* **2005**, *280*, 55–73.

[114] Bonrath, W.; Medlock, J.; Schütz, J.; Wüstenberg, B.; Netscher, T. Hydrogenation in the Vitamins and Fine Chemicals Industry - An Overview. In *Hydrogenation*; InTech: Rijeka, 2012; pp. 69–90.

[115] Izumi, Y.; Tanaka, Y.; Urabe, K. *Chem. Lett.* **1982**, *11*, 679–682.

[116] Uberman, P. M.; Costa, N. J. S.; Philippot, K.; C. Carmona, R.; dos Santos, A. A.; Rossi, L. M. *Green Chem.* **2014**, *16*, 4566–4574.

[117] Hou, R.; Wang, T.; Lan, X. *Ind. Eng. Chem. Res.* **2013**, *52*, 13305–13312.

[118] Pérez, D.; Olivera-Fuentes, C.; Curbelo, S.; Rodríguez, M. J.; Zeppieri, S. *Fuel* **2015**, *149*, 34–45.

[119] Prestianni, A.; Crespo-Quesada, M.; Cortese, R.; Ferrante, F.; Kiwi-Minsker, L.; Duca, D. *J. Phys. Chem. C* **2014**, *118*, 3119–3128.

[120] Amorim, C.; Keane, M. A. *J. Colloid Interf. Sci.* **2008**, *322*, 196–208.

[121] Cárdenas-Lizana, F.; Wang, X.; Lamey, D.; Li, M.; Keane, M. A.; Kiwi-Minsker, L. *Chem. Eng. J.* **2014**, *255*, 695–704.

[122] Cárdenas-Lizana, F.; Lamey, D.; Perret, N.; Gómez-Quero, S.; Kiwi-Minsker, L.; Keane, M. A. *Catal. Commun.* **2012**, *21*, 46–51.

[123] Ye, G.; Xie, D.; Qiao, W.; Grace, J. R.; Lim, C. J. *Int. J. Hydrogen Energy* **2009**, *34*, 4755–4762.

[124] Joback, K. G.; Reid, R. C. *Chem. Eng. Commun.* **1987**, *57*, 233–243.

[125] Yarulin, A.; Yuranov, I.; Cárdenas-Lizana, F.; Abdulkin, P.; Kiwi-Minsker, L. *J. Phys. Chem. C* **2013**, *117*, 13424–13434.

[126] Smirnov, M. Y.; Klembovskii, I. O.; Kalinkin, A. V.; Bukhtiyarov, V. I. *Kinet. Catal.* **2018**, *59*, 786–791.

[127] Juan-Juan, J.; Román-Martínez, M. C.; Illán-Gómez, M. J. *Appl. Catal. A Gen.* **2004**, *264*, 169–174.

[128] Nag, N. K. *Catal. Lett.* **1994**, *24*, 37–46.

[129] McCarty, J. G. *Catal. Today* **1995**, *26*, 283–293.

[130] Weissman, D. L.; Shek, M. L.; Spicer, W. E. *Surf. Sci.* **1980**, *92*, L59–L66.

[131] Papp, A.; Molnár, Á.; Mastalir, Á. *Appl. Catal. A Gen.* **2005**, *289*, 256–266.

[132] Da Silva, F. P.; Rossi, L. M. *Tetrahedron* **2014**, *70*, 3314–3318.

[133] Derrien, M. L. *Stud. Surf. Sci. Catal.* **1986**, *27*, 613–666.

[134] Morrill, C.; Grubbs, R. H. *J. Am. Chem. Soc.* **2005**, *127*, 2842–2843.

[135] Jewell, L.; Davis, B. *Appl. Catal. A Gen.* **2006**, *310*, 1–15.

[136] Nikoshvili, L.; Shimanskaya, E.; Bykov, A.; Yuranov, I.; Kiwi-Minsker, L.; Sulman, E. *Catal. Today* **2014**, *241*, 179–188.

[137] Sulman, E. M. *Russ. Chem. Rev.* **1994**, *63*, 923–936.

[138] Hansch, C.; Leo, A.; Taft, R. W. *Chem. Rev* **1991**, *91*, 165–195.

[139] Boitiaux, J. P.; Cosyns, J.; Robert, E. *Appl. Catal.* **1987**, *32*, 169–183.

[140] Morrill, T. C.; D'Souza, C. A. *Organometallics* **2003**, *22*, 1626–1629.

[141] Karlsson, E. A.; Bäckvall, J.-E. *Chem.Eur. J.* **2008**, *14*, 9175–9180.

[142] Behm, R. J.; Penka, V.; Cattania, M. -G.; Christmann, K.; Ertl, G. *J. Chem. Phys.* **1983**, *78*, 7486–7490.

[143] Bianchini, C.; Meli, A.; Oberhauser, W. *New J. Chem.* **2001**, *25*, 11–12.

[144] Ide, M. S.; Hao, B.; Neurock, M.; Davis, R. J. *ACS Catal.* **2012**, *2*, 671–683.

[145] Ponec, V. *Appl. Catal. A Gen.* **1997**, *149*, 27–48.

[146] Studt, F.; Abild-Pedersen, F.; Bligaard, T.; Sørensen, R. Z.; Christensen, C. H.; Nørskov, J. K. *Angew. Chemie Int. Ed.* **2008**, *47*, 9299–9302.

[147] Dobrovolná, Z.; Kačer, P.; Červený, L. *J. Mol. Catal. A Chem.* **1998**, *130*, 279–284.

[148] Sulman, E. M.; Matveeva, V.; Doluda, V.; Nikoshvili, L.; Bykov, A.; Demidenko, G.; Bronstein, L. Scientific Bases for the Preparation of Heterogeneous Catalysts. In *Preparation of the Polymer Stabilized and the Supported Nanostructured Catalysts*; Gaigneaux, E. M., Devillers, M., Hermans, S., Jacobs, P. A., Eds.; Elsevier: Leuven, 2010; pp 156–157.

[149] Crespo-Quesada, M.; Yarulin, A.; Jin, M.; Xia, Y.; Kiwi-Minsker, L. *J. Am. Chem. Soc.* **2011**, *133*, 12787–12794.

[150] Berguerand, C.; Yuranov, I.; Cárdenas-Lizana, F.; Yuranova, T.; Kiwi-Minsker, L. *J. Phys. Chem. C* **2014**, *118*, 12250–12259.

[151] Bahruji, H.; Bowker, M.; Hutchings, G.; Dimitratos, N.; Wells, P.; Gibson, E.; Jones, W.; Brookes, C.; Morgan, D.; Lalev, G. *J. Catal.* **2016**, *343*, 133–146.

[152] Tew, M. W.; Emerich, H.; Bokhoven, J. A. van. *J. Phys. Chem. C* **2011**, *115*, 8457–8465.

[153] Zhou, H.; Yang, X.; Li, L.; Liu, X.; Huang, Y.; Pan, X.; Wang, A.; Li, J.; Zhang, T. *ACS Catal.* **2016**, *6*, 1054–1061.

[154] Föttinger, K. PdZn Based Catalysts: Connecting Electronic and Geometric Structure with Catalytic Performance. In *Catalysis: Volume 25*; Spivey, J. J., Dooley, K. M., Ha, Y.-F., Eds.; Royal Society of Chemistry: Cambridge, 2013; pp 77–117.

[155] Karim, A. M.; Conant, T.; Datye, A. K. *Phys. Chem. Chem. Phys.* **2008**, *10*, 5584–5590.

[156] Karim, A.; Conant, T.; Datye, A. *J. Catal.* **2006**, *243*, 420–427.

[157] Conant, T.; Karim, A. M.; Lebarbier, V.; Wang, Y.; Girgsdies, F.; Schlögl, R.; Datye, A. *J. Catal.* **2008**, *257*, 64–70.

[158] Suwa, Y.; Ito, S.; Kameoka, S.; Tomishige, K.; Kunimori, K. *Appl. Catal. A Gen.* **2004**, *267*, 9–16.

[159] Wei, Z.; Sun, J.; Li, Y.; Datye, A. K.; Wang, Y. *Chem. Soc. Rev.* **2012**, *41*, 7994–8008.

[160] Okhlopkova, L. B.; Matus, E. V.; Prosvirin, I. P.; Kerzhentsev, M. A.; Ismagilov, Z. R. *J. Nanopart. Res.* **2015**, *17*, 475–490.

[161] Iwasa, N.; Takezawa, N. *Top. Catal.* **2003**, *22*, 215–224.

[162] Segura, Y.; López, N.; Pérez-Ramírez, J. *J. Catal.* **2007**, *247*, 383–386.

[163] Maksimov, G. M.; Zaikovskii, V. I.; Matveev, K. I.; Likholobov, V. A. *Kinet. Catal.* **2000**, *41*, 844–852.

[164] Maksimova, G. M.; Chuvilin, A. L.; Moroz, E. M.; Likholobov, V. A.; Matveev, K. I. *Kinet. Catal.* **2004**, *45*, 870–878.

[165] Khoudiakov, M.; Gupta, M. C.; Deevi, S. *Appl. Catal. A Gen.* **2005**, *291*, 151–161.

[166] Lindlar, H.; Dubuis, R. Palladium Catalyst for Partial Reduction of Acetylenes. In *Organic Syntheses*; John Wiley & Sons, Inc.: Hoboken, NJ, USA, 2003; Vol. 46, pp 89–89.

[167] Venezia, A. M.; Duca, D.; Floriano, M. A.; Deganello, G.; Rossi, A. *Surf. Interface Anal.* **1992**, *19*, 543–547.

[168] Turner, N. H.; Single, A. M. *Surf. Interface Anal.* **1990**, *15*, 215–222.

[169] Zhong, J. B.; Li, J. Z.; He, X. Y.; Zeng, J.; Lu, Y.; Hu, W.; Lin, K. *Curr. Appl. Phys.* **2012**, *12*, 998–1001.

[170] Jana, R.; Subbarao, U.; Peter, S. C. *J. Power Sources* **2016**, *301*, 160–169.

[171] Hachemi, I.; Jeništová, K.; Mäki-Arvela, P.; Kumar, N.; Eränen, K.; Hemming, J.; Murzin, D. Y. *Catal. Sci. Technol.* **2016**, *6*, 1476–1487.

[172] N. Iwasa, S. Masuda, N. Ogawa, N. T. *Appl. Catal. A Gen.* **1995**, *125*, 145–157.

[173] Wang, C.-B.; Gau, G.-Y.; Gau, S.-J.; Tang, C.-W.; Bi, J.-L. *Catal. Lett.* **2005**, *101*, 241–247.

[174] Gómez-Quero, S.; Cárdenas-Lizana, F.; Keane, M. A. *Ind. Eng. Chem. Res.* **2008**, *47*, 6841–6853.

[175] Iwasa, N.; Ogawa, N.; Masuda, S.; Takezawa, N. *Bull. Chem. Soc. Jpn.* **1998**, *71*, 1451–1455.

[176] Penner, S.; Jenewein, B.; Gabasch, H.; Klötzer, B.; Wang, D.; Knop-Gericke, A.; Schlögl, R.; Hayek, K. *J. Catal.* **2006**, *241*, 14–19.

[177] Kniep, B. L.; Girgsdies, F.; Ressler, T. *J. Catal.* **2005**, *236*, 34–44.

[178] Liu, J.; Qiao, B.; Song, Y.; Tang, H.; Huang, Y.; Liu, J. *J. Energy Chem.* **2016**, *25*, 361–370.

[179] Tran, S. B. T.; Choi, H. S.; Oh, S. Y.; Moon, S. Y.; Park, J. Y. *RSC Adv.* **2018**, *8*, 21528–21533.

[180] Lv, Y.; Yao, W.; Ma, X.; Pan, C.; Zong, R.; Zhu, Y. *Catal. Sci. Technol.* **2013**, *3*, 3136–3146.

[181] Wang, Y.; Zhang, J.; Xu, H. *Chin. J. Catal.* **2006**, *27*, 217–222.

[182] Castillejos-López, E.; Agostini, G.; Di Michel, M.; Iglesias-Juez, A.; Bachiller-Baeza, B. *ACS Catal.* **2017**, *7*, 796–811.

[183] Campbell, C. T.; Sellers, J. R. V. *Faraday Discuss.* **2013**, *162*, 9–30.

[184] Liewhiran, C.; Phanichphant, S. *Curr. Appl. Phys.* **2008**, *8*, 336–339.

[185] Lee, I.; Morales, R.; Albiter, M. A.; Zaera, F. *PNAS* **2008**, *105*, 15241–15246.

[186] Tonetto, G. M.; Damiani, D. E. *J. Mol. Catal. A Chem.* **2003**, *202*, 289–303.

[187] Parks, G. A. *Chem. Rev.* **1965**, *65*, 177–198.

[188] Webber, P. R.; Rojas, C. E.; Dobson, P. J.; Chadwick, D. *Surf. Sci.* **1981**, *105*, 20–40.

[189] Moulder, J. F.; Chastain, J.; King, R. C. Standard XPS Spectra of Elements. In *Handbook of X-ray Photoelectron Spectroscopy*; Chastain, J., Ed.; Perkin-Elmer Corporation: Minnesota, 1992; pp 118–119.

[190] Wang, H.; Gu, X.-K.; Zheng, X.; Pan, H.; Zhu, J.; Chen, S.; Cao, L.; Li, W.-X.; Lu, J. *Sci. Adv.* **2019**, *5*, 1-8.

[191] Liqiang, J.; Wang, B.; Baifu, X.; Shudan, L.; Keying, S.; Weimin, C.; Honggang, F. *J. Solid State Chem.* **2004**, *177*, 4221–4227.

[192] Gigola, C. E.; Moreno, M. S.; Costilla, I.; Sánchez, M. D. *Appl. Surf. Sci.* **2007**, *254*, 325–329.

[193] Horiuti, I.; Polanyi, M. *Trans. Faraday Soc.* **1934**, *30*, 1164–1172.

[194] Sheth, P. A.; Neurock, M.; Smith, C. M. *J. Phys. Chem. B* **2003**, *107*, 2009–2017.

[195] Sárkány, A.; Horváth, A.; Beck, A. *Appl. Catal. A Gen.* **2002**, *229*, 117–125.

[196] Kranich, W. L.; Weiss, A. H.; Schay, Z.; Guczi, L. *Appl. Catal.* **1985**, *13*, 257–267.

[197] McCue, A. J.; Guerrero-Ruiz, A.; Rodríguez-Ramos, I.; Anderson, J. A. *J. Catal.* **2016**, *340*, 10–16.

[198] Newton, M. D.; Lipscomb, W. N. *J. Am. Chem. Soc* **1967**, *89*, 4261–4267.

[199] Allenger, V. M.; McLean, D. D.; Ternan, M. *J. Catal.* **1991**, *131*, 305–318.

[200] Protasova, L. N.; Rebrov, E. V.; Choy, K. L.; Pung, S. Y.; Engels, V.; Cabaj, M.; Wheatley, A. E. H.; Schouten, J. C. *Catal. Sci. Technol.* **2011**, *1*, 768–777.

[201] Mohr, C.; Claus, P. *Sci. Prog.* **2001**, *84*, 311–334.

[202] Xie, S.; Choi, S. I.; Xia, X.; Xia, Y. *Curr. Opin. Chem. Eng.* **2013**, *2*, 142–150.

[203] Chen, Y.-J.; Yeh, C. *J. Catal.* **2001**, *200*, 59–68.

[204] Hao, Z.; An, L.; Wang, H. *Sci. China Ser. B Chem.* **2001**, *44*, 596–605.

[205] Jiang, T.; Huai, Q.; Geng, T.; Ying, W.; Xiao, T.; Cao, F. *Biomass Bioenerg.* **2015**, *78*, 71–79.

[206] Ding, E.; Jujjuri, S.; Sturgeon, M.; Shore, S. G.; Keane, M. A. *J. Mol. Catal. A Chem.* **2008**, *294*, 51–60.

[207] Pei, G. X.; Liu, X. Y.; Yang, X.; Zhang, L.; Wang, A.; Li, L.; Wang, H.; Wang, X.; Zhang, T. *ACS Catal.* **2017**, *7*, 1491–1500.

[208] Yin, M.; Wu, C.-K.; Lou, Y.; Burda, C.; Koberstein, J. T.; Zhu, Y.; O'brien, S. *J. Am. Chem. Soc* **2005**, *127*, 9506–9511.

[209] Meshesha, B. T.; Barrabés, N.; Llorca, J.; Dafinov, A.; Medina, F.; Föttinger, K. *Appl. Catal. A Gen.* **2013**, *453*, 130–141.

[210] Lopez, N.; Nørskov, J. K.; Janssens, T. V. W.; Carlsson, A.; Puig-Molina, A.; Clausen, B. S.; Grunwaldt, J.-D. *J. Catal.* **2004**, *225*, 86–94.

[211] Haruta, M.; Daté, M. *Appl. Catal. A Gen.* **2001**, *222*, 427–437.

[212] Marın-Astorga, N.; Pecchi, G.; Fierro, J. L. G.; Reyes, P. *Catal. Lett.* **2003**, *91*, 115–121.

[213] Lin, R.; Albani, D.; Fako, E.; Kaiser, S. K.; Safonova, O. V.; López, N.; Pérez-

Ramírez, J. *Angew. Chemie* **2019**, *131*, 514–519.

[214] Kim, W.-J.; Moon, S. H. *Catal. Today* **2012**, *185*, 2–16.

[215] Trost, B. M.; Tracy, J. S. *Isr. J. Chem.* **2018**, *58*, 18–27.

[216] Sheldon, R. A.; Arends, I.; Hanefeld, U. Green Chemistry and Catalysis. In *Introduction: Green Chemistry and Catalysis*; Wiley: Weinheim, 2007; pp 1–43.

[217] Ibhadon, A.; Kansal, S. *J. Chem. Eng. Process Technol.* **2017**, *9*, 1–15.

[218] Bridier, B.; Pérez-Ramírez, J. *J. Catal.* **2011**, *284*, 165–175.

[219] Drault, F.; Comminges, C.; Can, F.; Pirault-Roy, L.; Epron, F.; Le Valant, A. *Materials* **2018**, *11*, 819–832.

[220] Cherkasov, N.; Bai, Y.; Rebrov, E. *Catalysts* **2017**, *7*, 1–16.

[221] Deng, D.; Yang, Y.; Gong, Y.; Li, Y.; Xu, X.; Wang, Y. *Green Chem.* **2013**, *15*, 2525–2531.

[222] Vernuccio, S.; von Rohr, P. R.; Medlock, J. *Ind. Eng. Chem. Res.* **2015**, *54*, 11543–11551.

[223] Kim, S. K.; Lee, J. H.; Ahn, I. Y.; Kim, W.-J.; Moon, S. H. *Appl. Catal. A Gen.* **2011**, *401*, 12–19.

[224] Choi, J.; Zhang, S.; Hill, J. M. *Catal. Sci. Technol.* **2012**, *2*, 179–186.

[225] Semagina, N.; Renken, A.; Laub, D.; Kiwi-Minsker, L. *J. Catal.* **2007**, *246*, 308–314.

[226] Zakarina, N. A.; Zakumbaeva, G. D.; Toktabaeva, N. F.; Dyusenbina, B. B.; Litvyakova, E. N.; Kuanyshev, A. S. *Kinet. Catal.* **1983**, *24*, 733–737.

[227] Bönnemann, H.; Brijoux, W.; Siepen, K.; Hormes, J.; Franke, R.; Pollmann, J.; Rothe, J. *Appl. Organomet. Chem.* **1997**, *11*, 783–796.

[228] Yarulin, A.; Yuranov, I.; Cárdenas-Lizana, F.; Alexander, D. T. L.; Kiwi-Minsker, L. *Appl. Catal. A Gen.* **2014**, *478*, 186–193.

[229] Shahid, M.; Pinelli, E.; Dumat, C. *J. Hazard. Mater.* **2012**, *219–220*, 1–12.

[230] González-Fernández, A.; Pischetola, C.; Kiwi-Minsker, L.; Cárdenas-Lizana, F. *J. Phys. Chem. C* **2020**, *124*, 3681-3691.

[231] Bieszczad, B.; Gilheany, D. G. *Org. Biomol. Chem.* **2017**, *15*, 6483–6492.

[232] Sokolov, S.; Radnik, J.; Schneider, M.; Rodemerck, U. *Int. J. Hydrogen Energy* **2017**, *42*, 9831–9839.

[233] Domínguez-Domínguez, S.; Berenguer-Murcia, Á.; Cazorla-Amorós, D.; Linares-Solano, Á. *J. Catal.* **2006**, *243*, 74–81.

[234] Domínguez-Domínguez, S.; Berenguer-Murcia, Á.; Pradhan, B. K.; Linares-Solano, Á.; Cazorla-Amorós, D. *J. Phys. Chem. C* **2008**, *112*, 3827–3834.

[235] Domínguez-Domínguez, S.; Berenguer-Murcia, Á.; Linares-Solano, Á.; Cazorla-Amorós, D. *J. Catal.* **2008**, *257*, 87–95.

[236] Wu, T.; Jiang, T.; Hu, B.; Han, B.; He, J.; Zhou, X. *Green Chem.* **2009**, *11*, 798-803.

[237] Chen, L. F.; Wang, J. A.; Valenzuela, M. A.; Bokhimi, X.; Acosta, D. R.; Novaro, O. *J. Alloys Compd.* **2006**, *417*, 220–223.

[238] Xinghua, Z.; Tiejun, W.; Longlong, M.; Chuangzhi, W. *Fuel* **2010**, *89*, 2697–2702.

[239] Carlsson, A. F.; Bäumer, M.; Risse, T.; Freund, H.-J. *J. Chem. Phys* **2003**, *119*, 10885–10894.

[240] Nasar, A. Novel Chitosan-based Nanocomposites for Dye Removal Applications. In *Chitosan-based Adsorbents for Wastewater Treatment*; Materials Research Foundations; Materials Research Forum LLC: Aligargh, 2018; pp 57–81.

[241] Usami, Y.; Kagawa, K.; Kawazoe, M.; Matsumura, Y.; Sakurai, H.; Haruta, M. *Stud. Surf. Sci. Catal.* **1998**, *118*, 83–90.

[242] Nolte, P.; Stierle, A.; Balmes, O.; Srot, V.; van Aken, P. A.; Jeurgens, L. P. H.; Dosch, H. *Catal. Today* **2009**, *145*, 243–250.

[243] Cárdenas-Lizana, F.; Gómez-Quero, S.; Hugon, A.; Delannoy, L.; Louis, C.;

Keane, M. A. *J. Catal.* **2009**, *262*, 235–243.

[244] García-Mota, M.; Bridier, B.; Pérez-Ramírez, J.; López, N. *J. Catal.* **2010**, *273*, 92–102.

[245] Zhivonitko, V. V.; Skovpin, I. V.; Crespo-Quesada, M.; Kiwi-Minsker, L.; Koptyug, I. V. *J. Phys. Chem. C* **2016**, *120*, 4945–4953.

[246] Borodziński, A.; Cybulski, A. *Appl. Catal. A Gen.* **2000**, *198*, 51–66.

[247] van der Drift, R. C.; Bouwman, E.; Drent, E. *J. Organomet. Chem.* **2002**, *650*, 1–24.

[248] Tsud, N.; Johánek, V.; Stará, I.; Veltruská, K.; Matolín, V. *Surf. Sci.* **2000**, *467*, 169–176.

[249] Noack, K.; Zbinden, H.; Schlögl, R. *Catal. Lett.* **1990**, *4*, 145–155.

[250] Crespo-Quesada, M.; Grasemann, M.; Semagina, N.; Renken, A.; Kiwi-Minsker, L. *Catal. Today* **2009**, *147*, 247–254.

[251] Alves, J. A.; Bressa, S. P.; Martinez, O. M.; Barreto, G. F. *Chem. Eng. J.* **2007**, *125*, 131–138.

[252] Molero, H.; Bartlett, B. F.; Tysoe, W. T. *J. Catal.* **1999**, *181*, 49–56.

[253] Aramendia, M. A.; Borau, V.; Jimenez, C.; Marinas, J. M.; Sempere, M. E.; Urbano, F. J.; Villar, L. *Stud. Surf. Sci. Catal.* **1993**, *75*, 2435–2438.

[254] Bridier, B.; Karhánek, D.; Pérez-Ramírez, J.; López, N. *ChemCatChem* **2012**, *4*, 1420–1427.

[255] Metiu, H.; Chrétien, S.; Hu, Z.; Li, B.; Sun, X. *J. Phys. Chem. C* **2012**, *116*, 10439–10450.

[256] Chou, P.; Vannice, M. A. *J. Catal.* **1987**, *104*, 1–16.

[257] Sangeetha, P.; Shanthi, K.; Rao, K. S. R.; Viswanathan, B.; Selvam, P. *Appl. Catal. A Gen.* **2009**, *353*, 160–165.

[258] Mustard, D. G.; Bartholomew, C. H. *J. Catal.* **1981**, *67*, 186–206.

[259] Fu, Q.; Wagner, T.; Olliges, S.; Carstanjen, H.-D. *J. Phys. Chem. B* **2005**, *109*, 944–951.

[260] Sárkány, A.; Zsoldos, Z.; Furlong, B.; Hightower, J. W.; Guczi, L. *J. Catal.* **1993**, *141*, 566–582.

[261] Juszczyk, W.; Karpinski, Z.; Lomot, D.; Pielaszek, J.; Sobczak, J. W. *J. Catal.* **1995**, *151*, 67–76.

[262] Goetz, J.; Volpe, M. A.; Sica, A. M.; Gigola, C. E.; Touroude, R. *J. Catal.* **1997**, *167*, 314–323.

[263] Bensalem, A.; Bozon-Verduraz, F. F.; Perrichon, V. *J. Chem. Soc. Faraday Trans.* **1995**, *91*, 2185–2189.

[264] Bond, G. C. *Metal-Catalyzed Reactions of Hydrocarbons*; Springer US: New York, 2006; Vol. 2006.

[265] Monteiro, R. S.; Dieguez, L. C.; Schmal, M. *Catal. Today* **2001**, *65*, 77–89.

[266] Wojcieszak, R.; Genet, M. J.; Eloy, P.; Ruiz, P.; Gaigneaux, E. M. *J. Phys. Chem. C* **2010**, *114*, 16677–16684.

[267] Nosova, L. V.; Stenin, M. V.; Nogin, Y. N.; Ryndin, Y. A. *Appl. Surf. Sci.* **1992**, *55*, 43–48.

[268] Baetzold, R. C. *J. Catal.* **1973**, *29*, 129–137.

[269] Peng, S.-Y.; Xu, Z.-N.; Chen, Q.-S.; Wang, Z.-Q.; Lv, D.-M.; Sun, J.; Chen, Y.; Guo, G.-C. *ACS Catal.* **2015**, *5*, 4410–4417.

[270] Efremenko, I.; Sheintuch, M. *J. Catal.* **2003**, *214*, 53–67.

[271] Wang, N.; Li, S.; Zong, Y.; Yao, Q. *J. Aerosol Sci.* **2017**, *105*, 64–72.

[272] Claus, P.; Berndt, H.; Mohr, C.; Radnik, J.; Shin, E.-J.; Keane, M. A. *J. Catal.* **2000**, *192*, 88–97.

[273] Militello, M. C.; Simko, S. J. *Surf. Sci. Spectra* **1994**, *3*, 395–401.

[274] Okhlopkova, L. B.; Cherepanova, S. V.; Prosvirin, I. P.; Kerzhentsev, M. A.;

Ismagilov, Z. R. *Appl. Catal. A Gen.* **2018**, *549*, 245–253.

[275] Bragina, G. O.; Smirnova, N. S.; Krivoruchenko, D. S.; Markov, P. V.; Baeva, G. N.; Stakheev, A. Y. *Kinet. Catal.* **2017**, *58*, 763–770.

[276] Yao, K. X.; Zeng, H. C. *J. Phys. Chem. C* **2007**, *111*, 13301–13308.

[277] Choo, H.; He, B.; Liew, K. Y.; Liu, H.; Li, J. *J. Mol. Catal. A Chem.* **2006**, *244*, 217–228.

[278] Bayer, A.; Flechtner, K.; Denecke, R.; Steinrück, H.-P.; Neyman, K. M.; Rösch, N. *Surf. Sci.* **2006**, *600*, 78–94.

[279] Koczkur, K. M.; Mourdikoudis, S.; Polavarapu, L.; Skrabalak, S. E. *Dalt. Trans.* **2015**, *44*, 17883–17905.

[280] Tamtögl, A.; Kratzer, M.; Killman, J.; Winkler, A. *J. Chem. Phys* **2008**, *129*, 224706–224714.

[281] Dent, A. L.; Kokes, R. J. *J. Phys. Chem.* **1969**, *73*, 3772–3780.

[282] Huang, W.; McCormick, J. R.; Lobo, R. F.; Chen, J. G. *J. Catal.* **2007**, *246*, 40–51.

[283] Wang, Z.; Yang, L.; Zhang, R.; Li, L.; Cheng, Z.; Zhou, Z. *Catal. Today* **2016**, *264*, 37–43.

[284] Vilé, G.; Albani, D.; Almora-Barrios, N.; López, N.; Pérez-Ramírez, J. *ChemCatChem* **2016**, *8*, 21–33.

[285] Vitos, L.; Ruban, A. V.; Skriver, H. L.; Kollár, J. *Surf. Sci.* **1998**, *411*, 186–202.

[286] Armbrüster, M.; Behrens, M.; Föttinger, K.; Friedrich, M.; Gaudry, É.; Matam, S. K.; Sharma, H. R. *Catal. Rev.* **2013**, *55*, 289–367.

[287] Smith, G. K.; Lin, S.; Lai, W.; Datye, A.; Xie, D.; Guo, H. *Surf. Sci.* **2011**, *605*, 750–759.

[288] Nozawa, K.; Endo, N.; Kameoka, S.; Pang Tsai, A.; Ishii, Y. *J. Phys. Soc. Japan* **2011**, *80*, 064801-064814.

[289] Amorim, C.; Wang, X.; Keane, M. A. *Chinese J. Catal.* **2011**, *32*, 746–755.

[290] Nikoshvili, L. Z.; Bykov, A. V.; Khudyakova, T. E.; LaGrange, T.; Héroguel, F.; Luterbacher, J. S.; Matveeva, V. G.; Sulman, E. M.; Dyson, P. J.; Kiwi-Minsker, L. *Ind. Eng. Chem. Res.* **2017**, *56*, 13219–13227.

[291] González-Fernández, A.; Pischetola, C.; Cárdenas-Lizana, F. *Catalysts* **2019**, *9*, 924–936.

[292] Stakheev, A. Y.; Mashkovskii, I. S.; Baeva, G. N.; Telegina, N. S. *Russ. J. Gen. Chem.* **2010**, *80*, 618–629.

[293] Albani, D.; Shahrokhi, M.; Chen, Z.; Mitchell, S.; Hauert, R.; López, N.; Pérez-Ramírez, J. *Nat. Commun.* **2018**, *9*, 2634–2645.

[294] Musolino, M. G.; Caia, C. V.; Mauriello, F.; Pietropaolo, R. *Appl. Catal. A Gen.* **2010**, *390*, 141–147.

[295] Cherkasov, N.; Ibhadon, A. O.; McCue, A.; Anderson, J. .; Johnston, S. K. *Appl. Catal. A Gen.* **2015**, *497*, 22–30.

[296] Maccarrone, M. J.; Lederhos, C. R.; Torres, G.; Betti, C.; Coloma-Pascual, F.; Quiroga, M. E.; Yori, J. C. *Appl. Catal. A Gen.* **2012**, *441*, 90–98.

[297] Simagina, V.; Likholobov, V.; Bergeret, G.; Gimenez, M.; Renouprez, A. *Appl. Catal. B Environ.* **2003**, *40*, 293–304.

[298] Hou, R.; Yu, W.; Porosoff, M. D.; Chen, J. G.; Wang, T. *J. Catal.* **2014**, *316*, 1–10.

[299] Hillebrecht, F. U.; Fuggle, J. C.; Bennett, P. A.; Zołnierek, Z.; Freiburg, C. *Phys. Rev. B* **1983**, *27*, 2179–2193.

[300] Salagre, P.; Fierro, J. L. G.; Medina, F.; Sueiras, J. E. *J. Mol. Catal. A Chem.* **1996**, *106*, 125–134.

[301] Sakthivel, S.; Shankar, M.; Palanichamy, M.; Arabindoo, B.; Bahnemann, D.; Murugesan, V. *Water Res.* **2004**, *38*, 3001–3008.

[302] Yamakawa, T.; Tatami, J.; Wakihara, T.; Komeya, K.; Meguro, T.; MacKenzie,

K. J. D.; Takagi, S.; Yokouchi, M. *J. Am. Ceram. Soc.* **2006**, *89*, 171–175.

[303] Jujjuri, S.; Ding, E.; Shore, S. G.; Keane, M. A. *J. Mol. Catal. A Chem.* **2007**, *272*, 96–107.

[304] Insorn, P.; Kitiyanan, B. *Catal. Today* **2015**, *256*, 223–230.

[305] Brown, M. E.; Dollimore, D.; Galwey, A. K.; Bamford, C. H.; Tipper, C. F. H. Decopomposition Reactions of Binary Compounds. In *Reactions in the Solid State Vol. 22*; Elsevier: Amsterdam, 1980; pp 151–153.

[306] Nag, N. K. *J. Phys. Chem. B* **2001**, *105*, 5945–5949.

[307] Frieske, H.; Wicke, E. *Ber. Bunsen-Ges. Phys. Chem* **1973**, *77*, 48–52.

[308] Aduriz, H. R.; Bodnariuk, P.; Coq, B.; Figueras, F. *J. Catal.* **1989**, *119*, 97–107.

[309] Li, F.; Zhang, Q.; Wang, Y. *Appl. Catal. A Gen.* **2008**, *334*, 217–226.

[310] Otto, K.; Haack, L. P.; Devries, J. E. *Appl. Catal. B Environ.* **1992**, *1*, 1–12.

[311] Li, F.; Yi, X.; Fang, W. *Catal. Lett.* **2009**, *130*, 335–340.

[312] Louis, C.; Cheng, Z. X.; Che, M. *J. Phys. Chem.* **1993**, *97*, 5703–5712.

[313] Nakagawa, Y.; Nakazawa, H.; Watanabe, H.; Tomishige, K. *ChemCatChem* **2012**, *4*, 1791–1797.

[314] Eley, D. D.; Pines, H.; Weisz, P. B. Catalytic Reactivity of Hydrogen on Palladium and Nickel Hydride Phase. In *Advances in Catalysis Vol.24*; Elsevier: Varsaw, 1975; pp 245–289.

[315] Khan, Z.; Dummer, N. F.; Edwards, J. K. *Philos. Trans. R. Soc. A Math. Phys. Eng. Sci.* **2018**, *376*, 20170058–20170070.

[316] Snider, J. L.; Streibel, V.; Hubert, M. A.; Choksi, T. S.; Valle, E.; Upham, D. C.; Schumann, J.; Duyar, M. S.; Gallo, A.; Abild-Pedersen, F. *ACS Catal.* **2019**, *9*, 3399–3412.

[317] Babu, S. N.; Lingaiah, N.; Prasad, P. S. S. *Appl. Catal. B Environ.* **2012**, *111–112*, 309–316.

[318] Mierczynski, P.; Mierczynska, A.; Ciesielski, R.; Mosinska, M.; Nowosielska, M.; Czylkowska, A.; Maniukiewicz, W.; Szynkowska, M. I.; Vasilev, K. *Catalysts* **2018**, *8*, 380–400.

[319] Pecharromán, C.; González-Carreño, T.; Iglesias, J. E. *J. Mater. Res.* **1996**, *11*, 127–133.

[320] Chen, H.; Brener, N. E.; Callaway, J. *Phys. Rev. B* **1989**, *40*, 1443–1449.

[321] Lu, P.; Teranishi, T.; Asakura, K.; Miyake, M.; Toshima, N. *J. Phys. Chem. B* **1999**, *103*, 9763–9682.

[322] Yuvaraj, S.; Fan-Yuan, L.; Tsong-Huei, C.; Chuin-Tih, Y. *J. Phys. Chem. B* **2003**, *107*, 1044–1047.

[323] Ren, S.; Qiu, J.; Wang, C.; Xu, B.; Fan, Y.; Chen, Y. *Chinese J. Catal.* **2007**, *28*, 651–656.

[324] Torrente-Murciano, L. *J. Nanoparticle Res.* **2016**, *18*, 87–94.

[325] Zhao, J.; Sarkar, A.; Manthiram, A. *Electrochim. Acta* **2010**, *55*, 1756–1765.

[326] Renouprez, A.; Faudon, J. F.; Massardier, J.; Rousset, J. L.; Delichère, P.; Bergeret, G. *J. Catal.* **1997**, *170*, 181–190.

[327] Liao, H.; Fisher, A.; Xu, Z. J. *Small* **2015**, *11*, 3221–3246.

[328] Clark, E. A.; Yeske, R.; Birnbaum, H. K. *Metall. Trans. A* **1980**, *11*, 1903–1908.

[329] Jak, M. J. J.; Konstapel, C.; van Kreuningen, A.; Verhoeven, J.; Frenken, J. W. M. *Surf. Sci.* **2000**, *457*, 295–310.

[330] Brun, M.; Berthet, A.; Bertolini, J. *J. Electron Spectros. Relat. Phenomena* **1999**, *104*, 55–60.

[331] Taylor, A. *J. Chem. Technol. Biotechnol.* **2007**, *53*, 215–215.

[332] Egelhoff, W. F. *Surf. Sci. Rep.* **1987**, *6*, 253–415.

[333] Hermann, P.; Guigner, J. M.; Tardy, B.; Jugnet, Y.; Simon, D.; Bertolini, J.-C. *J. Catal.* **1996**, *163*, 169–175.

[334] Bertolini, J. C.; Miegge, P.; Hermann, P.; Rousset, J. L.; Tardy, B. *Surf. Sci.* **1995**, *331–333*, 651–658.

[335] Cao, Y.; Nyborg, L.; Jelvestam, U. *Surf Interface Anal.* **2009**, *41*, 471–483.

[336] Loviat, F.; Czekaj, I.; Wambach, J.; Wokaun, A. *Surf. Sci.* **2009**, *603*, 2210–2217.

[337] Stakheev, A. Y.; Kustov, L. . *Appl. Catal. A Gen.* **1999**, *188*, 3–35.

[338] Pacchioni, G.; Rösch, N. *Surf. Sci.* **1994**, *306*, 169–178.

[339] Hermann, P.; Simon, D.; Sautet, P.; Bigot, B. *J. Catal.* **1997**, *167*, 33–42.

[340] Koeppel, R. A.; Wehrli, J. T.; Wainwright, M. S.; Trimma, D. L.; Cant, N. W. *Appl. Catal. A Gen.* **1994**, *120*, 163–177.

[341] Kuhn, M.; Lucas, M.; Claus, P. *Ind. Eng. Chem. Res.* **2015**, *54*, 6683–6691.

[342] Muscat, J. P. *Surf. Sci.* **1981**, *110*, 389–399.

[343] Park, J.-Y.; Lee, Y.-J.; Karandikar, P. R.; Jun, K.-W.; Bae, J. W.; Ha, K.-S. *J. Mol. Catal. A Chem.* **2011**, *344*, 153–160.

[344] Rojas, H.; Martínez, J. J.; Mancípe, S.; Borda, G.; Reyes, P. *React. Kinet. Mech. Catal.* **2012**, *106*, 445–455.

[345] Mahata, N.; Vishwanathan, V. *Adsorpt. Sci. Technol.* **1997**, *15*, 165–172.

[346] Ranganathan, E. S.; Bej, S. K.; Thompson, L. T. *Appl. Catal. A Gen.* **2005**, *289*, 153–162.

[347] Deuss, H.; van der Avoird, A. *Phys. Rev. B* **1973**, *8*, 2441–2444.

[348] Christmann, K. *Surf. Sci. Rep.* **1988**, *9*, 1–163.

[349] Ma, S.; Fei, S.; Huang, L.; Forrey, R. C.; Cheng, H. *ACS Omega* **2019**, *4*, 12498–12504.

[350] Malyala, R. V.; Rode, C. V.; Arai, M.; Hegde, S. G.; Chaudhari, R. V. *Appl. Catal. A Gen.* **2000**, *193*, 71–86.

[351] Lederhos, C.; Betti, C.; Liprandi, D.; Cagnola, E.; Quiroga, M. Alkyne Selective Hydrogenation with Mono- and Bimetallic- Anchored Catalysts. In *New Advances in Hydrogenation Processes - Fundamentals and Applications*; Ravanchi, M. T., Ed.; InTech: Rijeka, 2017; pp 15–36.

[352] Ojwach, S. O.; Ogweno, A. O. *Transit. Met. Chem.* **2016**, *41*, 539–546.

[353] Urmès, C.; Schweitzer, J.-M.; Cabiac, A.; Schuurman, Y. *Catalysts* **2019**, *9*, 180–193.

[354] Trimm, D. L.; Liu, I. O. Y.; Cant, N. W. *Appl. Catal. A Gen.* **2010**, *374*, 58–64.

[355] Goda, A. M.; Barteu, M. A.; Chen, J. G. *J. Phys. Chem. B* **2006**, *110*, 11823–11831.

[356] Yang, B.; Burch, R.; Hardacre, C.; Headdock, G.; Hu, P. *ACS Catal.* **2012**, *2*, 1027–1032.

[357] Maetz, P.; Touroude, R. *Catal. Letters* **1990**, *4*, 37–42.

[358] Farrar-Tobar, R. A.; Wei, Z.; Jiao, H.; Hinze, S.; de Vries, J. G. *Chem. Eur.J.* **2018**, *24*, 2725–2734.

[359] Ruta, M.; Semagina, N.; Kiwi-Minsker, L. *J. Phys. Chem. C* **2008**, *112*, 13635–13641.

[360] Jin, X.; Chaudhari, R. V. Hydrogenation by Metals. In *Handbook of Solid State Chemistry*; American Cancer Society: Utrecht, 2017; pp 339–392.

[361] Trimm, D. L.; Cant, N. W.; Liu, I. O. Y. *Catal. Today* **2011**, *178*, 181–186.

[362] Lambert, C. K.; Gonzalez, R. D. *Catal. Letters* **1999**, *57*, 1–7.

[363] Su, X.; Tang, N.-Y.; Toguri, J. M. *J. Phase Equilibria* **2002**, *23*, 140–148.

[364] Anjaneyulu, C.; da Costa, L. O. O.; Ribeiro, M. C.; Rabelo-Neto, R. C.; Mattos, L. V.; Venugopal, A.; Noronha, F. B. *Appl. Catal. A Gen.* **2016**, *519*, 85–98.

[365] Pan, Z.; Wang, R.; Chen, J. *Appl. Catal. B Environ.* **2018**, *224*, 88–100.

[366] Spanjers, C. S.; Sim, R. S.; Sturgis, N. P.; Kabius, B.; Rioux, R. M. *ACS Catal.*

2015, *5*, 3304–3315.

[367] Wong, F. H.; Tiong, T. J.; Leong, L. K.; Lin, K.-S.; Yap, Y. H. *Ind. Eng. Chem. Res.* **2018**, *57*, 3163–3174.

[368] Wong, F. H.; Tiong, T. J.; Leong, L. K.; Yap, Y. H. In *AIP Conference Proceedings*; AIP Publishing LLC, 2018; Vol. 2031, pp 1–5.

[369] Rubio-Marcos, F.; Manzano, C. V.; Reinosa, J. J.; Romero, J. J.; Marchet, P.; Martín-González, M. S.; Fernández, J. F. *J. Phys. Chem. C* **2011**, *115*, 13577–13583.

[370] Guczi, L.; Beck, A.; Horváth, A.; Koppány, Z.; Stefler, G.; Frey, K.; Sajó, I.; Geszti, O.; Bazin, D.; Lynch, J. *J. Mol. Catal. A Chem.* **2003**, *204–205*, 545–552.

[371] Porter, F.; International Lead Zinc Research Organization. *Zinc Handbook : Properties, Processing and Use in Design*; CRC Press: North Carolina, 1991.

[372] Li, Y.; Zhang, B.; Xie, X.; Liu, J.; Xu, Y.; Shen, W. *J. Catal.* **2006**, *238*, 412–424.

[373] Manukyan, K. V.; Avetisyan, A. G.; Shuck, C. E.; Chatilyan, H. A.; Rouvimov, S.; Kharatyan, S. L.; Mukasyan, A. S. *J. Phys. Chem. C* **2015**, *119*, 16131–16138.

[374] Richardson, J. T.; Scates, R.; Twigg, M. V. *Appl. Catal. A Gen.* **2003**, *246*, 137–150.

[375] Sehested, J.; Gelten, J. A. P.; Remediakis, I. N.; Bengaard, H.; Nørskov, J. K. *J. Catal.* **2004**, *223*, 432–443.

[376] Caizer, C.; Stefanescu, M. *J. Phys. D. Appl. Phys.* **2002**, *35*, 3035–3040.

[377] Wang, W.; Li, X.; Zhang, Y.; Zhang, R.; Ge, H.; Bi, J.; Tang, M. *Catal. Sci. Technol.* **2017**, *7*, 4413–4421.

[378] Velu, S.; Suzuki, K.; Vijayaraj, M.; Barman, S.; Gopinath, C. S. *Appl. Catal. B Environ.* **2005**, *55*, 287–299.

[379] Jafarbegloo, M.; Tarlani, A.; Mesbah, A. W.; Sahebdelfar, S. *J. Nat. Gas Sci.*

Eng. **2015**, *27*, 1165–1173.

[380] García, V.; Fernández, J. J.; Ruíz, W.; Mondragón, F.; Moreno, A. *Catal. Commun.* **2009**, *11*, 240–246.

[381] Qiao, Z.; Yan, L.; Cao, Z.; Xie, Y. *J. Alloys Compd.* **2001**, *325*, 180–189.

[382] Parmaliana, A.; Arena, F.; Frusteri, F.; Giordano, N. *J. Chem. Soc. Faraday Trans.* **1990**, *86*, 2663–2669.

[383] Murzinova, M. A.; Salishchev, G. A.; Afonichev, D. D. *Int. J. Hydrogen Energy* **2002**, *27*, 775–782.

[384] Amorim, C.; Keane, M. A. *J. Hazard. Mater.* **2012**, *211–212*, 208–217.

[385] Cardenas-Lizana, F.; Gomez-Quero, S.; Keane, M. A. *Catal. Letters* **2009**, *127*, 25–32.

[386] Smeds, S.; Salmi, T.; Lindfors, L. P.; Krause, O. *Appl. Catal. A Gen.* **1996**, *144*, 177–194.

[387] Bridier, B.; López, N.; Pérez-Ramírez, J. *J. Catal.* **2010**, *269*, 80–92.

[388] Rodríguez, J. C.; Marchi, A. J.; Borgna, A.; Monzón, A. *J. Catal.* **1997**, *171*, 268–278.

[389] Shin, E. W.; Choi, C. H.; Chang, K. S.; Na, Y. H.; Moon, S. H. *Catal. Today* **1998**, *44*, 137–143.

[390] Rodriguez, J. A.; Kuhn, M. *J. Phys. Chem.* **1996**, *100*, 381–389.

[391] Benseradj, F.; Sadi, F.; Chater, M. *Appl. Catal. A Gen.* **2002**, *228*, 135–144.

[392] Collins, S. E.; Chiavassa, D. L.; Bonivardi, A. L.; Baltanás, M. A. *Catal. Lett.* **2005**, *103*, 83–88.

[393] Wang, L.; Yin, C.; Yang, R. T. *Appl. Catal. A Gen.* **2016**, *514*, 35–42.

[394] Santolalla-Vargas, C. E.; Toriello, V. A.; de los Reyes, J. A.; Cromwell, D. K.; Pawelec, B.; Fierro, J. L. G. *Mater. Chem. Phys.* **2015**, *166*, 105–115.

[395] Kotsev, N. K.; Ilieva, L. I. *Catal. Lett.* **1993**, *18*, 173–176.

[396] Drouet, C.; Alphonse, P.; Rousset, A. *Solid State Ionics 123*, 25–37.

[397] Conner, W. C.; Falconer, J. L. *Chem. Rev.* **1995**, *95*, 759–788.

[398] Shi, Q.; Li, Z.; Li, B.; Hu, X. *J. Rare Earths* **2009**, *27*, 443–446.

[399] Hu, B.; Yin, Y.; Liu, G.; Chen, S.; Hong, X.; Tsang, S. C. E. *J. Catal.* **2018**, *359*, 17–26.

[400] Natesakhawat, S.; Ohodnicki, P. R.; Howard, B. H.; Lekse, J. W.; Baltrus, J. P.; Matranga, C. *Top. Catal.* **2013**, *56*, 1752–1763.

[401] Liu, F.; Liu, L.; Xue, D.; Li, F. *J. Fuel Chem. Technol.* **2016**, *44*, 477–482.

[402] Song, Y.; Laursen, S. *J. Catal.* **2019**, *372*, 151–162.

[403] Burch, R.; Chappell, R. J.; Golunski, S. E. *J. Chem. Soc. Faraday Trans. 1* **1989**, *85*, 3569–3578.

[404] Shi, C.; Zhu, A. M.; Yang, X. F.; Au, C. T. *Appl. Catal. A Gen.* **2004**, *276*, 223–230.

[405] Dongil, A. B. *Nanomaterials* **2019**, *9*, 1–18.

[406] Jaf, Z.; Altarawneh, M.; Miran, H. A.; Almatarneh, M. H.; Jiang, Z.-T.; Dlugogorski, B. Z. *ACS Omega* **2018**, *3*, 14380–14391.

[407] Hargreaves, J. S. J. *Coord. Chem. Rev.* **2013**, *257*, 2015–2031.

[408] Alexander, A.-M.; Hargreaves, J. S. J. *Chem. Soc. Rev.* **2010**, *39*, 4388–4401.

[409] Altarawneh, M.; Jaf, Z.; Oskierski, H.; Jiang, Z.-T.; Gore, J.; Dlugogorski, B. Z. *J. Phys. Chem. C* **2016**, *120*, 22270–22280.

[410] Demczyk, B. G.; Choi, J.-G.; Thompson, L. T. *Appl. Surf. Sci.* **1994**, *78*, 63–69.

[411] Dewangan, K.; Patil, S. S.; Joag, D. S.; More, M. A.; Gajbhiye, N. S. *J. Phys. Chem. C* **2010**, *114*, 14710–14715.

[412] Fuertes, A. *Mater. Horizons* **2015**, *2*, 453–461.

[413] Sakagami, H.; Asano, Y.; Takahashi, N.; Matsuda, T. *Appl. Catal. A Gen.* **2005**,

284, 123–130.

[414] Wang, D.; Zhu, Y.; Tian, C.; Wang, L.; Zhou, W.; Dong, Y.; Han, Q.; Liu, Y.; Yuan, F.; Fu, H. *Catal. Sci. Technol.* **2016**, *6*, 2403–2412.

[415] Cheng, X.; Wang, D.; Liu, J.; Kang, X.; Yan, H.; Wu, A.; Gu, Y.; Tian, C.; Fu, H. *Nanoscale* **2018**, *10*, 22348–22356.

[416] Zaman, S. F.; Pasupulety, N.; Al-Zahrani, A. A.; Daous, M. A.; Al-Shahrani, S. S.; Driss, H.; Petrov, L. A.; Smith, K. J. *Appl. Catal. A Gen.* **2017**, *532*, 133–145.

[417] Zaman, S. F.; Pasupulety, N.; Al-Zahrani, A. A.; Daous, M. A.; Driss, H.; Al-Shahrani, S. S.; Petrov, L. *Can. J. Chem. Eng.* **2018**, *96*, 1770–1779.

[418] Guerrero-Ruiz, A.; Zhang, Y.; Bachiller-Baeza, B.; Rodríguez-Ramos, I. *Catal. Lett.* **1998**, *55*, 165–168.

[419] Hao, Z.; Wei, Z.; Wang, L.; Li, X.; Li, C.; Min, E.; Xin, Q. *Appl. Catal. A Gen.* **2000**, *192*, 81–84.

[420] Perret, N.; Cárdenas-Lizana, F.; Lamey, D.; Laporte, V.; Kiwi-Minsker, L.; Keane, M. A. *Top. Catal.* **2012**, *55*, 955–968.

[421] Hu, J.; Zhou, Z.; Zhang, R.; Li, L.; Cheng, Z. *J. Mol. Catal. A Chem.* **2014**, *381*, 61–69.

[422] Nikoshvili, L. Z.; Makarova, A. S.; Lyubimova, N. A.; Bykov, A. V.; Sidorov, A. I.; Tyamina, I. Y.; Matveeva, V. G.; Sulman, E. M. *Catal. Today* **2015**, *256*, 231–240.

[423] Wei, R.; Zimmermann, W. *Microb. Biotechnol.* **2017**, *10*, 1302–1307.

[424] Colling, C. W.; Choi, J.-G.; Thompson, L. T. *J. Catal.* **1996**, *160*, 35–42.

[425] O'Connell, K.; Regalbuto, J. R. *Catal. Lett.* **2015**, *145*, 777–783.

[426] Freund, H.; Meijer, G.; Scheffler, M.; Schlögl, R.; Wolf, M. *Angew. Chemie Int. Ed.* **2011**, *50*, 10064–10094.

[427] Choi, J.-G.; Brenner, J. R.; Colling, C. W.; Demczyk, B. G.; Dunning, J. L.; Thompson, L. T. *Catal. Today* **1992**, *15*, 201–222.

[428] Mckay, D.; Hargreaves, J. S. J.; Rico, J. L.; Rivera, J. L.; Sun, X.-L. *J. Solid State Chem.* **2008**, *181*, 325–333.

[429] Zeng, H. C.; Ng, W. K.; Cheong, L. H.; Xie, F.; Xu, R. *J. Phys. Chem. B* **2001**, *105*, 7178–7181.

[430] Sha, X.; Chen, L.; Cooper, A. C.; Pez, G. P.; Cheng, H. *J. Phys. Chem. C* **2009**, *113*, 11399–11407.

[431] Sakagami, H.; Asano, Y.; Ohno, T.; Takahashi, N.; Itoh, H.; Matsuda, T. *Appl. Catal. A Gen.* **2006**, *297*, 189–197.

[432] Zhang, Y.-J.; Xin, Q.; Rodriguez-Ramos, I.; Guerrero-Ruiz, A. *Appl. Catal. A Gen.* **1999**, *180*, 237–245.

[433] Mestl, G.; Herzog, B.; Schlögl, R.; Knözinger, H. *Langmuir* **1995**, *11*, 3027–3034.

[434] Ozkan, U. S.; Zhang, L.; Clark, P. A. *J. Catal.* **1997**, *172*, 294–306.

[435] Bratan, V.; Munteanu, C.; Hornoiu, C.; Vasile, A.; Papa, F.; State, R.; Preda, S.; Culita, D.; Ionescu, N. I. *Appl. Catal. B Environ.* **2017**, *207*, 166–173.

[436] Choi, J.-G.; Lee, H. J.; Thompson, L. T. *Appl. Surf. Sci.* **1994**, *78*, 299–307.

[437] Zhang, Y.; Li, Y. *Stud. Surf. Sci. Catal.* **1997**, *112*, 457–464.

[438] Redjel, A.; Boudjahem, A.-G.; Bettahar, M. *Part. Sci. Technol.* **2018**, *36*, 710–715.

[439] Li, X. S.; Zhang, Y. J.; Xin, Q.; Ji, C. X.; Miao, Y. F.; Wang, L. *React. Kinet. Catal. Lett.* **1996**, *57*, 177–182.

[440] McCue, A.; McRitchie, C.; Shepherd, A.; Anderson, J. *J. Catal.* **2014**, *319*, 127–135.

[441] Lee, D. K. *Korean J. Chem. Eng.* **1990**, *7*, 233–235.

[442] Bridier, B.; Pérez-Ramírez, J. *J. Am. Chem. Soc* **2010**, *132*, 4231–4327.

[443] Hartog, A. J. D.; Deng, M.; Jongerius, F.; Ponec, V. *J. Mol. Catal.* **1990**, *60*, 99–

108.

[444] Shimazu, S.; Teramoto, W.; Iba, T.; Miura, M.; Uematsu, T. *Catal. Today* **1989**, *6*, 141–146.

[445] Kim, B.-J.; Lee, Y.-S.; Park, S.-J. *Int. J. Hydrogen Energy* **2008**, *33*, 4112–4115.

[446] Herrmann, J. M. *J. Catal.* **1984**, *89*, 404–412.

[447] Cárdenas-Lizana, F.; Hao, Y.; Crespo-Quesada, M.; Yuranov, I.; Wang, X.; Keane, M. A.; Kiwi-Minsker, L. *ACS Catal.* **2013**, *3*, 1386–1396.

[448] Bernal, S.; Botana, F. J.; Calvino, J. J.; López, C.; Pérez-Omil, J. A.; Rodríguez-Izquierdo, J. M. *J. Chem. Soc. Faraday Trans.* **1996**, *92*, 2799–2809.

[449] Wang, F.; Lu, G. *J. Power Sources* **2008**, *181*, 120–126.

[450] Hu, X.; Skadtchenko, B. O.; Trudeau, M.; Antonelli, D. M. *J. Am. Chem. Soc.* **2006**, *128*, 11740–11741.

[451] M. Chai, X. Liu, L. Li, G. Pei, Y. Ren, Y. Su, H. Cheng, A. Wang, T. Zhang, Chin. J. Catal. **2017,** *38*, 1338–1346.

[452] Bönnemann, H.; Brijoux, W.; Tilling, A. S.; Siepen, K. *Top. Catal.* **1997**, *4*, 217–227.

[453] Nash, C.; Yung, M.; Chen, Y.; Carl, S.; Thompson, L.; Schaidle, J. *Catalysis by Metal Carbides and Nitrides*; Wiley: New York, 2017.